

**FEDERAL UNIVERSITY OF SANTA CATARINA  
DEPARTMENT OF MECHANICAL ENGINEERING**

Jaime Andrés Lozano Cadena

**DESIGNING A ROTARY MAGNETIC  
REFRIGERATOR**

Florianópolis  
2015



Jaime Andrés Lozano Cadena

**DESENVOLVIMENTO DE UM SISTEMA DE  
REFRIGERAÇÃO MAGNÉTICA DO TIPO  
ROTATIVO**

Tese submetida ao Programa de  
Pós-Graduação em Engenharia  
Mecânica da Universidade Federal  
de Santa Catarina para a obtenção  
do título de Doutor em Engenharia  
Mecânica.

Orientador:

Prof. Jader Riso Barbosa Jr., Ph.D.

Coorientador:

Prof. Alvaro Toubes Prata, Ph.D.

Florianópolis

2015

Ficha de identificação da obra elaborada pelo autor,  
através do Programa de Geração Automática da Biblioteca Universitária da UFSC.

Lozano Cadena, Jaime Andrés

Desenvolvimento de um sistema de refrigeração magnética  
do tipo rotativo / Jaime Andrés Lozano Cadena ;  
orientador, Jader Riso Barbosa Jr. ; coorientador, Alvaro  
Toubes Prata. - Florianópolis, SC, 2015.  
255 p.

Tese (doutorado) - Universidade Federal de Santa  
Catarina, Centro Tecnológico. Programa de Pós-Graduação em  
Engenharia Mecânica.

Inclui referências

1. Engenharia Mecânica. 2. Refrigeração magnética. 3.  
Regenerador magnético ativo (RMA). 4. Efeito  
magnetocalórico (EMC). 5. Circuito magnético de ímãs  
permanentes. I. Barbosa Jr., Jader Riso. II. Prata, Alvaro  
Toubes. III. Universidade Federal de Santa Catarina.  
Programa de Pós-Graduação em Engenharia Mecânica. IV. Título.

Jaime Andrés Lozano Cadena

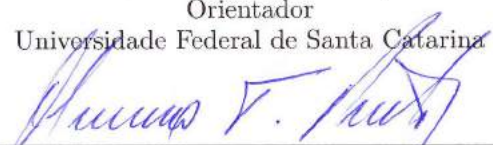
**DESENVOLVIMENTO DE UM SISTEMA DE  
REFRIGERAÇÃO MAGNÉTICA DO TIPO  
ROTATIVO**

Esta Tese foi julgada adequada para obtenção do Título de “Doutor em Engenharia Mecânica”, e aprovada em sua forma final pelo Programa de Pós-Graduação em Engenharia Mecânica da Universidade Federal de Santa Catarina.

Florianópolis, 8 de maio de 2015.

  
\_\_\_\_\_  
Prof. Jader Riso Barbosa Jr., Ph.D.  
Orientador

Universidade Federal de Santa Catarina

  
\_\_\_\_\_  
Prof. Alvaro Toubes Prata, Ph.D.  
Coorientador

Universidade Federal de Santa Catarina

  
\_\_\_\_\_  
Prof. Armando Albertazzi Gonçalves Jr., Dr. Eng.  
Coordenador do Curso

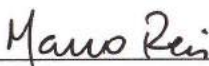


**Banca Examinadora:**



---

Prof. Jader Riso Barbosa Jr., Ph.D. – Presidente  
Universidade Federal de Santa Catarina



---

Prof. Mario de Souza Reis Jr., Dr. – Relator  
Universidade Federal Fluminense



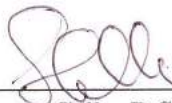
---

Dr. Christian Robert Haffenden Bahl  
Universidade Técnica da Dinamarca



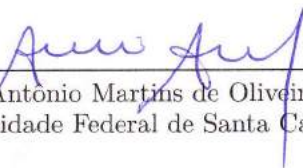
---

Prof. João Pedro Assumpção Bastos, Dr.  
Universidade Federal de Santa Catarina



---

Prof. Sergio Colle, D.Sc.  
Universidade Federal de Santa Catarina



---

Prof. Amir Antonio Martins de Oliveira Jr., Ph.D.  
Universidade Federal de Santa Catarina



# ABSTRACT

Magnetic refrigeration is an emerging cooling technology for applications at room-temperature. The magnetocaloric effect (MCE) is the thermal response of a magnetic material when subjected to a changing magnetic field. Magnetic refrigeration harvests the MCE in a regenerative thermodynamic cycle to transfer heat from a low-temperature environment to a high-temperature one by means of magnetic work in an active magnetic regenerator (AMR). In this thesis, several aspects of this technology were analyzed with contributions on four research fronts. First, a temperature controlled facility was constructed to improve the direct measurements of the MCE by means of the adiabatic temperature change,  $\Delta T_{\text{ad}}$ . Measurements of the benchmark magnetocaloric material gadolinium (Gd), and one of the most promising magnetic refrigerants, MnFe(P,As), were investigated. Second, a magnetic circuit with a 2-pole rotor-stator configuration with high magnetic flux regions of approximately 1 T was designed aiming at an efficient use of the Nd-Fe-B permanent magnets. A novel method to optimize the magnetic circuit was proposed by employing a magnet wedge concept. Third, a novel rotary magnetic refrigerator was designed and built at the Federal University of Santa Catarina (UFSC) using the optimized rotary magnetic circuit and a stationary AMR composed by 8 pairs beds packed with 1.7 kg of Gd spheres. Two low-friction rotary valves were developed to synchronize the hydraulic and magnetic cycles and positioned at the hot end to avoid heat generation in the cold end. The last part of this thesis comprised an experimental and thermodynamic performance analysis of the rotary magnetic cooler prototype developed at the Technical University of Denmark (DTU). A detailed study of the losses external to the regenerator and a methodology to breakdown the COP and the motor power was developed to quantify the efficiency improvements of the system and the major losses. The performance of both magnetic refrigerators were evaluated in terms of the regenerator temperature span, coefficient of performance (COP) and the overall second-law efficiency ( $\eta_{2\text{nd}}$ ) as a function of different operating conditions.

**Keywords:** Magnetic refrigeration, magnetocaloric effect (MCE), active magnetic regenerator (AMR), magnetic circuit, permanent magnet.



# RESUMO

A refrigeração magnética é uma tecnologia alternativa de refrigeração para aplicações ao redor da temperatura ambiente baseada no efeito magnetocalórico (EMC). Este efeito se manifesta por meio de uma variação instantânea na temperatura de um material magnético quando submetido a uma variação de campo magnético externo. Um regenerador magnético ativo (RMA) submetido a um ciclo termodinâmico regenerativo permite transferir calor de um reservatório de baixa temperatura para um de alta temperatura através do trabalho magnético. Neste trabalho de doutorado foi realizada uma análise desta tecnologia com contribuições em quatro frentes de pesquisa. Na primeira etapa foi desenvolvida uma câmara de temperatura controlada para melhorar a medição direta do EMC por meio da variação adiabática da temperatura,  $\Delta T_{ad}$ . Neste trabalho foram caracterizadas amostras do material magnetocalórico de referência, gadolínio (Gd), e amostras de um dos refrigerantes magnéticos mais promissores, MnFe(P,As). A segunda frente consistiu no projeto de um circuito magnético do tipo rotor-estator com dois polos magnéticos de fluxo magnético de aproximadamente 1 T visando o uso eficiente dos ímãs permanentes de Nd-Fe-B, por meio de uma metodologia proposta através do conceito de segmentos magnetizados. Na terceira etapa, foi projetado e construído um refrigerador magnético do tipo rotativo na Universidade Federal de Santa Catarina (UFSC) composto pelo circuito magnético otimizado e um RMA fixo com 8 pares de camadas empacotadas com 1.7 kg de esferas de Gd. A sincronização magneto-hidráulica foi realizada por duas válvulas rotativas de baixo atrito, desenvolvidas neste trabalho, ambas alocadas no lado quente do sistema para evitar geração de calor no lado frio. Na última parte desta tese, foi realizada uma análise experimental e termodinâmica de um sistema de refrigeração magnética desenvolvido na Universidade Técnica da Dinamarca (DTU). Um mapeamento detalhado das perdas externas ao regenerador e uma análise de decomposição do COP e da potência consumida pelo motor foram conduzidos para quantificar as melhoras na eficiência do sistema e as perdas mais relevantes. O desempenho de ambos sistemas foi avaliado em termos da amplitude de temperatura do regenerador, do coeficiente de performance (COP) e da eficiência de segunda lei da termodinâmica ( $\eta_{2nd}$ ) em função de diferentes condições de operação.

**Palavras-chave:** Refrigeração magnética, regenerador magnético ativo (RMA), efeito magnetocalórico (EMC), circuito magnético, ímã permanente.



# ACKNOWLEDGEMENTS

As Stephen Hawking once said, unlike to a theoretical work, experimental activities involve being part of a team. Accomplishing this Ph.D. thesis would have been impossible without the assistance of many great and inspirational people.

Firstly, I would like to acknowledge specially Prof. Jader Barbosa for his invaluable advices and patience, for always being available to reply a question and be opened for discussion, as well as for bravely read and comment on this manuscript. I am grateful to Prof. Alvaro Prata for the invitation to join POLO Labs and for his heartening during this work. His enthusiasm on innovation and emerging technologies is duly acknowledged.

A considerable *momentum* for this thesis was gained at Risø Labs of the Technical University of Denmark (DTU) and throughout their published work. I am much indebted to Dr. Christian Bahl for the opportunity to be part of his team and for the great discussions and knowledge transferred, as well as for the contributions and suggestions in this thesis. I am also indebted to Dr. Nini Pryds for the great chance to be a member of his research group.

Specially thanks are owed to one of the magnetic refrigeration references, Dr. Kurt Engelbrecht, with whom it was great, not only to work with, but to share an out-of-the-lab friendship. I benefited much from the published work of Dr. Rasmus Bjørk and the discussions about the magnetic circuit design. I am also much indebted to Dr. Kaspar Nielsen for his hospitality, magnetocaloric advices and the cakes. I extended my gratitude to Dr. Anders Smith, Lars von Moos and Dan Eriksen for the teachings. The technical training and teachings of Jørgen Geyti are also greatly appreciated. I acknowledge Dr. Armando Tura for the magnetocaloric design advices.

I would like to thank the jury members, Prof. Mario Reis, Prof. Sergio Colle, Prof. João Assumpção Bastos and Prof. Amir Oliveira for agreeing to evaluate this thesis and for their suggestions to improve this manuscript. Also, I thank Prof. Rogerio Ferreira.

I am very grateful to Paulo Trevizoli for his partnership in this endeavor and for all the fruitful discussions and knowledge shared

during this Ph.D. thesis. I owe a great debt to Matheus Capovilla for his invaluable and impassioned contributions to this work. Specially for the direct measurements and his assistance to mount, instrument and test the UFSC magnetic refrigerator. The gratitude is extended to Diego Alcalde for his support in the magnetic circuit design and characterization and to Fabio Canesin for his initial assistance. Also, I acknowledge the new members of our magnetocaloric team at Polo: Alan Nakashima, Jean Cararo and Guilherme Peixer.

I am grateful to the design and technical assistance of Marcelo Ribeiro, specially for the rotary valves and regenerator designs. The acknowledge is extended to Pedro Cardoso and Rafael Lima for their technical assistance. I am also thankful with Rafael Dantas for the rendered images. I extend my acknowledge to Luis Vieira, Nara Santos, Márcia dos Santos and Robson dos Santos.

I am deeply grateful to Dr. Dalton Bertoldi, a *passive* researcher, for his assistance in the experimental work and for his inspiring friendship. My grateful is extended to Pedro Magalhães for his geniality and cheerful support, specially in the uncertainty analysis. I also thank Daniel Hense for the discussions regarding experimental issues.

I specially thanks Prof. Cristiano Teixeira for his friendship and the prolific discussions about magnetism and life. I extend my acknowledges to the MAGMA group, specially to Prof. Paulo Wendhausen, Henrique Bez, Leonardo Lopes and Bruno Eggert.

I would like to thank my colleagues at Polo, specially, Pablo, Moisés, Fábio, Paulo, João Paulo, Fernando, Silvia, Eduardo, Camilo, Vinicius and Marco Diniz. I thank my Colombian friends in Florianópolis, specially, Renzo, Sergio, Tatiana, Julian, Juan Martin, Oscar, Leonardo, Alvaro, Yesid, Luis, Carlos and Jair. I acknowledge my friend Jonas. And I thank Brazil and Denmark and the worldwide people I have had the opportunity to meet.

I thank Lian Zhang, Ekkes Brück and BASF for the manganese samples and the magnetocaloric measurements of the gadolinium (Gd). I extend the acknowledge to Edson Santos and Jessee Azevedo for the Gd characterization.

I am greatly grateful to my family for their support and their teachings that made who I am today.

I specially acknowledge Virgínia for her affectionate encouragement and motivation on this journey.

Financial support from CNPq agency and Embraco is duly acknowledged.

*“The progressive development of man  
is vitally dependent on invention.  
It is the most important product  
of his creative brain.”*  
**Nikola Tesla**



# LIST OF FIGURES

Figure 1 – Illustration of the magnetocaloric effect (MCE) represented by the adiabatic and the isothermal magnetization processes in a $T$ - $S$ diagram. . . . .	39
Figure 2 – Pictorial description of a magnetic refrigeration cycle. . . . .	42
Figure 3 – Interconnection between the design parameters of a magnetic refrigerator (Barbosa <i>et al.</i> , 2014a). . . . .	44
Figure 4 – Magnetocaloric properties (a) $\Delta T_{\text{ad}}$ and (b) $\Delta S$ for a Gd for an applied magnetic field of 2 T (Pecharsky & Gschneidner Jr., 2006). . . . .	51
Figure 5 – Maximum magnetic entropy change for $\mu_0 \Delta H = 5$ T versus peak temperature for different families of magnetocaloric materials. . . . .	52
Figure 6 – Entropy variation for different samples based on $\text{La}(\text{Fe},\text{Si})_{13}$ for an applied magnetic field of 2 T and compared with Gd (Brück, 2005). . . . .	53
Figure 7 – Magnetization as a function of temperature for $\text{MnFeP}_{0.45}\text{As}_{0.55}$ for $\mu_0 H = 1$ T (Tegus <i>et al.</i> , 2002). . . . .	54
Figure 8 – Regenerator types: (a) rotary regenerator; (b) fixed-bed regenerator with two regenerative matrices. Adapted from Kuppan (2000). . . . .	57
Figure 9 – Rotary regenerators: (a) <i>Ljungstrom</i> type or a rotary regenerative matrix; and (b) <i>Rothemuhle</i> type or a stationary matrix with rotary sealing (Reay., 1979). . . . .	58
Figure 10 – Schematic description of the processes in a thermo-magnetic Brayton cycle. . . . .	59
Figure 11 – First generation of a rotary AMR developed at the Astronautics Corporation of America. . . . .	65
Figure 12 – Second generation of a rotary AMR developed at the Astronautics Corporation of America (Zimm <i>et al.</i> , 2007). . . . .	66

Figure 13 – Japanese AMR system: (a) Photograph of the second generation AMR and (b) system configuration (Okamura <i>et al.</i> , 2007). . . . .	67
Figure 14 – Compact permanent magnet AMR developed at UVic (a) Photograph of the system and (b) hydraulic schematics. . . . .	68
Figure 15 – AMR system developed at Risø - DTU: (a) Photograph of the device showing the magnet assembly, the flow manifold and the rotary valves; (b) The 24-bed regenerator assembly is installed in the magnetized gap. . . . .	69
Figure 16 – Typical hysteresis curve for a ferromagnetic material. . . . .	73
Figure 17 – Working point and its calculated energy product ( $BH$ ) for a Nd-Fe-B permanent magnet with linear demagnetization curve ( $\mathbf{B} = \mu_0\mu_r\mathbf{H} + \mathbf{B}_{rem}$ ). . . . .	74
Figure 18 – Typical demagnetization curves for the most important permanent magnets. Adapted from Bastos (2004). . . . .	75
Figure 19 – Schematic representation of the magnetic field distribution of a bar magnet: (a) magnetic field, $\mathbf{H}$ ; (b) induced field $\mathbf{B}$ and (c) $\mathbf{B}$ , $\mathbf{H}_{dem}$ and $\mathbf{M}$ inside the magnet. Adapted from Furlani (2001). . . . .	76
Figure 20 – Generic profiles of the magnetic field (continuous line) and the hydraulic blows on an AMR as a function of time (dashed line). Adapted from Bjørk & Engelbrecht (2011). . . . .	78
Figure 21 – (a) Magnetic system composed of two rotary concentric Halbach cylinders in the position of $\mu_0 H_{high}$ (Tura & Rowe, 2007) and (b) a complex double Y-shaped magnetic array. . . . .	80
Figure 22 – Rotor-stator magnetic circuits developed by (a) Okamura <i>et al.</i> (2007) and (b) Allab (2008) and Boucekara (2008). . . . .	81
Figure 23 – Static magnetic circuit of Bjørk <i>et al.</i> (2010a). . . . .	81
Figure 24 – Apparatus to measure the magnetocaloric effect via the direct method (Trevizoli <i>et al.</i> , 2012). . . . .	84
Figure 25 – Purpose-built temperature controlled chamber. . . . .	85
Figure 26 – Experimental apparatus inside the purpose-built temperature controlled chamber. . . . .	85
Figure 27 – (a) Copper coil heat exchanger and (b) Peltier system. . . . .	86

Figure 28 – Sample preparation: (a) Step-by-step preparation of a sample for the direct measurements and (b) sample with the polystyrene insulation (Trevizoli <i>et al.</i> , 2012). . . . .	86
Figure 29 – Typical experimental result of the temperature variation due to magnetization and demagnetization of a sample. . . . .	87
Figure 30 – Coordinate system employed for the calculation of the demagnetization factor of a rectangular prism body. The applied magnetic field, $\mathbf{H}_{\text{appl}}$ , is parallel to the $z$ -axis (Aharoni, 1998). . . . .	89
Figure 31 – Experimental $\Delta T_{\text{ad}}$ for sample Gd-1 while magnetization and demagnetization and calculated demagnetization curve from Nielsen <i>et al.</i> (2010) proposed constraint. . . . .	90
Figure 32 – Demagnetization factor dependence on $\Delta T_{\text{ad}}$ as a function of temperature. . . . .	91
Figure 33 – Internal magnetic field as a function of temperature for samples with $N_D = 0.213$ (continuous line) and $N_D = 0.687$ (discontinuous line) for an applied magnetic field of 1.75 T. . . . .	92
Figure 34 – Adiabatic temperature change for sample Mn-1 with an unusual effect at its first thermal cycles while magnetization. . . . .	93
Figure 35 – Direct measurement of the adiabatic temperature change for samples (a) Mn-1, (b) Mn-2 and (c) Mn-3 as a function of temperature while magnetization and demagnetization with an applied magnetic field of 1.75 T. . . . .	94
Figure 36 – Thermal hysteresis in the heating and cooling of the Mn-2 sample. . . . .	95
Figure 37 – Adiabatic temperature change of three MnFe(P,As) samples with different compositions when submitted under an applied magnetic field of 1.75 T. . . . .	96
Figure 38 – Photograph of the rotary magnetic refrigerator developed at Polo-UFSC. . . . .	99
Figure 39 – Cross section view of the magnetic circuit and stationary regenerator beds. . . . .	101
Figure 40 – Basic scheme of the working principle of the rotary device. . . . .	102

Figure 41 – Demagnetization factor, $N_D^{\text{bed}}$ , dependence on (a) length, (b) width and (c) height of the regenerator bed. . . . .	106
Figure 42 – (a) Mass flow rate dependence on $L_{\text{bed}}$ for different utilization factors, (b) pressure drop and (c) pumping power dependence on $L_{\text{bed}}$ for different particle diameters. . . . .	107
Figure 43 – Number of transfer units (NTU) and bed pressure drop dependence on (a) sphere diameters and (b) bed length of the regenerator. . . . .	110
Figure 44 – $B$ - $H$ curve of iron employed for simulations of the magnetic circuit (COMSOL Multiphysics <sup>®</sup> , 2011). . . . .	112
Figure 45 – Basic magnetic circuit dimensions (a) Cross section and (b) isometric views of the simple rotor-stator magnetic array. . . . .	113
Figure 46 – (a) Magnetic flux density and (b) energy product $ BH $ of the basic rotor-stator magnetic circuit. . . . .	114
Figure 47 – A single pair of uniformly magnetized wedges (Abele <i>et al.</i> , 1997). Magnetized regions are dot hatched. . . . .	115
Figure 48 – Schematic representation of one of the four magnetized wedges that compose the new rotor configuration with radius $R_{\text{rot}}$ . . . . .	116
Figure 49 – Geometrical constraints of the design of the magnetized wedges for the new rotor-stator configuration. Magnetized and iron regions are dot and line hatched, respectively. . . . .	117
Figure 50 – Results for $R_{\text{rot}} = 90$ mm, $L_{\text{rot}} = 150$ mm and $\varphi = 26^\circ$ : (a) Wedge volume, $V_{\text{wedge}}$ , dependence on $\alpha_1$ for different $\alpha_2$ and $\theta \geq 25^\circ$ , (b) Angle $\alpha_2$ and segment length $\overline{CG}$ and (c) $V_{\text{wedge}}$ dependence on angle $\alpha_1$ for $\theta = 25^\circ$ . . . . .	119
Figure 51 – Cross section view of the magnet array. . . . .	120
Figure 52 – Stationary 2D simulation of the magnetic flux density norm of the magnetic circuit with permanent magnets with $\ \mathbf{B}_{\text{rem}}\  = 1.4$ T. . . . .	121
Figure 53 – Quasi-static ( $f = 1$ Hz) 2D simulation results of the magnetic flux density norm of the magnetic circuit with permanent magnets with $\ \mathbf{B}_{\text{rem}}\  = 1.4$ T. . . . .	122
Figure 54 – Energy product calculated as $\ \mathbf{B} \cdot \hat{\mathbf{B}}_{\text{rem}}\  \ \mathbf{H} \cdot \hat{\mathbf{B}}_{\text{rem}}\ $ for permanent magnets with $\ \mathbf{B}_{\text{rem}}\  = 1.4$ T in the final magnetic circuit (from a 2D simulation). . . . .	123

Figure 55 – Demagnetization field calculated as $\ \mathbf{H} \cdot \hat{\mathbf{B}}_{\text{rem}}\ $ for high remanence permanent magnet <i>Shinetsu</i> N52 with $\ \mathbf{B}_{\text{rem}}\  = 1.47$ T in the final magnetic circuit (2D simulation). . . . .	124
Figure 56 – Photograph of the built magnetic circuit mounted over two bearings and pillars. . . . .	125
Figure 57 – Simulated (3D) and experimental magnetic flux density norm behavior as a function of the angle at the center of the magnetic gap height ( $R = 100$ mm). . . . .	126
Figure 58 – Experimental and numerical data of the magnetic flux density norm dependence on the length ( $z$ ) at different angles at the center of the air gap ( $R = 100$ mm). . . . .	127
Figure 59 – Three dimensional plot of the experimental magnetic flux density norm data in the air gap as a function of angle and length at the center of the magnetic gap ( $R = 100$ mm). . . . .	127
Figure 60 – Calculated $\Lambda_{\text{cool}}$ parameter from the 3D simulations of the magnetic flux density norm at the center of the magnetic gap (red line) as a function of the opening angle ( $\ \mathbf{B}_{\text{rem}}\  = 1.4$ T). . . . .	128
Figure 61 – Explosion view of the main components of the rotary device. . . . .	130
Figure 62 – Schematic diagram of the hydraulic system. . . . .	131
Figure 63 – (a) 8-port rotary valve and (b) rotary valve system composed of two identical rotary valves. . . . .	133
Figure 64 – Normalized (a) rotary valve (bedtype 0) and (b) bedtype 1 and bedtype 2 fluid flow profiles as a function of rotation angle and compared with the magnetic profile. . . . .	134
Figure 65 – Cutaway view of the regenerator, magnetic circuit and cold end flow distributor. . . . .	135
Figure 66 – Rendered image of the cold end including all of its components. . . . .	136
Figure 67 – Properties of the commercial Gd spheres. . . . .	138
Figure 68 – Parametric analysis of the (a) spatial and (b) time mesh size, and (c) the convergence tolerance for the 1D model developed by (Engelbrecht <i>et al.</i> , 2006) and modified for the conditions of the UFSC device. . . . .	140

Figure 69 – Resultant of the displacement (URES) for a bed pair when pressurized at 10 bar. The distortion scale is enlarged 50 times. . . . .	141
Figure 70 – (a) Cross-section view of a pair of regenerator beds and (b) a transversal cutaway view (A-A) of the regenerator bed. . . . .	142
Figure 71 – Regenerator ring. . . . .	143
Figure 72 – (a) Rendered and (b) photograph of the regenerator ring coupled with the channeling rings. (c) Exploded view showing all regenerator components: gaskets, screens, anchors, check valves and fixation screws. . . . .	144
Figure 73 – (a) Photograph of a stainless steel wire screen Mesh 100 inside one of the 6 mm regenerator channels and (b) an special die cutting tool developed to cut the screen. . . . .	145
Figure 74 – Photograph of the final regenerator ring filled with Gd and coupled with the hot (top) and cold (bottom) end flow distributors. . . . .	146
Figure 75 – Cutaway view of the screw-type cold heat exchanger showing the cartridge heater and the internal coiled channel through. . . . .	147
Figure 76 – Driver system. . . . .	148
Figure 77 – (a) Photograph and (b) 2D drawings of the dummy regenerator manufactured to estimate the torque to rotate the magnetic circuit. . . . .	149
Figure 78 – Results for the increasing torque as a function of the angle of rotation of the magnetic circuit. . . . .	150
Figure 79 – Rendered image of the final experimental setup. . . . .	152
Figure 80 – A photograph of the pressure drop experimental analysis of the dummy regenerator beds including the lines where each pressure transmitter were placed. . . . .	156
Figure 81 – System pressure drop ( $\Delta p_{\text{sys}}$ ) for the two empty and the two packed dummy beds as a function of the volumetric flow rate. . . . .	157
Figure 82 – Pressure drop for an empty and a packed dummy bed and the calculated porous media pressure drop as a function of the volumetric flow rate. . . . .	157

Figure 83 – A photograph of the pressure drop experimental analysis of the empty final regenerator beds including the flow distribution system and the lines where each pressure transmitter were placed. . .	158
Figure 84 – Comparison of the four different pressure drops for the empty final regenerator as a function of the volumetric flow rate. . . . .	159
Figure 85 – A photograph of the pressure drop experimental analysis of the individual final regenerator beds including the connection tools for individual bed tests. . . . .	159
Figure 86 – Hot-to-cold blow pressure drop ( $\Delta p_{\text{htcb}}$ ) for each of the sixteen regenerator beds packed with Gd spheres as a function of the volumetric flow rate.	160
Figure 87 – A photograph of the final experimental setup including the flow distribution system and the lines where each pressure transmitter and temperature detector were placed. . . . .	161
Figure 88 – System pressure drop ( $\Delta p_{\text{sys}}$ ) of the packed final regenerator operating at a frequency of 0.8 Hz. .	161
Figure 89 – <i>Opening-span curve</i> for a no-load experiment at $f = 0.8$ Hz, $\dot{V}_f = 150$ L/h and $T_{\text{bath}} = 295.15$ K. .	163
Figure 90 – Steady-state temperature behavior of the fluid at the inlets and outlets of the regenerator. $\dot{Q}_C = 60$ W, $\dot{V}_f = 150$ L/h, $f = 0.8$ Hz and $T_{\text{bath}} = 293.15$ K. . . . .	163
Figure 91 – Performance curves for different volumetric flow rates at an operating frequency of 0.4 Hz and hot reservoir temperature of approximately 295.7 K.	165
Figure 92 – System temperature span ( $\Delta T_{\text{sys}}$ ) as a function of the regenerator temperature span ( $\Delta T_{\text{reg}}$ ) for the experimental data of Fig. 91. . . . .	166
Figure 93 – No-load regenerator temperature span dependence on the utilization when the frequency and flow rate are varied for a hot reservoir temperature of approximately 295.7 K. . . . .	167
Figure 94 – Regenerator temperature span as a function of the hot reservoir temperature for a thermal load of 60 W, operating frequency of 0.8 Hz. . . . .	168

Figure 95 – Performance curves for different volumetric flow rates at an operating frequency of 0.8 Hz and an average hot reservoir temperature of approximately 294.1 K. . . . .	169
Figure 96 – System temperature span ( $\Delta T_{\text{sys}}$ ) as a function of the regenerator temperature span ( $\Delta T_{\text{reg}}$ ) for the experimental data of Fig. 95. . . . .	169
Figure 97 – Regenerator temperature span dependence on the AMR operating frequency for a thermal load of 60 W, a volumetric flow rate of 150 L/h and hot reservoir temperature of approximately 296.0 K ( $T_{\text{bath}} = 295.15$ K). . . . .	170
Figure 98 – Typical measurements of torque ( $\tau$ ) and motor power ( $\dot{W}_{\text{M}}$ ) at steady state for a frequency of 1.4 Hz and cooling capacity of 60 W. . . . .	170
Figure 99 – Time-averaged torque, $\bar{\tau}$ , and motor power, $\overline{\dot{W}_{\text{M}}}$ , as well as, their corresponding standard deviations ( $\sigma$ ) and the calculated transmission system power, $\dot{W}_{\text{tr}}(\bar{\tau})$ , as a function of the operating frequency. . . . .	171
Figure 100–Calculated COP results as a function of the temperature span for some of the non-zero thermal load and positive temperature span experiments. . . . .	172
Figure 101–Calculated $\eta_{2\text{nd}}$ as a function of the corresponding temperature span for the experimental results presented in Fig. 100. . . . .	173
Figure 102–Calculated COP and $\eta_{2\text{nd}}$ as a function of the actual motor power, $\dot{W}_{\text{M}}$ , at the operating frequencies for the experimental results presented in Fig. 97. . . . .	174
Figure 103–Calculated COP and $\eta_{2\text{nd}}$ as a function of the transmission power, $\dot{W}_{\text{tr}}$ , at the operating frequencies for the experimental results presented in Fig. 97.	174
Figure 104–Schematic representation of the cold end of the experimental device. . . . .	179
Figure 105–Breakdown of the motor power for different operating frequencies. Measurements were performed at 295 K. . . . .	189

Figure 106–Parasitic losses for the different components at different temperatures at the cold reservoir and an operating frequency of 1.5 Hz. $\dot{Q}_{\text{total}}$ corresponds to the total parasitic losses including also $\dot{Q}_{\text{fl}} = 17.3 \text{ W}$ . . . . .	190
Figure 107–Experimental data and numerical predictions of regenerator temperature span with and without the post-calculated parasitic losses for cooling loads of 200 and 400 W effect of hot reservoir temperature. . . . .	192
Figure 108–Experimental data and numerical predictions of the regenerator temperature span with and without the post-calculated parasitic losses for cooling loads of 200 and 400 W effect of volumetric flow rate. . . . .	194
Figure 109–Regenerator temperature span as a function of the scaling factor of the volumetric flow rate, total losses and sphere diameter for cases with volumetric flow rates of 400 L/h and 600 L/h and cooling capacity of 200 W and 400 W, respectively. . . . .	196
Figure 110–Comparison of COP, $\text{COP}_{\text{no-fl}}$ and $\text{COP}_{\text{AMR}}$ as a function of the hot reservoir temperature for cooling loads of 200 W and 400 W. . . . .	197
Figure 111–Comparison of COP, $\text{COP}_{\text{no-fl}}$ and $\text{COP}_{\text{AMR}}$ as a function of the volumetric flow rate for cooling loads of 200 W and 400 W. . . . .	197
Figure 112–Exergetic-equivalent cooling capacity as a function of the hot reservoir temperature for cooling capacities of 200 W and 400 W. . . . .	199
Figure 113–Exergetic-equivalent cooling capacity as a function of the volumetric flow rate for cooling capacities of 200 W and 400 W. . . . .	200
Figure 114–Overall and cycle second-law efficiency as a function of the hot reservoir temperature for cooling loads of 200 and 400 W. . . . .	200
Figure 115–Overall and cycle second-law efficiency as a function of the volumetric flow rate for cooling loads of 200 W and 400 W. . . . .	201
Figure 116–Coordinate system employed for the calculation of the demagnetization factor of a rectangular prism body. The applied magnetic field, $\mathbf{H}_{\text{appl}}$ , is parallel to the $z$ -axis (Aharoni, 1998). . . . .	234

Figure 117–SEM micrographs of the Gd spheres employed at the UFSC magnetic refrigerator at zooms (a) 27x and (b) 180x. . . . . 236

Figure 118–Transversal SEM micrograph at 500x indicating the presence of impurities in the interior of the Gd sphere as calcium (Ca) and oxygen (O). . . . . 236

Figure 119–EDS analysis have detected the presence of the element (a) Gd and the impurities (b) Ca and (c) O. . . . . 237

Figure 120–Properties of the commercial Gd spheres employed at UFSC device. . . . . 240

# LIST OF TABLES

Table 1 – Variables in the design of a magnetic refrigerator. Adapted from Tura (2005) . . . . .	43
Table 2 – Specifications of the state-of-the-art magnetic refrigerators using permanent magnets and Gd as magnetic refrigerant. . . . .	64
Table 3 – Typical properties of the most important permanent magnets at 293 K (Bastos, 2004; Furlani, 2001). . . . .	74
Table 4 – Selection properties for the most important permanent magnets (Ferreira & Costa, 2011). . . . .	74
Table 5 – Specifications of the developed magnetic circuits for magnetic refrigerators ( <sup>a</sup> induced field calculated in the Gd regenerators). Adapted from Bjørk (2010). . . . .	79
Table 6 – Specification of the samples. . . . .	89
Table 7 – Adiabatic temperature change and peak temperature ( $\sim T_C$ ) while magnetization and heating cycle of the samples when subjected to an applied magnetic field of 1.75 T. . . . .	93
Table 8 – Typical properties of the Nd-Fe-B employed for simulation of the magnetic circuits and those of the permanent magnet used in the actual magnetic circuit. . . . .	111
Table 9 – Dimensions of magnetized wedges and rotor in the final magnetic circuit. . . . .	120
Table 10 – Performance of the basic and final magnetic circuits from the 2D and 3D simulations in COMSOL Multiphysics <sup>®</sup> (2011) for $\ \mathbf{B}_{\text{rem}}\  = 1.4$ T. . . . .	129
Table 11 – Regenerator parameters. . . . .	145
Table 12 – Specifications of the instrumentation sensors. . . . .	151
Table 13 – Specifications of the equipments. . . . .	151
Table 14 – Expanded uncertainty (accuracy) of the transducers provided by the manufacturers. . . . .	153
Table 15 – Summary of selected experimental results and their calculated performance. . . . .	175
Table 16 – Specifications of the DTU rotary AMR. . . . .	179

Table 17 – Properties of the commercial Gd spheres implemented in the numerical model for the DTU device analysis. . . . .	181
Table 18 – Thermal resistances of the components at the cold end and the regenerator beds. . . . .	190
Table 19 – Selected experimental results obtained at the AMR running at an operational frequency of 1.5 Hz. . .	202
Table 20 – Element concentration in % in the Gd spheres. . .	238
Table 21 – Valores das concentrações obtidas para a amostra de Gd por ICP-MS: Analyte concentration in % in the Gd spheres. . . . .	238

# LIST OF SYMBOLS AND ABBREVIATIONS

## Roman

$A$	Area	$\text{m}^2$
$a, b, c$	Dimensions to calculate $N_D$	mm
$B$	Magnetic induction	T
$c$	Specific heat	J/kg
$d$	Diameter	mm
$E$	Energy	J
$f$	Frequency	Hz
$H$	Magnetic field	A/m
$h$	Convection coefficient	$\text{W}/\text{m}^2\text{K}$
$k$	Thermal conductivity	$\text{W}/\text{mK}$
$L$	Length	mm
$M$	Magnetization	$\text{Am}^2/\text{kg}$
$m$	Mass	kg
$N$	Number	
$Nu$	Nusselt number	
$p$	Pressure	bar
$Per$	Perimeter	mm
$Pr$	Prandtl number	
$R$	Radius	mm

$Re$	Reynolds number	
$\mathcal{R}$	Thermal resistance	K/W
$S$	Entropy	J/kg.K
$T$	Temperature	K
$t$	Time	s
$u$	Velocity	m/s
$V$	Volume	m <sup>3</sup>
$w$	Width	mm
$x$	Space	m

### Greek

$\alpha$	Angle	°
$\beta$	Compactness	m <sup>2</sup> /m <sup>3</sup>
$\Delta$	Change	
$\eta$	Efficiency	
$\Lambda_{cool}$	Figure of merit for magnetic circuits for M.R.	T <sup>2/3</sup>
$\mu$	Magnetic permeability	N/A <sup>2</sup>
$\mu$	Viscosity	N.s/m <sup>2</sup>
$\phi$	Utilization factor	
$\varepsilon$	Porosity	
$\rho$	Density	kg/m <sup>3</sup>
$\sigma$	Standard deviation	
$\tau$	Blow period	s
$\tau$	Torque	Nm
$\theta$	Angle	°
$\varphi$	Angle	°

### Composed and constants

$A_c$	Cross sectional area	$m^2$
$BH$	Energy product	$kJ/m^3$
$\Delta S$	Isothermal entropy change	$J/kg.K$
$\Delta T_{ad}$	Adiabatic temperature change	K
$Ex_Q$	Exergetic-equivalent cooling power	W
$f_f$	Friction factor	
$H_C$	Magnetic coercivity	$kA/m$
$\dot{m}$	mass flow rate	$kg/h$
$\mu_0$	Magnetic permeability of vaccum	$4\pi \times 10^{-7} N/A^2$
$\mu_r$	Relative magnetic permeability	
$N_D$	Averaged demagnetization factor	
$P_{field}$	Fraction of the cycle in the high field region	
$\dot{W}$	Power	W
$P_w$	Wetted perimeter	$m^2$
$\dot{Q}$	Heat/Parasitic loss	W
$\dot{Q}_C$	Cooling capacity	W
$T_C$	Curie temperature	K
$T_R$	Room temperature	K
$u_D$	Darcy velocity	$m/s$
$\Delta T_{reg}$	Regenerator temperature span	K
$V_m$	Magnetic scalar potential	
$\dot{V}$	Volumetric flow rate	$L/h$

### Subscript

2nd	Second-law
ad	Adiabatic
appl	Applied

C	Cold
field	Field
CE	Cold end
CHEX	Cold heat exchanger
comp	Component
cond	Conduction
cthb	Cold to hot blow
cy	Cycle
demag	Demagnetization
disp	Axial dispersion
e	External
eff	Effective
fl	Flow distributors
f	Fluid
gap	Magnetic gap
<i>H</i>	Isofield process
H	Hot
HHEX	Hot heat exchanger
high	High magnetic field region
htcb	Hot to cold blow
HT	Heat transfer
h	Hydraulic
hys	Hysteresis
i	Initial
i	Internal
id	Ideal cycle

in	Inlet of the pump
iron	Iron
low	Low magnetic field region
M	Electric motor
mag	Magnetization
magnet	Permanent magnet
max	Maximum value
ME	Mechanical and electrical
min	Minimum value
nl	No load
no-fl	Without flow distributors
out	Outlet of the pump
OP	Overall pumping
p	Particle
P	Pumping
R	Room
rad	Radiation
reg	Regenerator
rem	Remanence
rot	Rotor
s	Solid
sys	System
visc	Viscous
wedge	Wedge

### **Superscript**

bed	Bed
-----	-----

## Abbreviation

AMR	Active magnetic regenerator	
BRIRE	Baotou Research Institute of Rare Earth	
CFD	Computational fluid dynamics	
COP	Coefficient of performance	
DTU	Technical University of Denmark	
EDS	energy dispersive X-ray spectrometer	
EES	Engineering Equation Solver	
FEM	Finite Element Method	
Gd	Gadolinium	
ICP-MS	Inductively coupled plasma mass spectrometer	
MCE	Magnetocaloric effect	
MCM	Magnetocaloric material	
NTU	Number of transfer units	
PFA	Perfluoroalkoxy alkane	
PMMA	Polymethyl methacrylate	
POM	Polyacetal	
PPMS	Magnetic Property Measurement System	
PU	Polyurethane	
RAM	Random-access memory	
RTD	Resistance temperature detector	
SEM	Scanning electron microscope	
SQUID	Superconducting Quantum Interference Device	
URES	Displacement	mm
UVic	University of Victoria	
VMS	Vibrating Sample Magnetometer	

# CONTENTS

	Page
<b>1 INTRODUCTION . . . . .</b>	<b>39</b>
1.1 Motivation and objectives . . . . .	42
1.2 Thesis overview . . . . .	43
<b>2 LITERATURE REVIEW . . . . .</b>	<b>45</b>
2.1 Fundamentals of the magnetocaloric effect . . . . .	45
2.1.1 Thermodynamics of the magnetocaloric effect . . . . .	45
2.1.2 Experimental characterization of the MCE . . . . .	47
2.2 Magnetocaloric materials . . . . .	48
2.2.1 Gadolinium (Gd) . . . . .	50
2.2.2 Promising magnetocaloric materials . . . . .	52
2.2.2.1 NaZn <sub>13</sub> -type structure system . . . . .	52
2.2.2.2 Fe <sub>2</sub> P-type structure system . . . . .	53
2.3 Regenerators . . . . .	54
2.4 Active magnetic regenerator (AMR) . . . . .	58
2.5 Magnetic refrigerators . . . . .	61
2.5.1 State-of-the-art magnetic refrigerators . . . . .	63
2.5.1.1 Astronautics – USA system . . . . .	64
2.5.1.2 Japanese system . . . . .	66
2.5.1.3 Canadian system . . . . .	67
2.5.1.4 Danish system . . . . .	67
2.6 AMR Modeling . . . . .	69
2.7 Magnetic circuits for magnetic refrigerators . . . . .	70
2.7.1 Fundamentals of magnetism and magnetic materials . . . . .	71
2.7.2 Demagnetization field . . . . .	75
2.7.3 Modeling a magnetic circuit . . . . .	76
2.7.4 Desired characteristics of a magnetic circuit for a magnetic refrigerator . . . . .	77
2.7.5 State-of-the-art magnetic circuits . . . . .	79
2.8 Summary and specific objectives . . . . .	81
<b>3 DIRECT MEASUREMENT OF THE MCE . . . . .</b>	<b>83</b>
3.1 Direct measurement of the MCE . . . . .	83

3.2	Experimental apparatus and procedure . . . . .	84
3.3	Experimental work . . . . .	88
3.4	Results . . . . .	90
3.4.1	Gd samples . . . . .	90
3.4.2	Mn-based samples . . . . .	92
3.5	Summary . . . . .	96
<b>4</b>	<b>DESIGNING A NOVEL ROTARY MAGNETIC REFRIGERATOR . . . . .</b>	<b>99</b>
4.1	Design concepts . . . . .	100
4.2	Initial design constraints and specifications . . . . .	102
4.3	Designing the magnetic circuit . . . . .	109
4.3.1	Optimization of the rotor-stator magnetic circuit configuration . . . . .	114
4.3.2	Characterization of the magnetic circuit . . . . .	124
4.4	Designing the flow distribution system . . . . .	129
4.4.1	Designing the rotary valve system . . . . .	132
4.4.2	Designing the flow distributors and the cold end . . . . .	134
4.5	Designing the regenerator . . . . .	135
4.5.1	Adapting a 1D numerical AMR model . . . . .	136
4.5.2	Final dimensions of the regenerator . . . . .	139
4.5.3	Assembling the regenerator . . . . .	143
4.6	Ancillary components . . . . .	146
4.6.1	Thermal components . . . . .	146
4.6.2	Driver system . . . . .	148
4.6.3	Instrumentation and control components . . . . .	150
4.6.4	Equipment information . . . . .	151
<b>5</b>	<b>EXPERIMENTAL ANALYSIS OF THE UFSC MAGNETIC REFRIGERATOR . . . . .</b>	<b>155</b>
5.1	Pressure drop analysis . . . . .	155
5.2	Experimental analysis . . . . .	162
5.3	Experimental results . . . . .	165
5.4	Performance evaluation results . . . . .	172
5.5	Summary . . . . .	175
<b>6</b>	<b>PERFORMANCE ANALYSIS OF THE DTU MAGNETIC REFRIGERATOR . . . . .</b>	<b>177</b>
6.1	Introduction . . . . .	177
6.2	Experimental work . . . . .	178
6.3	Modeling . . . . .	180
6.3.1	Numerical simulation . . . . .	180

6.3.2	Analysis of parasitic losses . . . . .	181
6.4	Performance metrics . . . . .	184
6.4.1	Exergetic-equivalent cooling capacity . . . . .	186
6.4.2	Second-law efficiency . . . . .	187
6.5	Results and discussions . . . . .	187
6.5.1	Parasitic losses . . . . .	187
6.5.2	Experimental results . . . . .	191
6.5.2.1	Hot reservoir temperature dependence . . . . .	192
6.5.2.2	Volumetric flow rate dependence . . . . .	194
6.5.3	Inputs Sensitivity . . . . .	195
6.5.4	Performance evaluation results . . . . .	196
6.5.4.1	COP analysis . . . . .	196
6.5.4.2	Exergetic-equivalent cooling capacity . . . . .	199
6.5.4.3	Second law efficiency . . . . .	199
6.6	Summary . . . . .	202
<b>7</b>	<b>CONCLUSIONS . . . . .</b>	<b>205</b>
<b>8</b>	<b>RECOMMENDATIONS FOR FUTURE WORK</b>	<b>209</b>
	<b>BIBLIOGRAPHY . . . . .</b>	<b>211</b>
	<b>LIST OF PUBLICATIONS . . . . .</b>	<b>229</b>
	Papers in peer-reviewed journals . . . . .	229
	Papers in preparation for peer-reviewed journals . . . . .	230
	Papers in conference proceedings . . . . .	230
	<b>APPENDIX A DEMAGNETIZATION FACTOR .</b>	<b>233</b>
	<b>APPENDIX B CHARACTERIZATION OF THE</b>	
	<b>        Gd SPHERES . . . . .</b>	<b>235</b>
	<b>APPENDIX C UNCERTAINTY ANALYSIS . . .</b>	<b>241</b>
	<b>ANNEX A DATASHEET FOR SINTERED Nd-Fe-</b>	
	<b>        B . . . . .</b>	<b>253</b>



## Chapter 1

# INTRODUCTION

The interaction between heat and magnetism has fascinated researchers in the last two centuries. Experiences with electromagnetism usually involved changes in temperature caused by Joule heating, i.e., the interplay between moving particles and atomic ions. However, changes in temperature can also occur when a body is magnetized or demagnetized, which has been coined by Weiss & Piccard (1918) as the ‘*magnetocaloric effect*’ (MCE). This effect is characterized by two thermodynamic quantities, i.e., the *adiabatic temperature change*,  $\Delta T_{\text{ad}}$ , and the *isothermal entropy change*,  $\Delta S$ , and illustrated in Fig. 1. The temperature-entropy ( $T$ - $S$ ) diagram in this figure is for a ferromagnetic material between two constant magnetic fields,  $H_i$  and  $H_f$ , in the vicinity of the magnetic transition temperature, i.e., the Curie temperature ( $T_C$ ) (Smith *et al.*, 2012).

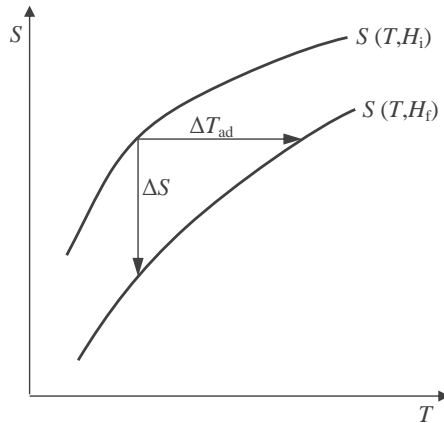


Figure 1 – Illustration of the magnetocaloric effect (MCE) represented by the adiabatic and the isothermal magnetization processes in a  $T$ - $S$  diagram. The horizontal line represents the adiabatic temperature change and the vertical line the entropy change both between two isofield lines,  $H_i$  and  $H_f$ . Adapted from Pecharsky & Gschneidner Jr. (1999) and Smith *et al.* (2012).

The reversible nature of the MCE has motivated its use in a broad range of energy-related applications, such as thermomagnetic motors, generators and, more recently, refrigerators. Although the discovery of the MCE is attributed to Weiss & Piccard (1918), Lord Kelvin already knew that the effect was reversible and larger around the  $T_C$  for a ferromagnet (Smith, 2013). In the nineteenth century, notable inventors, such as Stefan (1871), Edison (1888) and Tesla (1889), proposed several devices in which the MCE was used to either generate electricity or mechanical work. However, only in the 1920's its application in cryogenics was demonstrated by two Nobel laureates, Debye (1926) and Giaque (1927). Working independently, they attained temperatures below the liquefaction of helium through adiabatic demagnetization of paramagnetic salts. Since then, the MCE has been employed to attain the lowest temperatures (of the order of microkelvin), aiming primarily at the liquefaction of gases, as the known magnetocaloric materials exhibit the largest effects at very low temperatures.

The first magnetic heat pump working near room temperature was developed by Brown (1976). This device used gadolinium (Gd) as the magnetocaloric material (refrigerant). Announced by Urbain *et al.* (1935) the discovery of the ferromagnetic rare-earth element, Gd, with a Curie temperature near room temperature ( $T_C \sim 293$  K). Brown implemented a regenerative thermodynamic cycle using a 7 T superconducting magnet and a porous heat exchanger, with which a no-load temperature span (i.e., the difference between the hot and cold side temperatures) of 47 K was attained. Barclay & Steyert Jr. (1982) patented the concept of active magnetic regenerator (AMR), which allows for higher temperature spans than those given by the MCE of the material alone. Thus, when a magnetic field is alternated over a regenerative porous bed filled with magnetocaloric material and transversal fluid flows are performed, much higher temperature spans can be obtained (Chen *et al.*, 1992).

Near-room temperature magnetic cooling had two decades of relative stillness until the discovery of the ‘giant’ magnetocaloric effect in  $\text{Gd}_5\text{Si}_2\text{Ge}_2$  by Pecharsky & Gschneidner (1997). Since then, an increasing number of laboratory demonstration prototypes have been reported in the literature (Gschneidner Jr. & Pecharsky, 2008; Yu *et al.*, 2010; Kitanovski *et al.*, 2015). Today, magnetic refrigeration for near-room temperature applications is in the spotlight for its potential to develop thermodynamic efficiencies close to the Carnot limit (Brown, 1976) through the use of internally reversible cycles.

Both the scientific community and industrial corporations — e.g., BASF, Samsung, GE, Astronautics Corp., Haier and Whirlpool, to name a few — are working towards developing this technology.

Magnetic refrigeration makes use of regenerative thermodynamic cycles (e.g., Brayton, Ericsson, Stirling), to transfer heat from a low-temperature environment to a high-temperature one by means of magnetic work. Permanent magnet arrangements allow for a recovery of part of the magnetic work needed to magnetize the solid refrigerant, and the reduction of the required work input makes the theoretical potential for large efficiency of magnetic refrigeration very attractive. That aside, magnetic cooling has other potential advantages, such as: (i) the absence of harmful gases used in conventional vapor compression systems; (ii) more compact layouts, since the working material (i.e., refrigerant) is a solid; (iii) less noise generation due to a reduced number of moving parts; (iv) possibility of recycling magnets and solid refrigerants at the end of life (Smith *et al.*, 2012) and (v) the ability to apply the technology in almost any scale. Even though magnetic refrigeration has these potentials, there are still some technological challenges that need to be overcome, specially the reduction in costs and the environmental impacts due to the use of rare-earth elements (Monfared *et al.*, 2014; Langebach *et al.*, 2014).

A pictorial description of a simple magnetic refrigeration cycle is shown in Fig. 2. When a ferromagnetic material at room temperature,  $T_R$ , is magnetized adiabatically, its temperature increases by  $\Delta T_{ad}$ . With the material now above room temperature, heat can be rejected,  $\dot{Q}_H$ , to an external body or ambient, while holding the applied magnetic field. After the material regains thermal equilibrium at  $T_R$ , it is demagnetized and cooled down by  $\Delta T_{ad}$ , thus being able to absorb heat,  $\dot{Q}_C$ , from the desired substance or internal ambient, before it reaches equilibrium at  $T_R$ .

A state-of-the-art magnetic refrigeration system is composed basically by an AMR (i.e., a porous regenerative matrix containing the magnetocaloric material), a magnetic circuit to promote the change in magnetic field and a hydraulic system synchronized with the magnetic field profile. As will be seen in this thesis, building a magnetic refrigeration device is a highly interdisciplinary task (Sandeman, 2012).

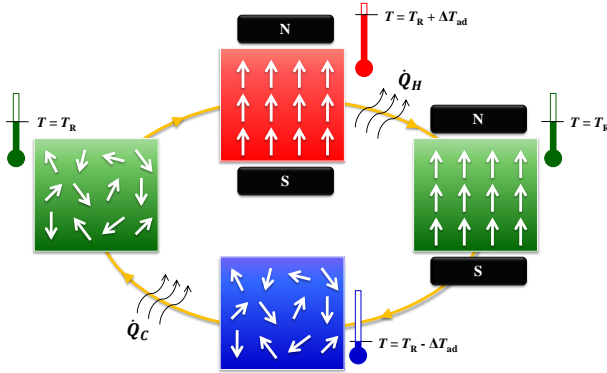


Figure 2 – Pictorial description of a magnetic refrigeration cycle.

## 1.1 MOTIVATION AND OBJECTIVES

As mentioned above, research efforts are currently being made worldwide to develop the potential of magnetic refrigeration by focusing on four main fronts: (i) synthesis of working materials with high MCE and suitable mechanical and thermal properties, (ii) magnetic circuits that allow for large and fast field changes in volumes big enough to accommodate the regenerative matrices, (iii) detailed mathematical modeling of the AMR for a better understanding of the conjugate heat transfer and fluid flow phenomena through the porous magnetocaloric matrix and (iv) the development of new thermo-magnetic systems with configurations designed to improve efficiency and approach commercial applications.

This work was motivated by the possibility to contribute concurrently in the four main fronts presented above, with the aim of designing a novel magnetic refrigerator prototype with a cooling capacity similar to that of a domestic refrigerator. The design of such thermo-magnetic systems depends on a great number of geometric, magnetic and hydraulic variables, for instance those summarized in Table 1. As will be seen, a significant effort was placed in this thesis on the design of optimized magnetic circuits and hydraulic flow distribution systems.

A combined understanding of electromagnetism, magnetocaloric and mechanical design was required to accomplish this goal of the project. It is also necessary to understand the behavior of the magnetocaloric properties of promising materials under real operating

Table 1 – Variables in the design of a magnetic refrigerator. Adapted from Tura (2005)

<i>Geometric</i>	<i>Magnetic</i>	<i>Hydraulic</i>
Porosity	Field intensity	Heat transfer fluid
Magnetocal. material	Field distribution	Utilization, $\phi$
Regenerator shape	Magnetic gap	Operating frequency
Matrix geometry	Number of poles	Pressure drop
Aspect ratio	Torque	Hot in temperature
Casing material	Length	Hydraulic-magnetic
Magnetocaloric mass	Magnet mass	synchronization

conditions. For this reason, this work is also aimed at developing an experimental setup for direct measurements of the adiabatic temperature change of magnetocaloric materials over a wide range of conditions.

The performance of a magnetic cooling system as a function of the variables in Table 1 cannot be determined using only mathematical modeling techniques and basic thermodynamic analysis. Resolving the interconnection between the design parameters and the associated fabrication and cost limitations, as represented in Fig. 3 is a complex task and requires of a thorough understanding of the role of each variable in the performance of the final system. This can only be achieved through careful design and experimentation, and this thesis represents the first step in this direction by the research group at the POLO Laboratories at the Federal University of Santa Catarina.

## 1.2 THESIS OVERVIEW

This thesis is divided into eight chapters. Chapter 2 reviews the basic thermodynamics of the MCE, magnetocaloric materials, magnetic circuits for magnetic refrigeration and the state of the art in magnetic cooling systems. Chapter 3 presents an experimental program dedicated to the quantification of the adiabatic temperature change of promising magnetocaloric materials via the so-called direct method. In Chapter 4 the design, construction and experimental evaluation of the rotary magnetic cooling prototype developed at Polo-UFSC are presented in detail. Chapter 5 presents the experimental results obtained with the Polo-UFSC device, together with a basic thermodynamic analysis. Chapter 6 presents the performance analysis of the state-of-the-art rotary active magnetic refrigerator

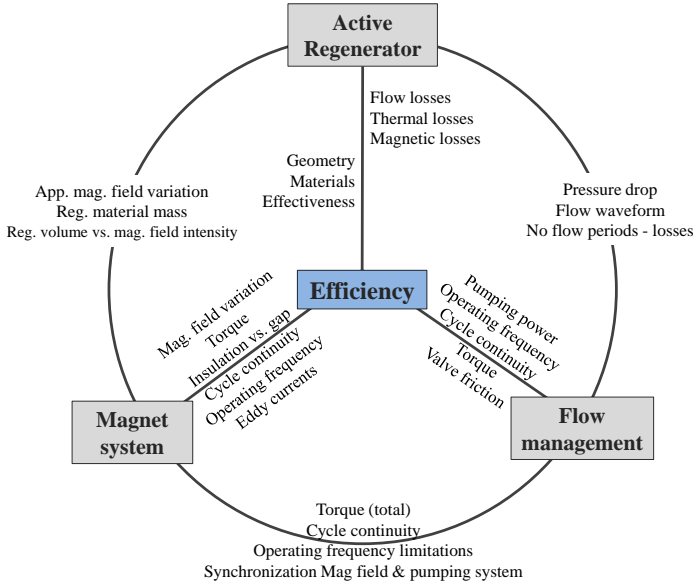


Figure 3 – Interconnection between the design parameters of a magnetic refrigerator (Barbosa *et al.*, 2014a).

developed at Risø, Technical University of Denmark (DTU). Next, conclusions and recommendations for future works are presented in Chapter 7 and 8, respectively.

In addition, a list of research papers published during this Ph.D. thesis in peer-reviewed journals as well as in conference proceedings and papers in preparation to be submitted to journals is presented.

Furthermore, three appendixes are included. Appendix A presents the analytical expression to calculate the demagnetization factor of a rectangular prismatic body. In Appendix B the characterization of the Gd spheres employed at UFSC magnetic refrigerator are presented. Finally, Appendix C presents the uncertainty analysis of the UFSC magnetic refrigerator.

## Chapter 2

# LITERATURE REVIEW

This chapter presents a literature review of the thermodynamics of the magnetocaloric effect (MCE), materials with large MCE around room temperature, their characterization and application in magnetic refrigeration. A detailed review of the concept and development of active magnetic regenerators (AMRs) is carried out. The state of the art in magnetic refrigeration systems and their dedicated magnetic circuits are also described. Finally, a review of numerical modeling of AMRs and magnetic circuits are performed, followed by the specific objectives of the work.

## 2.1 FUNDAMENTALS OF THE MAGNETOCALORIC EFFECT

The magnetocaloric effect (MCE) is the thermal response of a substance to the application of an external magnetic field. This effect is due to the interplay between the magnetic field and the magnetic and lattice degrees of freedom (Pecharsky & Gschneidner Jr., 1999). Inversely to the decrease in spin order when heat is absorbed by a ferromagnetic material, the MCE is the heat released by the application of a magnetic field. For an instantaneous adiabatic magnetization the temperature of the substance rises (Cullity, 1972). An overview on the fundamental aspects of the magnetocaloric effect are presented next.

### 2.1.1 Thermodynamics of the magnetocaloric effect

When the material is magnetized adiabatically, the ordering of the magnetic moments decreases the magnetic entropy, but a compensation is given by an increase in the lattice entropy causing a rise in temperature, i.e.  $\Delta T_{\text{ad}} = T_{\text{f}} - T_{\text{i}}$  (see Fig. 1). On the other hand, for an isothermal magnetization, the total entropy of the system is reduced by  $\Delta S = S(T_{\text{i}}, H_{\text{i}}) - S(T_{\text{i}}, H_{\text{f}})$ , which corresponds to a transfer of heat to the surroundings. Adiabatic and isothermal magnetization and demagnetization processes are the basis for a number of thermodynamic magnetic cycles, including the Ericsson and Brayton cycles.

The fundamental Maxwell relation for an isobaric-isochoric magnetic system (as for most of the magnetocaloric materials) relates the MCE quantities with the magnetization,  $M$ , as follows:

$$\left(\frac{\partial S}{\partial H}\right)_T = \mu_0 \left(\frac{\partial M}{\partial T}\right)_H \quad (2.1)$$

where  $\mu_0$  is the vacuum permeability. Integration of Eq. (2.1) for an isothermal magnetization process yields the isothermal entropy change,  $\Delta S$ :

$$\Delta S = \mu_0 \int_{H_i}^{H_f} \left(\frac{\partial M}{\partial T}\right)_H dH \quad (2.2)$$

which can be used to determine the MCE from magnetization data as a function of temperature and magnetic field. Likewise, the MCE can be calculated from the isofield specific heat capacity,  $C_H(T, H)$ , defined as:

$$\left(\frac{\partial S}{\partial T}\right)_H = \frac{C_H(T, H)}{T} \quad (2.3)$$

Eq. (2.3) can be integrated to find the entropy change if the specific heat capacity as a function of temperature and magnetic field is known. For a magnetic field change,  $\Delta H = H_f - H_i$ , one has:

$$\Delta S = S(T)_{H_f} - S(T)_{H_i} = \int_0^T \frac{C_H(T, H_f)}{T} dT - \int_0^T \frac{C_H(T, H_i)}{T} dT \quad (2.4)$$

Eqs. (2.2) and (2.4) represent two ways of determining the isothermal entropy change of a magnetocaloric material as a function of temperature and magnetic field.

If a magnetic field is applied adiabatically, an expression for an infinitesimal temperature change can be deduced by combining Eqs. (2.1) and (2.3) as follows:

$$dT = -\mu_0 \frac{T}{C_H(T, H)} \left(\frac{\partial M(T, H)}{\partial T}\right)_H dH \quad (2.5)$$

Integration of Eq. (2.5) using appropriate functions for  $C_H(T, H)$  and  $M(T, H)$  results in the adiabatic temperature change for an external magnetic field change,  $\Delta H = H_f - H_i$ :

$$\Delta T_{\text{ad}}(T_i, H_i, H_f) = T_i - T_f = -\mu_0 \int_{H_i}^{H_f} \frac{T}{C_H(T, H)} \left(\frac{\partial M(T, H)}{\partial T}\right)_H dH \quad (2.6)$$

The adiabatic temperature change can also be obtained from the total entropy,  $S(T, H)$ , which is held constant (see Fig. 1):

$$S(T_i, H_i) = S(T_i + \Delta T_{\text{ad}}(T_i, H_i, H_f), H_f) \quad (2.7)$$

It is important to point out that the MCE does not depend only on the magnetic field change,  $\Delta H$ , but also on the initial magnetic field,  $H_i$ , as can be inferred from Eq. (2.7).

### 2.1.2 Experimental characterization of the MCE

The magnetocaloric effect can be defined either by the isothermal entropy change or by the adiabatic temperature change. At the same time, there are two approaches to experimentally determine the MCE: (i) direct and (ii) indirect measurements. The former is a more intuitive characterization of the MCE using the definition of the adiabatic temperature change for a thermally insulated sample. It can be performed straightforwardly by measuring the temperature change in a sample subjected to a magnetic field change at different temperatures. This technique was used in this thesis and an experimental apparatus was developed as described in chapter 3.

Different methods and apparatuses for direct measurement of  $\Delta T_{\text{ad}}$  have been reported in literature. The main difference between them is related to how the magnetic field is generated. Some devices make use of an electromagnet (Zhang *et al.*, 2000; Canepa *et al.*, 2005), others superconductor coils (Benford & Brown, 1981; Gopal *et al.*, 1997; Gschneidner Jr. & Pecharsky, 2000; Rosca *et al.*, 2010) and, most recently, permanent magnet assemblies (Huang *et al.*, 2005; Madireddi *et al.*, 2009; Bahl & Nielsen, 2009; Khovaylo *et al.*, 2010; Trevizoli *et al.*, 2012).

The indirect approach to measure the MCE requires more sophisticated equipment, as well as quasi-static conditions to avoid deviation from thermodynamic equilibrium. Indirect measurements are normally preferred due to the versatility of the experimental equipment involved, which are available in materials developing institutes. The most common indirect characterization method is via  $\Delta S$  calculated through Eq. (2.2). This approach requires magnetization data as a function of temperature and magnetic field readily obtained from commercial magnetometers, such as SQUID (Superconducting Quantum Interference Device) or VSM (Vibrating Sample Magnetometer). Alternatively,  $\Delta S$  can be determined from Eq. (2.4) via measurements of the specific heat capacity using scanning or adiabatic calorimeters.  $\Delta T_{\text{ad}}$  can be determined indirectly

from Eq. (2.6) using temperature-dependent magnetization and specific heat data. A summary of indirect measurement techniques to calculate the MCE was presented by Pecharsky & Gschneidner Jr. (1999).

It should be pointed out that care must be taken when applying indirect techniques to first-order transition materials, since discontinuities in the MCE, latent heat and thermal hysteresis render the thermodynamic assumptions presented in Section 2.1 invalid. In this sense, the direct measurement approach to determine  $\Delta T_{\text{ad}}$  becomes more attractive for first-order materials. More detailed discussions on the application of indirect characterization methods in first-order materials have been presented by Caron *et al.* (2009), Giguère *et al.* (1999), Moore *et al.* (2012), Smith *et al.* (2012).

## 2.2 MAGNETOCALORIC MATERIALS

In principle, all materials in the universe are magnetic and, hence, possess magnetocaloric properties. However, a material can only be considered magnetocaloric when it manifests a perceptible MCE. As can be inferred from Eqs. (2.2) and (2.5), a significant MCE would result either from a large change in magnetization or from a large external magnetic field change. The former is a material-dependent property, while the latter depends on a magnetic field generator. An abrupt change in magnetization occurs close to the magnetic phase transition, which for a ferromagnetic material<sup>1</sup> corresponds to the Curie temperature,  $T_C$ . This temperature is defined as the ordering temperature where a transition from a ferromagnetic phase to a paramagnetic phase occurs and the material loses its spontaneous magnetization. Usually,  $T_C$  is experimentally characterized by the maximum value of the magnetization change with temperature,  $\left| \left( \frac{\partial M}{\partial T} \right)_H \right|_{\text{max}}$ . However, due to the dependence of the MCE peak temperature on the magnetic field, other properties or characteristics have been proposed to determine the  $T_C$  of magnetocaloric materials (Bahl & Nielsen, 2009). As will be shown in this thesis, the peak temperatures of the MCE properties ( $\Delta S$ ,  $\Delta T_{\text{ad}}$  and  $C_H$ ) of certain magnetocaloric materials do not coincide, as can be also inferred from Eqs. (2.2) and (2.5) (Nielsen, 2010).

---

<sup>1</sup> From this point onwards in this thesis, only ferromagnetic materials will be considered when referring to magnetocaloric materials.

Ferromagnetic materials are classified according to their phase transition order either as (i) first-order or (ii) second-order. A single magnetic phase transition of a ferromagnetic material is considered second-order, while a first-order phase transition involves latent heat. If a magnetic transition is accompanied by a structural transition, the magnetization change is discontinuous and the phase transition is first-order (Smith *et al.*, 2012). Magnetocaloric materials exhibiting a magneto-structural phase transition are considered to have a ‘giant’ MCE due to a large, though narrow, peak in  $\Delta S$  (Pecharsky & Gschneidner, 1997). First-order transitions are normally accompanied by a thermal hysteresis,  $\Delta T_{\text{hys}}$ , which corresponds to a different response of the material when subjected to heating and cooling, and is found around the transition temperature. In principle, hysteresis is considered an undesirable effect in practical applications. A more detailed discussion on hysteresis related phenomena is presented by Smith *et al.* (2012). An experimental study was carried out by von Moos *et al.* (2014). Some magnetocaloric compounds allow the possibility of tuning its  $T_C$  by slight changes in their chemical composition; the MCE is graded from one temperature range to another. From an application point of view, this can be very interesting for it allows larger temperature spans to be reached in the so-called multistage AMRs (see Section 2.2.2).

In terms of  $\Delta T_{\text{ad}}$  and  $\Delta S$ , the MCE does not scale linearly with the magnetic field, but with a power smaller than unity around the transition temperature. For second-order transition materials, this power is usually around  $2/3$ , i.e.  $\Delta T_{\text{ad}} \propto \mu_0 H^{2/3}$ , as predicted by the mean field theory (Oesterreicher & Parker, 1984). This relationship, together with the influence of the demagnetization field is important in the design of the magnetic circuit, as will be detailed in Section 2.7.2.

Second-order materials have a reversible MCE (Bahl & Nielsen, 2009) while some first-order materials can have an irreversible MCE due to the hysteretic losses (Morrison *et al.*, 2009). For materials exhibiting a reversible MCE, an important constraint for  $\Delta T_{\text{ad}}$  upon magnetization and demagnetization is defined by Nielsen *et al.* (2010) as:

$$\Delta T_{\text{ad,mag}}(T, H_i, H_f) = -\Delta T_{\text{ad,demag}}(T + \Delta T_{\text{ad,mag}}(T, H_i, H_f), H_f, H_i) \quad (2.8)$$

The above relationship is also referred to as ‘theoretical demagnetization’. For irreversible magnetocaloric materials, the equality in Eq. (2.8) becomes an inequality due to the generation of

entropy so that:  $\Delta T_{\text{ad,mag}} > -\Delta T_{\text{ad,demag}}$  (Nielsen *et al.*, 2010).

The ideal magnetocaloric material for refrigeration applications at around room temperature should have the following characteristics: (i) a large MCE over an appropriate temperature range around room temperature, (ii) low magnetic and thermal hysteresis, (iii) suitable thermal properties (high thermal conductivity and large thermal capacity) for optimal thermal behavior of the regenerator, (iv) chemical stability to avoid corrosion, (v) suitable mechanical properties to simplify processing, (vi) low electrical resistance to minimize eddy currents (vii) environmentally friendly, and (viii) low raw material and fabrication costs (Gschneidner Jr. & Pecharsky, 2008; Sandeman, 2012).

The benchmark magnetocaloric material for applications at room temperature is gadolinium (Gd). Since the pioneering work of Brown (1976), Gd has been employed in most room-temperature magnetic refrigerators developed so far (Yu *et al.*, 2010). It is the only element with  $T_C$  around room-temperature with a relatively large MCE. Nevertheless, the pursuit of suitable magnetocaloric working materials is one of the main challenges in magnetic refrigeration research. Since the publication of the ‘giant’ MCE in  $\text{Gd}_5\text{Si}_2\text{Ge}_2$  by Pecharsky & Gschneidner (1997), several families of intermetallic compounds have been found to have similar characteristics. Among them, the most promising systems are the  $\text{Fe}_2\text{P}$  (Tegus *et al.*, 2002) and  $\text{NaZn}_{13}$  (Fujieda *et al.*, 2002) related compounds (see Section 2.2.2). Detailed reviews of magnetocaloric materials for room-temperature applications were carried out by Pecharsky & Gschneidner Jr. (2006), Brück (2007), Smith *et al.* (2012), Franco *et al.* (2012) and Liu *et al.* (2012).

### 2.2.1 Gadolinium (Gd)

Gadolinium (Gd) is the only pure element with a near room-temperature Curie temperature and a second-order phase transition from a ferromagnetic to a paramagnetic state. According to Bahl & Nielsen (2009), the  $T_C$  of Gd ranges between 290 and 297 K for low magnetic fields, depending on the measuring technique employed and on the purity of the sample (Dan'kov *et al.*, 1998).

Dan'kov *et al.* (1998) reported a maximum MCE of 3.8 K for an applied magnetic field of 1 T in extremely pure Gd samples. While Benford & Brown (1981) reported a value of 3.6 K for the same applied magnetic field. Nevertheless,  $\Delta T_{\text{ad}}$  is lower in commercial grade Gd, which typically has a maximum MCE of 2.8 K/T at

the Curie temperature for magnetic fields up to 2 T (approximately the maximum achievable magnetic field with permanent magnet arrays) (Spichkin *et al.*, 2007). The point of maximum  $\Delta T_{\text{ad}}$  is close to the  $T_C$  and increases with  $\Delta H$  (Pecharsky *et al.*, 2001).

Compiling experimental data from very pure Gd samples at high fields obtained by Pecharsky & Gschneidner Jr. (2006), Bahl & Nielsen (2009) found the following relation between the  $\Delta T_{\text{ad}}$  of Gd and the internal magnetic field:  $\Delta T_{\text{ad}}[\text{K}] = 3.675 (\mu_0 H[\text{T}])^{0.7}$ . On the other hand, for commercial grade Gd samples, the same authors obtained the following expression:  $\Delta T_{\text{ad}}[\text{K}] = 2.85(5) (\mu_0 H[\text{T}])^{0.78(3)}$ .

Gd is still the best performing magnetocaloric material available for room-temperature applications due to its large  $\Delta T_{\text{ad}}$ , low  $C_H$  and high thermal conductivity (Smith *et al.*, 2012). Besides that, Gd has good chemical stability with commercial automotive antifreeze solutions (a mixture of distilled water, ethylene glycol and some corrosion inhibitors) (Engelbrecht *et al.*, 2011). It also has good mechanical processing characteristics, being commercially available in a variety of shapes, including spheres and plates.

The typical magnetocaloric properties of Gd metal are shown in Fig. 4 for an applied magnetic field of 2 T. Fig. 4(a) shows the adiabatic temperature change,  $\Delta T_{\text{ad}}$ , and Fig. 4(b) the isothermal entropy change. The former peaks at  $\Delta T_{\text{ad}} \sim 5.7$  K, while the latter peaks at  $\Delta S \sim 5.5$  J/kg.K (Gschneidner Jr. & Pecharsky, 2006).

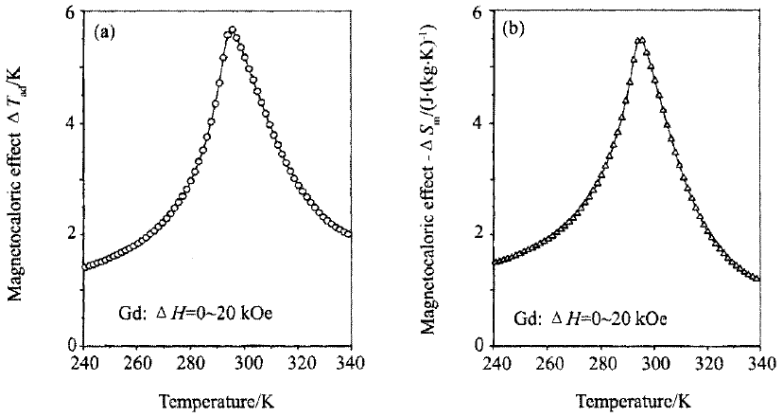


Figure 4 – Magnetocaloric properties (a)  $\Delta T_{\text{ad}}$  and (b)  $\Delta S$  for a Gd for an applied magnetic field of 2 T (Pecharsky & Gschneidner Jr., 2006).

## 2.2.2 Promising magnetocaloric materials

After the discovery of the ‘giant’ MCE, the search for promising magnetocaloric refrigerants focused on rare-earth compounds due to their high ordering temperatures. Intermetallic lanthanum-based compounds, such as  $\text{La}(\text{Fe},\text{Si})_{13}$ , which crystallize in the  $\text{NaZn}_{13}$ -type structure (1:13 phase) (Palstra *et al.*, 1984), and the transition-metal-based compounds  $\text{MnFe}(\text{P},\text{As})$ , which crystallize in the  $\text{Fe}_2\text{P}$ -type structure (Tegus *et al.*, 2002), are among the most promising magnetic refrigerants for near room-temperature magnetic cooling.

Detailed reviews of magnetocaloric materials for applications at room temperature have been carried out by Gschneidner Jr. *et al.* (2005), Liu *et al.* (2012), Franco *et al.* (2012) and Liu (2014). Fig. 5 summarizes the maximum  $\Delta S$  for different families of magnetocaloric materials for a  $\mu_0\Delta H$  of 5 T, having Gd as a reference. An interesting viewpoint paper about the search for new magnetocaloric refrigerants has been written by Sandeman (2012).

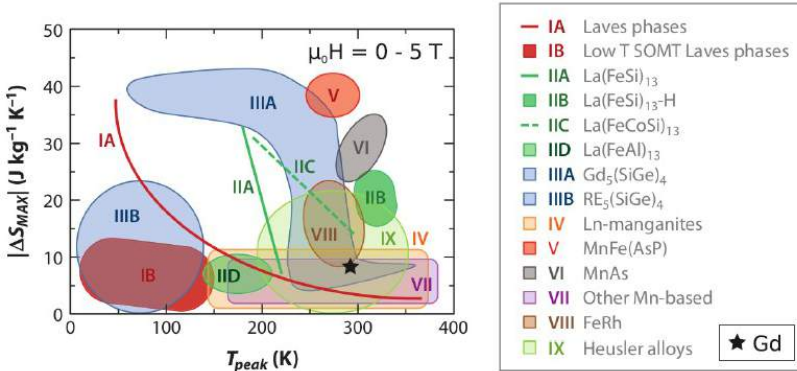


Figure 5 – Maximum magnetic entropy change for  $\mu_0\Delta H = 5 \text{ T}$  versus peak temperature for different families of magnetocaloric materials (Franco *et al.*, 2012; Pecharsky & Gschneidner Jr., 1999).

### 2.2.2.1 $\text{NaZn}_{13}$ -type structure system

Attention has been focussed on materials with first-order phase transitions which have shown large  $\Delta S$ . For a given stoichiometry, the  $\text{La}(\text{Fe},\text{Si})_{13}$  compounds exhibit  $T_C$  at about 195 K (Fujita *et al.*, 1999). This transition temperature can be increased up to 330 K by interstitial modification with small atoms, such as hydrogen,

carbon, or even boron, through additional processes, i.e., hydrogenation, which promotes the expansion of the lattice and, consequently, an increase in  $T_C$  (Fujita *et al.*, 2003; Chen *et al.*, 2003; Gutfleisch *et al.*, 2005; Teixeira *et al.*, 2012). Also,  $T_C$  can be increased by the substitution of some atoms of iron for cobalt or manganese (Yan *et al.*, 2008; Jasinski *et al.*, 2010; Krautz *et al.*, 2012). Fig. 6 shows the isothermal entropy change for different samples of  $\text{La}(\text{Fe},\text{Si})_{13}$  for  $\Delta H = 2$  T. La is the most abundant rare-earth element, which turns this compound more economically attractive than those based on Gd or Ge. Katter *et al.* (2008) proposed a powder metalurgy-based method for large-scale production of this material. Other researches have explored these magnetocaloric compounds and their application in magnetic refrigerators (Shen *et al.*, 2009; Liu *et al.*, 2012).

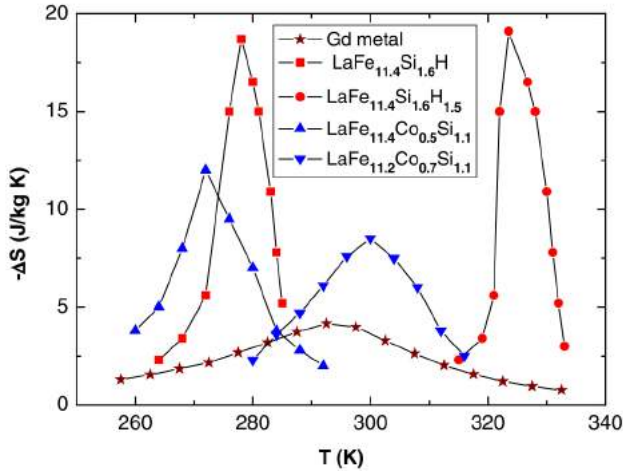


Figure 6 – Entropy variation for different samples based on  $\text{La}(\text{Fe},\text{Si})_{13}$  for an applied magnetic field of 2 T and compared with Gd (Brück, 2005).

### 2.2.2.2 $\text{Fe}_2\text{P}$ -type structure system

Transition-metal-based compounds tend to order magnetically at higher temperatures than rare-earth compounds (Brück *et al.*, 2004). Among them, a manganese-based compound,  $\text{MnFe}(\text{P},\text{As})$ , was found to have a first-order phase transition around room tem-

perature with a large MCE (Tegus *et al.*, 2002) and a variable transition temperature as a function of the chemical composition (Tegus, 2003).

Brück *et al.* (2008) reviewed the structure and properties of Mn-based intermetallic compounds. Concerns regarding toxicity (arsenic), led to a complete substitution of this element by silicon (Si) and germanium (Ge), still keeping the same crystal structure and the large MCE around room temperature (Tegus *et al.*, 2004; Dagula *et al.*, 2005; CamThanh *et al.*, 2006; Lozano, 2009).

As a result of the first-order transition, a  $\Delta T_{\text{hys}}$  of about 1 to 2 K is present in the Mn-based alloys. Fig. 7 shows the magnetization as a function of temperature for  $\text{MnFeP}_{0.45}\text{As}_{0.55}$ , which has a much more abrupt transition than the (smooth) second-order transition of Gd.

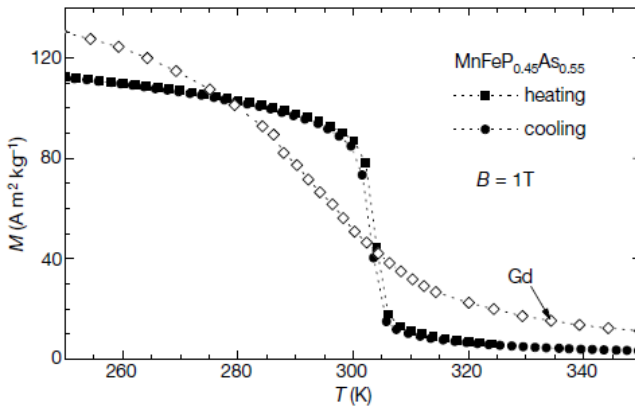


Figure 7 – Magnetization as a function of temperature for  $\text{MnFeP}_{0.45}\text{As}_{0.55}$  for  $\mu_0 H = 1$  T (Tegus *et al.*, 2002).

Manganese-based materials are one of the most promising solid refrigerants for applications near room-temperature. The  $T_C$  of the Mn-based materials can be tuned by varying the phosphorus (P) and arsenic (As) ratio in its composition (Brück, 2007).

### 2.3 REGENERATORS

A *regenerator* or a *regenerative heat exchanger* can be defined as a storage type heat exchanger in which the same flow passages are alternatively occupied by hot and cold fluid streams (Shah &

Bell, 2000). The permeable solid material which composes the regenerator is referred to as the *matrix* or *packed bed*. A heat transfer fluid performs the heat exchange with the regenerative packed bed over periodically continue cycles. The thermal cycle of a regenerator consists basically of two processes: a *hot blow* or a period of time in which a hot fluid flows through the regenerative matrix rejecting heat to the porous solid, and a *cold blow* or a period of time in which a cold fluid flows through the regenerative matrix absorbing heat from the porous solid (Shah & Sekulić, 2003). Thus, the regenerator acts as a transient “thermal sponge” that stores energy during a hot blow and rejects it back to the fluid in a cold blow (Mills, 1995). The cyclic repetition of the two blows establishes a temperature profile along the length of the matrix.

Kuppan (2000) pointed out some of the merits of a regenerator over a recuperator<sup>2</sup>: (i) high compactness,  $\beta$ , which means a large interstitial surface area per unit volume of the bed ( $m^2/m^3$ ), (ii) the use of less expensive and simple heat transfer surfaces (a regenerator can be made from a bed of particles (Nellis & Klein, 2009)), (iii) periodic flow reversals allows for self-cleaning of the regenerator, and (iv) the use of simple headers designs. A regenerator is also preferred over a recuperator in applications where heat demand and/or supply is cyclic or intermittent (Erk, 1990). However, regenerators also present some disadvantages in comparison with recuperators: (i) more changes of flow direction are required representing more flow losses, (ii) restrictions in pressure drop and (iii) fluid carryover, leakage losses and blow mixing (Shah & Bell, 2000).

The temperature of the heat transfer fluid and the temperature of regenerative matrix are function of both, the position and the time of operation (Shah & Bell, 2000). In turn, the performance of the regenerator is a function of the mass of the solid,  $m_s$ , the mass of the fluid — which itself depends on the blow period,  $\tau$ , so that  $m_f = \dot{m}_f \tau$  — and the specific heat capacities of the solid,  $c_s$ , and fluid,  $c_f$  (Schmidt & Willmott, 1981). These parameters are related by the dimensionless quantity *utilization factor* (or simply *utilization*),  $\phi$ , defined as (Shah & Sekulić, 2003; Rowe *et al.*, 2005b):

$$\phi = \frac{m_f c_f}{m_s c_s} \quad (2.9)$$

---

<sup>2</sup> A *recuperator* is defined as a heat exchanger in which heat transfer between fluids takes place through a separating heat transfer surface, and ideally the fluids do not mix or leak (Shah & Sekulić, 2003).

The utilization is the ratio of thermal capacities of the fluid and solid. Due to the dependence of the specific heat capacity on the temperature,  $\phi$  may differ between the blows, even if the mass of fluid is kept constant.

According to Schmidt & Willmott (1981), the desirable properties of a thermal storage regenerator are: (i) high specific heat, (ii) high thermal diffusivity (high thermal conductivity), (iii) high density, (iv) chemical and mechanical stability and (v) low cost. The performance of the regenerator is favored by a high thermal volumetric capacity of the solid,  $\rho_s c_s$ , and a low effective thermal conductivity in the direction of the flow to minimize the longitudinal (axial) conduction (Shah & Sekulić, 2003). The effectiveness of the storage process depends on a high regenerative thermal capacity,  $m_s c_s$ , for a better regenerator thermal performance (Shah & Bell, 2000). The packed bed should have an open porosity (with unobstructed pores) to avoid pressure drop losses, dead fluid volume and contamination. A variety of geometries and structures can be used as regenerator matrices, namely, packed spheres or particles, parallel plates, dense-mesh wire screen (either stacked, punched, or sintered), corrugated metal ribbons, and etched foil (Yaron *et al.*, 1996).

Another important parameter employed to characterize the performance of regenerators is the *number of transfer units* (NTU) defined as (Nellis & Klein, 2009):

$$NTU = \frac{\bar{h} A_{HT}}{\dot{m}_f c_f} \quad (2.10)$$

where  $\bar{h}$  corresponds to the average heat transfer coefficient and  $A_{HT}$  is the heat transfer area (interstitial surface area).

As in recuperators, the counterflow arrangement is preferred since a thermal effectiveness higher than any other configuration can be attained. The two basic regenerator designs are classified as *rotary* and *fixed-bed or reciprocating* (Nellis & Klein, 2009). As the name implies, in a rotary regenerator the regenerative matrix rotates continuously around an axis. Thus, a fixed spatial fraction of the matrix is in the hot blow while another in the cold blow. In this case, the fluid can be continuously pumped from one side of the matrix to the other as shown in Fig. 8a. Instead, in a fixed-bed regenerator the fluid is pumped alternatively through the matrix by means of valves with periodic hot and cold blows (Kuppan, 2000). A fixed-bed regenerator system containing two or more identical beds

allows for a continuous operation of the hot and cold blows, maintaining a periodic flow in each bed, as shown in Fig. 8b. Periodically, one matrix absorbs heat from the fluid during the hot blow, while the other matrix rejects heat to the fluid during the cold blow; after an interval of time, the valves are switched to invert the flow in each matrix.

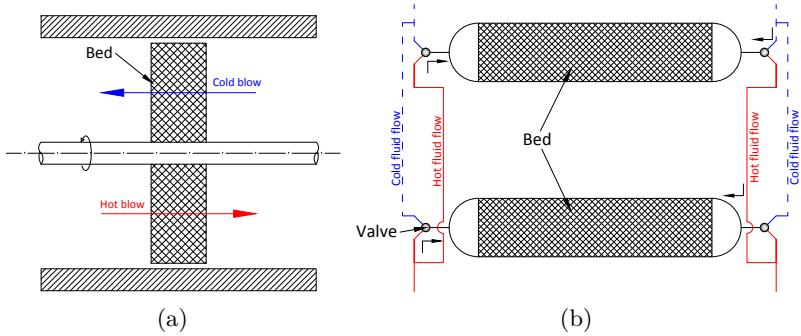


Figure 8 – Regenerator types: (a) rotary regenerator; (b) fixed-bed regenerator with two regenerative matrices. Adapted from Kuppam (2000).

An advantage of fixed-bed regenerators is that matrix materials can be easily removed, cleaned and replaced. However, the additional flow switching mechanisms represent more complexity and cost (Kuppam, 2000). Likewise, a disadvantage of rotary regenerators is that seal leakage can reduce the effectiveness. They also require additional input work to rotate the matrix or the headers (Shah & Sekulić, 2003). Rotary regenerators are classified according to the rotating component. The rotary regenerative matrix or *Ljungstrom*-type regenerator is shown in Fig. 9.a and the stationary matrix with a rotary seal or *Rothemuhle*-type regenerator is shown in Fig. 9.b. The design of rotary sealing for rotary regenerator is a difficult task, especially if the blows are at different pressures. Similarly, the design of rotating drives is a challenging mechanical design problem (Shah & Sekulić, 2003).

Several factors must be considered in regenerator design, including: (i) the selection of the regenerator type, construction material and heat transfer fluid; (ii) geometrical design (porosity, cross-section area, length, hydraulic diameter and  $\beta$ ); (iii) thermal design (NTU, effectiveness, axial conduction, thermal leakages, heat transfer process and cyclic temperature distributions) (iv) hydraulic

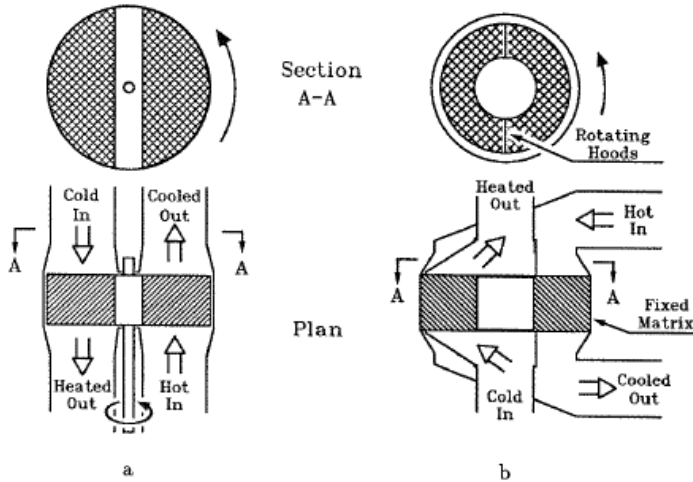


Figure 9 – Rotary regenerators: (a) *Ljungstrom* type or a rotary regenerative matrix; and (b) *Rothemuhle* type or a stationary matrix with rotary sealing (Reay., 1979).

design (sealing, pressure drop and flow switching), (v) mechanical design (pressure loads and rotation drive) (Kuppan, 2000).

## 2.4 ACTIVE MAGNETIC REGENERATOR (AMR)

Regenerators can also be classified as *passive* or *active*. In passive regenerators, the matrix acts as an energy storage medium resulting from the temperature difference between the fluid streams. Stirling and Gifford-McMahon engines and refrigerators are classical applications of passive regenerators, in which they represent a fundamental element of its operation (Kuppan, 2000). In contrast, in active regenerators the solid matrix can generate a temperature difference, being at the same time a medium for energy storage and a heat source or sink. One of the most interesting types of active regenerator is the well-known *active magnetic regenerator* (AMR), which is a fundamental part of a magnetic refrigerator (Barclay & Steyert Jr., 1982). In this component, the construction material of the regenerative bed is a magnetocaloric material which is cycled in and out of a magnetic field while a heat transfer fluid flows through the magnetic matrix creating a temperature gradient along the bed. Through cyclic operation of an AMR, a regenerator temperature

span,  $\Delta T_{\text{reg}}$ , larger than the limited  $\Delta T_{\text{ad}}$  of a magnetocaloric material is created, enabling the use of the magnetic refrigerator in applications that require a large temperature lift (Barclay, 1983).

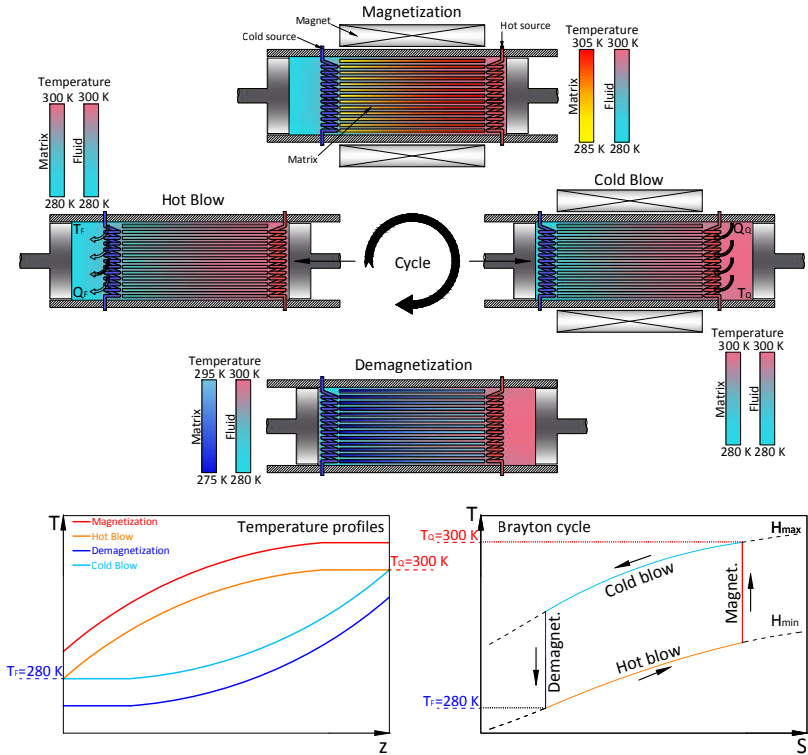


Figure 10 – Schematic description of the processes in a thermo-magnetic Brayton cycle. The diagram on the left shows the axial temperature profiles in the regenerator bed after each process. The  $T$ - $S$  diagram on the right represents an ideal Brayton cycle for a regenerator temperature span of 20 K between the hot and cold heat exchangers at 300 and 280 K, respectively (Barbosa *et al.*, 2014b).

A magnetic refrigerator can be designed according to a number of idealized thermodynamic cycles, such as the Brayton, Stirling, Ericsson, and even the Carnot cycle. The thermo-magnetic regenerative Brayton cycle is the basis of the so-called AMR cycle (see Fig. 10), which is the cycle most frequently encountered in practical applications (Yu *et al.*, 2010; Kitanovski *et al.*, 2015). As seen

in the  $T$ - $S$  diagram in Fig. 10, the thermo-magnetic Brayton cycle is composed of two isofield and two isentropic processes.

In an active regenerator, a heat transfer fluid flows periodically between the magnetocaloric bed located between a hot-side and a cold-side heat exchanger. Each cross-section segment of the magnetocaloric matrix in an AMR experiences a Brayton cycle over a small temperature difference corresponding to the  $\Delta T_{\text{ad}}$  of the magnetocaloric material at the local temperature and magnetic field change. Ideally, these can be combined into one extending Brayton cycle between a larger temperature span, as shown in Fig. 10. Thus, an AMR device in which each segment undergoes the processes described above consists of the following idealized steps (Rowe *et al.*, 2005a):

1. *Adiabatic magnetization*: by increasing adiabatically the magnetic field applied on the regenerator, the total entropy of the magnetic solid matrix remains constant. However, the decrease of the magnetic entropy due to the magnetic field variation is compensated by an increase in the lattice and electronic entropy contributions. As a result, the temperature of the magnetic material increases by  $\Delta T_{\text{ad,mag}}(T, \Delta H)$ .
2. *Constant magnetic field cold blow*: after the adiabatic magnetization and maintaining the applied magnetic field (isofield process), cold fluid (at  $T_{\text{CHEX}}$ ) flows through the matrix, cools down the solid phase (which releases heat to the fluid) and rejects heat to a hot source (ambient) at  $T_{\text{HHEX}}$ .
3. *Adiabatic demagnetization*: similarly to the adiabatic magnetization, the adiabatic demagnetization process reduces the temperature of the solid material, which undergoes an adiabatic temperature change  $\Delta T_{\text{ad,demag}}(T, -\Delta H)$ .
4. *Constant magnetic field hot blow*: hot fluid (at  $T_{\text{HHEX}}$ ) returns through the matrix, and the solid phase removes heat from the fluid phase, increasing the internal energy of the matrix. At the cold end, the fluid absorbs heat from a cold source at  $T_{\text{CHEX}}$ .

Contrary to what occurs in ideal AMR systems, in which the magnetization and demagnetization steps occur instantaneously, in an actual AMRs, depending on the design characteristics of the field generator, the field change steps are executed over a specific time interval, according to a specified mathematical function or *waveform*

(e.g., sinusoidal, rectified sinusoidal etc.). Therefore, some degree of superposition is expected between the field change and fluid flow steps. Trevizoli *et al.* (2014) showed that the field change waveform influences significantly the thermal performance of AMRs. As expected, best results are obtained with the instantaneous field change (square wave or Rademacher function), but this is difficult to implement in practice using permanent magnet arrays. Other important aspects to be taken into account in AMR design are the need for large magnetic field changes and a low demagnetization factor, as will be further explored in Section 2.7.2.

The time- and space-dependent regenerator temperature profile is expected to reach, after a few cycles, a periodic steady state (PSS) in which the temperature profiles are identical at the same position and time of consecutive cycles. As will be seen, the regenerator physics is successfully described by partial differential equations for the fluid flow and conjugate fluid-solid heat transfer in the regenerative matrix.

## 2.5 MAGNETIC REFRIGERATORS

A magnetic refrigerator is composed mainly by an AMR, a magnetic field generator and a flow distribution system. Other important ancillary components are the heat exchangers, electrical motor and control system. At (cyclic) steady state, a cooling capacity,  $\dot{Q}_C$ , matching an applied heat load is transferred from a cold heat exchanger (CHEx) to a hot heat exchanger (HHEx), while maintaining a temperature span in the regenerator. Work is transferred to the system in the form of a net magnetic work,  $\dot{W}_{\text{mag}}$ , applied on the magnetocaloric material and other forms of work (power) to overcome solid friction between sliding parts, pump the fluids through the regenerator (viscous friction) and supply current to electrical and control systems.

The performance of a magnetic refrigerator is highly dependent on the MCE (i.e., the *refrigerating effect*) of the magnetocaloric material and on the effectiveness of the regenerative matrix. The MCE itself depends on the applied field change and its orientation, magnetic properties of the magnetocaloric material and on the geometry of the material and regenerator. The effectiveness, in turn, depends on the solid phase thermophysical properties, matrix geometry, thermal capacity, porosity and operating parameters, such as frequency, fluid flow rate (velocity), thermal load and tempera-

ture of the sources (Rowe *et al.*, 2005a; Nielsen *et al.*, 2012). Magnetic refrigerators are evaluated by the *performance curve* for different operating conditions, which intend to characterize the temperature difference attained at a certain applied thermal load ( $\dot{Q}_C$  vs.  $\Delta T_{\text{reg}}$  curve). Usually, the maximum cooling capacity,  $\dot{Q}_{C,\text{max}}$ , is reached when  $T_{\text{HHEx}} \sim T_{\text{CHEx}}$  and a maximum temperature span,  $\Delta T_{\text{reg,max}}$ , is attained in a no-load test.

The design of a magnetic refrigerator should balance the magnetic forces, operating frequency, sealing and regenerator design (Rowe & Barclay, 2002). Higher operating frequencies, in principle, reduce the amount of magnetocaloric material and the permanent magnet requirements for an equivalent cooling capacity. However, higher working pressures and more pumping power may be required. The mass of magnetocaloric material is one of the most influential parameters in the design and performance of a magnetic refrigerator, since it directly affects the size of the magnetic circuit and the intensity of the magnetic forces (Rowe & Barclay, 2002).

The performance of the cooling system can be evaluated in terms of the coefficient of performance (COP), which is defined as the ratio between the cooling capacity and the power consumption of the system,

$$\text{COP} = \frac{\dot{Q}_C}{\dot{W}_P + \dot{W}_M} \quad (2.11)$$

where  $\dot{W}_P$  and  $\dot{W}_M$  are the electrical powers required to drive the fluid pump and the motor that moves the regenerator or the magnet assembly, respectively.

The COP of an ideal (Carnot), i.e. totally reversible, refrigerator device,  $\text{COP}_{\text{id}}$ , is defined as:

$$\text{COP}_{\text{id}} = \frac{\dot{Q}_C}{\dot{W}_{\text{id}}} \quad (2.12)$$

where  $\dot{W}_{\text{id}}$  is the power consumed by an ideal cooling cycle operating within the temperature limits of the hot and cold environments,  $T_H$  and  $T_C$ , respectively. For a magnetic refrigerator, it corresponds to an ideal magnetic power since there is no fluid friction in the entire (ideal) device.

In terms of the hot and cold environment temperatures, the

COP of the ideal (Carnot) device is given by:

$$\text{COP}_{\text{id}} = \frac{T_{\text{C}}}{T_{\text{H}} - T_{\text{C}}} \quad (2.13)$$

The second law (or exergy) efficiency,  $\eta_{2\text{nd}}$ , has been used as a performance metric to compare different cooling technologies (Hermes & Barbosa, 2012). It is defined as the ratio of the power consumed by the actual device to that of a reversible system within the same temperature span associated with the hot and cold environments ( $\Delta T_{\text{sys}}$ ). In terms of the COPs, it is given by,

$$\eta_{2\text{nd}} = \frac{\text{COP}}{\text{COP}_{\text{id}}} \quad (2.14)$$

where COP and  $\text{COP}_{\text{id}}$  are calculated from Eqs. (2.11) and (2.13), respectively.

Experiments on a 450-liter top-mount household vapor compression refrigerator at ambient temperatures ranging from 298.4 to 316.3 K indicated a second-law efficiency of  $\sim 21\%$  (Gonçalves *et al.*, 2011).

### 2.5.1 State-of-the-art magnetic refrigerators

Magnetic refrigerators are classified as *reciprocating* or *rotary*. In a reciprocating AMR cooler, there are less moving components, but a limitation in the operating frequency due to higher inertia. On the other hand, rotary AMRs are able to perform at higher frequencies with multiple regenerators, thus, more magnetocaloric mass, yet more complex flow distribution system designs. Nowadays, the state-of-the-art magnetic refrigerators operate at frequencies between 0.5 to 4 Hz.

Magnetic refrigerators are also classified according to the magnetic field change generation which can be performed by three different configurations: a stationary regenerator with a moving magnetic circuit, a stationary magnetic circuit with a moving regenerator or a pulsed field stationary regenerator using an electromagnetic or superconducting coil.

Normally, a reciprocating AMR has a stationary regenerator with one bed (Trevizoli *et al.*, 2011), two beds (Tura & Rowe, 2011; Velazquez *et al.*, 2014), or multiple beds (Kawanami *et al.*, 2006). Alternatively, but less common, reciprocating AMRs can have a stationary magnetic circuit and moving bed (Bahl *et al.*,

2008). Likewise, rotary AMR systems with multiple stationary beds and rotating magnets have been demonstrated by Okamura *et al.* (2006), Zimm *et al.* (2007), Russek *et al.* (2010); and rotary regenerators with stationary magnet have been shown to operate effectively at higher cycle frequencies by Zimm *et al.* (2006), Tušek *et al.* (2010), Engelbrecht *et al.* (2012). Furthermore, the use of AMRs with an electromagnetic coil has been demonstrated by Yu *et al.* (2006) or with a superconducting coil by Brown (1976), Blumenfeld *et al.* (2002), Richard *et al.* (2004). Gschneidner Jr. & Pecharsky (2008), Yu *et al.* (2010) reviewed the magnetic refrigerators and heat pumps built before 2010. Romero *et al.* (2013) reviewed the room temperature linear reciprocating magnetic refrigerators. Recently, Kitanovski *et al.* (2015) performed a more updated review.

Most AMR devices built to this day use Gd as the magnetic refrigerant. Also, most devices employ magnetic circuits based on permanent magnets. Packed spheres are the most common bed geometry (Zimm *et al.*, 2006; Tura & Rowe, 2011; Engelbrecht *et al.*, 2012), followed by packed particles (Lu *et al.*, 2005; Okamura *et al.*, 2006; Gao *et al.*, 2006) and parallel plates (Bahl *et al.*, 2008; Trevizoli *et al.*, 2011).

In the following, the most relevant rotary magnetic refrigerators built using permanent magnets are reviewed: (i) Astronautics Corporation of America, (ii) Chubu Electric Power Co. Inc., (iii) University of Victoria (UVic) and (iv) Technical University of Denmark (DTU). Some of the specifications of these magnetic refrigerators are summarized in Table 2.

Table 2 – Specifications of the state-of-the-art magnetic refrigerators using permanent magnets and Gd as magnetic refrigerant.

Magnetic Refrigerator	Type	$\mu_0 H_{\text{high}}$ [T]	$m_{\text{Gd}}$ [kg]	Operating point
				$\Delta T_{\text{ad}}$ at $Q_{\text{C}}$ (W/kg-Gd)
Russek <i>et al.</i> (2010)	Rot.MC	1.4	0.89	8.1 K at 400 W (449 W/kg)
Okamura <i>et al.</i> (2007)	Rot.MC	1.1	4.0	5.2 K at 150 W (37.5 W/kg)
Tura & Rowe (2011)	Rot.MC	1.4	0.11	10 K at 50 W (454.5 W/kg)
Engelbrecht <i>et al.</i> (2012)	Rot.Reg.	1.24	2.8	18.9 K at 200 W (71.4 W/kg)

Magnetic refrigerator type: (Rot.MC) Rotary magnetic circuit and (Rot.Reg.) Rotary regenerators.

### 2.5.1.1 Astronautics – USA system

Zimm *et al.* (2006) developed the first ‘compact’ magnetic refrigerator at the Astronautics Corporation of America, shown in Fig. 11. This device is composed of a stationary circuit of permanent

magnets with a maximum applied magnetic field in the gap of 1.5 T, in which a porous magnetocaloric wheel rotates in a range of operating frequencies between 0.5 and 4 Hz. Pump and valves connected to the wheel control the fluid flow through the six beds. Three different kinds of magnetocaloric material were tested: (i) packed spheres of Gd with diameters in the 425-500- $\mu\text{m}$  range, (ii) packed spheres of Gd-Er alloy (94%-6%) with diameters between 250 and 355  $\mu\text{m}$  and (iii) irregular particles of  $\text{La}(\text{Fe}_{0.88}\text{Si}_{0.12})_{13}\text{H}_{1.0}$  alloy with sizes between 250 and 500  $\mu\text{m}$ . The largest cooling power attained was 50 W at an operating frequency of 1 Hz for a layered bed of Gd and Gd-Er alloy for a volumetric flow rate of 40 L/h. The maximum temperature span was 25 K at 4 Hz, also at 40 L/h.

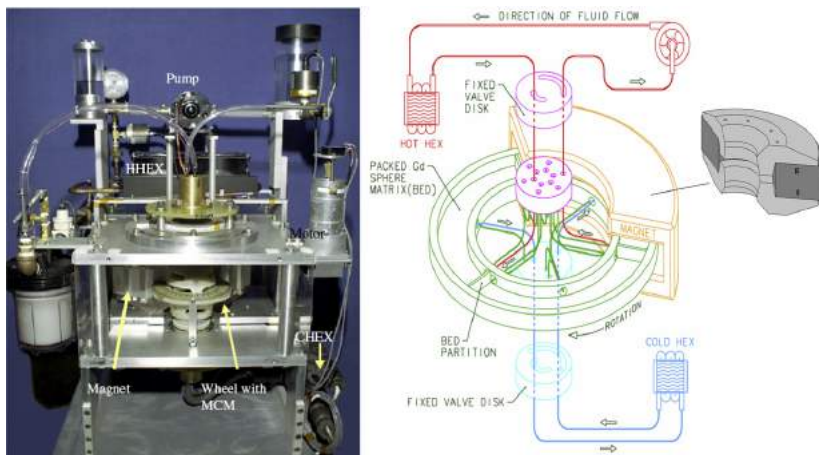


Figure 11 – First generation of a rotary AMR developed at the Astronautics Corporation of America. Photograph of the machine (left side) and the flow schematic of the AMR (right side). The highlight magnetic circuit consists of  $\text{Nd}_2\text{Fe}_{17}\text{B}$  permanent magnets (dark gray) and steel (light gray) (Zimm *et al.*, 2006).

Zimm *et al.* (2007) built a second generation of AMR at Astronautics and later Russek *et al.* (2010) upgraded this system including twelve packed beds of Gd spheres with diameters between 250 and 350  $\mu\text{m}$  and a total mass of 0.89 kg. A 1.4-T magnetic circuit developed by Chell & Zimm (2006) rotates over the stationary magnetocaloric matrices, as shown in Fig. 12. The device attained a maximum cooling power of 844 W at zero temperature span and 400 W at a temperature span of 8.1 K, both at a flow rate of 600 L/h

and operating frequency of 3.33 Hz. Water with corrosion inhibitors was the heat transfer fluid. The device operated continuously with a maximum reported operating frequency of 4.7 Hz, and an exergetic equivalent cooling power,  $Ex_Q$ , of 14 W was obtained. Efficiency was not reported.

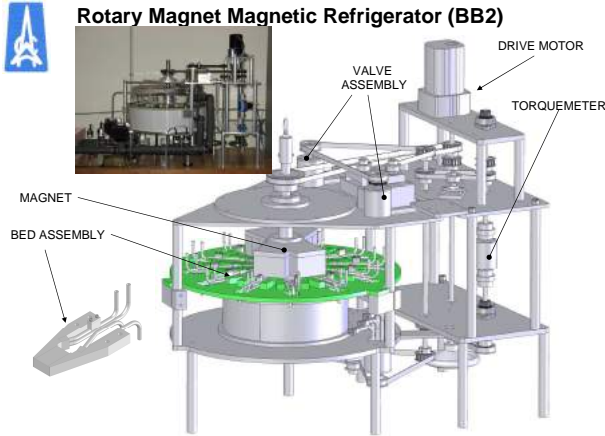


Figure 12 – Second generation of a rotary AMR developed at the Astronautics Corporation of America (Zimm *et al.*, 2007).

### 2.5.1.2 Japanese system

Okamura *et al.* (2006) developed a rotating-magnet type AMR at the Tokyo Institute of Technology in cooperation with the Chubu Electric Power Co. Inc., shown in Fig. 13. This system uses a rotor-stator type magnetic circuit with a 0.77-T high magnetic field and magnetic torque of 52 Nm, which rotates inside four stationary beds composed by four layers of Gd-alloys. This system demonstrated a maximum cooling capacity of 60 W and a 30 W capacity with a  $\Delta T_{\text{reg}}$  of 5.3 K.

Okamura *et al.* (2007) improved the Japanese system by replacing the magnetic circuit for a 1.1-T unit. The configuration of the beds was changed to reduce pressure drop and filled with 4 kg of Gd spheres. With these improvements, the system obtained a maximum cooling capacity of 540 W and a cooling power of 150 W at a  $\Delta T_{\text{reg}}$  of 5.2 K, both at 762 L/h and 0.4 Hz. The device does not rotate continuously, and the maximum frequency reported was 0.4 Hz. Water was employed as heat transfer fluid.

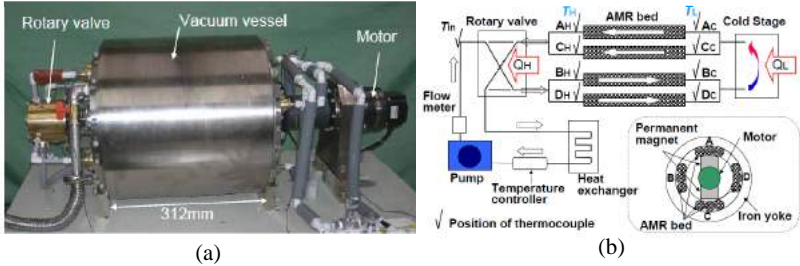


Figure 13 – Japanese AMR system: (a) Photograph of the second generation AMR and (b) system configuration (Okamura *et al.*, 2007).

### 2.5.1.3 Canadian system

Tura & Rowe (2007) developed a compact AMR at the University of Victoria (UVic), which consisted of two rotary magnetic circuits with two stationary magnetocaloric beds, as shown in Fig. 14. The device uses a fluid displacer to distribute the fluid flow and the Halbach arrays of NdFeB permanent magnets generate a  $\mu_0 \Delta H$  between 0.1 and 1.4 T. Tura & Rowe (2009) employed 110 g of 0.3-mm Gd spheres, and the system generated a no-load temperature span of 29 K. Tura & Rowe (2011) upgraded the device to produce a cooling power of 50 W at a  $\Delta T_{\text{reg}}$  of 10 K at a maximum operating frequency of 4 Hz and an utilization of 0.62. A mixture of water-glycol (80-20%) was employed as heat transfer fluid. A maximum COP of 1.6, which included all motor inefficiencies and drive loss, was calculated for a cooling capacity of 50 W at a  $\Delta T_{\text{reg}}$  of 2.5 K and a frequency of 1.4 Hz. It was claimed that the COP could be increased to 2.2 if the motor inefficiency were removed (Tura & Rowe, 2011).

### 2.5.1.4 Danish system

Among the state-of-the-art magnetic refrigerators developed so far, special attention is given to the Danish system, which was experimentally and numerically evaluated in this thesis. The results obtained with this device are described in Chapter 6 and in four peer-reviewed publications (Engelbrecht *et al.*, 2012; Lozano *et al.*, 2013; Lozano *et al.*, 2014; Bahl *et al.*, 2014).

Bahl *et al.* (2011) developed a high frequency rotary AMR at the Technical University of Denmark (Risø - DTU), shown in

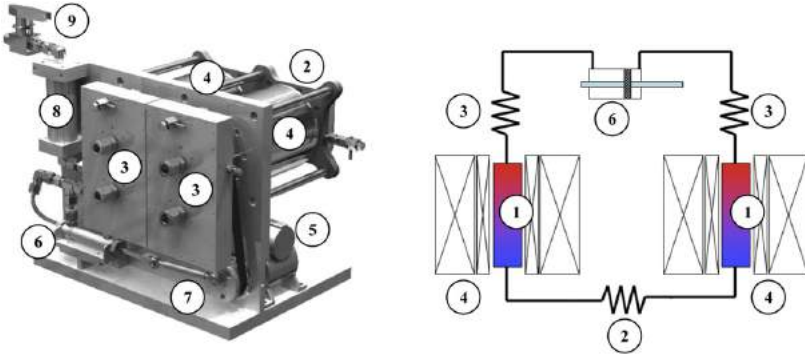


Figure 14 – Compact permanent magnet AMR developed at UVic (a) Photograph of the system and (b) hydraulic schematics. The numbers indicate the main components: (1) AMRs, (2) Cold heat exchanger, (3) Hot heat exchanger, (4) Halbach permanent magnet cylinders, (5) DC gear motor, (6) Hydraulic displacer, (7) Crank mechanism, (8) Accumulator and (9) Valve (Tura & Rowe, 2011).

Fig. 15.a. The AMR itself consists of 24 Gd-sphere packed regenerators which rotate inside a four-pole static permanent magnet assembly (Fig. 15.b). The regenerator beds, fabricated in nylon, of 100 mm length were packed with 2.8 kg of Gd spheres sieved to diameters between 0.25 and 0.8 mm. The permanent magnet assembly, designed and optimized by Bjørk *et al.* (2008), generates a maximum magnetic flux density of 1.24 T in four high field regions and approximately 0 T in four low field regions (Bjørk *et al.*, 2011) (see Section 2.7.5). Fluid flow is provided by a continuously operating gear pump and flow distributor system. The flow distributors are designed such that a minimum of eight regenerator beds are open to flow at any given time to minimize fluctuations in flow to the regenerator. The heat transfer fluid is a mixture of 20% automotive antifreeze (ethylene glycol) and 80% water by volume.

The machine was able to operate at frequencies up to 10 Hz, which is the highest AMR operating frequency up-to-date, at a  $\Delta T_{\text{reg}}$  of 12.1 K and 200 W (Lozano *et al.*, 2014), and to produce a cooling capacity of 1010 W at a  $\Delta T_{\text{reg}}$  of 0.3 K (Bahl *et al.*, 2014). A maximum no-load  $\Delta T_{\text{S}}$  of 25.4 K was attained. An experimental peak on the temperature span of 18.9 K with 200 W cooling capacity was reached at 2.25 Hz and the refrigerator was able to absorb a cooling capacity of 100 W at a  $\Delta T_{\text{reg}}$  of 21 K and

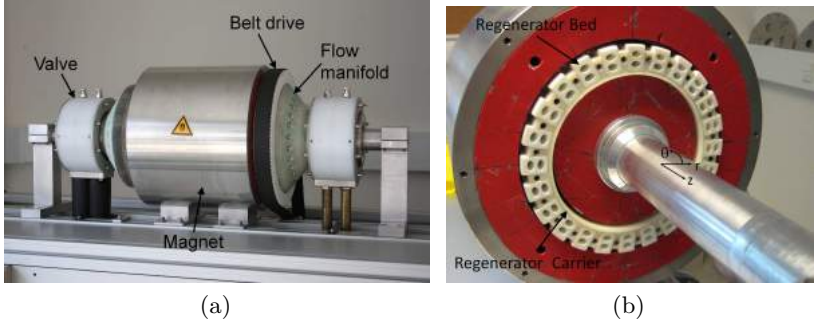


Figure 15 – AMR system developed at Risø - DTU: (a) Photograph of the device showing the magnet assembly, the flow manifold and the rotary valves; (b) The 24-bed regenerator assembly is installed in the magnetized gap. The plane  $z = 0$  is at the center of the magnet (Engelbrecht *et al.*, 2012).

2 Hz (Engelbrecht *et al.*, 2012). Additionally, a cooling capacity of 200 W was produced at a span of 16.8 K with a COP of 0.69. The attained overall second-law efficiency is around 5% (Lozano *et al.*, 2013). Further details about the design, operation and experimental and numerical results can be found in Chapter 6 of this thesis.

## 2.6 AMR MODELING

Several numerical models of AMR systems have been reported in literature and recently reviewed by Nielsen *et al.* (2011). One-dimensional models are characterized for being practical and flexible for use in both design and analysis of AMRs (Aprea & Maiorino, 2010). In this work, predictions and performance analysis of AMRs were conducted using the 1-D AMR model from Ref. (Engelbrecht *et al.*, 2006) using an implicit solver. The energy equation for the heat transfer fluid, which includes the viscous dissipation term, is given by:

$$\dot{m}_f c_f \frac{\partial T_f}{\partial x} + h A_{HT} (T_f - T_s) + \rho_f A_c \varepsilon c_f \frac{\partial T_f}{\partial t} - \varepsilon k_{disp} A_c \frac{\partial^2 T_f}{\partial x^2} = \left| \frac{f_f \dot{m}_f^3}{2 \rho_f^2 A_c^2 d_h} \right| \quad (2.15)$$

where  $T$  is temperature,  $\rho$  is density,  $h$  is the interstitial heat transfer coefficient,  $\varepsilon$  is the porosity,  $k_{disp}$  is the axial thermal conductivity of the fluid due to molecular conduction and axial dispersion,  $f_f$  is

the friction factor and  $A_C$  is the cross sectional area. The terms represent (from left to right) the fluid enthalpy change resulting from advection, interstitial heat transfer with the solid, energy storage, energy transfer due to axial dispersion associated with mixing of the fluid, and viscous dissipation due to friction losses.

The energy equation for the solid regenerator material is given by:

$$hA_{HT}(T_f - T_s) + k_{\text{eff}} \frac{\partial^2 T_s}{\partial x^2} = (1 - \varepsilon) \rho_s T_s \left( \frac{\partial s_s}{\partial B} \right)_T \frac{\partial B}{\partial t} + (1 - \varepsilon) \rho_s c_{B,s} \frac{\partial T_s}{\partial t} \quad (2.16)$$

where  $B$  is the internal magnetic field of the solid regenerator that is corrected for the demagnetizing field and  $k_{\text{eff}}$  is the effective thermal conductivity of the solid matrix. The terms (from left to right) represent the interstitial heat transfer with the flowing fluid, non-dispersive or static axial conduction (through the matrix and fluid), magnetic work transfer, and energy storage. A detailed description of the model is given in Ref. (Engelbrecht, 2008).

It is worth to highlight the importance of knowing the exact behavior of the properties of solid refrigerant samples used in experimental devices for an accurate prediction and interpretation of thermal performance results. For instance, the thermodynamic properties of Gd can be obtained either by the mean field theory (Benford & Brown, 1981; Petersen *et al.*, 2008a; Liu *et al.*, 2007) or calculated from indirect measurements of pure Gd (Dikeos, 2006; Sarlah *et al.*, 2006) or commercial Gd (Dan'kov *et al.*, 1998; Lozano *et al.*, 2014) and employed in numerical models (Siddikov *et al.*, 2005; Lozano *et al.*, 2013).

## 2.7 MAGNETIC CIRCUITS FOR MAGNETIC REFRIGERATORS

Magnetic field changes are the driving force in a magnetic refrigerator. The magnetic field generator is usually the most expensive, voluminous and heavy component of a magnetic refrigerator. Therefore, special care must be taken in order to design an efficient magnet for a new magnetic refrigerator. This section introduces some fundamentals of magnetism, the desired characteristics of a magnetic circuit for magnetic refrigerators as well as the state-of-the-art of magnetic refrigeration applications.

Three different kinds of magnetic field generator have been used in magnetic refrigerators: (i) superconducting coils (Brown,

1976; Zimm *et al.*, 1998; Rowe *et al.*, 2005b), (ii) electromagnetic coils (Yu *et al.*, 2006; Coelho *et al.*, 2009) and (iii) permanent magnet arrays (Chell & Zimm, 2006; Buchelnikov *et al.*, 2007; Chen *et al.*, 2007; Okamura *et al.*, 2007; Tura & Rowe, 2007; Zimm *et al.*, 2007; Bahl *et al.*, 2008; Tušek *et al.*, 2010; Bjørk *et al.*, 2010a). Superconducting coils can generate very high magnetic fields, but they themselves need cooling by liquid helium or liquid nitrogen. Thus, in the case of low and medium cooling capacities, the use of such coils becomes unfeasible. Electromagnetic coils are capable of generating high magnetic fields. However, they require high electric power and are subjected to Joule heating<sup>3</sup>.

Consequently, magnetic circuits based on permanent magnets arrays became more attractive for domestic and commercial applications (low and medium cooling capacities). Most magnetic cooling devices developed in the last decade or so have used permanent magnets, as no electrical energy is required, as well as, more compact magnetic refrigerators can be designed (Bjørk *et al.*, 2010). Some of the magnetic circuits designed and constructed for this purpose are presented in Section 2.7.5. All of them make use of neodymium-iron-boron (Nd-Fe-B) permanent magnets.

### 2.7.1 Fundamentals of magnetism and magnetic materials

Magnetism is the physical phenomena of substances in response, at the atomic or sub-atomic levels, to an applied magnetic field. Such a response is quantified in terms of the magnetization,  $\mathbf{M}$ . In nature, all materials are magnetic, i.e. every material can be classified according to its type of magnetism as diamagnetic, paramagnetic, ferromagnetic, antiferromagnetic or ferrimagnetic. The same material can exhibit different types of magnetism at different conditions, such as temperature, pressure and magnetic field. In this thesis, only ferromagnetic/paramagnetic materials are considered.

Magnetic materials can be classified in terms of the magnetic permeability,  $\mu$ , a property defined as the capacity of the material to allow the passage of magnetic flux density (also known as magnetic

<sup>3</sup> According to the Biot-Savart law, the power needed to generate a magnetic flux density of 1.2 T over a magnetic gap of 16 mm  $\times$  40 mm  $\times$  100 mm, which can allocate an hypothetical regenerator of 350 g of Gd with  $\varepsilon = 30\%$ , would be approximately 1244 W. The cooling power required to cool the coil may be higher than the cooling capacity generated by the magnetic refrigerator itself.

induction)  $\mathbf{B}$  when a magnetic field  $\mathbf{H}$  is applied on the material. Thus:

$$\mathbf{B} = \mu\mathbf{H} \quad (2.17)$$

The relative magnetic permeability,  $\mu_r$  of a material is defined as:

$$\mu_r = \frac{\mu}{\mu_0} \quad (2.18)$$

where  $\mu_0$  is the permeability of the free space<sup>4</sup>. In SI units, the constitutive relation between  $\mathbf{B}$ ,  $\mathbf{H}$  and  $\mathbf{M}$  is:

$$\mathbf{B} = \mu_0 (\mathbf{H} + \mathbf{M}) \quad (2.19)$$

A material can be considered as paramagnetic or diamagnetic when  $\mu \sim \mu_0$ ; if  $\mu_r \geq 1$  the state is paramagnetic, else it is diamagnetic. For the materials dealt with in this work,  $\mu_r > 1$ , which is also a characteristic of ferromagnetic materials. Ferromagnetism disappears when the thermal energy is higher than the magnetic exchange energy. Such a transition occurs at a specific temperature, known as Curie temperature,  $T_C$ . Above this phase transition temperature, the substance behaves as a paramagnetic material (Callister, 2002).

Ferromagnetic (and ferrimagnetic) materials exhibit a phenomenon known as magnetic hysteresis, discovered by the German physicist Emil Warburg (1846-1931). The hysteresis or  $B(H)$  curve of a ferromagnet is illustrated in Fig. 16. The most important properties of a ferromagnetic material are defined in this curve. The material is considered saturated when it attains a saturation induction,  $B_S = \mu_0(H + M_S)$ , where  $M_S$  is the saturation magnetization. In the absence of a magnetic field ( $H = 0$ ) the material conserves an induction known as magnetic remanence,  $B_{\text{rem}}$ . The macroscopic magnetic induction is removed when a magnetic field is applied in the opposite direction, known as coercive field or coercivity,  $H_C$ .

According to the value of coercivity, the ferromagnetic materials are classified as *soft* or *hard* (Spaldin, 2003). Soft magnetic materials have  $H_C$  usually lower than 1000 A/m, so they are easy to magnetize and demagnetize ( $\mu \gg 1$ ), e.g. iron. On the other hand, hard magnetic materials, also known as *permanent magnets*, require high magnetic fields to remove their magnetic induction ( $H_C > 10000$  A/m). Permanent magnets store energy, which is placed in

<sup>4</sup>  $\mu_0 = 4\pi \times 10^{-7} \text{ N/A}^2$ .

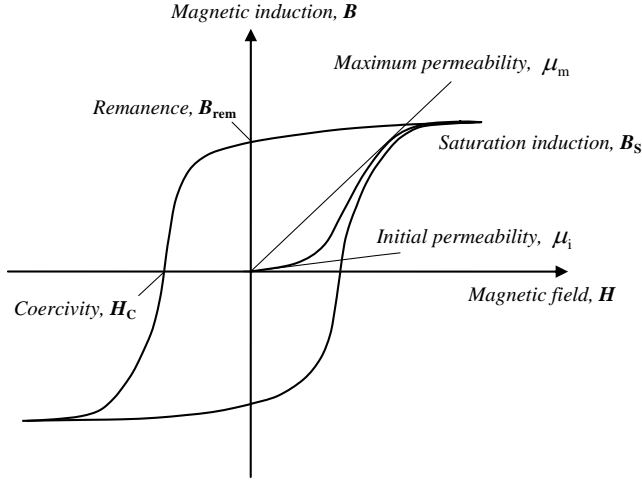


Figure 16 – Typical hysteresis curve for a ferromagnetic material.

the material when magnetized and may stay indefinitely if the production and handling are adequate (Cullity, 1972). The constitutive relation of a hard magnetic material is:

$$\mathbf{B} = \mu_0 \mu_r \mathbf{H} + \mathbf{B}_{\text{rem}} \quad (2.20)$$

The *working point* of a permanent magnet in an application lies usually at the second quadrant of the  $B(H)$  hysteresis curve, known also as the demagnetization curve, as that shown in Fig. 17 for a Nd-Fe-B magnet with a linear demagnetization curve,  $\|\mathbf{B}_{\text{rem}}\| = 1.4 \text{ T}$  and  $\mu_r = 1.05$ . An *energy product* ( $BH$ ) is defined as the energy that the permanent magnet supplies to the magnetic circuit and its maximum value is considered as the *maximum energy density* of the permanent magnet  $(BH)_{\text{max}}$ . This quantity is the most common figure of merit for a permanent magnet and it is granted as the ideal working point for a magnet within the circuit (Campbell, 1999; Bjørk, 2010). For the demagnetization curve in Fig. 17,  $(BH)_{\text{max}} \sim 371 \text{ kJ/m}^3$ .

The most important permanent magnets are the alnico (Al-Ni-Co), ferrite (iron oxide compound), samarium-cobalt (Sm-Co) and neodymium-iron-boron (Nd-Fe-B) magnets. Their typical properties at 293 K are summarized in Table 3. Other useful properties needed to select permanent magnets are presented in Table 4. Fig. 18 shows a comparison of the demagnetization curves for the

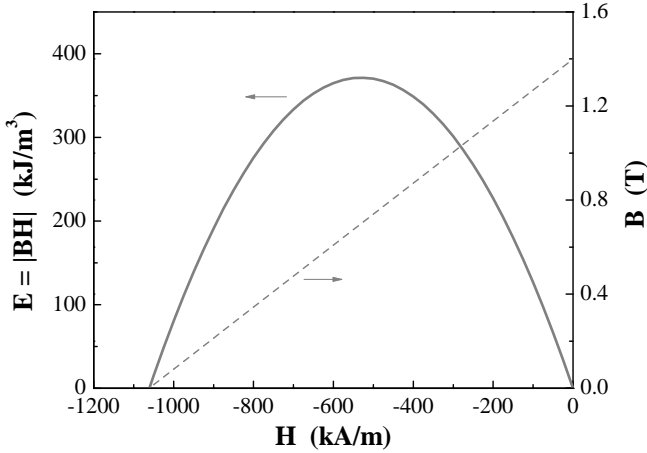


Figure 17 – Working point and its calculated energy product ( $BH$ ) for a Nd-Fe-B permanent magnet with linear demagnetization curve ( $\mathbf{B} = \mu_0\mu_r\mathbf{H} + \mathbf{B}_{\text{rem}}$ ), with  $\|\mathbf{B}_{\text{rem}}\| = 1.4$  T and  $\mu_r = 1.05$ . The maximum energy density for this permanent magnet  $(BH)_{\text{max}} \sim 371$  kJ/m<sup>3</sup>.

Table 3 – Typical properties of the most important permanent magnets at 293 K (Bastos, 2004; Furlani, 2001).

Permanent Magnet	$ B_{\text{rem}} $ [T]	$ H_C $ [kA/m]	$ BH _{\text{max}}$ [kJ/m <sup>3</sup> ]	$\mu_r$ [–]
Alnico	0.71 - 1.25	43.8 - 160	52 - 82	2.0 - 6.4
Ferrite	0.23 - 0.42	147 - 280	8.4 - 31.8	1.1
Sm-Co	0.83 - 1.12	480 - 800	128 - 192	1.05 - 1.3
Nd-Fe-B	1.08 - 1.47	830 - 1115	225 - 415	1.03 - 1.06

Table 4 – Selection properties for the most important permanent magnets (Ferreira & Costa, 2011).

Permanent magnet	$T_C$ [K]	Cost [€/kg]	Density [kg/m <sup>3</sup> ]	Energy/cost [J/€]
Alnico	1173	32.4	7300	0.17
Ferrite	723	4.9	4500	1.46
Sm-Co	1023	162	8500	0.16
Nd-Fe-B	583	81	7500	0.56

permanent magnets presented in Tables 3 and 4. As can be seen, the demagnetization curve for Nd-Fe-B can be considered linear to facil-

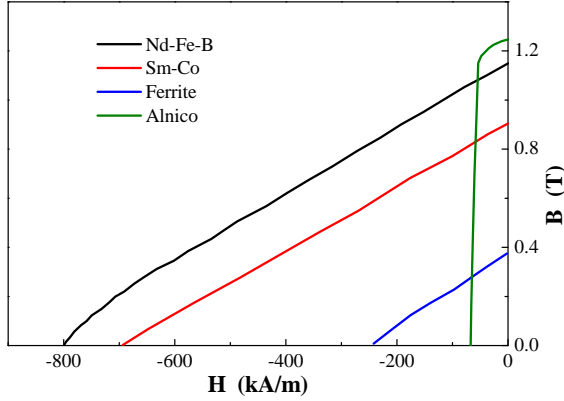


Figure 18 – Typical demagnetization curves for the most important permanent magnets. Adapted from Bastos (2004).

itate its simulation (Fig. 17). Of all permanent magnets,  $\text{Nd}_2\text{Fe}_{17}\text{B}$  exhibits the best performance, being the preferred magnetic field generator for magnetic refrigerators.

### 2.7.2 Demagnetization field

The internal magnetic field,  $\mathbf{H}$ , of a magnetized body is lower than the applied external magnetic field,  $\mathbf{H}_{\text{appl}}$ , due to the generation of a field in the opposite direction inside the material, known as the demagnetization field,  $\mathbf{H}_{\text{dem}}$ . The magnetic field inside the material is given by:

$$\mathbf{H} = \mathbf{H}_{\text{appl}} + \mathbf{H}_{\text{dem}} \quad (2.21)$$

The demagnetization field is proportional to the magnetization but with an opposite direction:

$$\mathbf{H}_{\text{dem}} = -\mathbb{N} \cdot \mathbf{M}(T, \mathbf{H}) \quad (2.22)$$

where  $\mathbb{N}$  corresponds to the demagnetization tensor, which depends mainly on the geometry of the body (Smith *et al.*, 2012). If a homogeneous demagnetization is considered (neglecting magnetic anisotropy), the demagnetization tensor becomes a scalar,  $N_{\text{D}}$ , known as the *averaged demagnetization factor*. For a single sphere,  $N_{\text{D}} = \frac{1}{3}$ , while for a rectangular prism it is calculated from the Aharoni (1998) equation presented in Appendix A.

A schematic representation of the magnetic field distribution of a bar magnet is presented in Fig. 19. As can be seen, in the interior of the body,  $\mathbf{H}$  lies in an opposite direction to  $\mathbf{B}$ , but the two are aligned outside the bar. This corresponds to a flux conservation, as can be inferred from Fig. 18.

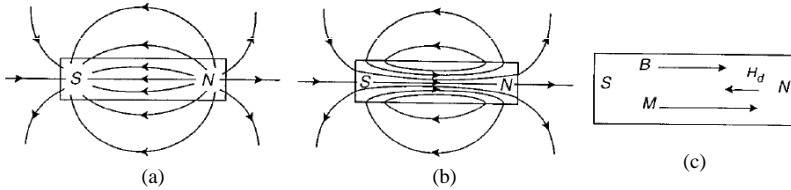


Figure 19 – Schematic representation of the magnetic field distribution of a bar magnet: (a) magnetic field,  $\mathbf{H}$ ; (b) induced field  $\mathbf{B}$  and (c)  $\mathbf{B}$ ,  $\mathbf{H}_{\text{dem}}$  and  $\mathbf{M}$  inside the magnet. Adapted from Furlani (2001).

A magnet system design should carefully avoid self-demagnetization of the permanent magnets while in operation, which means that  $|\mathbf{H}| < H_C$  at all times. Also, the properties of the magnets depend on temperature, mainly the coercivity, so it is important not to subject the magnets to temperatures close to their Curie temperature, since they could self-demagnetize.

### 2.7.3 Modeling a magnetic circuit

In order to design a magnetic circuit composed of permanent magnets, an understanding of some basic electromagnetism is required. In recent years, the need to solve electromagnetic problems for different geometries has prompted the use of commercial software for solving numerically the governing equations. The software package COMSOL (2008)<sup>5</sup>, which uses the finite element method (FEM), has been used consistently by the magnetic refrigeration community.

A typical magnetic circuit design is initiated with the solution of the magnetostatic problem. For modeling the magnetic circuit at low frequencies and determine the eddy currents in the stator, a quase-static magnetodynamic analysis should be employed.

<sup>5</sup> Comsol Multiphysics employs the solver Pardiso and a parallel sparse direct linear solver.

The magnetostatic theory neglects the time-dependent terms of the Maxwell equations ( $\frac{\partial \mathbf{B}}{\partial t} = 0$ ) yielding the well-known fundamental Maxwell equation:

$$\nabla \cdot \mathbf{B} = 0 \quad (2.23)$$

Eq. (2.23) demonstrates that the magnetic flux density is a conservative field. The Maxwell equations are solved using potential functions like the magnetic scalar potential,  $V_m$ , defined as:

$$\mathbf{H} = -\nabla V_m \quad (2.24)$$

Substituting the above expression into Eq. (2.20) and imposing Eq. (2.23) the following Poisson equation is found:

$$\nabla \cdot (\mu_0 \mu_r \nabla V_m - \mathbf{B}_{\text{rem}}) = 0 \quad (2.25)$$

For the simulation of an air or vacuum region (including the magnetic gap), Eq. (2.23) becomes the laplacian of the magnetic scalar potential, i.e.,  $\nabla^2 V_m = 0$ . For a soft magnetic material, such as iron, the constitutive relationship is its own  $BH$  curve, i.e.,  $\mathbf{B} = f(|\mathbf{H}|) \frac{\mathbf{H}}{|\mathbf{H}|}$ . Each of these equations can be solved using the Finite Element Method (FEM) to calculate the magnetic flux density distribution in a magnetic circuit.

#### 2.7.4 Desired characteristics of a magnetic circuit for a magnetic refrigerator

The ideal magnetic circuit for a magnetic refrigerator should be capable of generating a high magnetic field in a large magnetic gap region using the smallest possible amount of permanent magnet material. It is also very important for the magnetic circuit to have a large region with a low magnetic field, since the MCE of the magnetocaloric material is proportional to the magnetic field change. Therefore, a large magnetic field change in a large region would result in higher cooling capacities. However, the size of these regions is directly proportional to the mass of the permanent magnet, and hence to the cost of Nd-Fe-B (Bjørk, 2010). As a consequence, the most effective magnetic circuits are those in which the magnets are used at every instant of the operation, since magnets are usually expensive and a large work may be required to operate the system.

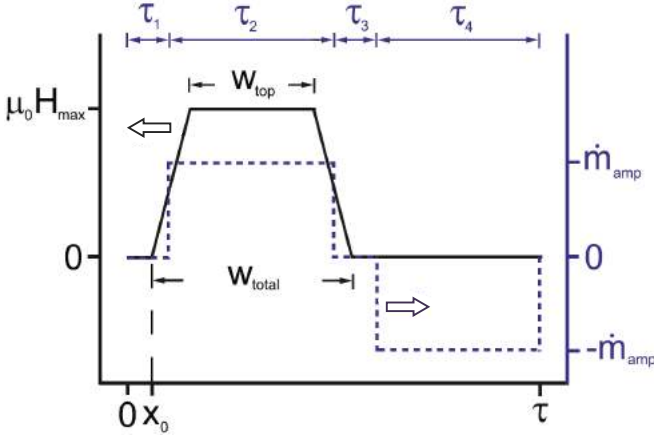


Figure 20 – Generic profiles of the magnetic field (continuous line) and the hydraulic blows on an AMR as a function of time (dashed line). Adapted from Bjørk & Engelbrecht (2011).

Bjørk & Engelbrecht (2011) studied the influence of the change in magnetic field on the AMR behavior, more specifically the synchronization between the magnetic and the hydraulic profiles. The 1-D numerical model developed by Engelbrecht *et al.* (2006) was used. Fig. 20 shows the generic profiles of the magnetic field and the hydraulic blows in the AMR as a function of the AMR cycle period, where  $w_{\text{total}}$  corresponds to the magnetization period including the magnetization and demagnetization ramps and  $\tau$  is the AMR cycle period. The cold and hot blows are considered to have a constant period  $\tau_2 = \tau_4 = 0.4\tau$ , respectively, with ‘waiting’ periods  $\tau_1 = \tau_3 = 0.1\tau$ . Bjørk & Engelbrecht (2011) concluded that the ramp from minimum to maximum magnetic field does not need to be fast (i.e., instantaneous change), but it is very important that the fluid flow and the magnetic profiles are synchronized. The optimum synchronization for the case analyzed was found when  $w_{\text{total}} \sim 0.55\tau$ .

Bjørk *et al.* (2008) proposed a figure of merit, the  $\Lambda_{\text{cool}}$  parameter, to evaluate the performance of a magnetic circuit designed specifically for magnetic refrigeration:

$$\Lambda_{\text{cool}} \equiv \left[ \mu_0 H_{\text{high}}^{2/3} - \mu_0 H_{\text{low}}^{2/3} \right] \frac{V_{\text{field}}}{V_{\text{magnet}}} P_{\text{field}} \quad (2.26)$$

where  $\mu_0 H_{\text{high}}^{2/3}$  and  $\mu_0 H_{\text{low}}^{2/3}$  correspond to the average applied magnetic field in the high and low field regions to the power of 2/3, respectively (see Section 2.1).  $V_{\text{field}}$  is the volume of the high field region,  $V_{\text{magnet}}$  is the volume of the permanent magnets and  $P_{\text{field}}$  is the fraction of the cycle in which the magnetocaloric material is in the high field region. As can be seen,  $\Lambda_{\text{cool}}$  increases not only with a large field in the magnetization region but, also with a low magnetic field in the demagnetization region. This highlights the importance of minimizing the field in the low field regions.

The design of a new magnetic circuit can be optimized via the maximization of  $\Lambda_{\text{cool}}$  for a chosen average magnetic field in the high field region (Bjørk, 2010). Therefore, a compromise between a high field region volume and a large magnetic field change generated by the use of a low magnet volume should be optimized.  $\Lambda_{\text{cool}}$  is also favored if the magnetic circuit is in use most of time.

### 2.7.5 State-of-the-art magnetic circuits

This section presents some state-of-the-art magnetic circuits developed for magnetic refrigeration applications. They are evaluated in terms of the  $\Lambda_{\text{cool}}$  parameter. Bjørk *et al.* (2010) performed a broader review of the magnetic systems for room-temperature applications. Some of the published magnetic circuits are summarized in Table 5.

Table 5 – Specifications of the developed magnetic circuits for magnetic refrigerators (<sup>a</sup>induced field calculated in the Gd regenerators). Adapted from Bjørk (2010).

Magnetic circuit	$V_{\text{magnet}}$ [L]	$V_{\text{field}}$ [L]	$\mu_0 H_{\text{high}}$ [T]	$\mu_0 H_{\text{low}}$ [T]	$P_{\text{field}}$	Type	$\Lambda_{\text{cool}}$ [T <sup>2/3</sup> ]
Bouчекara (2008)	0.82	0.20	$0.94^a$	0	0.9	R	0.21
Bjørk <i>et al.</i> (2010a)	7.30	2.00	0.87	0.06	1.0	S	0.21
Engelbrecht <i>et al.</i> (2009)	0.50	0.07	1.03	0	0.5	HC	0.07
Okamura <i>et al.</i> (2007)	3.38	0.80	1.00	0	0.9	R	0.21
Tura & Rowe (2007)	1.03	0.05	1.40	0.1	0.5	CHC	0.03
Tušek <i>et al.</i> (2009)	0.65	0.11	0.97	0.1	1.0	S	0.13
Zheng <i>et al.</i> (2009)	0.50	0.09	0.93	0	0.9	C	0.15
Chell & Zimm (2006)	4.70	0.15	1.90	0.1	0.9	Y	0.03

Magnet type: (R) rotary, (S) static, (HC) Halbach cylinder, (CHC) concentric Halbach cylinders, (C) "C" shaped and (Y) "Y" shaped.

Tura & Rowe (2007) developed a magnetic system composed of two concentric Halbach cylinders in which the regenerator is located in the inner bore and the magnets rotate to generate the magnetic field change (Fig. 21a). Chell & Zimm (2006) designed a

complex double Y-shaped magnetic array (Fig. 21b) in which the stationary regenerators are placed in the gap and the magnetic circuits rotate (Zimm *et al.*, 2007).

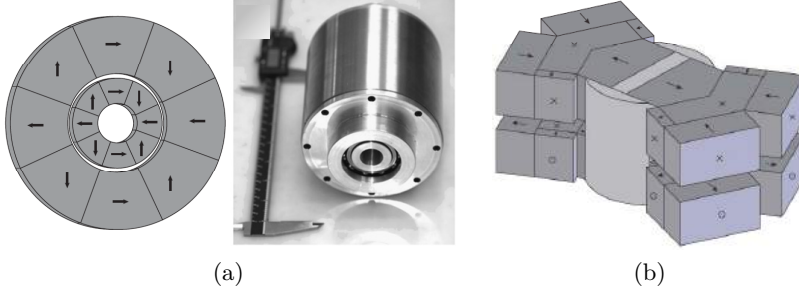


Figure 21 – (a) Magnetic system composed of two rotary concentric Halbach cylinders in the position of  $\mu_0 H_{\text{high}}$  (Tura & Rowe, 2007) and (b) a complex double Y-shaped magnetic array (dark grey segments are permanent magnet and light grey are iron) (Chell & Zimm, 2006; Zimm *et al.*, 2007).

Okamura *et al.* (2007) developed a rotor-stator magnetic circuit with a high  $\Lambda_{\text{cool}}$ . In this system, four stationary regenerators are placed in a ring-shape magnetic gap (Fig. 22a). The rotor is composed by permanent magnet and iron segments, while the stator is composed by a laminated iron alloy. Allab (2008) analyzed different geometries of magnetic arrays for magnetic refrigeration and proposed the use of a simple rotor-stator configuration (Fig. 22b) in which the rotor is made entirely of Nd-Fe-B and the stator has 4 ‘wings’ that allow for high induction fields in the regenerators. However, the wings generate a very high torque in the rotor. Bouchekara (2008) performed an optimization-based analysis of this magnetic system to reduce the magnetic forces.

(Bjørk *et al.*, 2010a) designed one of the most advanced magnet systems for magnetic refrigeration to this date. The system is composed of two concentric cylinders (Fig. 23) made from segments of permanent magnet (dark grey) and iron (light grey). Four regions of high field and four regions of low field are created between the cylinders. The design procedure detailed in (Bjørk *et al.*, 2011) consisted of an algorithm which improves the high and low field regions in an ideal Halbach system described in (Bjørk *et al.*, 2010). Enclosing the low field region with an equipotential line (constant  $\mathbf{B}$ ) and

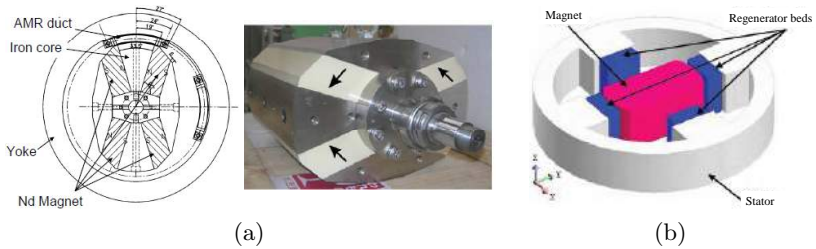


Figure 22 – Rotor-stator magnetic circuits developed by (a) Okamura *et al.* (2007) and (b) Allab (2008) and Boucekara (2008).

substituting all magnet in the enclosed region by soft magnetic material shields the low field region and reduces the flux density in this region, increasing  $\Lambda_{cool}$ . After the magnet optimization, the magnetic system can be segmented into permanent magnet and iron segments.

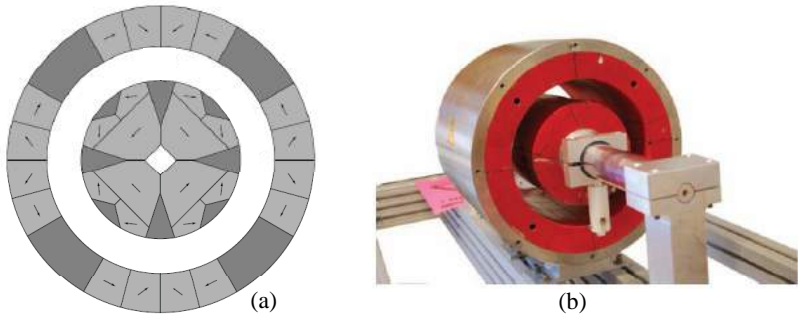


Figure 23 – Static magnetic circuit of Bjørk *et al.* (2010a).

## 2.8 SUMMARY AND SPECIFIC OBJECTIVES

This section presented a review of the literature on a series of topics related to near room-temperature magnetic refrigeration. A number of challenges and opportunities for technical and scientific development have been identified in the four main research fronts of magnetic cooling, namely: (i) synthesis of promising working materials with high MCE, (ii) optimized and cost-effective magnetic circuits, (iii) development of high effectiveness AMR configurations

and (iv) development of efficiency-oriented thermo-magnetic cooling systems. With these in mind, and to achieve the general objective of this thesis, the following specific objectives have been outlined:

- To develop an experimental infrastructure to enable the characterization of promising magnetocaloric materials via direct measurement of their adiabatic temperature change;
- Study the influence of the AMR parameters by means of analytical and numerical simulations to assist the design of magnetic refrigerator components;
- Design and build a high efficiency rotor-stator magnetic circuit;
- Develop a high performance rotary magnetic refrigerator with stationary regenerators;
- Experimentally characterize the magnetic refrigerator at different operating conditions of temperature, frequency and flow rate.
- Develop a method to evaluate the thermodynamic performance of magnetic cooling devices and apply it to a state-of-the-art magnetic refrigerator.

## Chapter 3

# DIRECT MEASUREMENT OF THE MAGNETOCALORIC EFFECT

This chapter presents a brief introduction to the direct method to characterize the magnetocaloric effect (MCE) and the experimental facility developed in this thesis to perform the measurements. Samples of benchmark magnetocaloric materials (e.g., Gd) and more recent and promising magnetic refrigerants were characterized.

### 3.1 DIRECT MEASUREMENT OF THE MCE

As mentioned previously, the so-called direct approach to characterize the magnetocaloric effect (MCE) via the adiabatic temperature change,  $\Delta T_{\text{ad}}$ , is less expensive and simpler in terms of experimentation and data analysis than the indirect approach. Moreover, depending on the nature of the experimental procedure of the direct method, adiabatic and quasi-static conditions (compulsory in the indirect approach) need not to be fulfilled. This ensures more realistic results from the point of view of the application in a refrigeration system, since it is likely that, in this case, there will be heat transfer to or from the solid refrigerant over a finite amount of time.

The custom-built experimental facility for direct measurements of the  $\Delta T_{\text{ad}}$  designed and built by Trevizoli *et al.* (2012) showed a satisfactory agreement with direct measurement results and those obtained via an indirect approach reported in the open literature (Dan'kov *et al.*, 1997). The differences between the two databases were attributed to Gd sample purity and distinct experimental conditions.

In this thesis, a purpose-built temperature controlled chamber was constructed to accommodate and to improve the experimental facility originally developed by Trevizoli *et al.* (2012). Samples of gadolinium (Gd) and of the promising magnetic refrigerant MnFe(P,As) have been characterized via direct measurements of  $\Delta T_{\text{ad}}$  to evaluate their performance when subjected to a variation of the applied magnetic field at different temperatures, their reversibility and the dependence of the MCE on the sample geometry.

### 3.2 EXPERIMENTAL APPARATUS AND PROCEDURE

The experimental apparatus developed by Trevizoli *et al.* (2012) is shown in Fig. 24. The magnetic field is provided by a C-shaped  $\text{Nd}_2\text{Fe}_{14}\text{B}$  Halbach permanent magnet with a volume of uniform magnetic flux density of 1.75 T. The magnetic field was measured using a LakeShore 425 model gaussmeter and a transversal gaussmeter probe model HMMT-6J04-VF, with an uncertainty of  $\pm 1\%$  of the experimental value. A pneumatic actuator (controlled by a solenoid valve) with a nylon arm was used to traverse the sample into and out of the magnet with a change of magnetic field of the order of milliseconds.

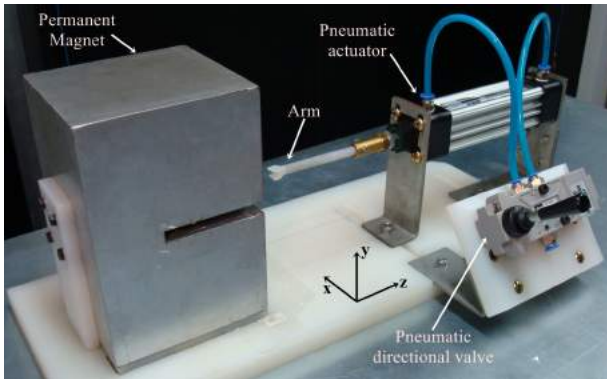


Figure 24 – Apparatus to measure the magnetocaloric effect via the direct method (Trevizoli *et al.*, 2012).

The apparatus is placed inside a 29-liter temperature controlled chamber, as shown in Figs. 25 and 26. The temperature inside the chamber is controlled by a mixture of water and ethylene-glycol (50% vol.) flowing through a copper coil heat exchanger (Fig. 27(a)) connected to a thermostatic bath. Two Peltier modules connected to fan-assisted aluminum heat spreaders were installed in the chamber to accelerate the heating and cooling rates of the sample (Fig. 27(b)). Thermal insulation is achieved with a 100-mm thick polystyrene foam layer. The temperature inside the chamber can be set between 250 and 350 K, with an accuracy of  $\pm 0.05$  K.

Magnetic refrigerant samples can be characterized in bulk or powder form. Bulk form samples are shaped from two rectangular plates (prims). Between the plates, a 0.13 mm (0.005 in) diameter



Figure 25 – Purpose-built temperature controlled chamber.



Figure 26 – Experimental apparatus inside the purpose-built temperature controlled chamber.

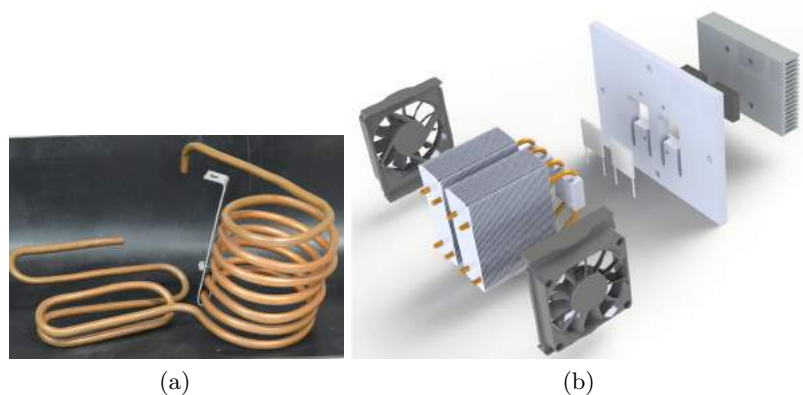


Figure 27 – (a) Copper coil heat exchanger and (b) Peltier system.

T-type thermocouple is carefully placed to enable the characterization of the magnetic temperature change. T-type thermocouples were chosen for their greatest homogeneity of the component wires, which reduces errors due to temperature gradient in a magnetic field (Green & Schroeder, 1988). The thermocouple tip is positioned in the center of the gap between the plates and, to improve thermal contact, the gap is filled with a thin layer of a high-density ceramic-base thermal grease to minimize the interference with the magnetic field (Fig. 28(a)). The samples were thermally insulated with a 5-mm layer of expanded polystyrene foam, as seen in Fig. 28(b).

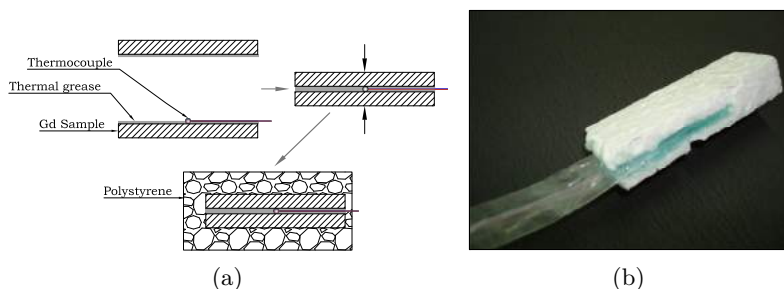


Figure 28 – Sample preparation: (a) Step-by-step preparation of a sample for the direct measurements and (b) sample with the polystyrene insulation (Trevizoli *et al.*, 2012).

A T-type thermocouple built-in a copper cylinder to improve its temperature stability was placed inside the chamber to monitor the ambient temperature. Both thermocouples, ambient and sample, were calibrated between 278 and 308 K, following the process described by Trevizoli *et al.* (2009).

A typical measurement of the magnetocaloric temperature change consists of the following steps. Once the sample stabilizes at the desired temperature, a solenoid valve activates the pneumatic actuator placing the sample inside the magnet, which causes an instantaneous change of the magnetic field on the sample from 0 to 1.75 T (magnetization). The sample stays in the magnetic field for a few seconds before the solenoid valve is closed and the sample is moved out of the magnetic field (demagnetization). Fig. 29 shows the results of a typical measurement, which consists of three steps: temperature stabilization before (de)magnetization, the (de)magnetization process (which initiates with a thermocouple signal interference due to the magnetic field change) and finally the (de)magnetization. This measurement procedure is repeated five times for each desired temperature to guarantee reproducibility and decrease experimental uncertainty, which was calculated as  $\pm 0.20$  K.

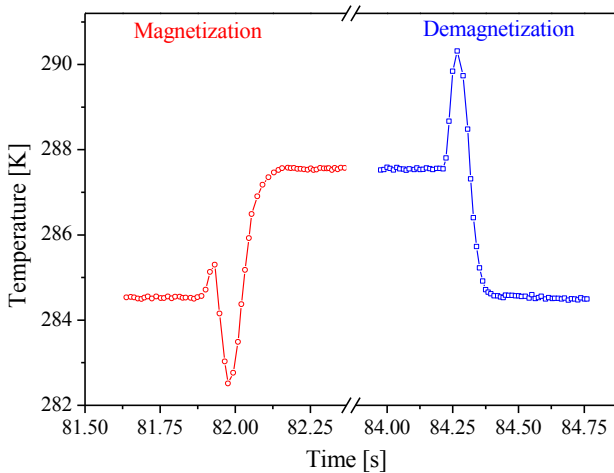


Figure 29 – Typical experimental result of the temperature variation due to magnetization and demagnetization of a sample.

The adiabatic temperature change,  $\Delta T_{\text{ad}}$ , is taken as the dif-

ference between the average plateau temperatures of the sample when it is out and in the magnetic field. A heat conduction model derived by Trevizoli *et al.* (2009) was used to calculate the instantaneous magnetocaloric temperature change. The temperature fluctuations (spikes) due to the magnetic induction of the thermocouple when it is moving in and out of the magnetic field have been excluded from the averaging.

The influence of the sample shape on the magnetic field is taken into consideration through the sample averaged demagnetization factor,  $N_D$ . For prismatic bodies, the demagnetization factor can be calculated according to the algebraic relationships proposed by Aharoni (1998). These relationships are presented in Appendix A.  $N_D$  is responsible for reducing the intensity of the internal magnetic field,  $\mathbf{H}$ , in comparison with the applied magnetic field,  $\mathbf{H}_{\text{appl}}$  (Eqs. (2.21) and (2.22)). Thus, for an isothermal sample, considering homogeneous demagnetization, the average internal magnetic field,  $H_{\text{int}}$ , is calculated as (Bahl & Nielsen, 2009; Smith *et al.*, 2010):

$$H_{\text{int}} = H_{\text{appl}} - N_D M \quad (3.1)$$

where  $H_{\text{appl}}$  corresponds to the average applied magnetic field and  $M$  is the average magnetization as a function of field and temperature. In the present measurements,  $\mu_0 H_{\text{appl}} = 1.75$  T and  $\mu_0$  is the permeability of free space.

### 3.3 EXPERIMENTAL WORK

Two samples fabricated from commercial Gd plates with a claimed purity 99.5%wt have been measured with parallel (sample Gd-1) and perpendicular (sample Gd-2) applied magnetic field along the 7.2 mm dimension. The geometry of the samples were of a rectangular prism as that shown in Fig. 30. The corresponding dimensions and demagnetization factors of the samples tested in this work are summarized in Table 6. The experimental results for the Gd samples were generated as a means of validating the experimental apparatus and procedure.

It is expected that the level of chemical impurities in these Gd samples is about the same as in the Gd spheres employed in both magnetic refrigerators tested in this thesis. However, the Gd spheres could not be characterized directly in this experimental facility due to their shape. However, a complete magnetocaloric

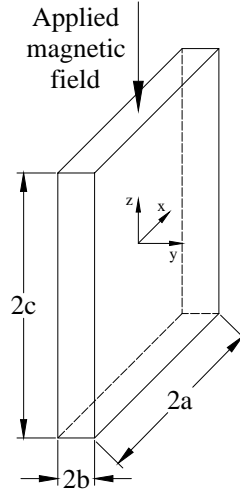


Figure 30 – Coordinate system employed for the calculation of the demagnetization factor of a rectangular prism body. The applied magnetic field,  $\mathbf{H}_{\text{appl}}$ , is parallel to the  $z$ -axis (Aharoni, 1998).

Table 6 – Specification of the samples.

Sample	$2a$ (mm)	$2b$ (mm)	$2c$ (mm)	$N_D$ (–)
Gd-1	14.8	2.0	7.2	0.213
Gd-2	14.8	7.2	2.0	0.687
Mn-1	6.5	3.2	4.7	0.458
Mn-2	6.7	2.0	5.0	0.579
Mn-3	6.0	2.0	4.7	0.558

characterization by indirect methods of the UFSC Gd spheres was carried out at the BASF facilities in The Netherlands, as detailed in Appendix B, and of the DTU Gd spheres at the DTU facilities in Denmark, as detailed in Section 4.5.1.

Additionally, three samples of MnFe(P,As) synthesized at BASF with a slightly different chemical composition have been characterized. The geometry of the samples were also of a rectangular prism and the dimensions and demagnetization factors of the Mn-based samples are summarized in Table 6. These samples were produced via high-energy ball milling plus sintering and homogenization heat treatment at high temperatures. The adiabatic temperature change

as a function of temperature was obtained for all the samples. The temperature changes resulting from magnetization and demagnetization of the samples were measured so as to verify the reversibility of the magnetocaloric effect. Additionally, measurements were taken in both heating up and cooling down modes to quantify the thermal hysteresis.

## 3.4 RESULTS

### 3.4.1 Gd samples

The magnetocaloric effect was experimentally investigated for sample Gd-1, as shown in Fig. 31 for  $\Delta T_{\text{ad}}$  as a function of temperature for both magnetization and demagnetization. The reversibility of the MCE of Gd as proposed by Nielsen *et al.* (2010) was verified by the calculated  $\Delta T_{\text{ad,demag}}$  using Eq. (2.8) and the experimental  $\Delta T_{\text{ad,mag}}$  data. The shift of the demagnetization curve with respect to that for magnetization is a consequence of this constraint. An excellent agreement is observed, which is an important validation of the experimental procedure.

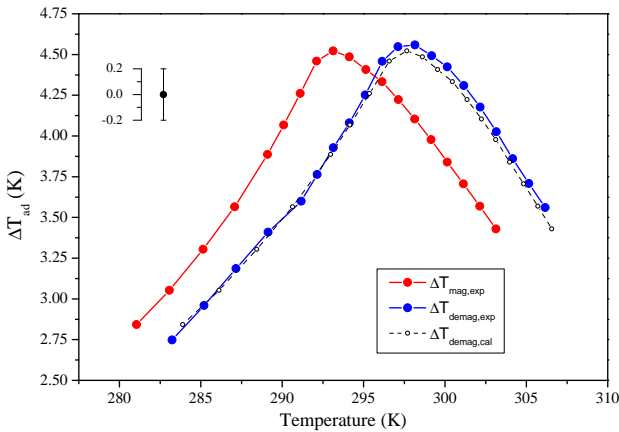


Figure 31 – Experimental  $\Delta T_{\text{ad}}$  for sample Gd-1 while magnetization and demagnetization and calculated demagnetization curve from Nielsen *et al.* (2010) proposed constraint.

The importance of the demagnetization factor is verified in Fig. 32, which clearly shows the dependence of  $\Delta T_{\text{ad}}$  on the sample

geometry, since it decreases when  $N_D$  increases.

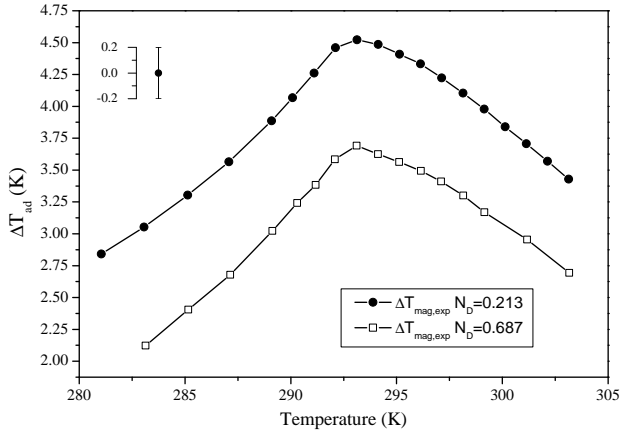


Figure 32 – Demagnetization factor dependence on  $\Delta T_{\text{ad}}$  as a function of temperature.

The internal field,  $\mu_0 H_{\text{int}}$ , calculated from Eq. (3.1) for both Gd samples as a function of temperature is shown in Fig. 33. The magnetization was taken from the experimental results of the commercial grade Gd spheres employed at the UFSC magnetic refrigerator which are presented in Appendix B (Fig. 120(a)). The results for  $\mu_0 H_{\text{int}}$  are in accordance with those presented by Bahl & Nielsen (2009) for commercial grade Gd plates. In this geometry, even small values of  $N_D$  can represent a significant temperature dependence of  $H_{\text{int}}$ , specially at lower temperatures when the material becomes more ferromagnetic.

The maximum experimental  $\Delta T_{\text{ad}}$  for samples Gd-1 and Gd-2 were 4.52 K and 3.69 K, respectively, both found at an initial temperature of 293.1 K and for an applied magnetic field of 1.75 T. As shown in Fig. 32, the calculated  $\mu_0 H_{\text{int}}$  at 293.1 K for both samples is approximately 1.56 T and 1.15 T, respectively. In comparison with literature, specifically the expressions of  $\Delta T_{\text{ad}}$  presented in Section 2.2.1, the experimental results obtained in this work relay halfway between those of pure Gd obtained by Pecharsky & Gschneidner Jr. (2006) and the commercial grade Gd tested by Bahl & Nielsen (2009). That is probably due to the high magnetic field in which the samples have been tested here, and, also, due to larger

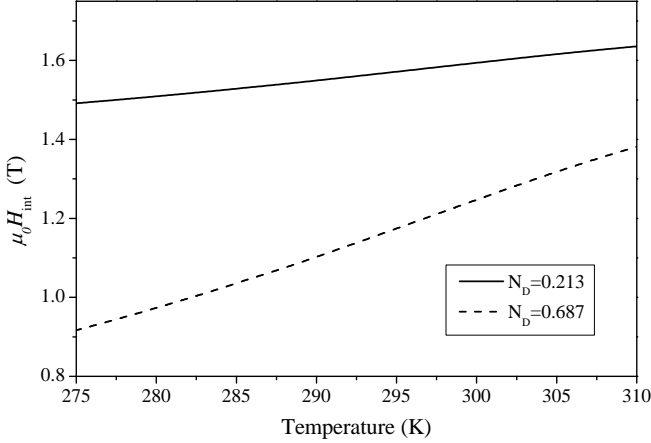


Figure 33 – Internal magnetic field as a function of temperature for samples with  $N_D = 0.213$  (continuous line) and  $N_D = 0.687$  (discontinuous line) for an applied magnetic field of 1.75 T.

experimental uncertainties in this work or the presence of less impurities in the Gd samples.

### 3.4.2 Mn-based samples

Direct measurements were also carried out for three samples of MnFe(P,As) of different compositions. When performing the first measurement in sample Mn-1 an interesting result was found. Fig. 34 shows the magnetization curves for sample Mn-1, which was initially cooled down to 275 K. The sample was then heated, as magnetization and demagnetization  $\Delta T_{\text{ad}}$  measurements were carried out up to 304 K. However, when experiments were subsequently performed cooling the sample, an increase in the magnetocaloric effect was observed. A  $\Delta T_{\text{ad}}$  curve that could be reproduced in a subsequent measurement cycle was only observed after the second heating cycle of the sample. To avoid measurement errors, a pre-training cycles were carried out with the other samples to remove the effect just described. After eliminating the training effect in sample Mn-1, a maximum adiabatic temperature change of 3.9 K was attained at a peak temperature (considered as  $T_C$ ) of 290 K for an applied magnetic field of 1.75 T. The results of the Mn-based samples are summarized in Table 7.

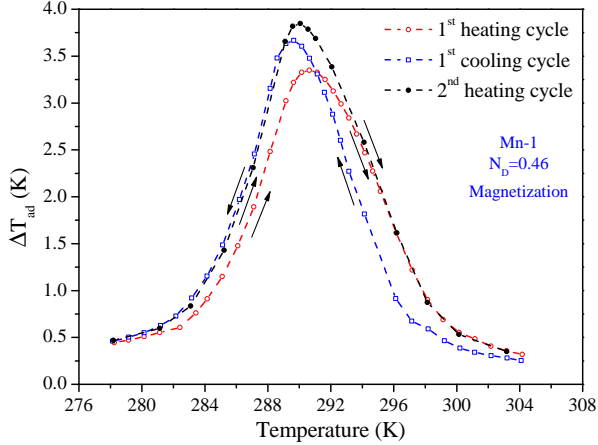
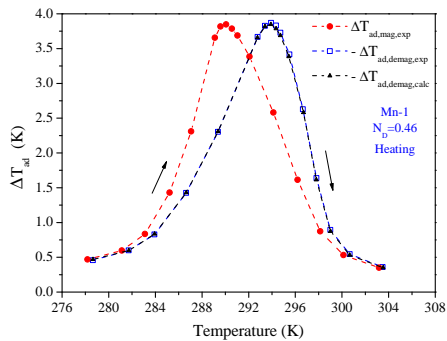


Figure 34 – Adiabatic temperature change for sample Mn-1 with an unusual effect at its first thermal cycles while magnetization.

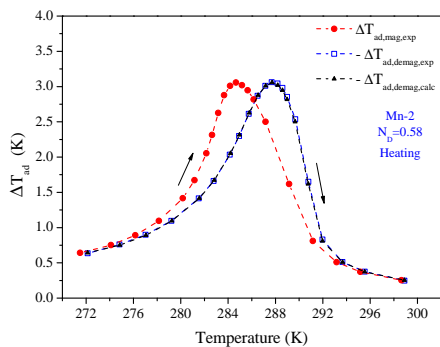
Table 7 – Adiabatic temperature change and peak temperature ( $\sim T_C$ ) while magnetization and heating cycle of the samples when subjected to an applied magnetic field of 1.75 T.

Sample	$\Delta T_{\text{ad}}$ (K)	$T_C$ (K)	$N_D$ (-)
Mn-1	3.9	290.0	0.458
Mn-2	3.1	284.7	0.579
Mn-3	3.0	313.7	0.558

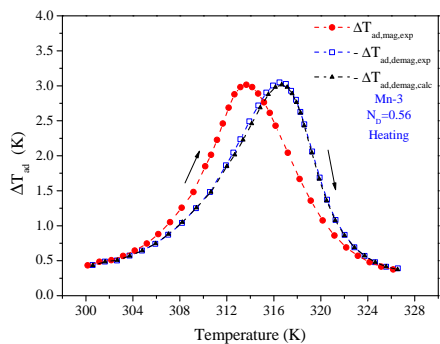
The experimental MCE of the Mn-based samples was measured during magnetization and demagnetization, as shown in Figs. 35(a)-(c). Before acquiring these data, the samples were subjected to heating-cooling thermal cycles to eliminate training effects. The reversibility of the MCE of the Mn-based samples was verified by calculating the demagnetization curve from Eq. (2.8) and overlapping it over the experimental curves, represented by solid triangles in Figs. 35(a)-(c). If the measurement is considered adiabatic, it suggests that the field-induced phase transition is fully reversible within the accuracy of the measurement since an excellent agreement between the experimental and calculated curve is observed.



(a)



(b)



(c)

Figure 35 – Direct measurement of the adiabatic temperature change for samples (a) Mn-1, (b) Mn-2 and (c) Mn-3 as a function of temperature while magnetization and demagnetization with an applied magnetic field of 1.75 T.

Fig. 36 shows the magnetization and demagnetization curves for Mn-2 sample subjected to heating (increasing temperature) and cooling (decreasing temperature) ramps. Since the Mn-based compounds undergo a first-order transition, a thermal hysteresis is expected to occur around the transition temperature. For all the samples, a thermal hysteresis of approximately  $\sim 0.6$  K was observed during magnetization measurements. Thermal hysteresis is, in principle, an undesirable effect in the context of the application of these materials in AMR devices and a more detailed study of this effect in these compounds is presented by von Moos *et al.* (2014). Before acquiring the data shown in Fig. 36, the sample was subjected to heating-cooling thermal cycles to eliminate training effects.

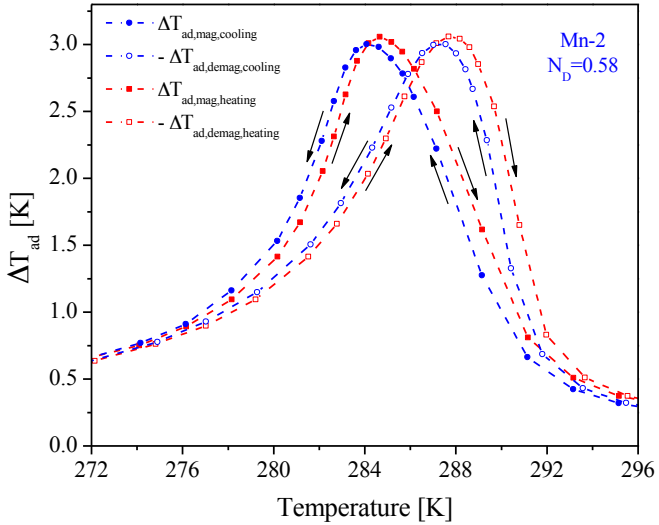


Figure 36 – Thermal hysteresis in the heating and cooling of the Mn-2 sample.

One of the main advantages of first-order compounds is the possibility of tuning its  $T_C$ , which facilitates the construction of multi-layer AMRs to reach larger temperature spans in the regenerator. Fig. 37 shows the adiabatic temperature change of the three Mn-based samples with different compositions and different Curie temperatures. The difference in the adiabatic temperature change between the samples is due to the distinct values of  $N_D$  for each sample. To calculate the actual internal field, the magnetization as a function of temperature and magnetic field should be measured,

but this is out of the scope of this thesis.

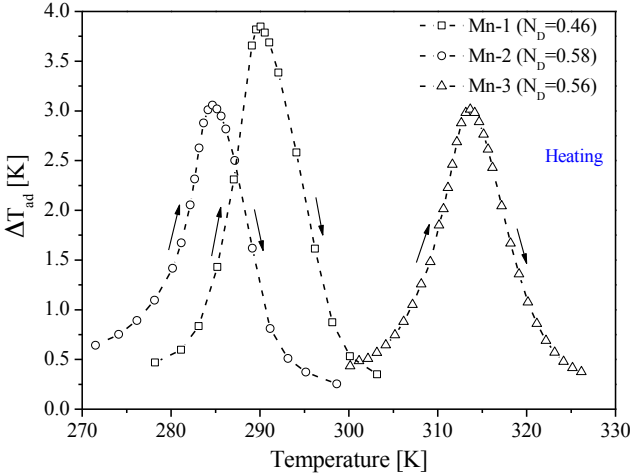


Figure 37 – Adiabatic temperature change of three MnFe(P,As) samples with different compositions when submitted under an applied magnetic field of 1.75 T.

### 3.5 SUMMARY

A temperature controlled facility was constructed to allow more accurate measurements of  $\Delta T_{\text{ad}}$  of magnetocaloric materials via the direct approach. Measurements of Gd samples performed using this setup were in good agreement with experimental  $\Delta T_{\text{ad}}$  results found in the literature. The differences observed can be attributed mainly to impurities in the samples and heat loss, which are inevitable in direct measurements techniques.

The characterization of the three samples of the first-order magnetic refrigerant MnFe(P,As) resulted in a maximum  $\Delta T_{\text{ad}}$  of 3.9 K for an applied magnetic field change from 0 to 1.75 T. A training effect was found in these samples, which consisted of a lower adiabatic temperature change during the first measurement thermal cycle. Direct measurement procedures that involve both thermal and field cycles have demonstrated a thermal hysteresis of about 0.6 K for all three samples. The advantage of tuning the Curie temperature together with the low cost of the raw materials and

the synthesis methods make the MnFe(P,As) compounds promising room-temperature magnetic refrigerants.

The present work enabled understanding the performance of magnetocaloric materials when subjected to the variation of an applied magnetic field at different temperatures as well as the reversibility of the MCE. The dependence of the internal magnetic field investigation due to the sample geometry and its influence on the magnetocaloric properties could represent a partial loss of the magnetocaloric material performance in the application. The learning of these fundamental aspects of the MCE were vital for the design and analysis of the magnetic refrigerators described in the following chapters.



## Chapter 4

# DESIGNING A NOVEL ROTARY MAGNETIC REFRIGERATOR

The need to better understand the physical mechanisms responsible for improving the thermodynamic performance of magnetocaloric devices has motivated the construction of the rotary magnetocaloric refrigerator prototype illustrated in Fig. 38. The main motivation for this design is to reduce the thermal and mechanical losses found in state-of-the-art magnetic refrigerators.

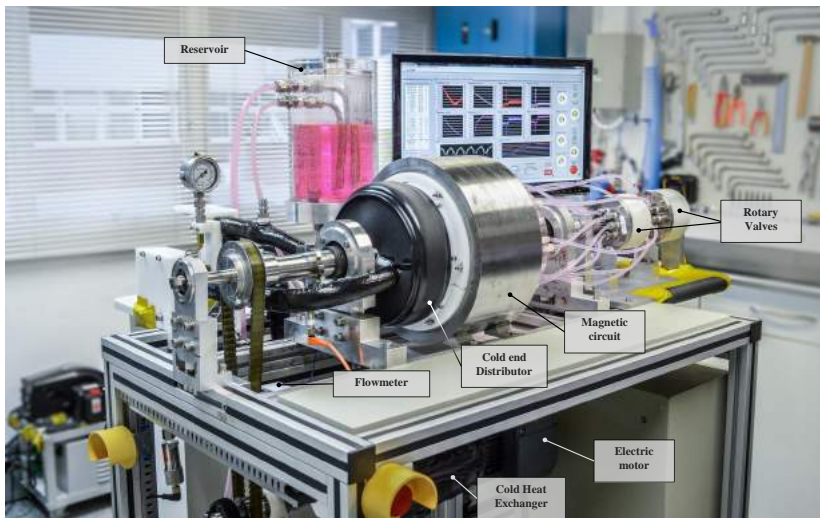


Figure 38 – Photograph of the rotary magnetic refrigerator developed at Polo-UFSC.

The design of a novel magnetic refrigerator is a multidisciplinary task characterized by the synergistic development of magnetic, thermal, hydraulic, electrical, mechanical and instrumentation subsystems. The design procedure of the Polo-UFSC rotary magnetic refrigerator described in this chapter consisted in the following steps (Engelbrecht *et al.*, 2015):

1. Choice of AMR and magnetic circuit configuration;
2. Selection of the magnetocaloric and magnet materials and heat transfer fluid;
3. Choice of geometry (shape) and mass of magnetocaloric material;
4. Setting of initial design constraints via analytical calculations of the AMR;
5. Design of the magnetic circuit;
6. Design of the flow distribution system and pump selection;
7. Design of the regenerator;
8. Selection of the heat exchangers and its components (thermal bath and electrical resistance);
9. Selection of the driving components (motor, pulleys and belt);
10. Selection of the instrumentation sensors;
11. Selection of the data acquisition system and control devices.

This chapter follows the above sequence of topics in the following sections, where a detailed description of the conception of the components of the novel rotary device is presented.

## 4.1 DESIGN CONCEPTS

The rotary magnetic circuit-stationary regenerator configuration was chosen for the present study due to the following characteristics: (i) higher operating frequencies with low magnetic forces, (ii) higher magnetized volume, (iii) continuous pumping of the fluid with less leakage, (iv) compactness, and (v) a magnetic circuit with a more efficient use of the magnets. Nevertheless, this configuration presents some design challenges such as a complex flow distribution system and the magnetic circuit itself.

The present AMR design concept consists of 16 packed beds of Gd spheres and a rotor-stator magnetic circuit. A cross-section view of the rotary system is presented in Fig. 39. The magnetic circuit comprises a stator of laminated electrical steel sheets and a rotor built with segments of Nd-Fe-B permanent magnet and iron (Section 4.3). The magnetic circuit generates two regions of high magnetic field and two regions of low magnetic field in an annular magnetic gap. Thus, the operating frequency of the AMR is twice that of the rotor. The ring-shaped stationary regenerator was fabricated in polyoxymethylene (POM), also known as polyacetal, with 16 beds packed with approximately 1.7 kg of Gd spheres with diam-

eters between 425 and 600  $\mu\text{m}$  and a porosity,  $\varepsilon$ , of approximately 40% (Section 4.5). Being a benchmark magnetocaloric material for room temperature applications, Gd was chosen due to its large MCE, availability in different shapes and well known physical properties. The heat transfer fluid is a mixture of distilled water and commercial ethylene glycol with corrosion inhibitors.

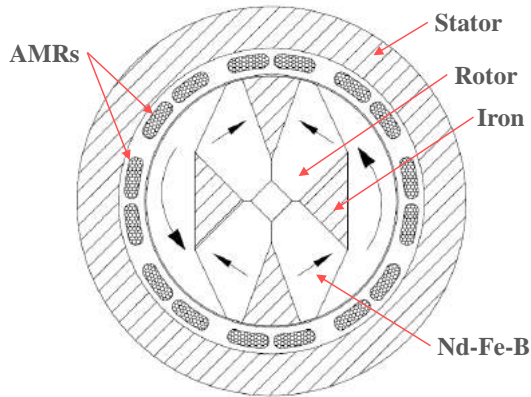


Figure 39 – Cross section view of the magnetic circuit and stationary regenerator beds.

The device has been designed so that the fluid flow is always unidirectional in the hot and cold heat exchangers, as schematically shown in Fig. 40. Two rotary valves specially designed and built in this thesis are placed at the hot end to avoid undesirable heat generation due to seal friction at the cold end. The rotary valves are synchronized with the magnetic rotor to generate alternative blows through the magnetocaloric beds. At the cold end, check valves placed in the regenerator channels and a flow distributor direct the fluid flow towards the cold heat exchanger. The desired flow rate of the glycol solution is set by a gear pump controlled by a frequency inverter and a flow by-pass. The flow rate is measured by an electromagnetic flow meter at the hot end and by a paddle wheel flow meter at the cold end. It is important to point out that a stationary flow system was chosen instead of a rotary one for its better control of fluid leakages. The magnetic circuit as well as the flow distribution system are driven by three-phase electrical motors.

To facilitate the explanation of the flow loop, Fig. 40 shows only two regenerator beds (dephased by  $90^\circ$  in Fig. 39). In the 2-pole

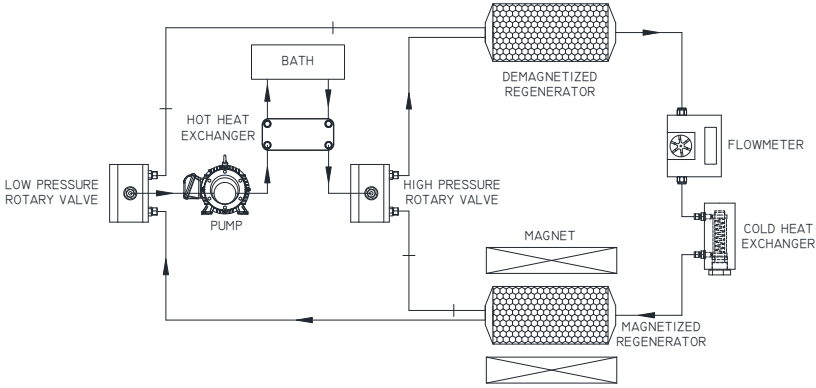


Figure 40 – Basic scheme of the working principle of the rotary device.

arrangement shown in Fig. 39, regenerator pairs dephased by  $180^\circ$  undergo the same process in the AMR cycle. For example, at the rotor position shown in Fig. 39, the regenerator pairs at “12 o’clock” and “6 o’clock” are being magnetized and experiencing a cold-to-hot blow, while the regenerator pairs at “3 o’clock” and “9 o’clock” are being demagnetized and experiencing a hot-to-cold blow. This way the flow distribution system works continuously and the magnet is employed most of the time.

#### 4.2 INITIAL DESIGN CONSTRAINTS AND SPECIFICATIONS

As suggested by Rowe & Barclay (2002), the design of a magnetic refrigerator starts with the definition of the mass of magnetocaloric material, which has a great influence on the size of the device and the magnitude of the magnetic forces involved. The next task is to fit the magnetocaloric material as a compact packed bed in a region with the largest possible change in magnetic field.

In the present design, the *kick off* value for the Gd mass was about 2 kg. From the literature review, this quantity of Gd corresponds to a performance close to that of a domestic refrigerator, at least from the cooling power point of view (see Table 2). Therefore, for a porosity of 36 %, which is typical of a packed bed of spheres, a regenerator volume of about 0.4 L is required. However, since a continuous porous ring is complex to design and operate, a discretization into individual regenerators is inevitable.

The regenerator is to be allocated inside the magnetic gap of

the rotor-stator magnetic circuit, which should also house the casing and fluid channels. Thus, the magnetic circuit design should include a parametrization study to balance the dimensions of the magnetic gap (height, length and hydraulic diameter) with a desirable applied magnetic field change and low magnetic forces.

For efficiency improvement, one needs to maximize the cooling capacity or minimize the input work (or both). Thermodynamically, the minimum (ideal) work is the power consumed by an ideal cooling cycle operating within the temperature limits of the hot and cold environments,  $T_H$  and  $T_C$ , respectively. For the present system, it corresponds to an ideal magnetic work, Eq. (2.12). However, a real device requires some additional work (power consumption) due to: (i) magnetic forces between the beds and the magnet, (ii) electromagnetic losses in the magnetocaloric material and the stator, (iii) mechanical losses, (iv) hydraulic losses (pressure drop due to fluid friction), and (v) thermal losses. Consequently, a device which minimizes the magnetic forces and parasitic losses is desired. The present AMR design is specifically focused on enhancing performance by:

- increasing operating frequencies by using a rotary configuration;
- increasing flow rates by having a continuous flow of the heat transfer fluid;
- increasing magnetocaloric density by employing a large magnetocaloric mass;
- reducing the magnetic interaction torque required to rotate the magnet within the regenerator by using an almost continuous magnetocaloric regenerator ring;
- reducing pressure drop by employing large flow openings at hydraulic system;
- reducing parasitic thermal losses at the cold end by having rotary valves only at the hot end and by insulating the cold end.

The design of the AMR depends mainly on the interaction between the magnetic circuit, flow distribution and regenerator dimensioning. The magnetic circuit is the most expensive and voluminous part of the cooling circuit, so an optimum and effective system configuration is mandatory. For instance, the applied magnetic field is inversely proportional to the height of the magnetic gap, which is obviously a limitation for the regenerator height. Additionally, the regenerator height is inversely proportional to the demagnetization field.

The packed bed of spheres was chosen as the geometry of the Gd regenerator for its large specific surface area (high NTU) and relative easiness with which small hydraulic diameters,  $d_h$ <sup>1</sup>, can be attained. Spheres are easy to pack into a bed and are commercially available. Moreover, spheres reduce eddy currents within the magnetocaloric regenerator, which are generated by the alternative applied magnetic field.

In the present analysis, the heat transfer fluid was chosen as a mixture of 20% ethylene glycol and 80% water (vol.), whose thermophysical properties were obtained from the Brineprops2 library available in EES (Melinder, 1997).

A preliminary analysis was carried out to specify the dimensions of the regenerator beds: width,  $w_{\text{bed}}$ , length,  $L_{\text{bed}}$ , and height,  $h_{\text{bed}}$  as well as the particle diameter,  $d_p$ . The parameters employed in the comparison were the utilization,  $\phi$ , demagnetization factor,  $N_D$ , pressure drop,  $\Delta p$ , and the number of transfer units, NTU.

The parameter constraints and ranges of the analytical study were initially defined based on the expertise gathered from state-of-the-art devices. In the regenerator design, the casing plays an important role due to structural and thermal aspects; a few millimeters must be added to the magnetic gap to accommodate the casing.

As demonstrated in the previous chapter, the demagnetizing field exerts a great influence on the performance of the magnetocaloric material. For a packed-sphere bed, the overall average demagnetizing factor,  $N_D^{\text{bed}}$ , is calculated as (Bleaney & Hull, 1941):

$$N_D^{\text{bed}} = \frac{1}{3} + (1 - \varepsilon) \left( N_{\text{bed}} - \frac{1}{3} \right) \quad (4.1)$$

where the first term,  $N_{\text{sphere}} = \frac{1}{3}$ , is the demagnetizing factor for a sphere and  $N_{\text{bed}}$  is the demagnetization factor for a prismatic solid calculated using Eq. (A.1) proposed by Aharoni (1998) and presented in Appendix A.  $N_{\text{bed}}$  is calculated using the dimensions of the bed, considering the applied magnetic field parallel to the bed height.  $N_D^{\text{bed}}$  is assumed independent of the particle diameter.

Demagnetization factors for different bed dimensions were evaluated and the results are shown in Figs. 41(a)-(c). The depen-

<sup>1</sup> For instance, in the case of  $d_{\text{sphere}} = 0.4$  mm the same  $d_h$  for flat plates would require spacing of 0.075 mm which is extremely difficult to built (Engelbrecht *et al.*, 2015)

dence of  $N_D^{\text{bed}}$  on the bed length is much smaller than on the bed height. Thus, critical values for the regenerator height and the magnetic gap must be determined. A larger magnetic gap will result in a larger magnetic circuit for the same  $\mu_0 H$ , meaning that either the beds get wider or the number of beds increase, which increases also the device complexity. Increasing the width of the beds is desired to reduce magnetic forces and pressure drop, but wider beds would result in higher  $N_D^{\text{bed}}$  (Fig. 41(b)). Wider beds also need a wider magnetic flux generation into the magnetic gap, which is complex and, again, require a larger magnetic circuit (Engelbrecht *et al.*, 2015). Thus, beds with dimensions:  $w_{\text{bed}} = 30$  mm,  $L_{\text{bed}} = 100$  mm,  $h_{\text{bed}} = 16$  mm and porosity  $\varepsilon = 0.36$  result in  $m_{\text{Gd,bed}} \sim 0.24$  kg,  $N_{\text{bed}} \sim 0.58$ , and an overall demagnetization factor  $N_D^{\text{bed}} \sim 0.49$ .

The pressure drop was calculated using the Ergun (1952) correlation for a packed-sphere bed:

$$\frac{\Delta p_{\text{bed}}}{L_{\text{bed}}} = 150 \frac{(1 - \varepsilon)^2}{\varepsilon^3} \frac{\mu_f u_D}{d_p^2} + 1.75 \frac{(1 - \varepsilon)}{\varepsilon^3} \frac{\rho_f u_D^2}{d_p} \quad (4.2)$$

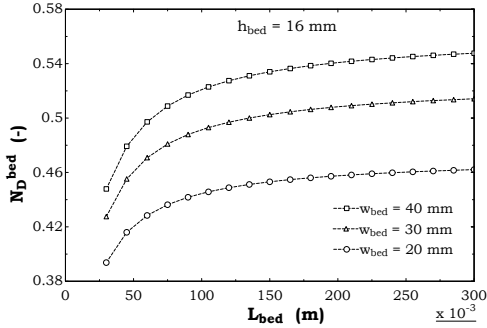
where  $\mu_f$  and  $\rho_f$  are the viscosity and density of the heat transfer fluid, and  $u_D$  is the superficial cross-sectional fluid velocity (Darcy velocity) defined as  $u_D = \frac{\dot{m}_f}{\rho_f A_c}$ , where  $\dot{m}_f$  is the fluid mass flow rate and  $A_c$  is the regenerator cross-sectional area. The fluid pumping power,  $\dot{W}_P$ , is calculated based on the viscous power of the working fluid,  $\dot{W}_{\text{visc}}$ , through the regenerator beds defined as:

$$\dot{W}_{\text{visc}} = \frac{\dot{m}_P}{\rho_f} \Delta p_P \quad (4.3)$$

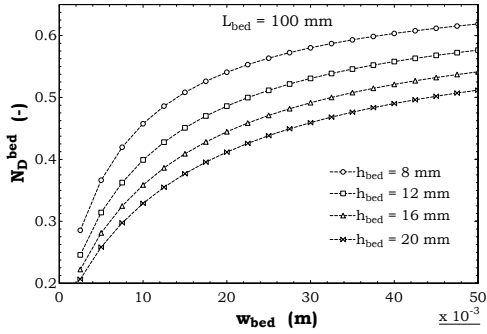
where  $\dot{m}_P$  corresponds to the pump flow rate. And the fluid pumping power is defined as follows:

$$\dot{W}_P = \frac{\dot{W}_{\text{visc}}}{\eta_{\text{OP}}} \quad (4.4)$$

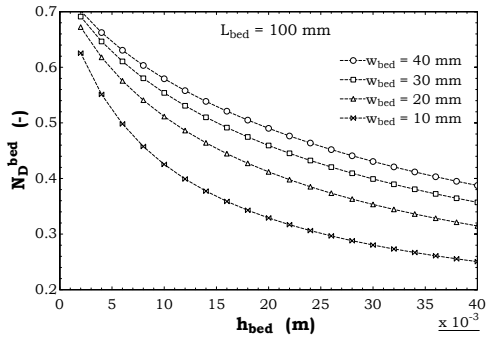
where  $\eta_{\text{OP}}$  is the overall pump efficiency, assumed equal to 0.7.



(a)

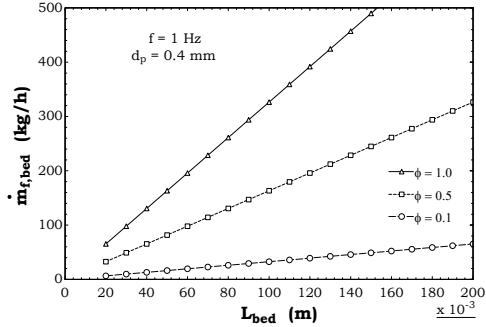


(b)

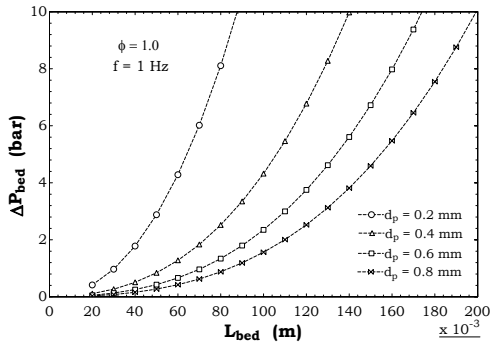


(c)

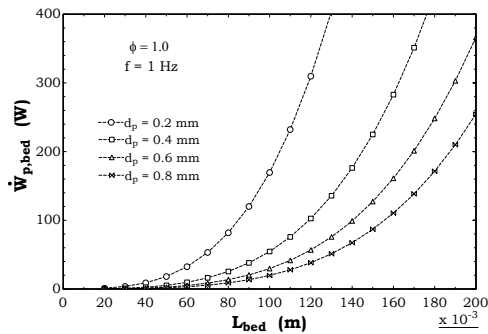
Figure 41 – Demagnetization factor,  $N_D^{\text{bed}}$ , dependence on (a) length, (b) width and (c) height of the regenerator bed.



(a)



(b)



(c)

Figure 42 – (a) Mass flow rate dependence on  $L_{bed}$  for different utilization factors, (b) pressure drop and (c) pumping power dependence on  $L_{bed}$  for different for different particle diameters.

The pressure drop was observed to depend mainly on the bed length, particle diameter and flow rate (or utilization). Assuming a constant bed cross-section area of  $A_c = 500 \text{ mm}^2$  and an operating frequency of 1 Hz, the mass flow rate for different utilization factors, Eq. (2.9), behaves as a function of the bed length as shown in Fig. 42(a). The single-blow pressure drop and pumping power as a function of the bed length for different particle diameters and  $\phi = 1.0$  ( $\varepsilon = 0.36$ ) are shown in Figs. 42(b) and (c), respectively. For a regenerator with  $L_{\text{reg}} = 100 \text{ mm}$ ,  $d_p = 0.4 \text{ mm}$  at  $\phi = 1.0$  ( $\dot{m}_f \sim 326.5 \text{ kg/h}$ ), the pressure drop,  $\Delta p_{\text{bed}}$ , and the pumping power per bed,  $\dot{W}_{\text{P,bed}}$ , are approximately 4.3 bar and 54.5 W, respectively. Considering the overall performance of an AMR with 8 beds, in which at any instant in time 2 beds are subjected to identical flow and magnetic profiles, the total Gd mass would be approximately 2.0 kg,  $\dot{m}_P \sim 653 \text{ kg/h}$ ,  $\Delta p_P \sim 8.6 \text{ bar}$  and  $\dot{W}_P \sim 218 \text{ W}$  (neglecting the pressure drop outside the beds).

Another important thermal parameter related to the regenerator is the number of transfer units, NTU, defined in Eq. (2.10). The NTU is proportional to the convective heat transfer coefficient between solid and fluid,  $h$ , defined as:

$$h = \frac{\text{Nu}k_f}{d_h} \quad (4.5)$$

where  $k_f$  is the fluid thermal conductivity and Nu is the Nusselt number for a packed bed of spheres. Calculations were carried out using the Wakao & Kaguei (1982) correlation given by:

$$\text{Nu} = 2 + 1.1 \text{Re}^{0.6} \text{Pr}^{1/3} \quad (4.6)$$

where Re is the Reynolds number based on the sphere diameter,  $\text{Re} = \frac{u_D d_p \rho_f}{\mu_f \varepsilon}$  and Pr is the Prandtl number,  $\text{Pr} = \frac{c_f \mu_f}{k_f}$ .

In Eq.(4.5), the hydraulic diameter,  $d_h$ , is calculated for a packed bed of spheres as:

$$d_h = \frac{4A_c}{P_w} = \frac{2}{3} \frac{\varepsilon d_p}{(1 - \varepsilon)} \quad (4.7)$$

where,  $P_w$  is the wetted perimeter of the particle.

A large NTU is desired to compensate higher operating frequencies and utilizations (Nielsen *et al.*, 2015). Geometrically, the NTU is mostly influenced by the heat transfer surface area. For a

porous medium, the surface area is inversely proportional to the particle size. However, decreasing the particle size increases the pressure drop and the pumping power. Therefore, a balance between NTU and pressure drop should be found by selecting  $d_p$  and the volume of the regenerator (Engelbrecht *et al.*, 2015).

Fig. 43-a presents the NTU and  $\Delta p_{\text{bed}}$  dependence on  $d_p$  for  $\phi = 1.0$ ,  $f = 1$  Hz,  $A_c = 500$  mm<sup>2</sup> and two different bed lengths,  $L_{\text{bed}}$ , of 50 mm and 100 mm, respectively. Similarly, Fig. 43(b) shows the NTU and  $\Delta p$  dependence on  $L_{\text{bed}}$  for the same operating conditions and three different particle diameters,  $d_p$ , of 0.2 mm, 0.4 mm and 0.6 mm, respectively. As expected, the NTU increases when the particle size decreases and when the length or size of the bed is increased. However, this heat transfer enhancement is offset by an increase in pressure drop. Consequently, the use of spheres with diameters below 0.4 mm and beds longer than 120 mm, in particular, would result in more complex and costly devices capable of working at higher pressures. The volume of the regenerator or the increase in bed length have a lower influence on the NTU, but a larger impact on the pressure drop. For instance, for a regenerator with  $L_{\text{reg}} = 100$  mm and  $d_p = 0.4$  mm at  $\phi = 1.0$  ( $\dot{m}_f \sim 326.5$  kg/h and  $\Delta p_{\text{bed}} 4.3$  bar),  $\text{Nu} \sim 48.0$  and  $\text{NTU} \sim 218.2$ .

The analysis carried out in this section indicated that a 2-kg Gd regenerator with 8 packed-sphere beds with  $d_p \sim 0.4$  mm and  $L_{\text{bed}} \sim 100$  mm can give adequate heat transfer at workable pressure drops. A cross-sectional area of the beds of approximately 500 mm<sup>2</sup> is sufficient for them to fit into the magnetic gap with a balanced  $N_D^{\text{bed}}$ . These specifications were the starting point of the design of the magnetic circuit and the regenerator detailed in the next sections.

### 4.3 DESIGNING THE MAGNETIC CIRCUIT

One of the crucial aspects of a new magnetic refrigerator concerns the efficient use of the magnet system, since the permanent magnet is one of the most expensive materials of the system. The magnetic flux density within a magnetic gap volume is directly proportional to the permanent magnet mass and to the dimensions of the magnetic gap, specially the height,  $h_{\text{gap}}$ . Therefore, the design of a new magnetic circuit is strongly connected to the dimensions of the regenerator beds, mainly to the height,  $h_{\text{bed}}$ . The efficient use of the permanent magnets within the magnetic circuit depends

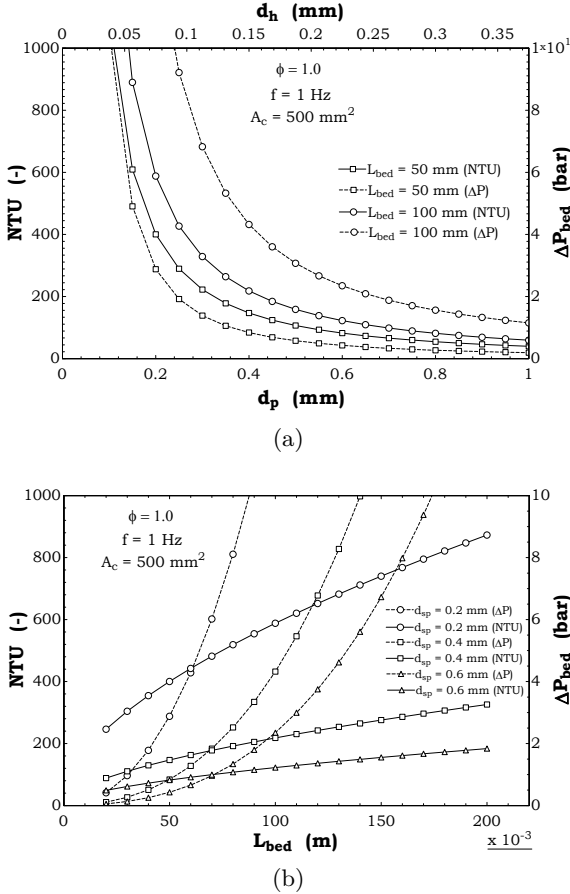


Figure 43 – Number of transfer units (NTU) and bed pressure drop dependence on (a) sphere diameters and (b) bed length of the regenerator.

on a working point that results in an energy product ( $BH$ ) closer to that of the maximum energy density of the magnet ( $BH$ )<sub>max</sub>. For a permanent magnet with remanence of 1.4 T, the maximum energy density is about  $371 \text{ kJ/m}^3$ . The optimization of the energy product of the permanent magnet within the circuit was one of the most important achievements of this thesis.

The rotor-stator configuration for the magnetic circuit was chosen for its ability to easily perform magnetic field changes over

porous magnetocaloric beds located within the magnetic gap. The magnetic circuit design aimed for a high average permanent magnet energy product,  $(\overline{BH})$ , which generates an homogeneous magnetic flux density,  $\mu_0 H$ , of nearly 1 T within a magnetic gap region larger than a regenerator bed ( $w_{\text{bed}}$ ). Another concern in the design of a new magnetic circuit is the reduction of the magnetic force required to generate a magnetic field change within the regenerator beds.

In the rotor-stator configuration, analogously to an electric generator, the stator conducts alternating magnetic fields due to the rotation of the rotor. Consequently, the stator demands a material with a low magnetic coercivity (small hysteresis area), such as an electrical steel (or silicon steel Fe-Si), to reduce hysteresis losses. Additionally, the stator should be built in laminated sheets to decrease eddy currents induced by the alternating magnetic fields.

As in most room-temperature magnetic refrigerator prototypes, Nd-Fe-B was selected as the permanent magnet material for the new magnetic circuit. Table 8 presents the properties of the Nd-Fe-B employed for simulations of the magnetic circuit (with a linear demagnetization curve) together with the properties of the permanent magnet used in the actual magnetic circuit. The latter is the neodymium sintered *Shinetsu* grade N52 material, which has a magnetic remanence higher than that used in the simulation. However, this material was selected only after confirming that, despite its low coercivity, it would not self-demagnetize within the magnetic circuit. Self-demagnetization occurs when  $\mathbf{H}$  in the direction of  $\mathbf{B}_{\text{rem}}$  exceeds  $H_c$ . The selected permanent magnet has the highest available magnetic remanence and was preferred for allowing higher magnetic flux densities in the magnetic gap. The complete material datasheet for the actual permanent magnet can be found in Annex A.

Table 8 – Typical properties of the Nd-Fe-B employed for simulation of the magnetic circuits and those of the permanent magnet used in the actual magnetic circuit.

Nd-Fe-B	$B_{\text{rem}}$ [T]	$\mu_r$ [-]	$H_c$ [kA/m]	$\rho$ [kg/m <sup>3</sup> ]	$(BH)_{\text{max}}$ [kJ/m <sup>3</sup> ]
Theoretical	1.40	1.05	1061	7500	371
<i>Shinetsu</i> N52	1.47	-	850	7500	414

The properties of the soft magnetic material needed in the magnetic circuit simulations were assumed equal to those of iron,

which were obtained from COMSOL Multiphysics<sup>®</sup> (2011). Fig. 44 shows the  $B$ - $H$  curve for iron. The rotor of the actual magnetic circuit was assembled with steel S235JR and the stator consists of 150 sheets of laminated steel M600-65A.

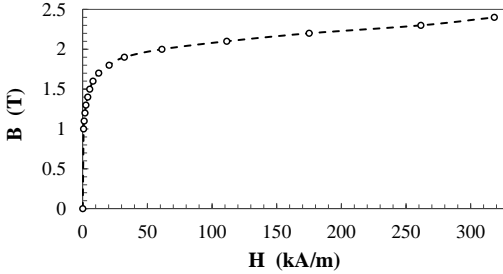


Figure 44 –  $B$ - $H$  curve of iron employed for simulations of the magnetic circuit (COMSOL Multiphysics<sup>®</sup>, 2011).

The magnetic circuit design starts by defining first the volume of magnetic gap,  $V_{\text{gap}}$ , for a regenerator ring. From the preliminary analysis and simulations of the magnetic circuit in COMSOL, a basic rotor-stator magnetic circuit was selected with the following characteristics: rotor radius  $R_{\text{rot}} = 90$  mm, rotor width  $w_{\text{rot}} = 90$  mm, stator internal radius  $R_{\text{stat},i} = 110$  mm, stator external radius  $R_{\text{stat},e} = 140$  mm, rotor and stator lengths  $L_{\text{rot}} = L_{\text{stat}} = 150$  mm (Fig. 45). The above dimensions result in  $V_{\text{gap}} = 1.89$  L, with a magnetic gap height  $h_{\text{gap}} = 20$  mm and a perimeter in the center of the magnetic gap  $Per_{\text{gap}} (R_{\text{gap},c} = 100 \text{ mm}) = 628.3$  mm. Although it has been previously defined that the regenerator volume should be about 0.4 L, an oversized magnetic gap would allow for future scaling of the magnetocaloric density as well as for more room for the regenerator casing and mechanical structure since some extra volume is required for the discretization of the beds and casing. With the selected  $h_{\text{gap}}$ , a regenerator bed with approximately 10 mm in height could be easily accommodated by leaving a tolerance for the regenerator casing and for the rotor to move.

The magnetic flux density and the energy product of the basic rotor-stator configuration are shown in Fig. 46. The  $V_{\text{magnet}}$  of this configuration is 2.32 L and the magnetized region volumes  $V_{\text{field}}$  for opening angles of  $45^\circ$  and  $90^\circ$  at the magnetic gap (schematized at Fig. 46-b) are 0.472 and 0.944 L, respectively. The average high magnetic flux densities  $\mu_0 \bar{H}_{\text{mag}}$  for those opening angles are

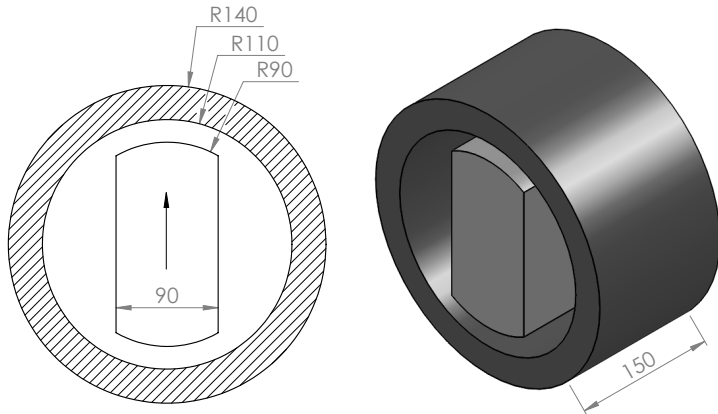


Figure 45 – Basic magnetic circuit dimensions (a) Cross section and (b) isometric views of the simple rotor-stator magnetic array. Light grey is permanent magnet and dark grey is soft magnetic material. The arrow indicates the direction of  $\mathbf{B}_{\text{rem}}$ .

0.866 and 0.645 T, respectively, and the low magnetic flux densities  $\mu_0 \overline{H}_{\text{demag}}$  are 0.256 and 0.062 T, respectively. The corresponding values of  $\Lambda_{\text{cool}}$  are 0.103 and 0.240 T<sup>2/3</sup>, respectively, considering the magnetic array used at all times ( $P_{\text{field}} = 1$ ). The results are summarized in Table 10 together with those of the final magnetic circuit. The average magnetic induction in the stator is 1.38 T, with a maximum of 1.74 T, which is adequate for electrical steel.

The average energy product of the permanent magnet within the magnetic circuit is calculated as the norm product of the components of  $\mathbf{B}$  and  $\mathbf{H}$  parallel to  $\mathbf{B}_{\text{rem}}$ ,  $\|\mathbf{B} \cdot \hat{\mathbf{B}}_{\text{rem}}\| \|\mathbf{H} \cdot \hat{\mathbf{B}}_{\text{rem}}\|$ , since the components perpendicular to  $\mathbf{B}_{\text{rem}}$  have no influence on the permanent magnet<sup>2</sup> and where  $\hat{\mathbf{B}}_{\text{rem}} = \frac{\mathbf{B}_{\text{rem}}}{\|\mathbf{B}_{\text{rem}}\|}$  corresponds to the unit vector in the direction of  $\mathbf{B}_{\text{rem}}$  (Bjørk, 2010). The 2D simulated average energy product of the permanent magnet in the basic magnetic circuit is 192.8 kJ/m<sup>3</sup> (Fig. 46-b).

Similarly, the demagnetization field can be assumed to act only in the direction of the remanence,  $\|\mathbf{H} \cdot \hat{\mathbf{B}}_{\text{rem}}\|$ , and if that component of the magnetic field is higher than the coercivity of the

<sup>2</sup> For a permanent magnet with linear demagnetization curve, it is reasonable to assume that its performance is dominated by magnetocrystalline anisotropy (Campbell, 1999).

permanent magnet, it will demagnetize it. In the basic magnetic circuit, the average magnetic field in the direction of the remanence is  $-167.2 \text{ kA/m}$ , and no risk of demagnetization at any point of the rotor was found.

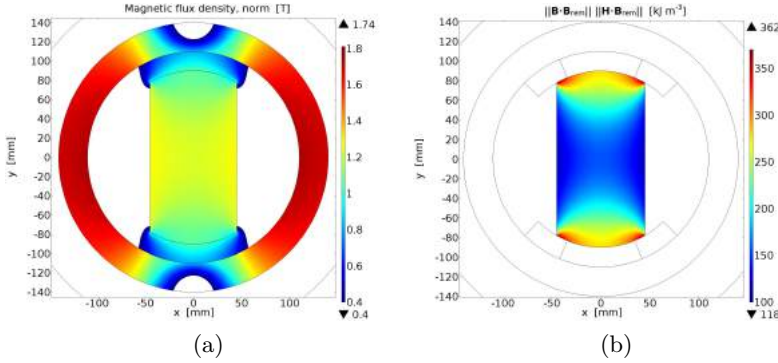


Figure 46 – (a) Magnetic flux density and (b) energy product  $|BH|$  of the basic rotor-stator magnetic circuit.

Although this basic configuration of the rotor-stator magnetic circuit results in an acceptable performance in magnetic refrigeration applications, there is still considerable room for improvement due to a somewhat inefficient use of the permanent magnets. Therefore, a geometrical optimization to improve both  $\Lambda_{\text{cool}}$  (function of  $\Delta\mu_0 H$  and  $V_{\text{magnet}}$ ) and the energy product of the permanent magnets was carried out.

### 4.3.1 Optimization of the rotor-stator magnetic circuit configuration

A novel method is proposed to optimize the rotor-stator configuration for a magnetic refrigerator. In the rotor, the *magnet wedges* concept of Abele *et al.* (1997) (Fig. 47) is applied to replace part of the permanent magnet by soft magnetic material, thus making a more efficient use of the former in the magnetic circuit.

Assuming a non-magnetic medium outside the wedges, the magnetized wedges generate highly uniform magnetic fields  $\mathbf{H}_i$  and  $\mathbf{H}_e$  parallel to  $\mathbf{y}$  axis when  $\mathbf{B}_{\text{rem}}$  is oriented at an angle  $\theta$  relative to  $\mathbf{y}$  axis:

$$\theta = \pm \left( \alpha_1 + \alpha_2 - \frac{\pi}{2} \right) \quad (4.8)$$

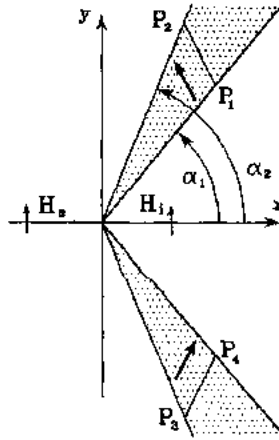


Figure 47 – A single pair of uniformly magnetized wedges (Abele *et al.*, 1997). Magnetized regions are dot hatched.

where  $\alpha_1$  and  $\alpha_2$  define the orientation of the surfaces of the wedges (Abele *et al.*, 1997). Segments  $\overline{P_1P_2}$  and  $\overline{P_3P_4}$  represent truncations parallel to the direction of  $\mathbf{B}_{\text{rem}}$  and symmetric to  $\mathbf{x}$  axis. The original purpose of these magnetized wedges was to generate high magnetic flux densities at levels of the order or even exceeding the permanent magnet remanence along the magnetic gap created between the magnetized wedges. Particularly, this wedge configuration has been employed in medical imaging applications.

In this work, it has been proven that when soft magnetic material, such as iron, is placed between the magnetized wedges, the highly uniform magnetic field within the wedges is conserved. This behavior favors the performance of the magnetic circuit since it: (i) reduces the permanent magnet density, (ii) confines the magnetic flux lines inside the rotor to ensure a very low magnetic field region in the magnetic gap and (iii) enables an efficient use of the permanent magnets by maintaining their operation with an energy product close to the maximum energy density. These improvements result in more compact and cheaper magnetic circuits for magnetic refrigeration.

By symmetrically arranging the magnetized wedges into the rotor, the magnetic flux density generated by the permanent magnets is confined into certain regions of the magnetic gap delimited by two iron segments placed at the ends of the rotor with an open-

ing angle,  $\varphi$ , which define the two regions of high magnetic field (Fig. 48). The length of the magnetic circuit was set at 150 mm to maintain a high magnetic flux density along the entire regenerator.

The number of permanent magnet segments determines the cost of the magnetic circuit (Bjørk, 2010). Therefore, only 4 symmetrical magnet segments have been employed in the present system to reduce material and manufacturing costs. The optimization methodology consisted in maximizing the permanent magnet density in the rotor considering the desired properties and conditions of the magnetic circuit. A schematic representation of one of the four magnetized wedges of the new rotor configuration is shown in Fig. 48. Here,  $C$  is the center of the rotor with radius  $R_{rot} = \overline{CA}$ . The segment  $\overline{CE}$  corresponds to the half width of the rotor. The magnetized wedge represented by the dot hatched region  $\overline{OP_2P_1}$  is analogous to that in Fig. 47.

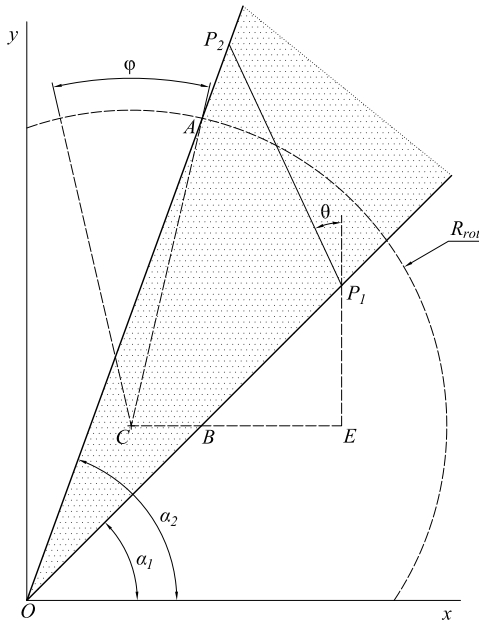


Figure 48 – Schematic representation of one of the four magnetized wedges that compose the new rotor configuration with radius  $R_{rot}$ . The magnetized regions are dot hatched.

The geometrical constraints of the design of the magnetized

wedge are shown in Fig. 49. From the initial numerical simulations of the magnetic circuits performed with COMSOL Multiphysics® (2011), it was found out that an iron opening angle  $\varphi = 26^\circ$  would result in regions of  $\mu_0 H_{\text{high}}$  covering about one quarter of the magnetic gap. This corresponds to one quarter of the AMR regeneration cycle, for which a plateau with a high magnetic flux density covers about 10% of the magnetic cycle. According to Bjørk (2010), a non-magnetic volume should be left in the center of the rotor to place a shaft, which was built in SAE 304 stainless steel in the final magnetic circuit. A square region was left for the shaft, whose diagonals are defined as  $\overline{CS_1} = \overline{CS_2} = 15$  mm. Segmentation of the permanent magnets should be linear instead of circular to facilitate manufacture.

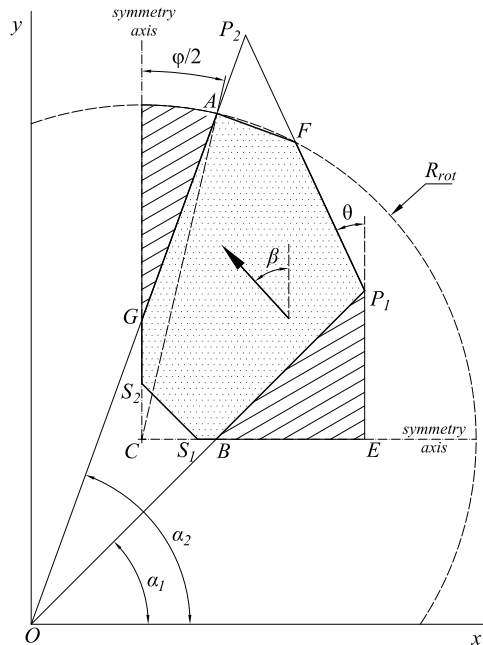


Figure 49 – Geometrical constraints of the design of the magnetized wedges for the new rotor-stator configuration. Magnetized and iron regions are dot and line hatched, respectively.

Due to the large number of variables in the optimization of the wedges, some assumptions were made based on the knowledge gained during the initial simulations of the magnetic circuit. Firstly,

to avoid magnetic flux leaks from the lateral iron segments into the region of  $\mu_0 H_{low}$ , the rotor width was defined as  $\overline{CE} = \frac{2}{3}R_{rot}$  and  $\overline{CB} = \frac{1}{3}\overline{CE}$ . Secondly, to better confine the high magnetic flux density into the magnetic gap and to improve the energy product of the permanent magnet, it was found that segment  $\overline{CG} \simeq \frac{1}{3}R_{rot}$ . Similarly, to avoid magnetic flux leaks by the permanent magnet region, the truncation angle was defined as  $\theta \geq 25^\circ$ . With these assumptions, the dimensions of the dot hatched region  $\overline{S_1S_2GAFP_1B}$  in Fig. 49 are determined.

An analytical study of the different wedge regions that satisfy the above conditions was carried out by varying the surface orientation angles  $\alpha_1$  and  $\alpha_2$ , which affect the wedge volume. A large wedge volume results in a larger magnetic flux density in the high field region, but is constrained by the desired distribution of the high field in the magnetic gap. Fig. 50-a shows the wedge volume dependence on  $\alpha_1$  for different values of  $\alpha_2$  when  $\theta \geq 25^\circ$  and  $\varphi = 26^\circ$ . Fig. 50-b presents the  $\alpha_2$  and segment ( $\overline{CG}$ ) dependence on  $\alpha_1$  for  $\theta = 25^\circ$ . Since  $\overline{CG} > 15$  mm,  $\alpha_1$  should be higher than  $41^\circ$  (that is  $\alpha_2 < 74^\circ$  for  $\theta = 25^\circ$ ). Fig. 50-c shows the wedge volume dependence on  $\alpha_1$  in the limiting case  $15 \text{ mm} < \overline{CG} < 45$  mm, considering the length of the rotor to be 150 mm.

Different geometries of magnetic circuits as a function  $\alpha_1$ ,  $\alpha_2$  and  $\theta$  were simulated in COMSOL Multiphysics<sup>®</sup> (2011), producing results similar to those in Figs. 50a-c. However, due to space limitations, these will not be presented here. The magnetic circuits were characterized by  $\Lambda_{cool}$  (Eq. (2.26)) and the energy product of the permanent magnets in the configuration. Due to the truncation of the wedges and the presence of iron segments, a better performance was found when  $\mathbf{B}_{rem}$  and  $\theta$  have different orientations, so the direction of  $\mathbf{B}_{rem}$  has been found by the parametrization of  $\beta$ . Also, the energy product of the magnets was found to improve when segment  $\overline{CG} \simeq \frac{1}{3}R_{rot}$ . The best performance was found for wedge segments with  $\alpha_1 = 45^\circ$ ,  $\alpha_2 = 70^\circ$ ,  $\theta = 25^\circ$  and  $\beta = 57^\circ$ . Table 9 summarizes the dimensions of the chosen magnetic circuit and magnetized wedges. Fig. 51 presents a cross-section view of the rotary system with the final dimensions and the construction materials.

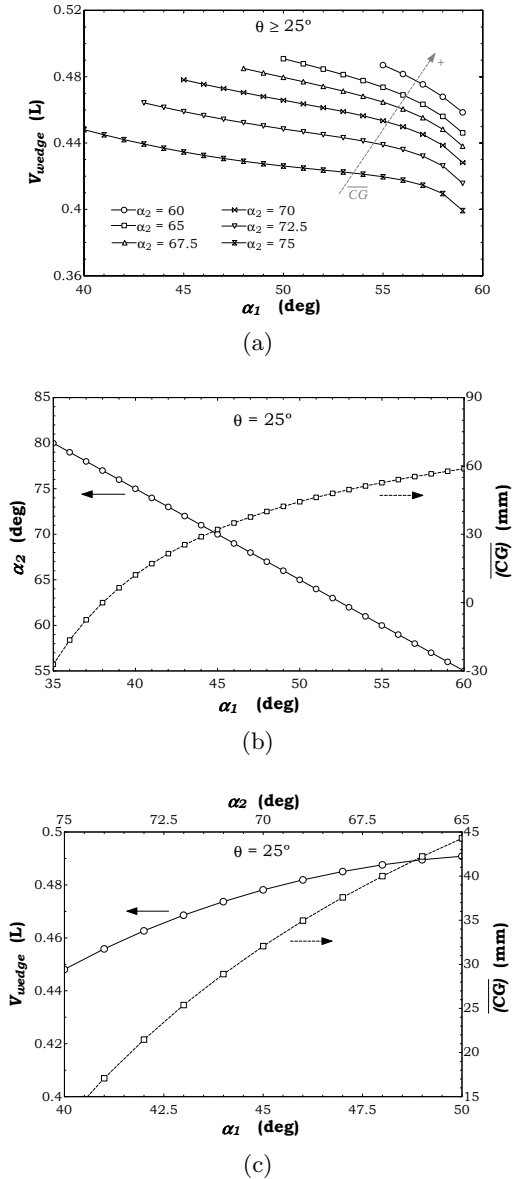


Figure 50 – Results for  $R_{rot} = 90$  mm,  $L_{rot} = 150$  mm and  $\varphi = 26^\circ$ : (a) Wedge volume,  $V_{wedge}$ , dependence on  $\alpha_1$  for different  $\alpha_2$  and  $\theta \geq 25^\circ$ , (b) Angle  $\alpha_2$  and segment length  $\overline{CG}$  and (c)  $V_{wedge}$  dependence on angle  $\alpha_1$  for  $\theta = 25^\circ$ .

Table 9 – Dimensions of magnetized wedges and rotor in the final magnetic circuit.

Variable	Value	Unit
$R_{rot}$	90	mm
$L_{rot}$	150	mm
$\varphi$	26	°
$\alpha_1$	45	°
$\alpha_2$	70	°
$\theta$	25	°
$\beta$	57	°
$A_{wedge}$	3188	mm <sup>2</sup>
$V_{wedge}$	0.478	L
$V_{magnet,rot}$	1.91	L
$V_{iron,rot}$	0.837	L

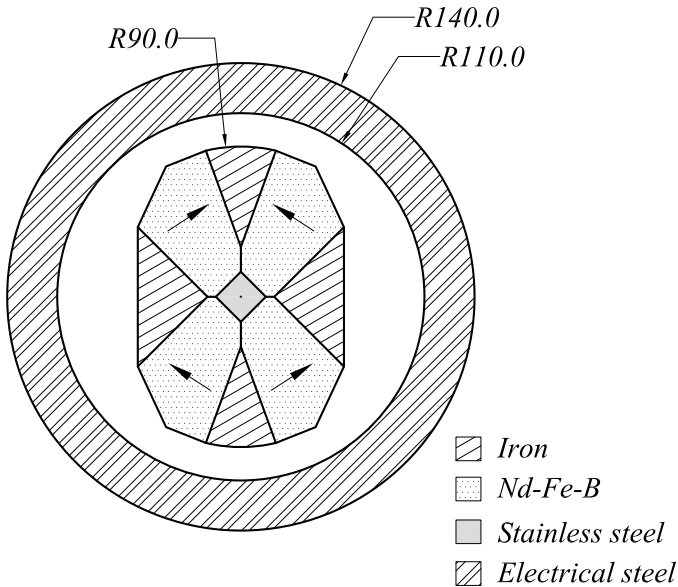


Figure 51 – Cross section view of the magnet array.

The magnetic flux density norm of the final magnetic circuit from 2D simulations is presented in Fig. 52. The resulting magnetic circuit with a 20-mm magnetic gap generates two regions of high and low average magnetic flux density that, for an opening angle of  $45^\circ$  in the magnetic gap (approximately an arc length of 78.5

mm), yielded averages  $\mu_0 H_{\text{high}}$  and (adjacent)  $\mu_0 H_{\text{low}}$  of 1.053 and 0.145 T, respectively. On the other hand, from 3D simulations the averages  $\mu_0 H_{\text{high}}$  and (adjacent)  $\mu_0 H_{\text{low}}$  were 0.856 and 0.122 T, respectively. For the 20-mm magnetic gap opening the values of  $\Lambda_{\text{cool}}$  obtained from the 2D and 3D simulations were 0.188 and 0.162  $\text{T}^{2/3}$ , respectively. These and other simulation results for the final magnetic circuit are summarized in Table 10.

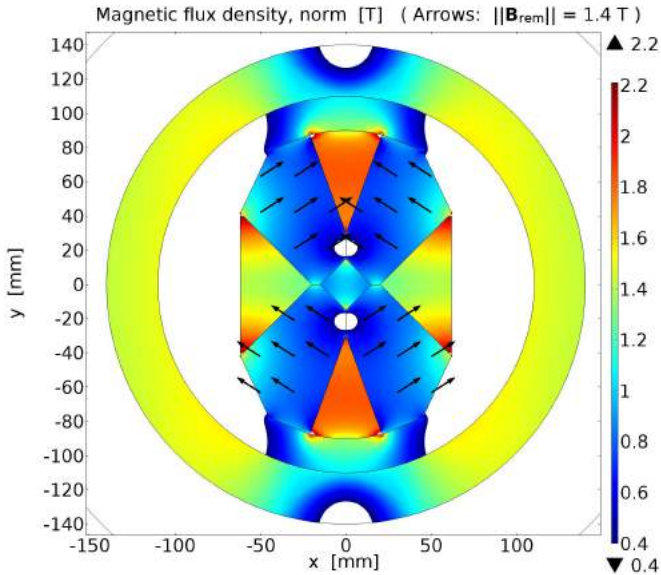


Figure 52 – Stationary 2D simulation of the magnetic flux density norm of the magnetic circuit with permanent magnets with  $\|\mathbf{B}_{\text{rem}}\| = 1.4 \text{ T}$ . The arrows indicate the direction of the remanence of the permanent magnet segments.

The average magnetic flux density in the stator is 1.32 T, which is considered low for electrical steel and satisfactory to reduce the eddy currents. The average magnetic flux densities in the lateral and vertical iron segments of the rotor are 1.51 T and 1.79 T, respectively.

A 2D quasi-static electromagnetic simulation of the magnetic circuit when the rotor is rotating at 1 Hz is presented in Fig. 53. The resulted average magnetic flux densities at this frequency in the stator and in the lateral and vertical iron segments were of about 1.54 T, 1.53 T and 1.80 T, respectively. The electrical conductivity

of the stator for this simulation was assumed to be equal to that of soft iron ( $5 \times 10^6 \text{ S/m}$ ). However, due to the lamination of the stator, the actual electrical conductivity may be much lower, so the eddy currents in the stator can be reduced. Thus, the magnetic flux density at the stator actually behaves slightly different to what is shown in Fig. 53, and the actual average magnetic flux density in the stator should be similar to that calculated from static simulations (Bastos, 2004).

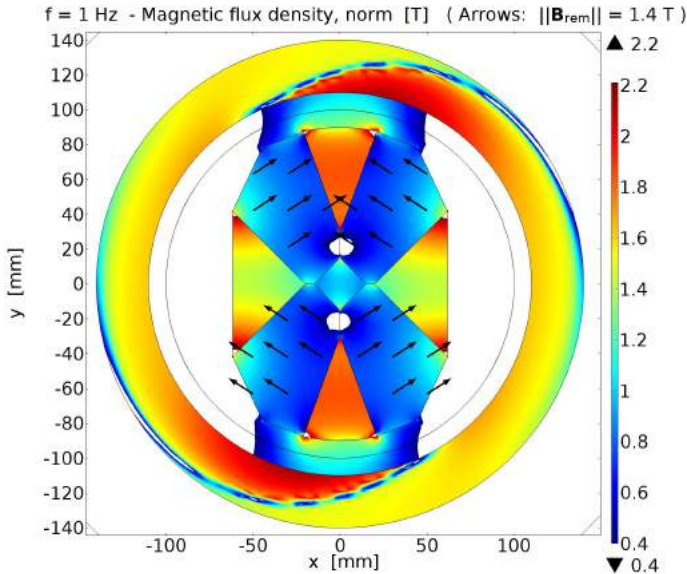


Figure 53 – Quasi-static ( $f = 1 \text{ Hz}$ ) 2D simulation results of the magnetic flux density norm of the magnetic circuit with permanent magnets with  $\|\mathbf{B}_{\text{rem}}\| = 1.4 \text{ T}$ . The arrows indicate the direction of the remanence of the permanent magnet segments.

The energy product calculated as  $\|\mathbf{B} \cdot \hat{\mathbf{B}}_{\text{rem}}\| \|\mathbf{H} \cdot \hat{\mathbf{B}}_{\text{rem}}\|$  for the permanent magnets with  $\|\mathbf{B}_{\text{rem}}\| = 1.4 \text{ T}$  in the final magnetic circuit from a 2D simulation is shown in Fig. 54. The maximum energy density for the simulated permanent magnet is about  $371 \text{ kJ/m}^3$ . The average energy product for the four segments of permanent magnet in the stationary magnetic circuit is  $346 \text{ kJ/m}^3$ . When operating at  $1 \text{ Hz}$ , it is  $345 \text{ kJ/m}^3$ . The average of the energy product from 3D simulations is  $335 \text{ kJ/m}^3$ . It can be concluded, therefore, that the permanent magnet in the magnetic circuit works

very close to the maximum in the greatest part of its volume. It is worth mentioning that the magnetic field and the energy product for the permanent magnets with the presence of the magnetocaloric regenerator within the magnetic gap will be different. They will be a function of the magnetocaloric material temperature and magnetization, and the operating frequency of the rotor.

For a permanent magnet with a remanence of 1.47 T, i.e. *Shinetsu* N52, the average energy product in the magnetic circuit is  $382.1 \text{ kJ/m}^3$ . If a linear demagnetization (with  $\mu_r = 1.05$ ) is considered, the maximum energy density is  $409.3 \text{ kJ/m}^3$  (from the manufacturer data-sheet it is  $414 \text{ kJ/m}^3$ ). The averages  $\mu_0 H_{\text{high}}$  and (adjacent)  $\mu_0 H_{\text{low}}$  for a magnetic gap opening of  $45^\circ$  are 1.096 and 0.153 T, respectively, which result in a  $\Lambda_{\text{cool}}$  of  $0.192 \text{ T}^{2/3}$ .

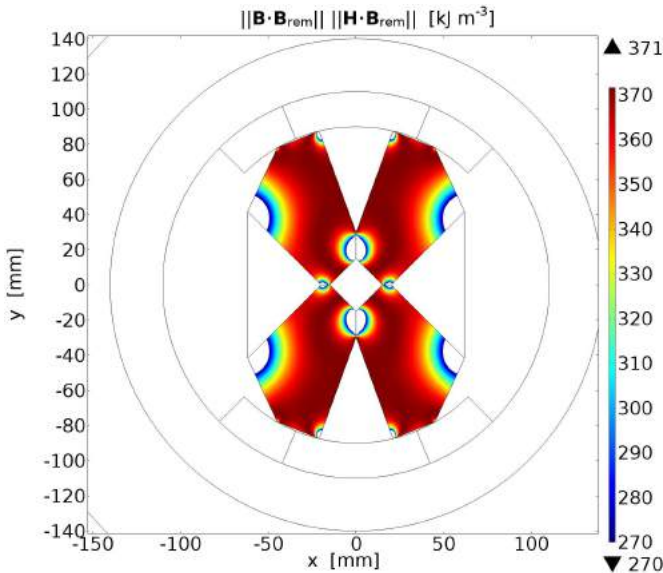


Figure 54 – Energy product calculated as  $\|\mathbf{B} \cdot \hat{\mathbf{B}}_{\text{rem}}\| \|\mathbf{H} \cdot \hat{\mathbf{B}}_{\text{rem}}\|$  for permanent magnets with  $\|\mathbf{B}_{\text{rem}}\| = 1.4 \text{ T}$  in the final magnetic circuit (from a 2D simulation).

A demagnetization analysis to investigate the use of the highest performance Nd-Fe-B *Shinetsu* N52 with  $\|\mathbf{B}_{\text{rem}}\| = 1.47 \text{ T}$  in the final magnetic circuit was performed by calculating  $\mathbf{H}$  in the direction of  $\mathbf{B}_{\text{rem}}$ , as shown in Fig. 55 for  $\|\mathbf{H} \cdot \hat{\mathbf{B}}_{\text{rem}}\| < -700 \text{ kA/m}$ . The regions with more chance to suffer demagnetization are those

where both magnetized wedges are confronted with almost opposite direction of  $\mathbf{B}_{\text{rem}}$ . In these regions, the magnetic field (red arrows) within the permanent magnet reaches magnitudes close to this limit in the opposite direction of the remanence (black arrows). However, it is considered that the N52 permanent magnets will not suffer a *considerable* demagnetization in this region since its coercivity is 850 kA/m at 20°C. Moreover, simulation results are usually over-estimated near the geometry boundaries due to abrupt changes of material properties and mesh. It is clear that the use of permanent magnets with a higher remanence results in an improved performance of the magnetic circuit.

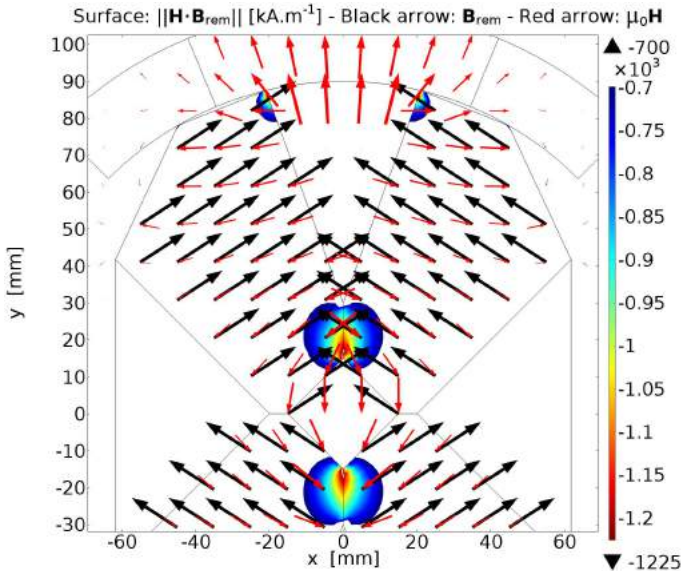


Figure 55 – Demagnetization field calculated as  $\|\mathbf{H} \cdot \hat{\mathbf{B}}_{\text{rem}}\|$  for high remanence permanent magnet *Shinetsu* N52 with  $\|\mathbf{B}_{\text{rem}}\| = 1.47$  T in the final magnetic circuit (2D simulation). The surface shown is the one where  $\|\mathbf{H} \cdot \hat{\mathbf{B}}_{\text{rem}}\| < -700$  kA/m. The black arrows indicate  $\mathbf{B}_{\text{rem}}$  and the red arrows indicate  $\mathbf{H}$ .

### 4.3.2 Characterization of the magnetic circuit

The magnetic circuit was manufactured at Bakker Magnetics in The Netherlands. Each magnetized wedge was assembled from three pieces of permanent magnet *Shinetsu* N52 with 50 mm in

length. Fig. 56 shows a photograph of the magnetic circuit mounted on two bearings. The rotor was covered by a 1-mm thick stainless steel plate to protect the permanent magnets and the cylinder was filled with resin Neomould 1982-W-1.

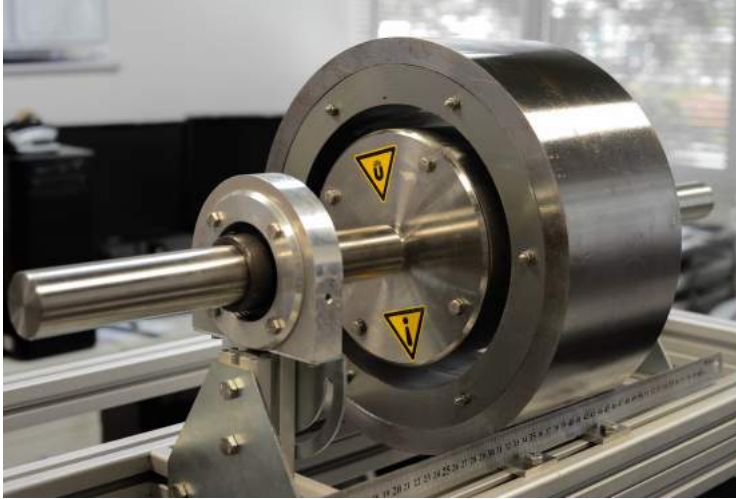


Figure 56 – Photograph of the built magnetic circuit mounted over two bearings and pillars.

The magnetic circuit was characterized and validated experimentally by measuring the magnetic flux density profile in the air gap as a function of angle, length and radial position. The measurements were performed with a LakeShore® 425 model gaussmeter and a transversal gaussmeter probe model HMMT-6J04-VF, with an uncertainty of  $\pm 1\%$  of the measured value. The gaussmeter probe was positioned in a purpose-built 3D traversing system.

Fig. 57 shows the magnetic flux density norm profile as a function of the angle measured at the center of the magnetic gap ( $R = 100$  mm). The experimental results are compared with the 3D simulation using a permanent magnet with a remanence of 1.4 T. A plateau spanning over  $20^\circ$  (longer than an arc length of 35 mm) with  $\mu_0 H \gtrsim 1$  T was obtained. The experimental flux densities at angles  $0^\circ$ ,  $22.5^\circ$ ,  $45^\circ$  and  $90^\circ$  were approximately 1.02, 0.52, 0.06 and 0.001 T, respectively. Thus, the region of high magnetic field in the magnetic gap can be considered to lie between  $-22.5^\circ$  and  $22.5^\circ$  with an average  $\mu_0 \bar{H}_{\text{high}} \sim 0.86$  T. The average flux density

in the adjacent region ( $22.5^\circ$  to  $67.5^\circ$ ) has an average  $\mu_0 \overline{H}_{\text{low}} \sim 0.16$  T. This magnetic system has the advantage to have a very low magnetic field region between  $67.5^\circ$  to  $112.5^\circ$ , with an average  $\mu_0 \overline{H}_{\text{low}} \sim 0.01$  T.

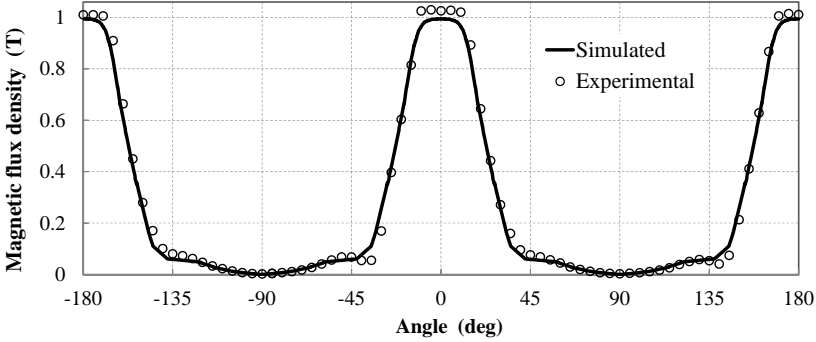


Figure 57 – Simulated (3D) and experimental magnetic flux density norm behavior as a function of the angle at the center of the magnetic gap height ( $R = 100$  mm). The simulation is for permanent magnets with  $\|\mathbf{B}_{\text{rem}}\| = 1.4$  T.

Fig. 58 shows the experimental and simulated magnetic flux density norm in the air gap as a function of the length,  $z$ , at different angles. Lengthwise, the magnetic field is very constant, with an average at  $0^\circ$  of  $\mu_0 \overline{H} \sim 0.96$  T, and, as expected, somewhat significant reductions in field intensity near the edges, i.e.  $\mu_0 H(0^\circ, z = 75$  mm,  $R = 100$  mm)  $\sim 0.75$  T. As can be seen, there is good agreement between the experimental data and the numerical model. Fig. 59 shows the three-dimensional distribution of the experimental data for the magnetic flux density norm in the air gap as a function of angle and length.

The  $\Lambda_{\text{cool}}$  parameter, Eq. (2.26), was employed to evaluate the performance of the magnetic circuit. Fig. 60 shows the calculated  $\Lambda_{\text{cool}}$  of the final magnetic circuit with  $\|\mathbf{B}_{\text{rem}}\| = 1.4$  T from the 3D simulation results as a function of the opening angle for hypothetical high field regions,  $V_{\text{field}}$ , in the magnetic gap. In this case,  $V_{\text{field}}$  is only function of the angle, as both the length and height of the magnetic gap are constant. A high performance has been reached due to an effective use of the permanent magnets. The total volume of permanent magnet in the rotor is approximately  $V_{\text{magnet}} \sim 1.91$  L. Considering the regions of high field and low field with opening

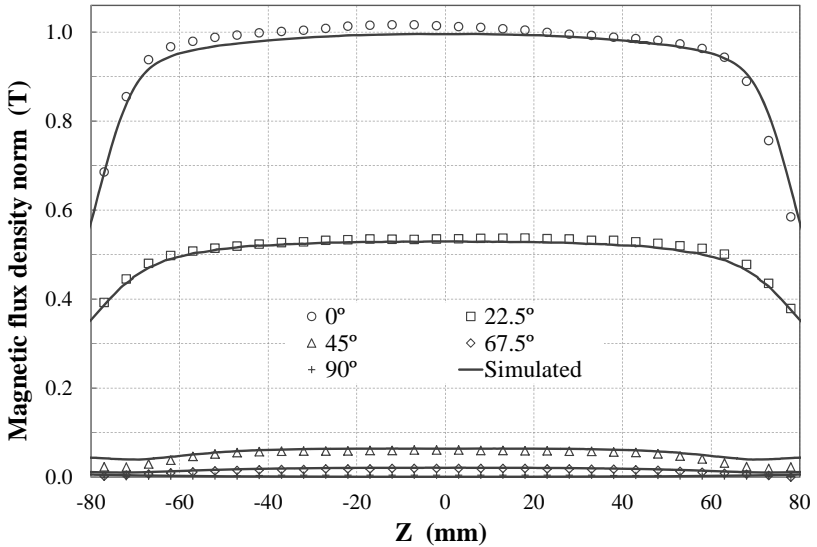


Figure 58 – Experimental and numerical data of the magnetic flux density norm dependence on the length ( $z$ ) at different angles at the center of the air gap ( $R = 100$  mm).

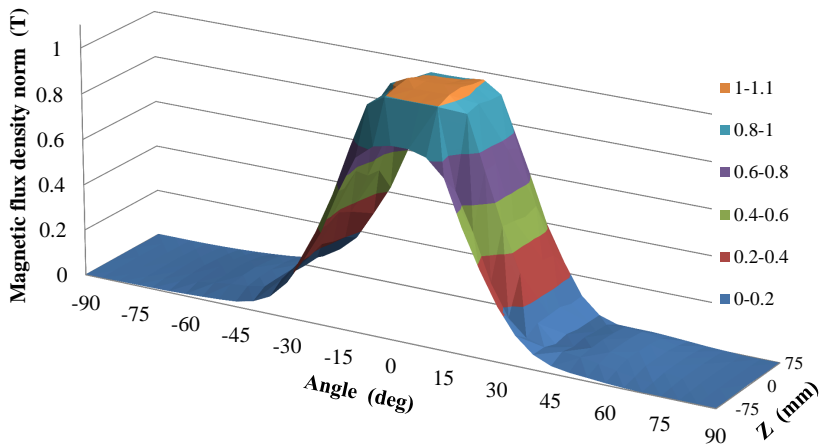


Figure 59 – Three dimensional plot of the experimental magnetic flux density norm data in the air gap as a function of angle and length at the center of the magnetic gap ( $R = 100$  mm).

angles of  $45^\circ$  and  $90^\circ$ , their volumes would be 0.472 and 0.943 L, respectively. For these regions the average high magnetic flux densities are 0.864 and 0.531 T, while the adjacent low average flux densities are 0.197 and 0.030 T, respectively. Assuming  $P_{\text{field}} = 1$ , i.e., that the magnet is being used all the time,  $\Lambda_{\text{cool,max}} \sim 0.141$  and  $0.276 \text{ T}^{2/3}$ , respectively. Despite  $\Lambda_{\text{cool}}$  was calculated using a remanence lower than that of the permanent magnet used in the actual system, this is, to the author's knowledge, still the highest  $\Lambda_{\text{cool}}$  achieved to this day in a magnetic circuit for magnetic refrigeration. Probably,  $\Lambda_{\text{cool}}$  also favors magnetic circuits with large regions of very low magnetic flux densities, as it is the case for the actual magnetic circuit.

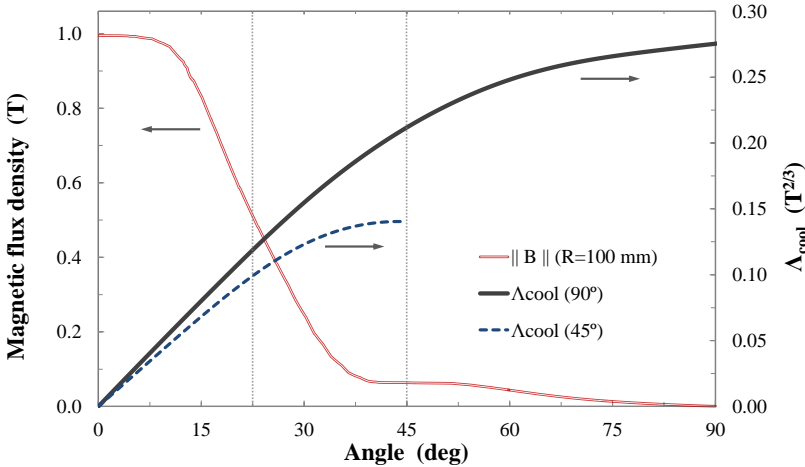


Figure 60 – Calculated  $\Lambda_{\text{cool}}$  parameter from the 3D simulations of the magnetic flux density norm at the center of the magnetic gap (red line) as a function of the opening angle ( $\|\mathbf{B}_{\text{rem}}\| = 1.4 \text{ T}$ ). The vertical dotted lines correspond to the boundaries between the high and low magnetic field regions for opening angles of  $45^\circ$  and  $90^\circ$ , respectively.

Table 10 summarizes the performance of the basic and final (optimized) magnetic circuits according to the 2D and 3D simulations using COMSOL Multiphysics<sup>®</sup> (2011) for  $\|\mathbf{B}_{\text{rem}}\| = 1.4 \text{ T}$ . The magnetic flux densities were calculated in three different ways: (i) average in the 2D area, (ii) average in the 3D volume and (iii) average in the center line of the 3D magnetic gap. The latter corre-

sponds to the results plotted in Figs. 57 and 60. It is important to point out that the actual performance is expected to be higher than presented in Table 10 since the remanence of the actual permanent magnet is higher, as seen in Fig. 57.

Table 10 – Performance of the basic and final magnetic circuits from the 2D and 3D simulations in COMSOL Multiphysics® (2011) for  $\|\mathbf{B}_{\text{rem}}\| = 1.4$  T. The magnetic flux densities were calculated as: (i) the average in the 2D area, (ii) the average in the 3D volume and (iii) the average in the center line of the 3D magnetic gap.

Variable	Angle	2D basic	2D final	3D final	Line (3D)	Unit
$ \overline{\mathbf{B}} _{\text{high}}$	45°	0.866	1.053	0.856	0.864	T
$ \overline{\mathbf{B}} _{\text{high}}$	90°	0.645	0.650	0.527	0.531	T
$ \overline{\mathbf{B}} _{\text{low}}$	45°	0.256	0.145	0.122	0.197	T
$ \overline{\mathbf{B}} _{\text{low}}$	90°	0.062	0.026	0.027	0.030	T
$\Lambda_{\text{cool}}$	45°	0.103	0.188	0.162	0.141	T <sup>2/3</sup>
$\Lambda_{\text{cool}}$	90°	0.240	0.328	0.278	0.276	T <sup>2/3</sup>
$ BH $	-	193	346	335	-	kJ m <sup>-3</sup>

#### 4.4 DESIGNING THE FLOW DISTRIBUTION SYSTEM

The flow distribution system is responsible for the alternating fluid flow in the regenerator beds synchronized with the magnetic circuit rotation. The regenerator consists of polyoxymethylene (POM) ring that is embedded into the magnetic gap and connected on each side to flow distributors, as shown in Fig. 61. Two rotary valves designed and built in the course of this thesis were placed at the hot end of the system. The valves are mechanically actuated by the same shaft of the magnetic circuit. Each valve was designed having eight ports to facilitate the flow distribution, while maintaining the symmetry with the two-pole magnetic circuit. The outer (static) part of the rotary valves is connected to the hot end flow distributor by PFA hoses. In the hot flow distributor, each channel is bifurcated to service the regenerator pairs. Therefore, at any instant in time the two magnetized bed pairs experience a cold blow, the two demagnetized bed pairs are opened for a hot blow and the four remaining bed pairs are closed for flow. Certainly, a higher and odd number of beds would be preferred to reduce the demagnetization factor and the forces needed to rotate the magnet, but this requires a larger number of magnetic poles and/or a more complex flow dis-

tribution system. A stationary flow system is preferred to control fluid leakages in the device.

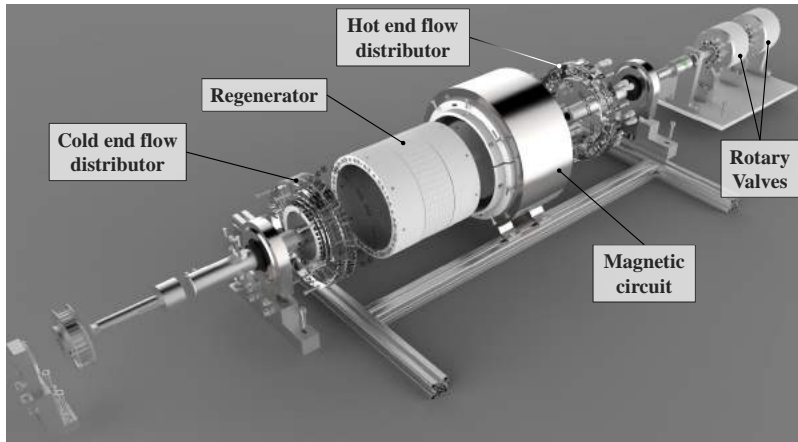


Figure 61 – Explosion view of the main components of the rotary device.

An schematic diagram of the hydraulic system is shown in Fig. 62. The central part of the diagram shows four beds; each of them representing the two bed pairs with the same flow profile. The regenerative cycle gives rise a temperature profile so that the left-hand side of the diagram is the hot end while the right-hand side is the cold end. To reduce parasitic losses at the cold end, most of the components in the device, including the rotary valves, are placed at the hot end.

The working principle of the flow distribution system consists of continuously pumping the heat transfer fluid, as indicated by the arrows in Fig. 62. At the particular instant in time depicted in the diagram, the first regenerator bed (13) is considered magnetized and the third regenerator bed (15) is considered as demagnetized. A fluid particle leaving the reservoir (1), is then suctioned by the gear pump (2) that increases the pressure and the velocity of the fluid stream. A needle valve (4) mounted in a flow bypass sets the flow rate, which is measured by an electromagnetic flow meter (5).

The temperature of the fluid entering the regenerator from the hot side, i.e., the so-called hot reservoir temperature ( $T_1$ ), is set by a parallel-plate heat exchanger (6) connected to a temperature-controlled bath (7). The flow passes through a 0.14-mm filter (8) and a purge valve (9) before entering the high pressure rotary valve (10)

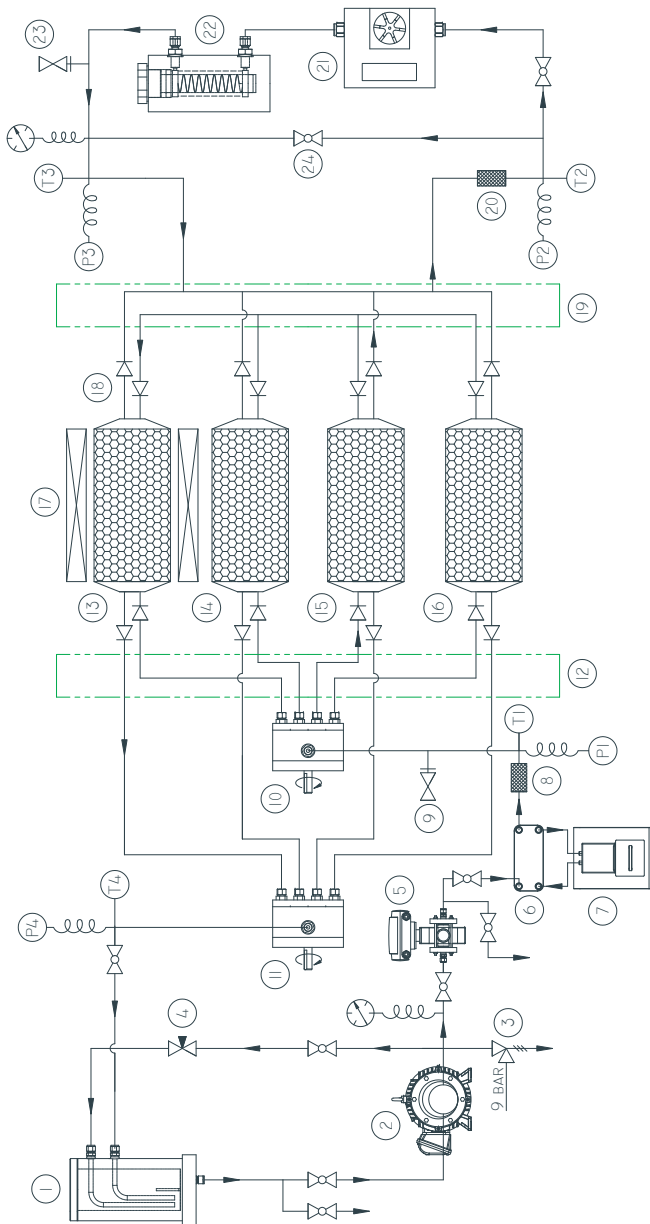


Figure 62 – Schematic diagram of the hydraulic system: (1) reservoir, (2) pump, (3) relief valve, (4) needle valve (flow bypass), (5) electromagnetic flow meter, (6) hot heat exchanger, (7) temperature controlled bath, (8) filter, (9) purge valve, (10) high pressure rotary valve, (11) high pressure rotary valve, (12) hot end flow distributor (13-16) regenerator beds, (17) magnet, (18) check valves, (19) cold end flow distributor, (20) filter, (21) paddle wheel flow meter, (22) cold heat exchanger, (23) purge valve, and (24) flow bypass.

at a pressure  $P_1$ . The valve allows fluid flow to the demagnetized beds (15) via the hot end flow distributor (12). The inlet and outlet ports of the regenerator are equipped with check valves (18) to direct the flow coming from the rotary valves. The cold end flow distributor (19) receives the cold fluid coming from the regenerator at a temperature  $T_2$  and pressure  $P_2$ . The fluid flow rate at the cold end is measured by a paddle wheel flow meter (21) before entering the screw-type heat exchanger (22) in which an immersion heat resistance is used to simulate a thermal load. A flow bypass at the cold end (24) controls the flow rate through the heat exchanger (22). After the thermal load is applied, the flow at a temperature  $T_3$  and pressure  $P_3$  returns to the magnetized beds (13) which are opened to flow by the low pressure rotary valve (11). Finally, the fluid flow returns to the reservoir (1) at a temperature  $T_4$  and pressure  $P_4$ .

The gear pump (Micropump model GL-H25), driven by a 1.1 kW electrical motor, is capable of giving a maximum differential pressure of 8.7 bar and a maximum flow rate of 1200 kg/h (for an ethylene-glycol mixture). The system has been designed so that the flow is always unidirectional in the hot and cold heat exchangers. Most of the tubing, connections and fittings were made from stainless steel for its reliability and resistance to corrosion and leakage. Flexible nylon tubing was used in parts of the system to facilitate connections and detect undesired air bubbles.

#### 4.4.1 Designing the rotary valve system

The valve system shown in Fig. 63 is responsible for the synchronization between the magnet and the flow through the regenerator beds. It consists of two identical rotary valves that are coupled through the main shaft. The valve system is placed at the hot end between the hot heat exchanger and the hot flow distributor and the reservoir. The valves operates mechanically at the same frequency of the magnetic circuit. Each valve is composed of a stationary stainless steel face with 8 openings and a rotating seal with 2 openings of  $45^\circ$  degrees for a symmetric fluid flow through the regenerator beds and continuous fluid flow at all times, avoiding any pressure peaks in the hydraulic system.

The rotary valve system generates a fluid flow profile as a function of the angle of rotation of the magnetic circuit as that shown in Fig. 64-a. However, since the flow is bifurcated at the hot end distributor before entering the regenerator, the bed pairs that are separated by an angle of  $19.2^\circ$  at the magnetic gap would have

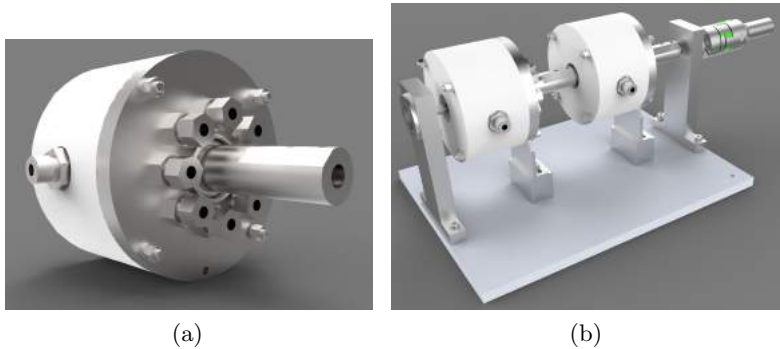


Figure 63 – (a) 8-port rotary valve and (b) rotary valve system composed of two identical rotary valves.

the same fluid flow profile but with different magnetic field profile. In other words, the fluid flow profile is dephased by  $\pm 9.6^\circ$  with respect to that of the rotary valve system, so the bed pairs can be classified either as *bedtype 1* and *bedtype 2*, respectively, as shown in Fig. 64-b. The rotary valve system fluid flow profile is denoted as *bedtype 0*.

The rotary valves were designed so as to have the versatility to change the angles (i) between the cold and hot blows, (ii) between the magnetic and flow profiles and (iii) the opening angle by substituting the sealing face. However, the influence of these angles in the system performance was not evaluated in this thesis due to time restrictions. The phase angle between the valves was fixed at  $90^\circ$  according to the best  $\Lambda_{cool}$  for the magnetic circuit. The maximum magnetic field ( $0^\circ$ ) was aligned with the center of the low pressure rotary valve flow opening.

The valve design aimed at minimizing the dimensions of the sealing face, which resulted in a contact area of  $13.3 \text{ cm}^2$ . This decreases the heat generation due to friction and the torque to operate them. The sealing face can sustain up to 2 mm of wear before replacing. This also helps to avoid leakage due to thermal expansion or contraction of the building materials. Independent tests showed that the rotary valves are capable of holding pressures differences at the sealing face as high as  $\pm 8 \text{ bar}$  (sealing externally and internally) at frequencies up to 2 Hz. The high pressure rotary valve works at the maximum pressure (pump outlet) while the low pressure rotary

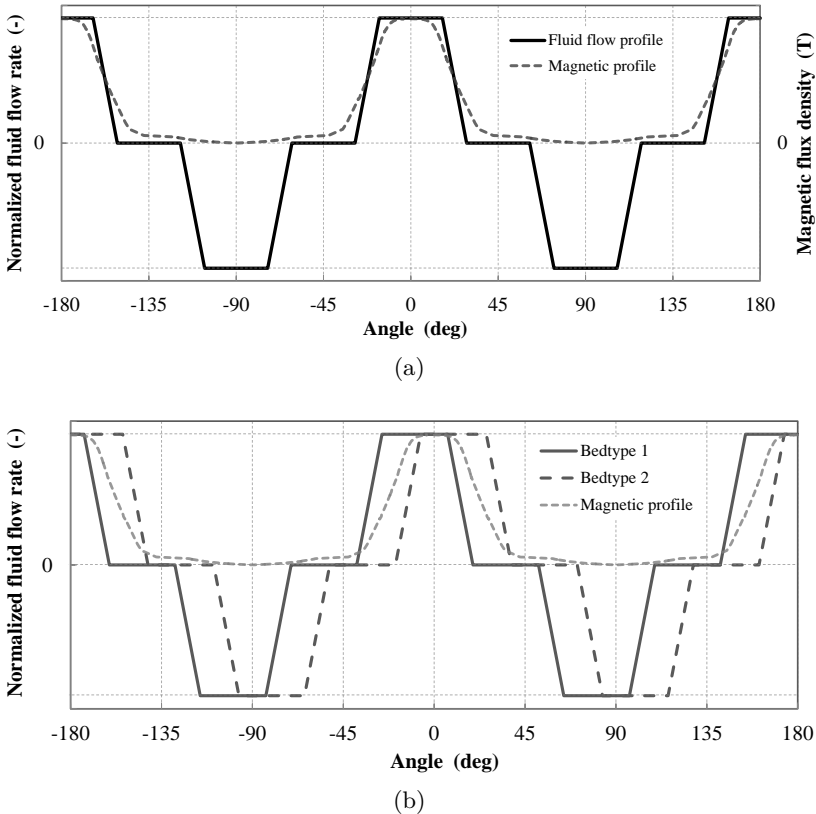


Figure 64 – Normalized (a) rotary valve (bedtype 0) and (b) bedtype 1 and bedtype 2 fluid flow profiles as a function of rotation angle and compared with the magnetic profile.

valve works on one side close to the atmospheric pressure and must hold the high pressure at the hot side of the demagnetized beds.

#### 4.4.2 Designing the flow distributors and the cold end

The absence of a rotary valve at the cold end requires the use of check valves in the channels of the regenerator beds, as shown in the cutaway view of the regenerator, magnetic circuit and cold end flow distributor in Fig. 65. The check valves prevent any flow bypassing the cold heat exchanger. Also, the fluid flow rate is measured at the cold end just before entering the heat exchanger. The

hot and cold end flow distributors were fabricated in acrylic resin (PMMA) to allow visual access to the correct functioning of the flow distribution, i.e., movement of the check valves.

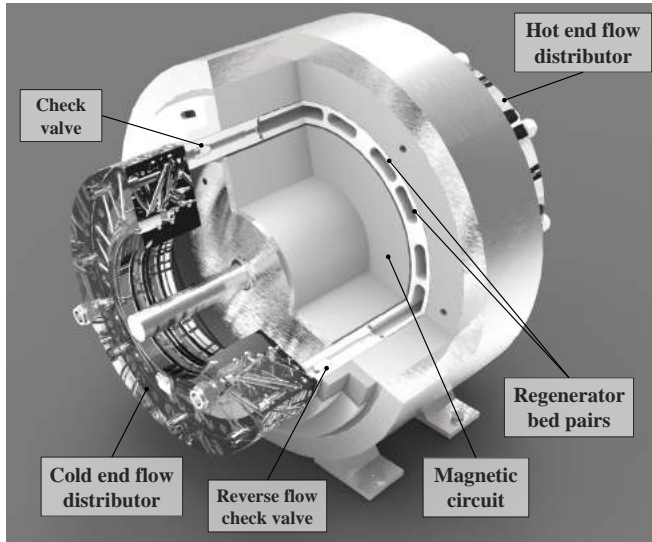


Figure 65 – Cutaway view of the regenerator, magnetic circuit and cold end flow distributor.

The cold end is important in the thermodynamic analysis of the device, as any heat transfer to the fluid flow after exiting the regenerator harms the system performance. Therefore, the cold end was designed to be as shorter (less surface area) as possible to avoid any heat gain from the ambient. A rendered image of the cold end is shown in Fig. 66. The cold end flow distributor and all tubing and connections at the cold end were thermally insulated by a 10 mm thickness polyurethane (PU) blanket.

## 4.5 DESIGNING THE REGENERATOR

The design of the regenerator depends on the designs of the magnetic circuit and flow distribution system, as well as on the magnetocaloric and heat transfer properties of the porous medium. Thus, designing a regenerator becomes an iterative task involving a large number of variables. Due to the complexity of the problems involved, a numerical simulation is required. However, due to time

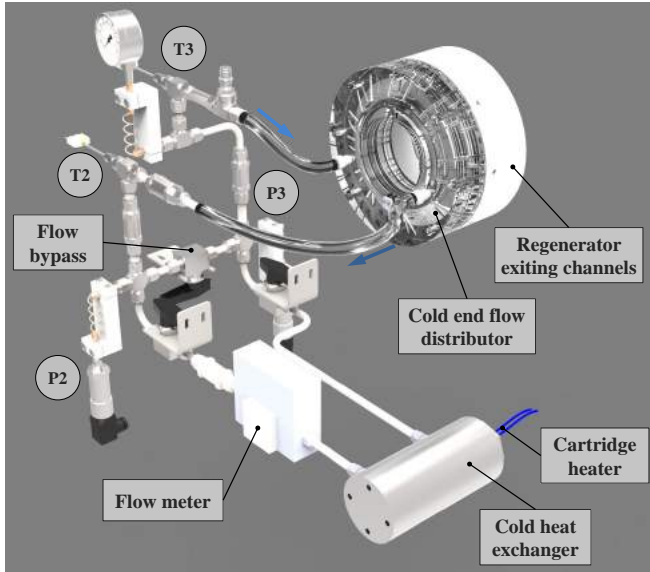


Figure 66 – Rendered image of the cold end including all of its components.

restrictions, a systematic evaluation of the influence of AMR parameters on the system performance was not carried out. Rather, the dimensions of some parameters were selected based on preliminary calculations, which were supplemented and verified by some numerical simulations. A 1D porous AMR model was adapted for the numerical simulations of the UFSC device, which is the same model used to analyze the DTU device, as will be described in detail in Chapter 6.

#### 4.5.1 Adapting a 1D numerical AMR model

The 1D AMR model developed by Engelbrecht *et al.* (2006) and presented in Section 2.6 was adapted for the actual device by implementing mainly sub-routines for: (i) Gd properties, (ii) demagnetization effects, (iii) magnetic profile, (iv) fluid flow profile and (v) defining the numerical mesh. The model was implemented in Matlab and solved in a i7-3770 (3.40 GHz, 4-core) computer with 16 GB of RAM.

Firstly, the magnetocaloric properties of the commercial-grade Gd spheres employed in both devices (DTU and UFSC) were imple-

mented in the AMR model as a property function. The properties were calculated based on measurements of the zero-field specific heat capacity,  $c_0$ , in a custom-built Differential Scanning Calorimeter (DSC) described in Ref. (Jeppesen *et al.*, 2008) and on magnetization measurements as a function of magnetic field and temperature performed in a LakeShore 7407 Vibrating Sample Magnetometer (VSM). The isothermal entropy change,  $\Delta S$ , was calculated from the magnetization data using the Maxwell relation (Eq. (2.1)). The calculated magnetocaloric properties of the Gd spheres are shown in Fig. 67. Entropy curves as a function of temperature and internal magnetic field were implemented in the 1D numerical model. The density of Gd was assumed constant at  $7901 \text{ kg/m}^3$  and the thermal conductivity was taken as  $11 \text{ W/(m.K)}$ .

It was found that for a magnetic field of 1 T,  $\Delta S$  peaks at  $3.2 \text{ J/kg.K}$  for 288 K. In turn,  $\Delta T_{\text{ad}}$  peaks at 3.1 K for 289.6 K. These values are lower than those of pure Gd (Dan'kov *et al.*, 1998) or those calculated from the mean field theory (Petersen *et al.*, 2008b). Differences can be attributed to impurities and possibly corrosion of the Gd spheres (Dan'kov *et al.*, 1998). Also, the measured Curie temperature in commercial Gd samples can be lower than that of for pure Gd (Pecharsky *et al.*, 2001).

The properties shown in Fig. 67 were obtained using the Gd employed in the DTU device, but the characterization of the Gd used in the UFSC device gave very similar results. The material was bought from the same supplier, Baotou Research Institute of Rare Earth, BRIRE, China. The Gd spheres were characterized by microscopy and elemental analysis at UFSC. Moreover, the magnetocaloric properties were measured in a magnetometer and a calorimeter at BASF in The Netherlands. A description of the characterization performed on the Gd spheres employed at UFSC is shown in Appendix B.

Demagnetization effects due to the geometry of the sample were not included in the calculations of  $\Delta S$  shown in Fig. 67 since a demagnetization function was later implemented in the numerical model of the regenerator. The demagnetization function gives the demagnetization factor as a function of temperature and magnetization characteristics of the magnetocaloric material in the regenerator bed. The average value of  $\mathbf{H}$  within the Gd spheres is calculated from  $\mathbf{H}_{\text{appl}}$  in the absence of the bed and the overall average demagnetizing factor,  $N_{\text{D}}^{\text{bed}}$ , calculated from the shape of the bed, Eq. (4.1), as given in Eq. (2.21).

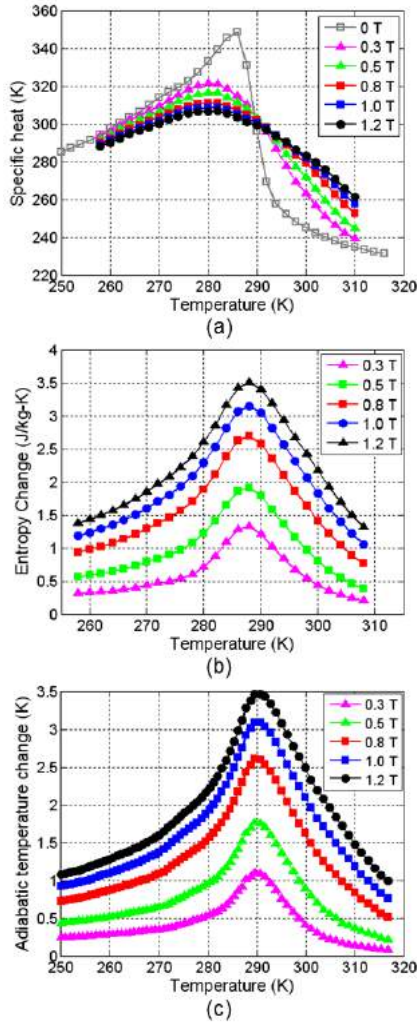


Figure 67 – Properties of the commercial Gd spheres. (a) Specific heat capacity (zero-field was measured while the field-dependence was calculated from  $\Delta S$ ), (b) entropy change integrated from  $C_H$  and (c) adiabatic temperature change derived from  $C_H$  and  $\Delta S$  data.

The magnetic field profile implemented for the UFSC device is shown in Fig. 57 as function of the angle (or time, as seen by the

AMR). Additionally, three different kinds of fluid flow profile were implemented: that of the rotary valve system (bedtype 0) as shown in Fig. 64-a, and those for bedtype 1 and bedtype 2 as shown in Fig. 64-b. In the model, the fluid flow profile is multiplied by the fluid flow rate.

A parametric analysis was carried out to determine the most suitable numerical mesh for the actual operating conditions. The analysis is based on the number of spatial steps,  $N_x$ , the number of time steps,  $N_t$  and the convergence tolerance,  $tol$ . The latter determines when the convergence (periodic steady state) is achieved (Engelbrecht, 2008):

$$\left| \frac{\Delta E_s + \Delta E_f}{E_{\max} - E_{\min}} \right| < tol \quad (4.9)$$

where  $\Delta E_s$  and  $\Delta E_f$  corresponds to the total energy change of the bed solid and fluid entering in the bed in one cycle, respectively. While  $E_{\max}$  and  $E_{\min}$  are the maximum and minimum values of the energy in the regenerator during a cycle, respectively.

The accumulated cooling capacity difference as a function of the numerical mesh parameters is shown in Fig. 68. By balancing the accuracy in the prediction of the cooling capacity and the time required for numerical convergence (computational time), the optimal numerical mesh for the UFSC device consisted of 80 spatial steps, 1000 time steps and a convergence tolerance of 0.0005.

#### 4.5.2 Final dimensions of the regenerator

The geometric variables that define the regenerator are: (i) the height,  $h_{\text{bed}}$ , (ii) length,  $L_{\text{bed}}$ , and (iii) width of the beds,  $w_{\text{bed}}$ , (iv) the number of beds,  $n_{\text{bed}}$ , and (v) the Gd sphere diameter,  $d_p$ .  $h_{\text{bed}}$  was defined during the design of the magnetic circuit, where it was set to about 10 mm to satisfy the requirements of the magnetic gap. The analytical study demonstrated that the regenerator pressure drop is strongly dependent on  $L_{\text{bed}}$  and  $d_p$ . Although small particle sizes favor the NTU, they should not be smaller than 0.4 mm to avoid high friction losses in the regenerator beds. Lengthwise, the magnetic circuit can accommodate regenerators with  $L_{\text{bed}} \leq 150$  mm. However, to avoid high pressure drops, the length of the beds should be shorter than 120 mm. In this manner, the beds fit into the high magnetic field plateau generated by the magnetic circuit (Fig. 58).

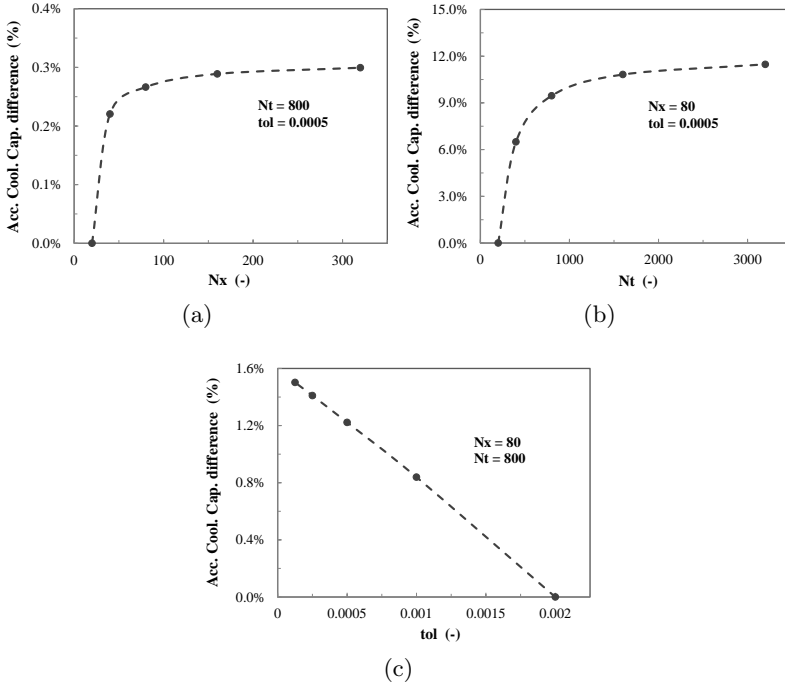


Figure 68 – Parametric analysis of the (a) spatial and (b) time mesh size, and (c) the convergence tolerance for the 1D model developed by (Engelbrecht *et al.*, 2006) and modified for the conditions of the UFSC device.

Regarding the width of the beds, it should be small in order to reduce  $N_D^{\text{bed}}$ . However, the device grows in complexity as the number of beds increases. On the other hand, magnetic forces decrease by having a more continuous regenerator ring, such as wider beds with less spacing in between. Eventually,  $n_{\text{bed}}$  and  $w_{\text{bed}}$  were determined by the perimeter of the magnetic gap,  $\text{Per}_{\text{gap}} = 628.3 \text{ mm}$  ( $360^\circ$ ) and by the opening of the high magnetic field generated by the magnetic circuit (Fig. 57). Since the flow distribution system was designed to have an 8-port rotary valve, the regenerator ring was, initially, divided into 8 beds with an opening angle in the magnetic gap of  $36^\circ$ , which results in  $w_{\text{bed}} \sim 63.4 \text{ mm}$ . The spacing left at the regenerator ring is used by the screws fixing the channeling rings.

It has been found later that having wide regenerator beds

could generate large stresses in the thin casing wall during operation at high pressures. Moreover, wider beds are susceptible to flow maldistribution. Therefore, a structural analysis of the casing was carried out using the SolidWorks Simulation<sup>®</sup> software to include an strengthening rib into the regenerator beds. Application of the von Mises criterion resulted in a longitudinal rib with a 4 mm thickness neck that divides each original bed into two beds that receive simultaneously the fluid flow from the rotary valves bifurcated at the hot end flow distributor.

Circular ribs were machined on the outer surface of the regenerator ring to create air cavities to suppress heat convection and mechanical deformation of the casing. The numerical simulation indicated that when the beds are pressurized at 10 bar the inner wall could have a maximum displacement (URES) of 0.17 mm and a maximum von Mises stress of 18.4 MPa (POM yield stress is about 63 MPa). Fig. 69 shows the resultant displacement with a 50 times distortion scale. Thus, effectively, the regenerator was split into 16 beds, each with an opening of  $16.8^\circ$ , i.e.,  $w_{\text{bed}} \sim 29.7$  mm. The beds were fabricated in a milling cutter and the edges were machined rounded with radius of 4.5 mm. The cross-section view of a pair of regenerator beds is shown in Fig. 70(a) and a transversal cutaway view (A-A) of the regenerator bed is presented in Fig. 70(b).

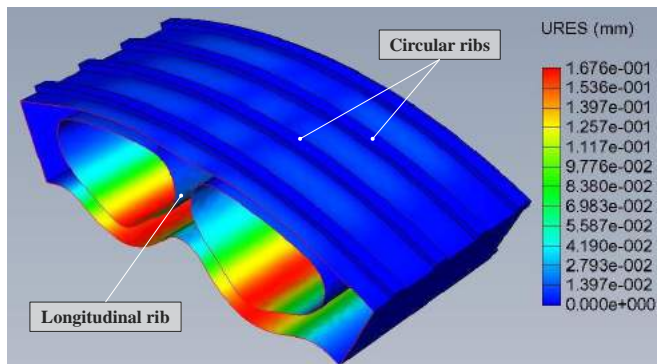


Figure 69 – Resultant of the displacement (URES) for a bed pair when pressurized at 10 bar. The distortion scale is enlarged 50 times. The image shows the second lengthwise half of the beds.

The resulting cross-sectional area per bed is  $A_{c,\text{bed}} \sim 279.7$  mm<sup>2</sup>. Calculations showed that a regenerator with a porosity  $\varepsilon \sim 0.36$ , a sphere diameter  $d_p \sim 0.4$  mm and  $L_{\text{bed}} \sim 80$  mm resulted

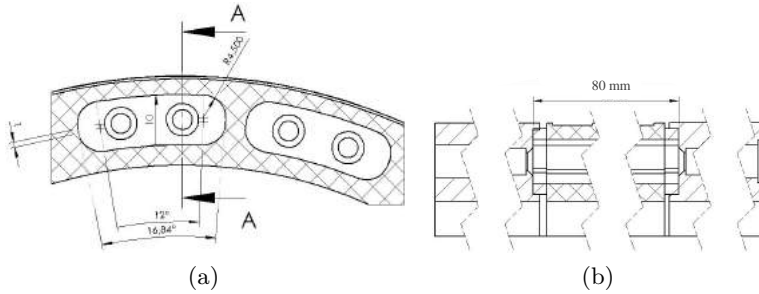


Figure 70 – (a) Cross-section view of a pair of regenerator beds and (b) a transversal cutaway view (A-A) of the regenerator bed.

in moderate pressure drops in the range of 0.2 to 2.5 bar for  $0.1 < \phi < 1.0$  and  $f = 1$  Hz. The final regenerator design shown in Fig. 71 can hold approximately 1.8 kg of packed Gd spheres. Depending on the pressure drop in the other device components (valves, heat exchangers, etc.) and on local pressure changes at the inlet and outlet of the regenerator, the pressure drop associated with the porous bed is such that the device can operate with moderate to high volumetric flow rates in the range of 50 to 400 L/h. A detailed analysis of the experimental regenerator pressure drop will be presented in Chapter 5.

The regenerator was made from polyoxymethylene (POM) for its good mechanical properties, machinability, low water absorption, very low magnetic permeability, and good dimensional stability. The regenerator beds are coupled with a channeling ring at each end, also manufactured in POM, as shown in Fig. 72(a) and Fig. 72(b). Each regenerator bed has four channels (i.e., two at the inlet and two at outlet, on each end), totalling 64 channels. Each channel is composed of: (i) a stainless steel mesh screen (Mesh 100, 0.15 mm) held in place by (ii) a POM stopper to hold the cyclical loads, (iii) an acetal check valve and (iv) a Buna-N o-ring. An exploded view of the regenerator ring with all of its components is shown in Fig. 72(c). The sealing between the beds and the channeling rings is made by nitrile gaskets. Stainless steel anchors were installed to avoid polyacetal wear.

The stainless steel wire screens were cut into 5.4-mm diameter circles to fit into the 6-mm diameter channels, as shown in Fig. 73(a). A special die cutting tool, shown in Fig. 73(b), was specially designed and fabricated for this purpose.

The fluid flow is unidirectional in each channel. The parallel

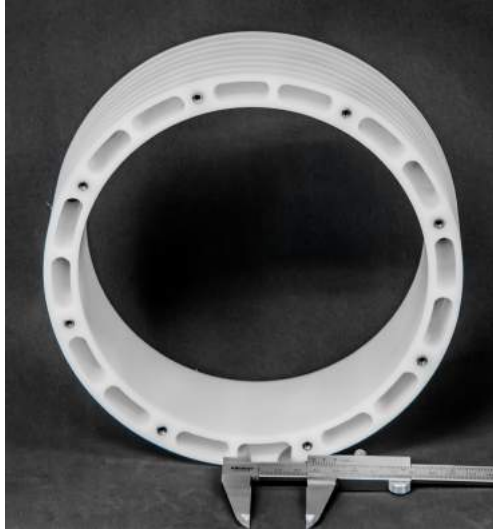


Figure 71 – Regenerator ring.

channels on each side are not interconnected to avoid dead volumes and losses due to fluid (blow) mixing (Jacobs, 2009). The entrances of the channels are tapered out to improve the flow distribution, although it is known that this increases the inlet pressure drop. The inlet and outlet channels are diagonally opposed to each other across the regenerator beds to improve mixing.

### 4.5.3 Assembling the regenerator

Prior to filling the regenerator with the Gd particles, a *dummy* pair of beds was built, assembled and tested to verify the mounting routine and the stability of the bed when applying high flow rates and pressures. Therefore, due to the numerous components involved in the assembly of the regenerator, two procedures were developed: (i) for filling the regenerator beds and (ii) mounting the regenerator ring and flow distributors.

To reduce the pressure drop at the ends, the central part of the regenerator beds was filled with Gd spheres sieved to diameters between 0.425 to 0.5 mm, while the ends were filled with diameters between 0.5 to 0.6 mm. The Gd spheres were randomly packed by pouring and compacting with a piston. As a result of the random packing and variations in particle size and bed dimensions, each

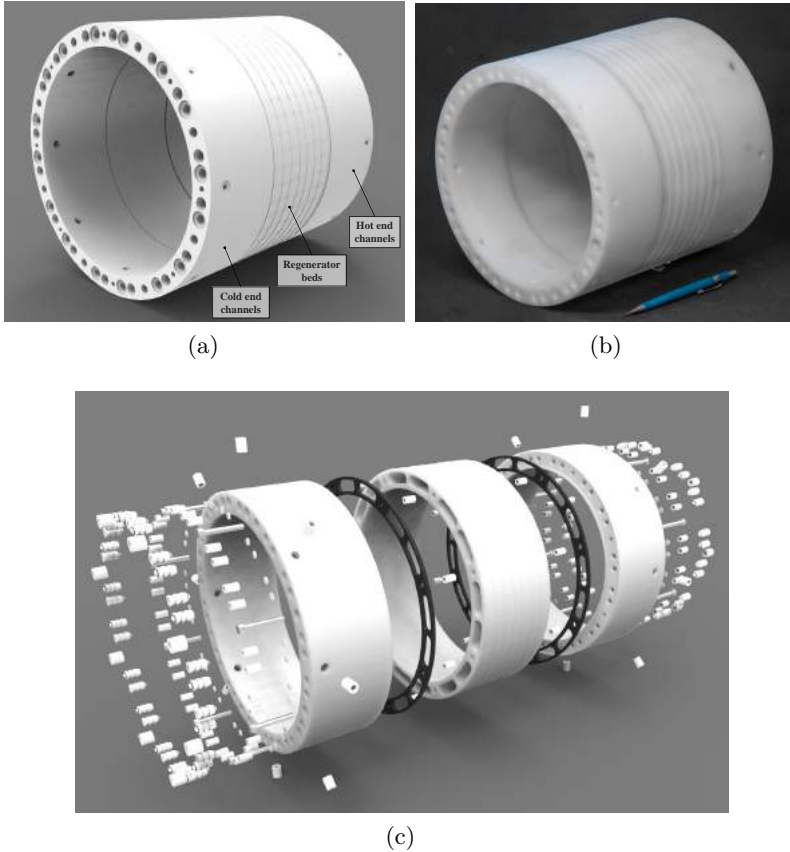


Figure 72 – (a) Rendered and (b) photograph of the regenerator ring coupled with the channeling rings. (c) Exploded view showing all regenerator components: gaskets, screens, anchors, check valves and fixation screws.

bed has a different mass of Gd. The mean mass of Gd per bed is  $\bar{m}_{\text{bed}} \sim 106.08 \pm 1.30$  g, totaling 1697.30 g. Approximately 90% of the Gd particle diameters were in the range between 0.425 and 0.5 mm, while 5% was between 0.5 and 0.6 mm at each end of the beds. The calculated porosity in the regenerator was approximately  $\varepsilon_{\text{reg}} \sim 40.3\%$ . The packing factor is low due to the rounded geometry of the beds. The resulting regenerator parameters are summarized in Table 11. The pressure drop was measured in each bed in the two flow

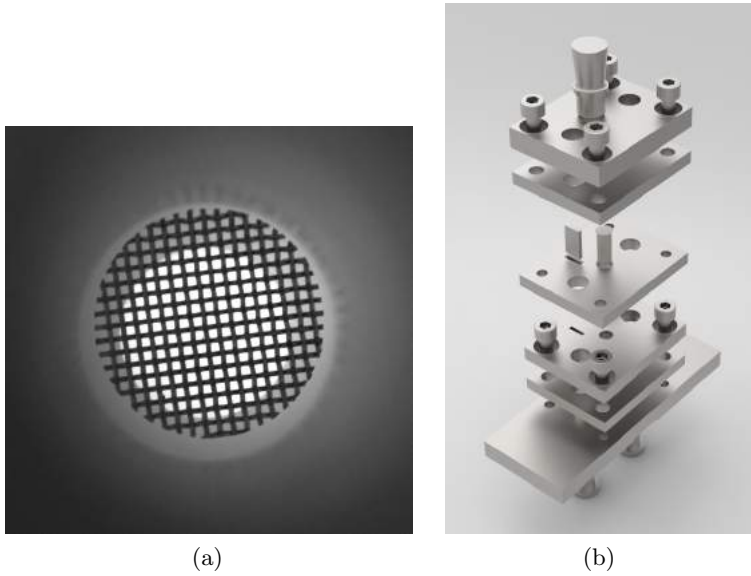


Figure 73 – (a) Photograph of a stainless steel wire screen Mesh 100 inside one of the 6 mm regenerator channels and (b) an special die cutting tool developed to cut the screen.

directions. The results will be explored in Chapter 5. Fig. 74 shows a photograph of the final regenerator ring filled with Gd spheres and connected to the hot and cold end flow distributors.

Table 11 – Regenerator parameters.

Parameter	Symbol	Value	Unit
Number of beds	$n_{\text{bed}}$	16	-
Length of the beds	$L_{\text{bed}}$	80	mm
Bed cross section area	$A_c$	280	mm <sup>2</sup>
Regenerator volume	$V_{\text{reg}}$	0.36	L
Total regenerator mass	$m_{\text{reg}}$	1.7	kg
Regenerator porosity	$\varepsilon$	0.40	-
Magnetocaloric material	Gd	Gadolinium	-
Spheres diameter	$d_p$	0.425 - 0.6	mm
Regenerator casing	POM	Polyacetal	-

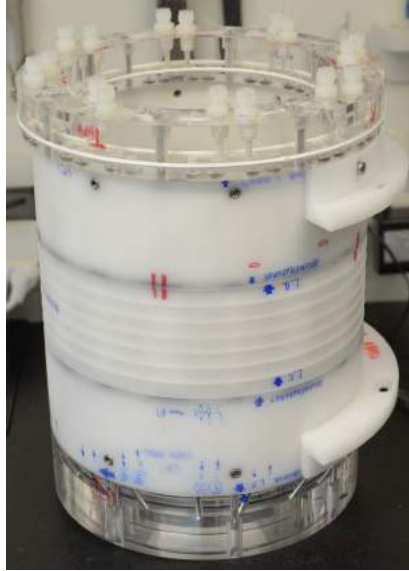


Figure 74 – Photograph of the final regenerator ring filled with Gd and coupled with the hot (top) and cold (bottom) end flow distributors.

## 4.6 ANCILLARY COMPONENTS

The ancillary components are shown in the schematic diagram of Fig. 62. This section describes these pieces of equipment and is divided into 4 subsections: (i) thermal, (ii) driving, (iii) instrumentation and control components and (iv) equipment information.

### 4.6.1 Thermal components

The thermal fluid transfers the heat it absorbs at the cold end to the environment (thermal reservoir) at hot end. Thus, two heat exchangers are required: one to simulate the thermal load and another to simulate the heat rejection to the external ambient, which is represented by the thermostatic bath. In Fig. 62, these components correspond to items (22), (6) and (7), respectively. Both heat exchangers were intentionally oversized to cover a wide range of conditions and to allow future modifications and improvements in the device. The designs of both heat exchangers are related, since the heat rejected at the hot end corresponds to that absorbed at the cold end plus the magnetic work and the heat gain (or lost) in the

circuit.

A cutaway view of the screw-type cold heat exchanger is shown in Fig. 75. This design ensures that the thermal load,  $\dot{Q}_C$ , simulated by a 25.4-mm diameter cartridge heater is completely absorbed by the heat transfer fluid with little loss to the ambient. The cold heat exchanger consists of a stainless steel cylinder with an external diameter of 80 mm and an internal coiled channel (screw) through which the fluid flows. The hydraulic diameter of the trapezoidal channel is approximately 6.3 mm and the screw fillets are not in contact with the heater to avoid any heat conduction through the housing. Nevertheless, the stainless steel cylinder was well insulated by a 20 mm layer of expanded PU. The heater resistance is approximately 180  $\Omega$ , which corresponds to a maximum heating load of approximately 269 W at 220 V.

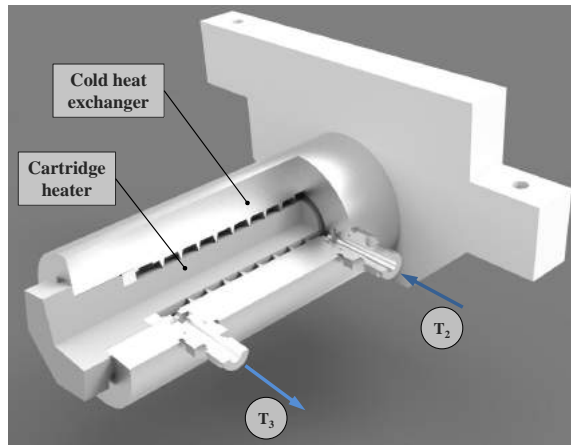


Figure 75 – Cutaway view of the screw-type cold heat exchanger showing the cartridge heater and the internal coiled channel through.

The fluid enters the cold heat exchanger at the temperature it leaves the regenerator after a hot blow,  $T_2$ , and exits it at  $T_3$ , which is the temperature at which it will enter the regenerator in a cold blow. These temperatures are measured as shown in Fig. 66. Therefore, the temperature difference at the cold end,  $\Delta T_{CE}$ , is given by:

$$\Delta T_{CE} = (T_3 - T_2) \simeq \frac{\dot{Q}_C}{\dot{m}_f c_f} \quad (4.10)$$

The difference between the last two terms in Eq. (4.10) is due

to parasitic heat gain at the cold end tubing and components. The thermal load is measured by a power meter transducer.

The hot end heat exchanger is of the brazed plate type with 24 parallel plates and  $0.31 \text{ m}^2$  total surface area. For an improved temperature control, it was (over) rated for a heat transfer duty of  $1.7 \text{ kW}$  at  $800 \text{ kg/h}$ . The temperature controlled bath, manufactured by Thermo Scientific, has a temperature stability of  $0.02 \text{ K}$ , a heating capacity of  $1.2 \text{ kW}$ , a cooling capacity of  $800 \text{ W}$  at  $20^\circ\text{C}$  and a maximum fluid rate of  $1020 \text{ L/h}$ . In the hot end heat exchanger, the fluid rejects the heat gained throughout the cycle and leaves at the so-called hot reservoir temperature,  $T_1$ , which is the temperature the fluid enters the regenerator in a hot blow. In contrast with the cold heat exchanger, at the hot heat exchanger it is more difficult to determine the heat transfer rate, since the temperature at which the fluid enters the heat exchanger is not measured directly, but inferred from the temperature of the fluid exiting the regenerator,  $T_4$ , which is measured upstream of the reservoir, pump and flow meter.

#### 4.6.2 Driver system

The driver system is composed of (i) an electrical motor, (ii) a gear reduction, (iii) torque transducer, (iv) two synchronized pulleys and (v) a belt, as shown in Fig. 76. The selection of these components depends mainly on the torque required to rotate the rotary valve system and the magnetic circuit for a desired maximum AMR operating frequency.

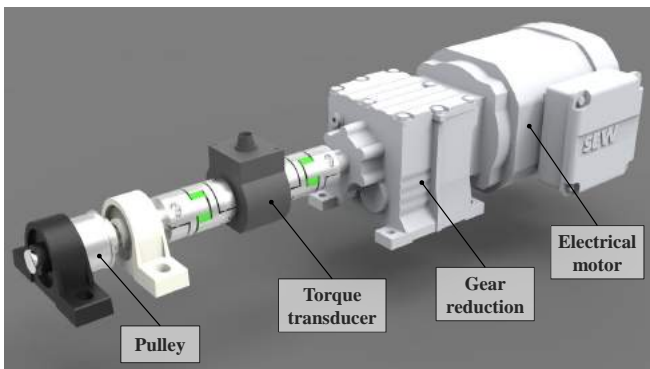


Figure 76 – Driver system.

An ancillary experimental setup was developed to estimate

the torque required to rotate the rotor when the magnetocaloric beds are in the magnetic gap. Since the higher magnetic force would be between beds with a larger separation between them (i.e., those separated by a screw), another dummy regenerator was manufactured in which two blocks of Gd were positioned inside the beds, as shown in Fig. 77. The dummy regenerator was placed inside the magnetic gap and the torque to rotate the rotor was measured with a D-Torq Topeak Wrench torque-meter. The results are shown in Fig. 78 only for increasing torque as a function of the rotation angle (clockwise and counter clockwise). The accuracies for clockwise and counter clockwise rotation were estimated at  $\pm 3\%$  and  $\pm 4\%$ , respectively. Although the maximum measured torque was 15.9 Nm, the further distant between the actual beds corresponds to the equilibrium position (angle  $0^\circ$ ), so to take the rotor apart from this position, the resultant torque would be maximum at the center of the bed (at about angle  $16^\circ$ ) of approximately 8.2 Nm. In the actual regenerator, the resultant torque would correspond to the double (two magnetic poles) times the packing factor, thus, approximately 10.5 Nm. With these information, a rotary torque transducer HBM model T22-20 Nm was selected.

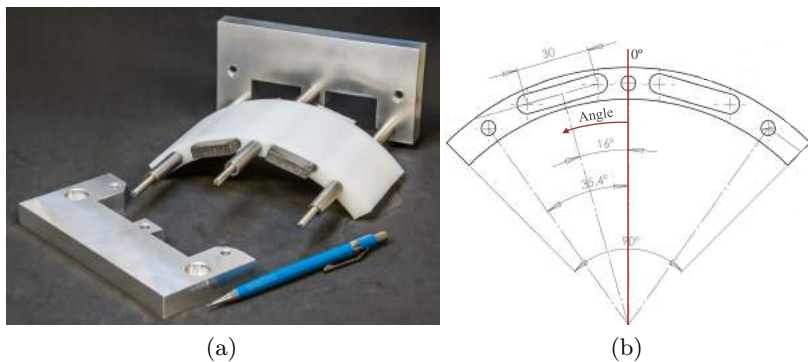


Figure 77 – (a) Photograph and (b) 2D drawings of the dummy regenerator manufactured to estimate the torque to rotate the magnetic circuit.

A 0.75-kW electrical motor coupled with a helical gear unit reduction delivers an output torque of 58 Nm at a maximum rotation of 124 RPM. The gearmotor is controlled by a frequency inverter. Synchronized pulleys, belt and tensioner avoid slippage due to the high and jittery torque. The pulleys have a ratio of 2:1, which allows

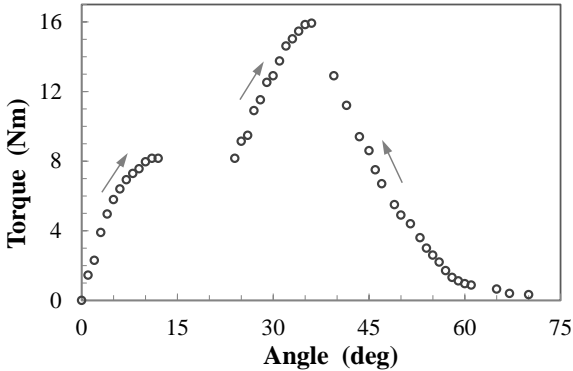


Figure 78 – Results for the increasing torque as a function of the angle of rotation of the magnetic circuit.

for operating AMR frequencies up to 8 Hz.

### 4.6.3 Instrumentation and control components

The experimental device is equipped with sensors to measure temperature, pressure, flow rate, frequency, torque and power. A data acquisition system is responsible for data logging and storage. The positions of the fluid temperature and pressure sensors are shown in Fig. 62.

The fluid temperatures were measured by Omega Pt-100 Class A resistance temperature detectors (RTDs). The ambient temperature was measured by a T-type thermocouple welded to a copper block and placed near the cold end to monitor the air temperature. Absolute pressures were measured by precision pressure transmitters (Wika P-30). The fluid flow rate was measured at the hot end by an electromagnetic flow meter (Krohne Optiflux 1100-C), and at the cold end by a digital paddle-wheel flow meter (Aalborg PWE4). The operating frequency was measured by an inductive sensor at the rotor shaft (Balluff BES). The torque was measured by a torque transducer at the driver shaft (HBM T22). The actual power consumption of the cartridge heater, the gearmotor driver and the motor pump were measured by power transducers (Kron WA-30) located between the main electrical supply and the heater or frequency inverters.

Sensors and other pieces of equipment were controlled automatically from a Labview program connected to a signal condition-

ing and data acquisition National Instruments SCXI Chassis. The operating frequency and the fluid flow rate were varied via frequency inverters that controlled the electrical motors. The fluid flow rate was also regulated manually by a needle valve which acted as a flow bypass. The heat load was set by varying the voltage input to the cartridge heater. The hot reservoir temperature was adjusted based on the temperature set in the thermostatic bath, the flow rate and the heat rejection rate. The room temperature was kept within  $293 \pm 1$  K by a room air conditioner.

A rendered image of the final layout of the experimental device is shown in Fig. 79.

#### 4.6.4 Equipment information

The specifications of the instrumentation sensors and the equipments are summarized in Tables 12 and 13, respectively.

Table 12 – Specifications of the instrumentation sensors.

Instrumentation sensors	Manufacturer	Model
Temperature	Omega	RTD Pt-100
Temperature	Omega	T-type thermocouple
Absolute pressure	Wika	P-30
Hot end fluid flow rate	Khrone	Optiflux 1100-C
Cold end fluid flow rate	Aalborg	PWE4
Operating frequency	Balluff	BES 516-209-S 27-E
Single-phase power transducer	Yokogawa	85A-0
Three-phase power transducer	Kron	WA-30
Torque transducer	HBM	T22

Table 13 – Specifications of the equipments.

Equipments	Manufacturer	Model
Acquisition system	NI	SCXI-1000
Thermostatic bath	Thermo Scientific	SC150-A40
Gearmotor	SEW	R17-DRE80S4
Frequency inverter	SEW	MC07B0008
Pump	Micropump	GL-H25
Motor of the pump	Weg	W22 Plus
Frequency inverter	Weg	CFW08

The expanded uncertainties and ranges of the transducers provided by the manufacturers are summarized in Table 14. A detailed



Figure 79 – Rendered image of the final experimental setup.

uncertainty analysis of the measured and calculated parameters has been carried out and is presented in Appendix C.

Table 14 – Expanded uncertainty (accuracy) of the transducers provided by the manufacturers.

Sensor	Accuracy	Range
Temperature (RTD)	$\pm (0.15 + 0.002 T) ^\circ\text{C}$	0 – 100 $^\circ\text{C}$
Temperature (Thermocouple)	$\pm 1 \text{ K}$	233 – 398 K
Absolute pressure	$\pm 0.016 \text{ bar}$	0 – 16 bar
Hot end fluid flow rate	$\pm 0.5\%$ of rate	0 – 1200 L/h
Cold end fluid flow rate	$\pm 11.3 \text{ L/h}$	9 – 1134 L/h
AMR Operating frequency	$\pm 0.24 \text{ mHz}$	0.06 – 2.06 Hz
Single-phase power transducer	$\pm 2.5 \text{ W}$	0 – 1000 W
Torque transducer	$\pm 0.3\%$ of torque	0 – 20 Nm
Three-phase power transducer	$\pm 8.2 \text{ W}$	0 – 3290.9 W



## Chapter 5

# EXPERIMENTAL ANALYSIS OF THE UFSC MAGNETIC REFRIGERATOR

An experimental analysis of the magnetic refrigeration system developed at Polo/UFSC is described in this chapter. Experimental measurements were performed to characterize the pressure drop in both empty and packed regenerator beds. Experimental results for different operating frequencies, fluid flow rates, hot reservoir temperatures and thermal loads are shown and discussed. The torque and motor power experimental results are presented as a function of the operating frequency. Finally, the thermodynamic performance of the device is evaluated in terms of the coefficient of performance (COP) and the overall second-law efficiency ( $\eta_{2nd}$ ).

The experimental sampling rate of the measured parameters presented in this chapter was 2 Hz and the sampling period was 120 s, resulting in about 240 samples. The result for each parameter corresponds to the time-averaged value of the measured samples for each experiment and the expanded uncertainty for those results is presented either as error bars at the plots or as the maximum value of the set. All the expanded uncertainties are expressed for a 95% level of confidence and their calculations are detailed in Appendix C.

### 5.1 PRESSURE DROP ANALYSIS

Detailed pressure drop analyses were carried out for the dummy and final regenerator beds, both without (empty) and with solid particles forming a packed porous medium. In the experimental device, the regenerators were instrumented with four absolute pressure transmitters at the inlet and outlet at each end of the regenerator beds (see Fig. 62). This allowed the determination of four different pressure differences defined as follows: (i) system pressure drop ( $\Delta p_{sys} = p_1 - p_4$ ), (ii) hot-to-cold blow pressure drop ( $\Delta p_{htcb} = p_1 - p_2$ ), (iii) cold end pressure drop ( $\Delta p_{CE} = p_2 - p_3$ ) and (iv) cold-to-hot blow pressure drop ( $\Delta p_{cthb} = p_3 - p_4$ ). The maximum expanded uncertainty of the pressure drops in this analysis was 0.041 bar. The volumetric flow rate ( $\dot{V}_f$ ) measured with

the electromagnetic flow meter had a maximum expanded uncertainty of  $1.35 \text{ L/h}$ . The fluid temperature and the room temperature were maintained at  $293 \pm 1 \text{ K}$  by the thermostatic bath and air conditioning system, respectively.

The dummy regenerator beds were placed directly in between the pressure transmitters, as seen in Fig. 80. Thus neither the influence of rotary valves, hoses nor the effect of flow distributors were included in its analysis. The dummy beds were packed with stainless steel spheres with diameter of approximately  $0.5 \text{ mm}$ . The fluid employed in these tests was deionized water.

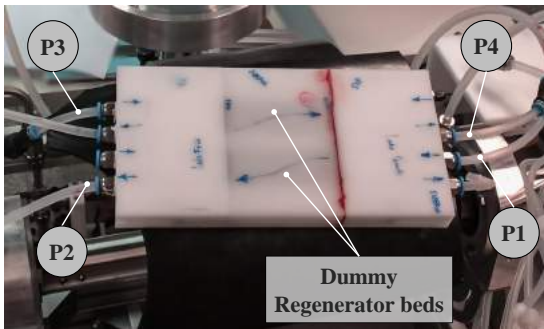


Figure 80 – A photograph of the pressure drop experimental analysis of the dummy regenerator beds including the lines where each pressure transmitter were placed.

Fig. 81 shows the system pressure drop ( $\Delta p_{\text{sys}}$ ) for the two empty and the two packed dummy beds as a function of the volumetric flow rate. Both the empty and the packed regenerator beds pressured drop analyses included the cold-end regenerator components (screens, stoppers and check valves). In this experiment, the cold end heat exchanger was bypassed, so the system pressure drop did not consider the pressure drop in the cold heat exchanger.

Similarly, Fig. 82 presents the hot-to-cold blow pressure drop ( $\Delta p_{\text{htcb}}$ ) for an empty and a packed dummy bed as a function of the volumetric flow rate. The pressure drop of the porous medium was calculated as the difference between the pressure drop of the packed bed and the pressure drop of the empty bed. This result is compared with the theoretical result for the pressure drop in a packed bed of  $0.5\text{-mm}$  diameter spheres calculated using the classical Ergun equation (Eq. 4.2). The differences between the experimental and calculated pressure drop are possibly due to the presence

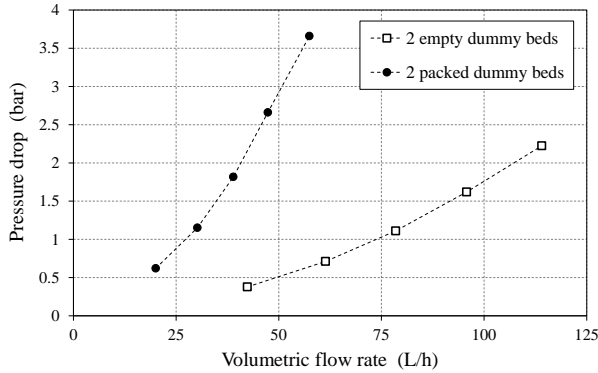


Figure 81 – System pressure drop ( $\Delta p_{\text{sys}}$ ) for the two empty and the two packed dummy beds as a function of the volumetric flow rate.

of spheres larger than 0.5 mm, entrance effects and the inclusion of the regenerator components at the hot end channeling. The pressure drop analysis in the dummy regenerator demonstrated that the entrances of the bed channeling represent almost similar pressure drop as the continuous cross-section area of the bed (considered as the *central bed*). Unfortunately, by the time that these results were obtained, the final regenerators were already fabricated, and the tapered entrances were maintained for the final regenerator.

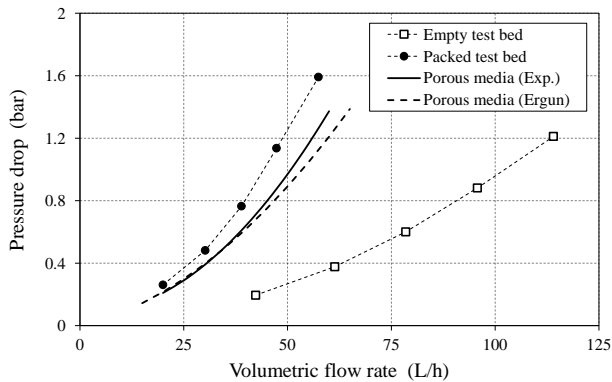


Figure 82 – Pressure drop for an empty and a packed dummy bed and the calculated porous media pressure drop as a function of the volumetric flow rate.

Fig. 83 shows the experimental analysis of the pressure drop of the empty final regenerators including the flow distribution system. The four different pressure drops of the empty final regenerator were measured as a function of the volumetric flow rate given by the electromagnetic flow meter. The results are shown in Fig. 84. The measurements include all the components of the machine except the Gd spheres and the regenerator components (screens, stoppers and valves) at the hot end. A mixture of 20% ethylene-glycol and 80% distilled water (vol. %) was employed as the heat transfer fluid. The mixture was allowed to flow into the cold heat exchanger, whose pressure drop,  $\Delta p_{\text{CE}}$ , at 200 L/h is approximately 0.55 bar. It is worth mentioning that, at any given time, there is continuous flow fluid in eight beds (four in a hot-to-cold blow and four in a cold-to-hot blow), while the eight remaining beds are closed for any type of flow. Thus, the flow rate in any bed experiencing a blow is about one quarter of the total pumped flow rate ( $\dot{m}_{\text{P}} \sim 4\dot{m}_{\text{bed}}$ ). The difference between the pressure drops of the hot-to-cold and cold-to-hot blows in Fig. 84 maybe due to the presence of a 40  $\mu\text{m}$  filter in the hot-to-cold flow line and small fabrication and tubing geometry differences.

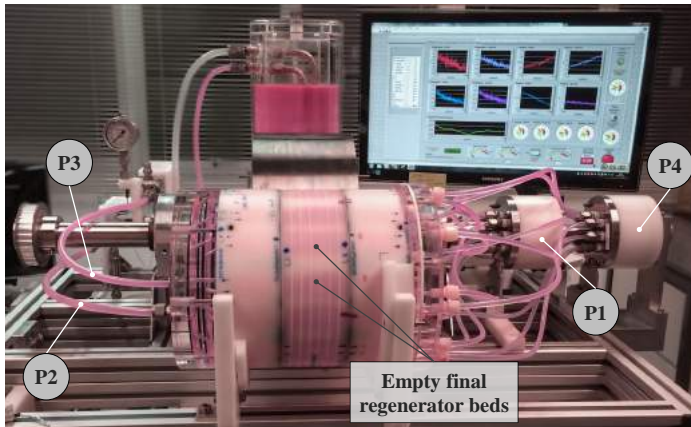


Figure 83 – A photograph of the pressure drop experimental analysis of the empty final regenerator beds including the flow distribution system and the lines where each pressure transmitter were placed.

The final regenerator was packed with Gd spheres as detailed in section 4.5.3, and the pressure drop was measured individually for each regenerator bed by employing a connection tool, as shown in Fig. 85. In this set of experiments, the pressure drop of the rotary

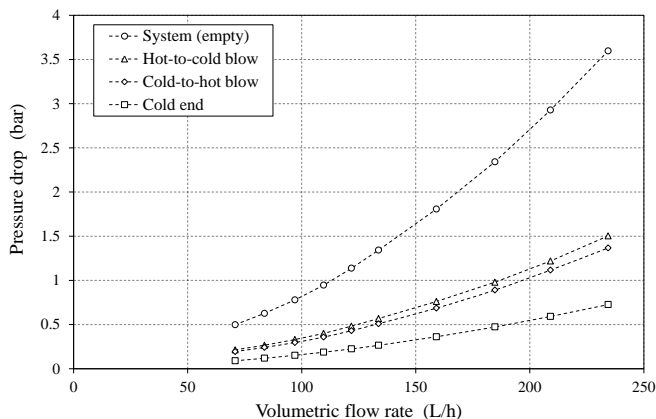


Figure 84 – Comparison of the four different pressure drops for the empty final regenerator as a function of the volumetric flow rate.

valves and flow distributors are not included.

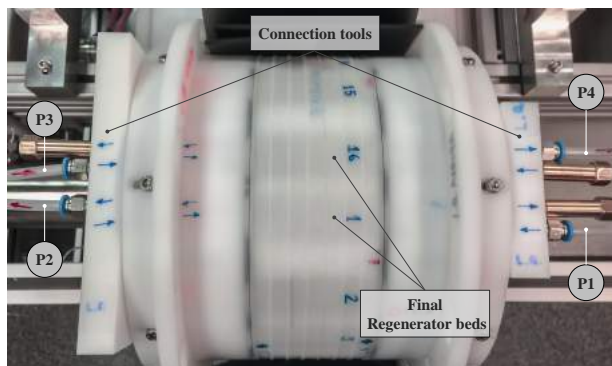


Figure 85 – A photograph of the pressure drop experimental analysis of the individual final regenerator beds including the connection tools for individual bed tests and the lines where each pressure transmitter were placed.

Fig. 86 shows the hot-to-cold blow pressure drop for each of the sixteen packed regenerator beds as a function of the volumetric flow rate. The dotted line corresponds to the pressure drop of an empty bed. The differences in pressure drop between the beds may be due to the slight variations in their dimensions and/or packing structure. The mean particle mass per bed was 106.08 g with

an standard deviation of 1.30 g. The regenerator porosity was estimated at 40.3%. The maximum relative variation of the pressure drop within the beds was as high as  $\pm 21.3\%$ . In this regenerator setup, it was not possible to rearrange the beds according to the flow resistance to minimize flow channeling between the beds, as recommended by Engelbrecht *et al.* (2012). The average  $\Delta p_{\text{htcb}}$  for a packed bed at 50 L/h was approximately 1.51 bar, while  $\Delta p_{\text{htcb}}$  for the empty regenerator (including the flow distribution components) at 200 L/h was approximately 1.13 bar.

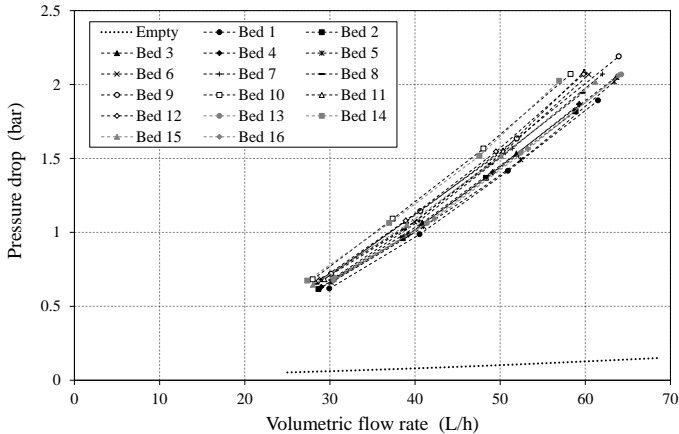


Figure 86 – Hot-to-cold blow pressure drop ( $\Delta p_{\text{htcb}}$ ) for each of the sixteen regenerator beds packed with Gd spheres as a function of the volumetric flow rate. The dotted line corresponds to the pressure drop of an empty bed.

The final regenerator was placed inside the magnetic circuit and the final experimental setup of the device is shown in Fig. 87. This figure indicates also the lines where pressure and temperature measurements were taken for the following experiments presented in this chapter.

Fig. 88 shows the system pressure drop ( $\Delta p_{\text{sys}}$ ) for the packed final regenerator at a frequency of 0.8 Hz as a function of the fluid flow rate measured by the turbine flow meter. Both the experimental absolute pressures and mass flow rate measured at the cold end show significant variations between beds. This can be related to variations in packing structure between adjacent beds (Fig. 86). The expanded uncertainty for such differences is included in Fig. 88 as error bars. The volumetric flow rate measured at the cold end flow meter was,

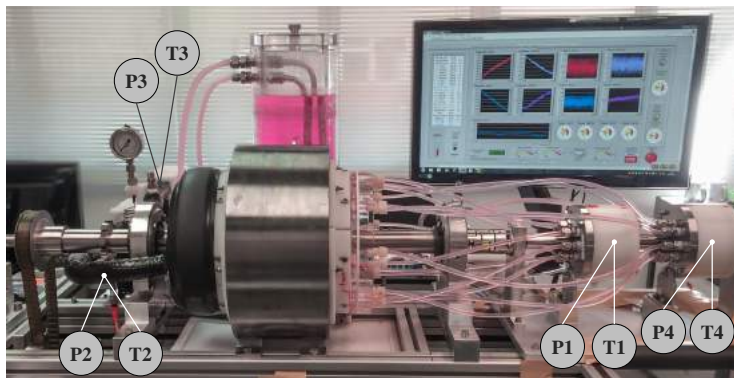


Figure 87 – A photograph of the final experimental setup including the flow distribution system and the lines where each pressure transmitter and temperature detector were placed.

on average, 4.96% lower than the volumetric flow rate measured at the hot end flow meter. This can be attributed to fluid internal leakages in the flow distribution system and within the regenerator beds before reaching the cold heat exchanger.

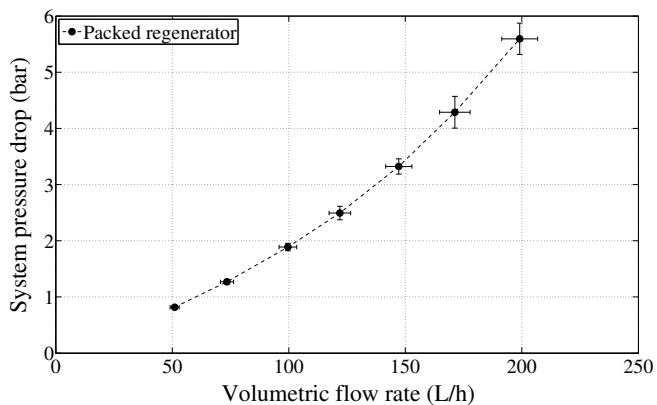


Figure 88 – System pressure drop ( $\Delta p_{\text{sys}}$ ) of the packed final regenerator operating at a frequency of 0.8 Hz. The expanded uncertainties of the system pressure drop and volumetric flow rate measured at the cold end are shown in the error bars.

## 5.2 EXPERIMENTAL ANALYSIS

The experimental setup allows mapping the four different parameters which influence the performance of the magnetic refrigerator: (i) operating frequency ( $f$ ), (ii) volumetric flow rate ( $\dot{V}_f$ ), (iii) hot reservoir temperature ( $T_H$ ) and (iv) thermal load ( $\dot{Q}_C$ ). The system performance was evaluated independently for each of the four parameters. In all experiments, the room temperature was maintained at  $293 \pm 1$  K by the room air conditioning system.

The system is instrumented with four resistance temperature detectors (RTDs) positioned at the inlet and outlet of the regenerator. Four different fluid temperatures are evaluated experimentally as follows (see Fig. 87):

- $T_1$ : Temperature of the fluid entering the regenerator from the hot end during the hot-to-cold blow (*hot blow*). This temperature can be assumed equal to the hot reservoir temperature ( $T_H$ ) set by the hot-side heat exchanger;
- $T_2$ : Temperature of the fluid exiting the regenerator at the cold end during the hot-to-cold blow. This temperature, also denoted as  $T_{C,out}$ , is the lowest temperature in the system;
- $T_3$ : Temperature of the fluid entering the regenerator from the cold end during the cold-to-hot blow (*cold blow*). This temperature can be assumed to represent the cold reservoir temperature ( $T_C$ );
- $T_4$ : Temperature of the fluid exiting the regenerator at the hot end during the cold-to-hot blow. This temperature, also denoted as  $T_{H,out}$ , is the highest temperature in the system.

Fig. 89 and 90 show the typical behavior of the fluid temperatures at the beginning of an experiment (*opening-span curve*) and after steady state is attained, respectively. Fig. 89 corresponds to a zero thermal load (no-load) experiment at an operating frequency of 0.8 Hz, a volumetric flow rate of 150 L/h and the thermostatic bath set at 295.15 K. Similarly, Fig. 90 shows the fluid temperatures at steady state for an applied thermal load of 60 W, a volumetric flow rate of 150 L/h, an operating frequency of 0.8 Hz and the thermostatic bath set at 293.15 K.

As can be inferred from Fig. 90, the following four temperature differences can be calculated from the temperatures measured in the system (Rowe, 2009; Trevizoli *et al.*, 2011):

- *Regenerator temperature span* ( $\Delta T_{reg}$ ): experimentally determined as the difference between the average temperature of

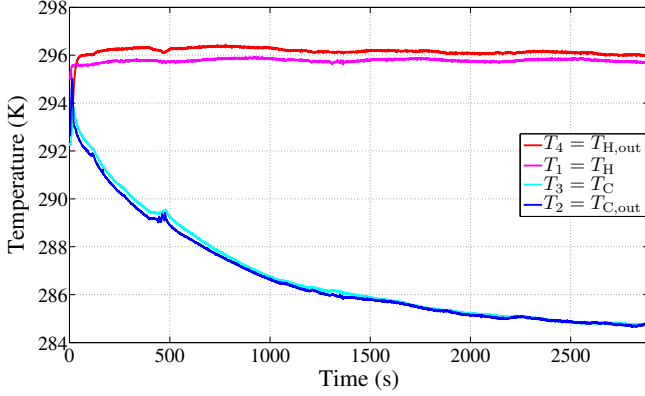


Figure 89 – *Opening-span curve* for a no-load experiment at  $f = 0.8$  Hz,  $\dot{V}_f = 150$  L/h and  $T_{\text{bath}} = 295.15$  K.

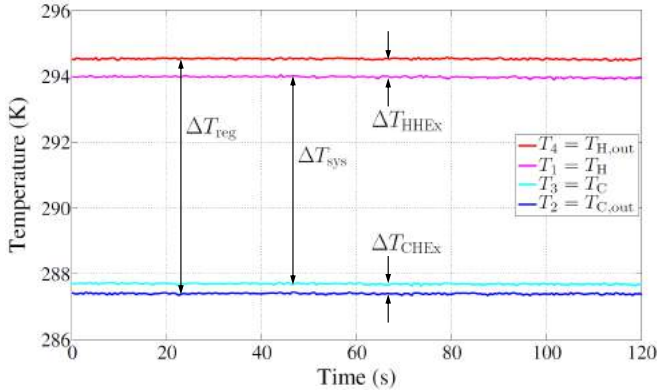


Figure 90 – Steady-state temperature behavior of the fluid at the inlets and outlets of the regenerator.  $\dot{Q}_C = 60$  W,  $\dot{V}_f = 150$  L/h,  $f = 0.8$  Hz and  $T_{\text{bath}} = 293.15$  K.

the fluid exiting the hot end of the regenerator and the average temperature of the fluid exiting the cold end of the regenerator:

$$\Delta T_{\text{reg}} = T_{\text{H,out}} - T_{\text{C,out}} = T_4 - T_2; \quad (5.1)$$

- *System temperature span* ( $\Delta T_{\text{sys}}$ ): defined as the difference between the hot and cold environment temperatures.  $\Delta T_{\text{sys}}$  can be experimentally determined as the difference between the average temperature of the fluid entering the hot end of the

regenerator from the hot heat exchanger and the average temperature of the fluid entering the cold end of the regenerator from the cold heat exchanger:

$$\Delta T_{\text{sys}} = T_{\text{H}} - T_{\text{C}} = T_1 - T_3; \quad (5.2)$$

- *Hot heat exchanger temperature difference* ( $\Delta T_{\text{HHEx}}$ ): defined as the difference between the average temperature of the fluid exiting the hot end of the regenerator and the average temperature of the fluid entering the hot end of the regenerator:

$$\Delta T_{\text{HHEx}} = T_{\text{H,out}} - T_{\text{H}} = T_4 - T_1; \quad (5.3)$$

- *Cold heat exchanger temperature difference* ( $\Delta T_{\text{CHEx}}$ ): defined as the difference between the average temperature of the fluid entering the cold end of the regenerator and the average temperature of the fluid exiting the cold end of the regenerator:

$$\Delta T_{\text{CHEx}} = T_{\text{C}} - T_{\text{C,out}} = T_3 - T_2. \quad (5.4)$$

The experiment is considered to reach steady state, as in Fig. 90, when the standard deviation of the regenerator temperature span is smaller than 0.03 K over a sampling period of 120 s ( $\sigma_{\Delta T_{\text{reg}}} < 0.03$  K). This value is much lower than the expanded uncertainty for an RTD at room temperature, which was approximately  $U_{T_i,95} \sim 0.22$  K.

As mentioned above, the independent variables in the experiments were the heat transfer fluid volumetric flow rate, the operating frequency, the hot reservoir temperature and the thermal load. The fluid flow rate and the frequency are combined in the dimensionless parameter utilization,  $\phi$  (Eq. 2.9). As in most of the literature on AMR systems, in this thesis, the experimental results will be reported in terms of  $\Delta T_{\text{reg}}$ . This temperature span corresponds to the largest temperature difference between the hot and cold sides of the system. Finite values of  $\Delta T_{\text{HHEx}}$  and  $\Delta T_{\text{CHEx}}$  are necessary to guarantee the required heat duties in the finite-size hot- and cold-side heat exchangers. It should be noted, however, that the heat exchangers must be carefully designed so that  $\Delta T_{\text{HHEx}}$  and  $\Delta T_{\text{CHEx}}$  are the lowest possible in order to keep the external irreversibility of the system at a minimum.

### 5.3 EXPERIMENTAL RESULTS

The expanded uncertainties of each experiment presented in this section are shown as error bars in the corresponding plots. The uncertainty analysis is presented in detail in Appendix C. The volumetric fluid flow rate reported here was measured by the cold end flow meter to account for possible internal leakages in the flow distribution system or in the regenerator beds. Also, this corresponds to the actual flow passing through the cold heat exchanger.

Performance curves at a constant AMR operating frequency of 0.4 Hz and a hot reservoir temperature of approximately 295.7 K ( $T_{\text{bath}} = 295.15$  K) are shown in Fig. 91. The evaluation of the physical properties of the Gd spheres revealed a Curie temperature around 290 K (see Fig. 120), so a better performance of the machine can be expected at these operating conditions. In these experiments, volumetric flow rates of 100, 125 and 150 L/h ( $\phi = 0.47, 0.58$  and 0.70, respectively) were held constant while the thermal load was increased gradually until steady state was attained at the desired  $\dot{Q}_C$ . At 150 L/h ( $\phi = 0.70$ ), the system was capable of providing a cooling capacity of 62.5 W while holding a regenerator temperature span of 6.1 K.

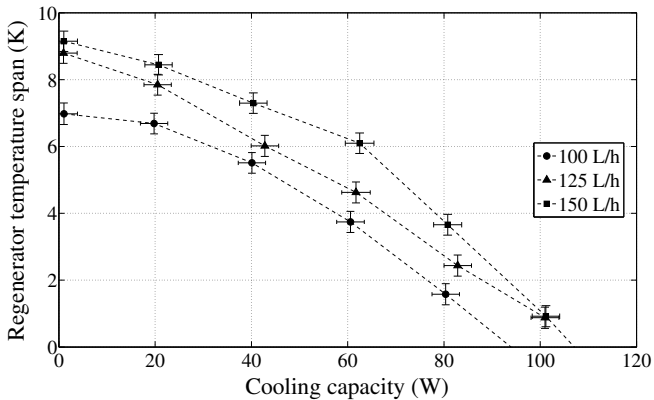


Figure 91 – Performance curves for different volumetric flow rates at an operating frequency of 0.4 Hz and hot reservoir temperature of approximately 295.7 K.

The performance curves in Fig. 91 are in good agreement with those normally found in the literature. For an AMR working at low temperature spans around the Curie temperature of the mag-

netocaloric material, the cooling capacity is usually large because the MCE of the material is also large for both magnetization and demagnetization at these temperatures (Chapter 3). On the other hand, if a large temperature span is desired, the cooling capacity will be reduced because the MCE is likely to be small at the temperatures corresponding to the ends of the regenerator. In theory, the magnetic circuit operates approximately at the room temperature ( $\sim 293.15$  K). At the conditions of very low temperature span in Fig. 91, it may be possible that the regenerator was slightly warmer than the magnetic circuit and the surrounding air and, as a result, heat transfer from the regenerator to its surroundings could have contributed to the increase in cooling capacity at very small temperature spans (see, for instance, the performance curve for 125 L/h).

Fig. 92 shows the behavior of the system temperature span ( $\Delta T_{\text{sys}}$ ) as a function of the regenerator temperature span ( $\Delta T_{\text{reg}}$ ) for the experiments presented in Fig. 91. As the cooling capacity is increased and the temperature spans decrease, the difference between them increases, which is clear evidence of the increase in heat transfer irreversibilities in the cold heat exchanger. The small difference between the spans in the no-load situation is likely due to parasitic losses (e.g., friction, heat leaks).

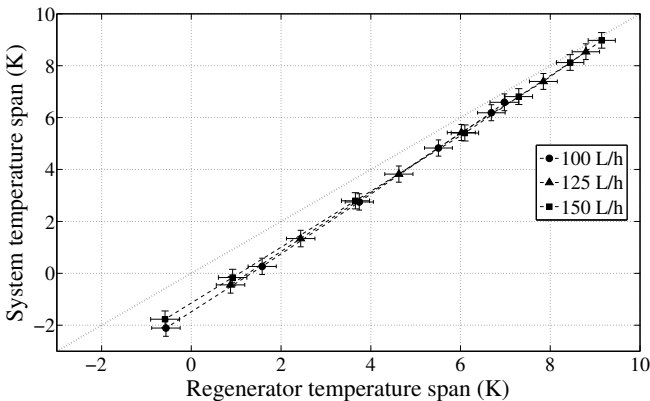


Figure 92 – System temperature span ( $\Delta T_{\text{sys}}$ ) as a function of the regenerator temperature span ( $\Delta T_{\text{reg}}$ ) for the experimental data of Fig. 91. The dotted line represents the specific case where  $\Delta T_{\text{sys}} = \Delta T_{\text{reg}}$ .

The dependence of the no-load regenerator temperature span on the utilization ( $\phi$ ) was investigated for two conditions: (i) fixed volumetric flow rate and (ii) fixed operating frequency, both for a

constant hot reservoir temperature of approximately 295.7 K (Fig. 93). In the former scenario, the flow rate was held at 150 L/h and the operating frequency was varied from 0.2 to 1.4 Hz ( $\phi = 1.43$  to 0.20, respectively). A peak on the regenerator temperature span of 12.0 K was found at 1 Hz ( $\phi = 0.28$ ). In the latter case, the operating frequency was held fixed at 0.8 Hz and the fluid flow rate was varied from 50 to 175 L/h ( $\phi = 0.12$  to 0.40) and a peak on  $\Delta T_{\text{reg}}$  of 11.7 K was found at  $\phi = 0.40$ .

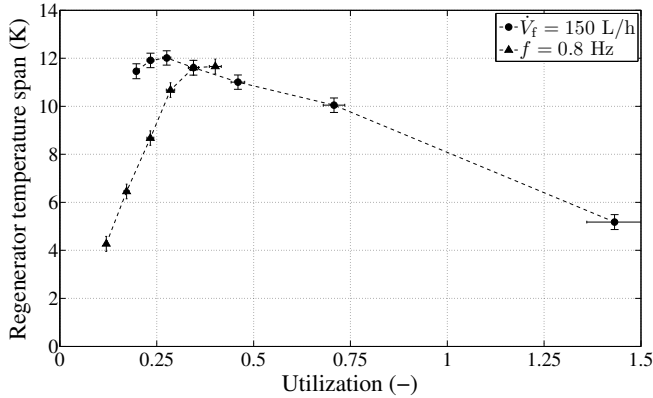


Figure 93 – No-load regenerator temperature span dependence on the utilization when the frequency and flow rate are varied for a hot reservoir temperature of approximately 295.7 K.

The influence of the hot reservoir temperature on the regenerator temperature span for an applied thermal load of 60 W was evaluated at an operating frequency of 0.8 Hz and different volumetric flow rates of 150, 175 and 200 L/h ( $\phi = 0.35$ , 0.41 and 0.47, respectively), as seen in Fig. 94. The hot reservoir temperature was varied gradually from approximately 290.2 to 301.8 K ( $T_{\text{bath}}$  from 289.15 to 301.15 K, respectively). The curves resemble that for the MCE of Gd, but with peaks at higher temperatures. This is probably due to the maximization of the MCE over the entire regenerator as the average temperature between the hot and cold ends approached the Gd Curie temperature (Trevizoli *et al.*, 2011). For instance, the peak of the regenerator temperature span was 8.2 K for a volumetric flow rate of 200 L/h and a hot reservoir temperature of 296.1 K.

Fig. 95 shows the performance curves for an operating frequency of 0.8 Hz, a hot reservoir temperature of approximately 294.1 K and different volumetric flow rates of 150, 175 and 200 L/h ( $\phi =$

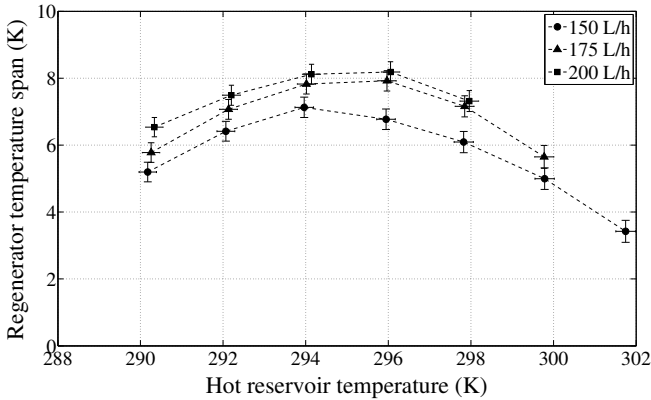


Figure 94 – Regenerator temperature span as a function of the hot reservoir temperature for a thermal load of 60 W, operating frequency of 0.8 Hz and volumetric flow rates of 150, 175 and 200 L/h ( $\phi = 0.35, 0.41$  and  $0.47$ , respectively).

0.35, 0.41 and 0.47, respectively). Due to pressure drop limitations, the fluid flow rate was not raised above 200 L/h. Like the results in Fig. 91, the regenerator temperature span was observed to increase with the flow rate irrespective of the cooling capacity. The maximum no-load  $\Delta T_{\text{reg}}$  was 10.6 K, while the maximum zero-span cooling capacity was 150.0 W, both at 200 L/h. At a cooling capacity of 80.4 W the regenerator was able to sustain a temperature span of 7.1 K, also at 200 L/h. It is important to point out that the interpolated maximum system capacity ( $\Delta T_{\text{sys}} = 0$ ) was approximately 139.8 W. The behavior of the system temperature span ( $\Delta T_{\text{sys}}$ ) as a function of the regenerator temperature span ( $\Delta T_{\text{reg}}$ ) for the experiments of Fig. 95 are shown in Fig. 96.

The dependence of the regenerator temperature span on the AMR operating frequency between 0.4 and 1.6 Hz ( $\phi = 0.70$  and 0.18, respectively) was evaluated for an applied thermal load of 60 W and the results are shown in Fig. 97. The experiments were carried out for a volumetric flow rate of 150 L/h and a hot reservoir temperature of approximately 296.0 K ( $T_{\text{bath}} = 295.15$  K). A peak of the  $\Delta T_{\text{reg}}$  was found at 7.1 K for a frequency of 1.4 Hz ( $\phi = 0.20$ ).

Fig. 98 shows typical measurements of torque ( $\tau$ ) and motor power ( $W_M$ ) as a function of time during steady-state operation for a frequency of 1.4 Hz (Fig. 97). The time dependence of these

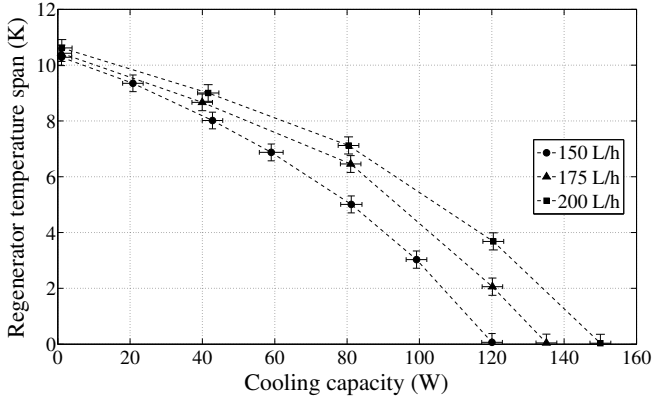


Figure 95 – Performance curves for different volumetric flow rates at an operating frequency of 0.8 Hz and an average hot reservoir temperature of approximately 294.1 K.

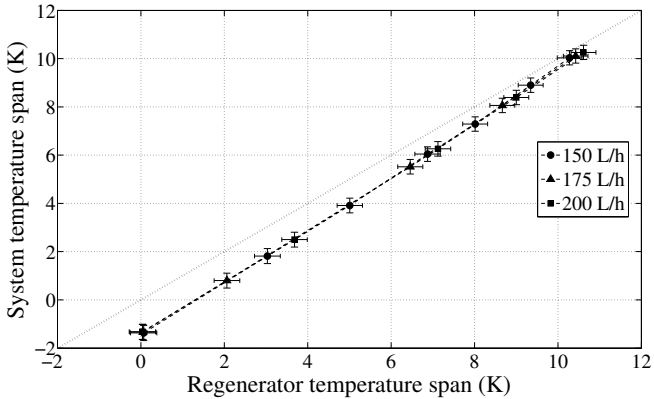


Figure 96 – System temperature span ( $\Delta T_{\text{sys}}$ ) as a function of the regenerator temperature span ( $\Delta T_{\text{reg}}$ ) for the experimental data of Fig. 95. The dotted line represents the specific case where  $\Delta T_{\text{sys}} = \Delta T_{\text{reg}}$ .

two parameters is intrinsic to the regenerator configuration due to the discretization of the regenerator beds and the forces required to magnetize and demagnetize each one of them. However, this alternating torque generated in the regenerator is somewhat obscured by the friction forces in the rotary valves, which demand a more continuous torque from the motor.

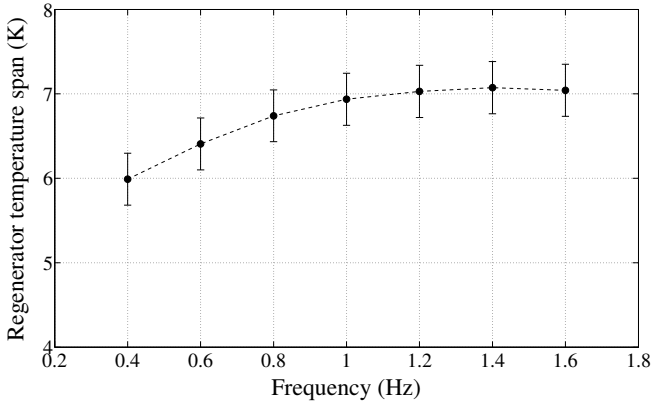


Figure 97 – Regenerator temperature span dependence on the AMR operating frequency for a thermal load of 60 W, a volumetric flow rate of 150 L/h and hot reservoir temperature of approximately 296.0 K ( $T_{\text{bath}} = 295.15$  K).

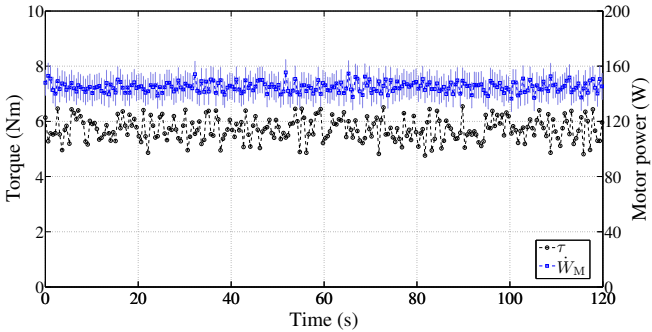


Figure 98 – Typical measurements of torque ( $\tau$ ) and motor power ( $\dot{W}_M$ ) at steady state for a frequency of 1.4 Hz and cooling capacity of 60 W.

The measurement uncertainties in Fig. 98 are presented as error bars and calculated, as will be seen, from Eqs. (C.6) and (C.5). The time-averaged torque,  $\bar{\tau}$ , and motor power,  $\bar{\dot{W}}_M$ , as a function of the operating frequency are shown in Fig. 99. These experiments correspond to the conditions of Fig. 97. Since these parameters varied with time, their standard deviations ( $\sigma$ ) are also presented in Fig. 99. From the time-averaged torque was calculated a transmis-

sion system power defined as  $\dot{W}_{\text{tr}}(\bar{\tau}) = \omega\bar{\tau} = 2\pi f\bar{\tau}$ , and the results are also shown in Fig. 99 as filled triangles.  $\dot{W}_{\text{tr}}(\bar{\tau})$  is equivalent to the power required to drive the transmission system with an ideal motor for each operating frequency. The transmission system includes the main components, such as the magnetic interaction to rotate the rotor within the regenerator beds and to operate the rotary valve system. It is worth mentioning that the torque transducer was placed on the motor shaft (Fig. 76), whose rotation frequency is equal to the AMR operating frequency. As the frequency increases, the magnetic circuit rotation inertia becomes higher, which reduces the average torque required to rotate the motor. On the other hand, the motor power increases proportionally to the operating frequency. The actual motor power accounts for electrical and mechanical internal losses, more specifically in the frequency inverter and gear couplings, respectively. Those losses are responsible for the large difference between the actual motor power,  $\dot{W}_{\text{M}}$ , for which the electrical motor is over-dimensioned for the actual operating conditions, to the transmission power,  $\dot{W}_{\text{tr}}$ , which represents the power that would be required by an ideal motor operating the actual AMR system at each corresponding frequency.

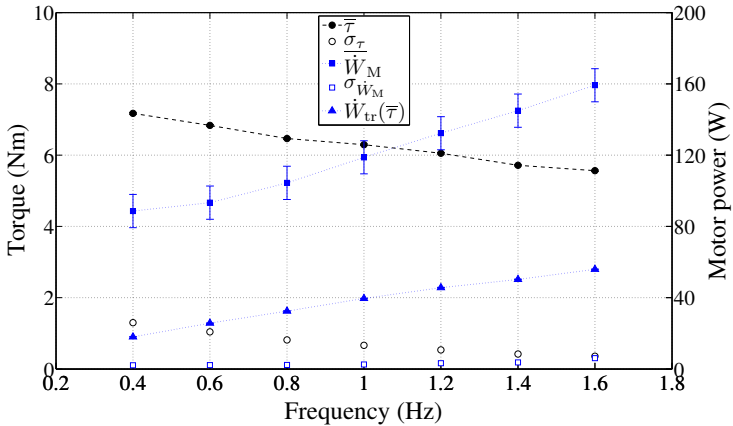


Figure 99 – Time-averaged torque,  $\bar{\tau}$ , and motor power,  $\dot{W}_{\text{M}}$ , as well as, their corresponding standard deviations ( $\sigma$ ) and the calculated transmission system power,  $\dot{W}_{\text{tr}}(\bar{\tau})$ , as a function of the operating frequency.

## 5.4 PERFORMANCE EVALUATION RESULTS

The thermodynamic performance of the device was evaluated in terms of the coefficient of performance (COP) and the overall second-law efficiency ( $\eta_{2nd}$ ). The actual COP is calculated based on Eq. (2.11), where  $\dot{Q}_C$  corresponds to the thermal load imposed by the electric heater at the cold heat exchanger and  $\dot{W}_M$  is the plug-power of the electrical motor. These two parameters are experimentally measured by the power transducers. Conversely, due to the manual bypassing of the fluid to set the volumetric flow rate, the fluid pumping power,  $\dot{W}_P$ , is calculated based on Eq. (4.4), where  $\dot{W}_{visc}$  represents the viscous power of the working fluid through the regenerator beds (Eq. (4.3)) and the pump discharge pressure is assumed equal to the system pressure drop,  $\Delta p_P \simeq \Delta p_{sys}$ . An overall pump efficiency,  $\eta_{OP}$ , was assumed equal to 0.7.

Fig. 100 shows the calculated COP as a function of the regenerator temperature span for several selected thermal loads and positive-span experiments. It can be inferred that the actual COP increases at higher thermal loads but at the expense of lower temperature spans. The average motor power for experiments at 0.4 and 0.8 Hz were 88.8 and 106.4 W, respectively. The average calculated pumping power for experiments at 150 and 200 L/h were 19.5 and 43.3 W, respectively. For instance, an experiment with an operating frequency of 0.8 Hz, a fluid flow rate of 175 L/h, a  $T_H$  of 294.1 K, a  $\dot{Q}_C$  of 81.0 W produced over a  $\Delta T_{reg}$  of 6.5 K and a COP of 0.58.

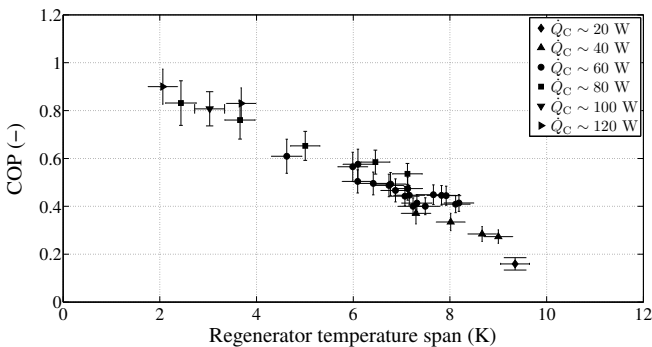


Figure 100 – Calculated COP results as a function of the temperature span for some of the non-zero thermal load and positive temperature span experiments.

The overall second law efficiency is calculated as the ratio of

the actual and ideal COP using Eq. 2.14. Fig. 101 shows the results for the calculated  $\eta_{2\text{nd}}$  as a function of the regenerator temperature span for the experimental results presented in Fig. 100.  $\eta_{2\text{nd}}$  accounts for all losses and quantifies the actual performance of the system in comparison with an ideal (Carnot) system operating between the same environment temperatures. The maximum value of  $\eta_{2\text{nd}}$  obtained for the present system was 1.16% for an experiment at an operating frequency of 0.8 Hz, fluid flow rate of 200 L/h, cooling power of 80.4 W,  $T_{\text{H}}$  of 294.1 K and  $\Delta T_{\text{reg}}$  of 7.1 K, where the calculated COP and  $\text{COP}_{\text{id}}$  were 0.54 and 45.99, respectively.

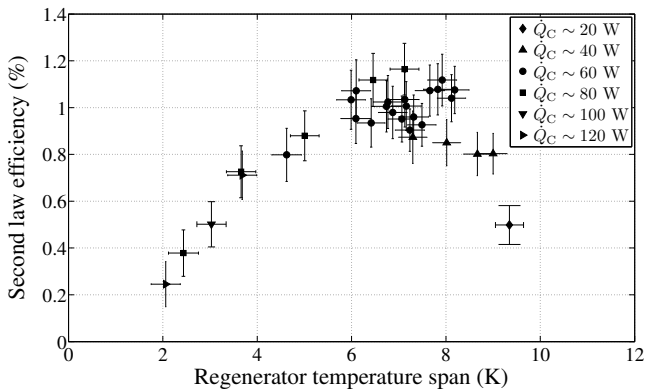


Figure 101 – Calculated  $\eta_{2\text{nd}}$  as a function of the corresponding temperature span for the experimental results presented in Fig. 100.

Fig. 102 shows the results of the calculated COP and  $\eta_{2\text{nd}}$  as a function of the time-averaged actual motor power,  $\overline{W}_{\text{M}}$ , at different operating frequencies. The regenerator temperature span, torque and motor power for this set of experiments were presented in Figs. 97 and 99, respectively. The performance of the system in terms of COP or  $\eta_{2\text{nd}}$  is quite similar, i.e., it decreases as the operating frequency increases. This is probably related to the dependence of the motor power on the frequency (Fig. 99). The actual motor is oversized for the conditions investigated, and the motor power represents a large portion in the input electricity to run the system. A more detailed study of performance dependence on torque and motor power breakdown of the present system is left for a further work.

The estimated performance, in terms of the COP and the  $\eta_{2\text{nd}}$ , that the actual AMR system would have in the case of employing

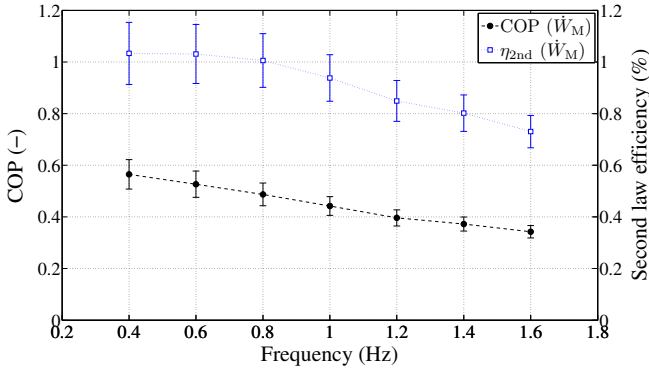


Figure 102 – Calculated COP and  $\eta_{2nd}$  as a function of the actual motor power,  $\dot{W}_M$ , at the operating frequencies for the experimental results presented in Fig. 97.

an ideal motor,  $\dot{W}_{tr}$ , for each operating frequency is presented in Fig. 103. The large increase in the device performance when employing an appropriate electrical motor for each set of operating conditions is due to the removal of the electrical and mechanical losses inherent to the actual over-dimensioned motor. The performance improvements by substituting the actual motor for a more appropriate motor at certain specific operating conditions would result in gains between 2.3 to 2.9 times the actual COP and  $\eta_{2nd}$ .

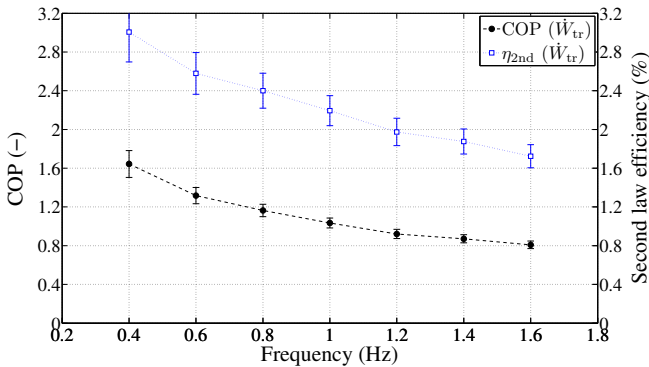


Figure 103 – Calculated COP and  $\eta_{2nd}$  as a function of the transmission power,  $\dot{W}_{tr}$ , at the operating frequencies for the experimental results presented in Fig. 97.

A summary of selected experimental results generated in this thesis and their calculated performance is presented in Table 15.

Table 15 – Summary of selected experimental results and their calculated performance.

$f$ (Hz)	$\dot{V}_f$ (L/h)	$\phi$ (–)	$T_H$ (K)	$\dot{Q}_C$ (W)	$\Delta T_{\text{reg}}$ (K)	$\dot{W}_M$ (W)	$\dot{W}_P$ (W)	COP (–)	$\eta_{2\text{nd}}$ (%)
1.4	151.7	0.20	296.0	61.6	7.1	145.0	20.7	0.37	0.80
0.8	174.2	0.41	296.0	61.0	7.9	108.1	29.3	0.44	1.12
0.8	201.5	0.47	294.2	80.4	7.1	106.5	43.7	0.54	1.16
0.4	150.0	0.70	295.8	62.5	6.1	89.5	19.1	0.58	1.07
0.8	176.6	0.41	294.1	81.0	6.5	107.5	31.1	0.58	1.12
0.8	151.7	0.36	294.0	81.2	5.0	103.8	20.7	0.65	0.88
0.4	150.5	0.70	295.9	80.8	3.7	87.6	18.6	0.76	0.73
0.8	200.4	0.47	294.3	120.4	3.7	103.0	42.1	0.83	0.71

## 5.5 SUMMARY

The experimental results obtained with the UFSC rotary magnetic refrigeration system are yet modest in comparison with other state-of-the-art magnetic refrigerators and with established cooling technologies. Improvements in the experimental performance and efficiency are expected at higher fluid flow rates and operating frequencies. It has been demonstrated that there is still room for improvements, specially regarding the regenerator configuration, for which a decrease in pressure drop, a better insulation with the magnet and the inclusion of a flow-mixture chamber is fundamental to enhance the AMR performance. Additionally, the asymmetry between the high and low field regions of the magnetic profile is detrimental to the AMR performance due to the existence of a no-flow period subjected to thermal conduction in the regenerator. Ways to improve the performance of the device are currently being sought and will be the subject of further studies.



## Chapter 6

# PERFORMANCE ANALYSIS OF THE DTU MAGNETIC REFRIGERATOR

Part of this Ph.D. thesis was carried out at the Technical University of Denmark (DTU). During this internship, the author was part of a research team dedicated to the development, operation and analysis of the magnetic refrigerator prototype built at the Energy Conversion Department, Risø Campus. This prototype is referred to as the Danish system in Section 2.5.1. The research activities were supervised by Drs. Christian Bahl and Kurt Engelbrecht. An extended version of the present chapter was published in Ref. (Lozano *et al.*, 2013).

## 6.1 INTRODUCTION

The machine evaluated in this chapter consists of a concentric four-pole permanent magnet assembly (Bjørk *et al.*, 2010b) with a 24-bed regenerator rotating continuously inside the magnet gap. The magnetic refrigerator and its performance are described in detail in Refs. (Bahl *et al.*, 2011; Engelbrecht *et al.*, 2012; Bahl *et al.*, 2014; Lozano *et al.*, 2014). This chapter presents experimental data, numerical results obtained using the 1-D AMR model (Engelbrecht & Bahl, 2010) and a detailed assessment of the system thermodynamic performance over a range of operating conditions. A parametric study of the regenerator temperature span,  $\Delta T_{\text{reg}}$ , cooling capacity,  $\dot{Q}_C$ , coefficient of performance (COP) and system efficiency was carried out over a range of different hot reservoir temperatures, volumetric flow rates and cooling capacities. The power consumption associated with several components were measured, which prompted new methods for improving the system performance and increasing its efficiency. A detailed thermal analysis of several system components was applied to improve agreement between the model and the experiments. The performance of the system was evaluated in terms of the COP, the exergetic-equivalent cooling capacity ( $Ex_Q$ ), and the overall second law efficiency,  $\eta_{2\text{nd}}$ .

## 6.2 EXPERIMENTAL WORK

The rotary AMR device consists of 24 Gd-sphere packed regenerators which rotate inside a four-pole static permanent magnet assembly. Table 16 presents the specifications of the AMR device. The 100-mm long regenerator beds, fabricated in nylon, were packed with Gd spheres sieved to diameters between 0.25 and 0.8 mm with a porosity of 0.36. The permanent magnet generates a maximum magnetic flux density of 1.24 T in the four high field regions and approximately 0 T in the four low field regions (also described in Section 2.7.5) (Björk *et al.*, 2011). The heat transfer fluid is a mixture of 20% automotive antifreeze (ethylene glycol) and 80% water (vol.). The antifreeze contains corrosion inhibitors that protect the Gd regenerator and lower the freezing temperature of the fluid. Thermal load is applied to the system at the cold end by an electric resistance heater. The experiments presented in this chapter were performed with an operating frequency of 1.5 Hz at a room temperature,  $T_R$ , of around 295 K. The hot reservoir temperature is set by a chiller connected to the AMR via a brazed plate heat exchanger. The temperature of the fluid is measured by four type E thermocouples at the hot in, hot out, cold in and cold out ports of the regenerator, respectively. These thermocouples are located directly upstream or downstream of the flow distributor, depending on flow direction. The thermocouples are positioned at approximately 200 mm from the edge of the permanent magnet and are not affected by the magnetic field (Fig 104).

The volumetric flow rate is measured at the hot and cold ends after the thermocouples by a Burket Type 8081 fluid flow meter. The volumetric flow rate is controlled by a manual valve that allows bypassing the fluid across a constant flow rate pump. The rotary valves have a contacting interface with small clearances between the rotating cylinder and valve openings. Valves are sealed by dynamic lip seals. The flow distributors are designed such that approximately in any given time eight beds are closed to fluid flow, while eight are experiencing flow from the hot to the cold end, and eight are experiencing flow from the cold to the hot end. At steady state, the cooling capacity of the device is the measured electrical power (cooling load) supplied to the resistance heater connected to the cold reservoir (Fig 104). The motor power consumption is measured by an Elmet-Pico power multimeter at the electrical plug of the frequency converter. The fluid flow distributor does not use a type of face seal that allows some internal leakage in the distributor. The

Table 16 – Specifications of the DTU rotary AMR.

Property	Value	Units
Magnetic poles	4	-
Magnetic field	1.24	T
Number of regenerators	24	-
Regenerator length	100	mm
Regenerator width	12.5	mm
Regenerator height	18.6	mm
Magnetocaloric material	Commercial Gd spheres	-
Sphere diameter	0.25 to 0.8	mm
Regenerator volume	23.3	cm <sup>3</sup>
Regenerator mass	0.118	kg
Total regenerator mass	2.8	kg
Operating frequency	0.25 to 10	Hz
Volumetric flow rate	50 to 600	L/h
Utilization factor	0.01 to 3.40	-

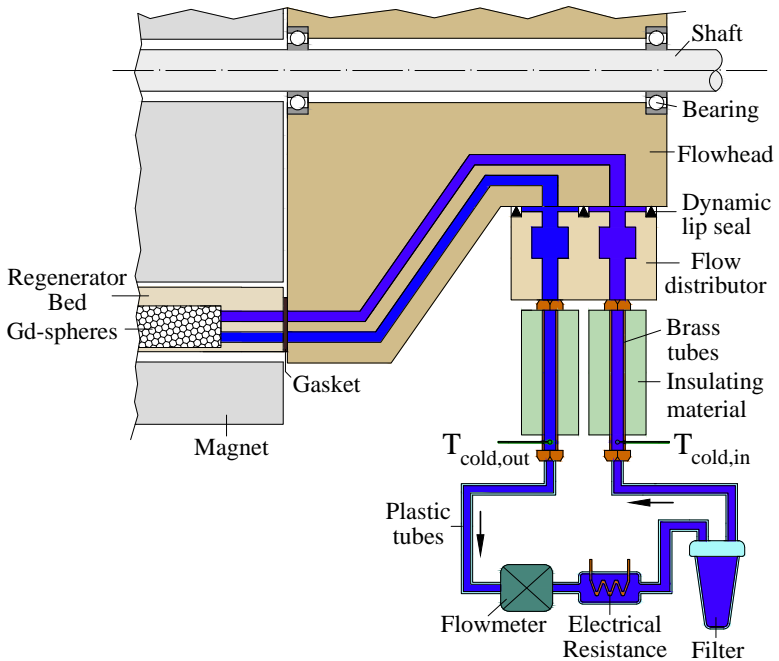


Figure 104 – Schematic representation of the cold end of the experimental device.

leakage causes fluid to bypass the regenerator directly on the hot end of the regenerator and to bypass the heater section on the cold end of the regenerator. Further details about the design, operation and experimental results can be found in Refs. (Bahl *et al.*, 2011; Engelbrecht *et al.*, 2012; Lozano *et al.*, 2014).

The regenerator temperature span is defined as the temperature difference between the time-averaged temperatures exiting the regenerator at the hot and cold ends. In this study, cooling loads of 200 and 400 W were applied to the system while varying the hot reservoir temperature and volumetric flow rate. The tests to determine the regenerator temperature span dependence on the hot reservoir temperature were performed at the 400 L/h volumetric flow rate (measured at the cold end). Alternatively, the tests to determine the regenerator temperature span as a function of the volumetric flow rate were carried out at a hot reservoir temperature of approximately 297.7 K.

The measurement uncertainty of the regenerator temperature span was estimated at approximately 1 K. This uncertainty is difficult to be determined because it depends on many factors, such as the intrinsic uncertainties in the temperature sensors themselves and change in flow conditions due to wearing of the sealing faces, parasitic losses and ageing of the plastic and materials.

## 6.3 MODELING

### 6.3.1 Numerical simulation

A detailed description of the model employed in this thesis was given in Section 2.6 and in Ref. (Engelbrecht, 2008). The model was adapted to describe the DTU device following the procedure described in Section 4.5.1 and Ref. (Engelbrecht & Bahl, 2010). A summary of the properties of the commercial Gd spheres implemented in the numerical model are presented in Table 17. The overall demagnetization factor calculated for the packed sphere regenerator beds was 0.365 based on Eq. (4.1).

The magnetic field profile as a function of the angular position in the gap was measured using a Hall probe inside the actual magnet. The temporal mass flow profile in each regenerator was calculated using the geometry of the flow distributors and flow inlets into the regenerator beds. However, the actual mass flow profile cannot be experimentally measured and may be slightly different for each regenerator bed due to variations in sphere packing and

Table 17 – Properties of the commercial Gd spheres implemented in the numerical model for the DTU device analysis.

Property	Value	Units
Sphere diameter	0.6	mm
Regenerator porosity	0.36	-
Density	7901	kg/m <sup>3</sup>
Thermal conductivity	11	W/(m·K)
Maximum $\Delta s_{\text{mag}}$ (at 288 K and 1 T)	3.2	J/(kg·K)
Maximum $\Delta T_{\text{ad}}$ (at 290 K and 1 T)	3.1	K
Regenerator demagnetization factor	0.365	-
Room temperature	295	K

flow path in each regenerator bed. Also, the small fluid leakage that occurs in both the hot and cold end flow distributors was ignored in the numerical model.

The steady-state temperature profile is determined by starting from a given temperature profile and stepping the governing equations forward until the temperature in every point of the regenerator is the same at the beginning and end of the cycle to within a numerical tolerance. The numerical mesh employed in the DTU device consisted of 40 spatial steps, 2000 time steps and a convergence tolerance of 0.00005.

The numerical model (Engelbrecht, 2008) considers only a porous regenerator subjected to a specified fluid flow in the presence of a varying magnetic field. It does not account for phenomena such as thermal and mechanical interaction with the polymer regenerator housing, heat losses from the regenerator to the ambient, or losses in the external tubing. In this thesis, losses to the ambient are post-calculated and subtracted from the cooling capacity predicted by the model. As will be seen, these losses to the ambient have a significant impact on the predicted performance and should be accounted for in a more detailed model of the AMR.

### 6.3.2 Analysis of parasitic losses

The entire system experiences thermal leakage either to the ambient in the form of heat losses or from the ambient in the form of an added cooling load, depending on the temperature of the specific part of the machine. Since the total area of tubing and flow distribution components is relatively large, it is important to predict the magnitude of the losses and to examine their impact on the

system performance. As mentioned above, the parasitic losses are post-calculated and subtracted from the predicted cooling capacity obtained by the 1-D AMR numerical simulation. This section discusses how losses from the various components are calculated. All losses are estimated based on correlations for simplified geometries available in the literature.

Using the electrical circuit analogy, a thermal resistance,  $\mathcal{R}$ , was calculated for each heat transport mechanism associated with each major component in the system:

$$\mathcal{R}_{\text{comp}} = \mathcal{R}_{\text{conv},i} + \mathcal{R}_{\text{cond}} + \frac{\mathcal{R}_{\text{conv},e} \mathcal{R}_{\text{rad}}}{\mathcal{R}_{\text{conv},e} + \mathcal{R}_{\text{rad}}} \quad (6.1)$$

where  $\mathcal{R}_{\text{cond}}$ ,  $\mathcal{R}_{\text{conv},i}$ ,  $\mathcal{R}_{\text{conv},e}$  and  $\mathcal{R}_{\text{rad}}$  are thermal resistances associated with the heat transport to the ambient due to conduction through the walls, internal and external convection and external radiation, respectively. It should be noted that the external convection and external radiation act in parallel with respect to the surface to ambient temperature difference. The thermal parasitic loss of each component,  $\dot{Q}_{\text{comp}}$ , is calculated as:

$$\dot{Q}_{\text{comp}} = \frac{T_{\text{R}} - T_{\text{C}}}{\mathcal{R}_{\text{comp}}}. \quad (6.2)$$

As shown in Fig 104, the cold end is composed mainly of a flowhead, a flow distributor, connecting tubes, and a filter. The experimental temperatures are measured downstream of the flow distributors, while the numerical model considers only the fluid temperature entering and exiting the regenerator bed ends. For modeling purposes, it was assumed that the fluid at the cold end has a uniform temperature throughout the cold end. For the calculation of thermal parasitic losses, a room temperature  $T_{\text{R}} = 295$  K was assumed, which is a close approximation to the average temperature for all experiments.

Brass tubes are used downstream of the flow distributor and plastic tubing are used upstream of it. In the experiments presented here thermal insulation was applied only to the brass tubes, while the remaining components at the hot and cold ends were not insulated. The thermal resistance of the tubes and filter at the cold end are calculated assuming that they behave as cylinders under free convection. The flowhead (fabricated in nylon) consists of 24 pairs of channels that allow the fluid flow from the beds into the flow distributor. Due to the relative complexity of the geometry, a 2D

numerical simulation was carried out in COMSOL (Multiphysics, 2008) to determine the heat transfer rate from the ambient to the cold fluid associated with a pair of channels, as shown in Fig. 104. It is assumed that each regenerator bed has the same inlet and outlet temperature and the difference between them is 1 K, which a typical value for regenerators investigated here. Since the inner diameter of the flowhead is quite large and not subjected to the ambient conditions, it is assumed adiabatic.

Several parasitic losses studies in AMR devices have shown that one of the main sources of irreversibility is the mechanical friction in the seals and bearings, which gives rise to inconsistency in experimental repeatability and represents a decrease in performance (Zimm *et al.*, 1998; Tura *et al.*, 2006; Arnold *et al.*, 2011).

In the present device, there is heating in the flow distributor due to friction between the dynamic lip seals and between the inner surface of the flow distributor with the outer surface of the flowhead. In order to calculate the heat generated at the seals, measurements of the motor power were performed with and without the flow distributor, for different frequencies at room temperature. The power consumption due to friction in the distributor was calculated as the difference between the motor power with and without the distributor.

In the numerical model the walls of the regenerator beds are considered adiabatic, but in reality there will be heat transfer to the ambient through the regenerator walls along the entire length of the regenerator. In this study, a calculation procedure to estimate the heat flow through the upper wall to or from the ambient is proposed. Since the regenerator beds are rotating in the gap of the concentric magnets, forced convection can be assumed to take place in the gaps around the regenerator beds. The distance between the beds and the magnets is much smaller than the diameter of the magnet, so a parallel-plate geometry, for which the laminar flow Nusselt number is 7.54, is assumed. It is important to note that there is a temperature gradient inside the beds in the axial direction. Therefore, thermal losses in the regenerator beds were calculated by the integral of the thermal gradient along the regenerator bed. Because of its relatively high thermal conductivity, the temperature of the magnet is assumed equal to that of the ambient. Heat transfer was only assumed to occur through the upper wall of the regenerator beds, while the remainder of their surface area was assumed adiabatic because the nylon wall thickness is larger in those places and

the inner diameter is not exposed directly to ambient.

Other parasitic losses were disregarded, such as those due to eddy currents in the Gd beds that are constantly magnetized and demagnetized. However, the total power due to eddy currents in the spheres is expected to be small in comparison with the cooling capacity of the AMR device because of the small particle size.

## 6.4 PERFORMANCE METRICS

The COP is defined as the ratio between the cooling capacity and the power consumption of the system. According to Gonçalves *et al.* (2011), the system COP can be calculated as the following product:

$$\text{COP} = \text{COP}_{\text{id}} \cdot \eta_e \cdot \eta_{\text{cy}} \cdot \eta_{\text{P}} \cdot \eta_{\text{ME}} \quad (6.3)$$

where the factors in Eq. (6.3) are detailed below. By definition, the actual COP can be calculated through Eq. (2.11), while the COP of an ideal refrigerator device,  $\text{COP}_{\text{id}}$ , is defined by Eq. (2.12) and it can be calculated in terms of the hot and cold environment temperatures using Eq. (2.13).

In order to account for external irreversibilities associated with hot and cold heat exchangers, the external thermodynamic efficiency can be defined as:

$$\eta_e = \frac{\text{COP}_{\text{id,e}}}{\text{COP}_{\text{id}}} \quad (6.4)$$

where  $\text{COP}_{\text{id,e}}$  is the Carnot COP calculated using the temperatures of the heat exchangers as follows:

$$\text{COP}_{\text{id,e}} = \frac{T_{\text{C}} - \Delta T_{\text{C}}}{(T_{\text{H}} + \Delta T_{\text{H}}) - (T_{\text{C}} - \Delta T_{\text{C}})} \quad (6.5)$$

where  $\Delta T_{\text{H}}$  and  $\Delta T_{\text{C}}$  correspond to the finite temperature differences at the hot and cold heat exchangers, respectively, due to the finite area for heat transfer. Thus, when  $\Delta T_{\text{C,H}} \rightarrow 0$  the system is externally reversible as  $\eta_e \rightarrow 1$ . For a specific cooling capacity,  $\eta_{\text{id,e}}$  can be seen as the ratio of magnetic powers needed to magnetize

and demagnetize the material between the limits of the environment temperatures and the heat exchangers temperatures as follows:

$$\eta_e = \frac{\dot{W}_{id}}{\dot{W}_{mag}} \quad (6.6)$$

As mentioned above, in the device evaluated in this chapter,  $T_H$  is set by a chiller connected to a heat exchanger. On the cold side, the cooling load is provided by an electric heater.

The internal thermodynamic losses associated with the cooling cycle are calculated based on the viscous power of the working fluid,  $\dot{W}_{visc}$ , through the regenerator beds, Eq. (4.3), and the magnetic power,  $\dot{W}_{mag}$ . Therefore, the cycle efficiency,  $\eta_{cy}$ , can be defined as:

$$\eta_{cy} = \frac{\dot{W}_{mag}}{\dot{W}_{mag} + \dot{W}_{visc}} \quad (6.7)$$

Based on the definitions in Eqs. (2.12), (6.4) and (6.7), the cycle COP, which accounts for internal and external thermal losses in the cooling cycle is given by:

$$\text{COP}_{cy} = \text{COP}_{id} \cdot \eta_e \cdot \eta_{cy} = \frac{\dot{Q}_C}{\dot{W}_{visc} + \dot{W}_{mag}} \quad (6.8)$$

The mechanical losses associated with the pumping of the fluid, i.e., losses at the pump, are calculated based on the fluid pumping power,  $\dot{W}_P$ , defined by Eq. (4.4), and  $\dot{W}_{mag}$ . So a pumping efficiency,  $\eta_P$ , can be defined as:

$$\eta_P = \frac{\dot{W}_{mag} + \dot{W}_{visc}}{\dot{W}_{mag} + \dot{W}_P} \quad (6.9)$$

The power,  $\dot{W}_M$ , needed to overcome the magnetic torque and rotate the flow distributors is provided by an electric motor. Thus, the combined mechanical and electrical efficiency is given by:

$$\eta_{ME} = \frac{\dot{W}_P + \dot{W}_{mag}}{\dot{W}_P + \dot{W}_M} \quad (6.10)$$

where  $\dot{W}_M$  is made up of three parts, namely, the magnetic power,  $\dot{W}_{mag}$ , the power needed to rotate the flow distributors over the flowhead (which gives rise to the oscillating flow in the regenerator

beds) and overcome friction between their sliding surfaces,  $\dot{W}_{fl}$ , and the power associated with other mechanical losses (i.e., those which remain when the flow distributors are not in place and when the system is not loaded with magnetic material in the regenerators - e.g., gear coupling, belt drive, frequency inverter, etc),  $\dot{W}_{nl}$ . Thus,

$$\dot{W}_M = \frac{\dot{W}_{mag} + \dot{W}_{fl}}{\eta_M} + \dot{W}_{nl} \quad (6.11)$$

where  $\eta_M$  is the electric motor efficiency, assumed to be 0.8.

Experimentally the motor power,  $\dot{W}_M$ , is measured as the plug power consumed by the frequency inverter. The motor power is broken into three parts, as shown in Eq. 6.11 which allows the definition of two additional (hypothetical) performance factors. The  $COP_{AMR}$  is the COP of the actual AMR excluding mechanical and electrical losses external to the regenerator, but intrinsic to the actual driving system. Thus:

$$COP_{AMR} = \frac{\dot{Q}_C}{\frac{\dot{W}_{visc}}{\eta_{OP}} + \left( \frac{\dot{W}_{mag} + \dot{W}_{fl}}{\eta_M} \right)} \quad (6.12)$$

In contrast, the  $COP_{no-fl}$  is defined so that it takes into account all mechanical and electrical losses in the system, but *excludes* the losses associated with friction in the flow distribution system.

$$COP_{no-fl} = \frac{\dot{Q}_C}{\dot{W}_P + \dot{W}_M - \frac{\dot{W}_{fl}}{\eta_M}} \quad (6.13)$$

While  $COP_{AMR}$  excludes the losses that take place outside the regenerator,  $COP_{no-fl}$  accounts for the losses associated with friction in the flow distribution system which, as shown above, have been estimated experimentally in the present chapter.

#### 6.4.1 Exergetic-equivalent cooling capacity

Although the COP is widely used to compare refrigeration systems, it is of limited significance when the temperature span is not specified. The exergetic-equivalent cooling capacity, given by:

$$Ex_Q = \dot{Q}_C \left( \frac{T_H}{T_C} - 1 \right) \quad (6.14)$$

is an important parameter to quantify the performance of an AMR as it is directly proportional to the temperature span and cooling capacity, indicating that a high performance refrigerator is one in which a large thermal load is transferred to the hot thermal reservoir over a large temperature span (Rowe, 2011). Note that  $Ex_Q$  is not equal to the actual cooling capacity of the machine but it is equivalent to the reversible power input required to remove heat at a rate of  $\dot{Q}_C$  and reject it to the environment at  $T_H$ . In other words,  $Ex_Q = \dot{W}_{id}$  (Kanoğlu *et al.*, 2012).

### 6.4.2 Second-law efficiency

The second law (or exergy) efficiency,  $\eta_{2nd}$ , is defined as the ratio of the power consumed by the actual device to that of a reversible system within the same system temperature span associated with the hot and cold environments. In terms of the COPs, it is given by Eq. 2.14.

The second-law efficiency associated with the thermodynamic performance of the cooling cycle only,  $\eta_{2nd,cy}$ , takes into account the irreversibilities due to the viscous losses and magnetization and demagnetization process in the AMR. Thus,

$$\eta_{2nd,cy} = \frac{COP_{cy}}{COP_{id}} \quad (6.15)$$

allows for a comparison of the present system with different cooling technologies using the same thermodynamic baseline. Therefore, it helps to provide indications of where system improvements can be made.

## 6.5 RESULTS AND DISCUSSIONS

### 6.5.1 Parasitic losses

The motor power was measured at different operating frequencies and load conditions as follows: (i) with the regenerators and both flow distributors installed,  $\dot{W}_M$ ; (ii) with the regenerators, but without the flow distributors (see Fig. 104),  $\dot{W}_{no-fl}$ ; (iii) only with the frequency inverter that controls the motor,  $\dot{W}_{ni}$ . The friction loss associated with the flow distribution system is computed

as follows:

$$\frac{\dot{W}_{\text{fl}}}{\eta_{\text{M}}} = \dot{W}_{\text{M}} - \frac{\dot{W}_{\text{mag}}}{\eta_{\text{M}}} - \dot{W}_{\text{nl}} = \dot{W}_{\text{M}} - \dot{W}_{\text{no-fl}} \quad (6.16)$$

where the two terms on the right of the second equality are determined experimentally. It is important to point out that  $\dot{W}_{\text{M}}$  was measured for each experiment presented in this work as a function of the regenerator temperature span, while  $\dot{W}_{\text{no-fl}}$  and  $\dot{W}_{\text{nl}}$  were measured at an average temperature of 295 K at zero regenerator temperature span as it is impossible to maintain a temperature gradient across the regenerator without the flow distributors. As can be seen from Fig. 105,  $\dot{W}_{\text{fl}}/\eta_{\text{M}}$  varies approximately linearly with frequency. The friction heat generated in the flow distributor is rejected to the working fluid, to the flow distributor housing and to the ambient. A full thermal analysis of the flow distributors was outside the scope of this thesis, so it was assumed that half the friction heat is transferred to the fluid. The heat load due to friction in the flow distributor which is transferred to the fluid at the cold end is calculated by  $\dot{Q}_{\text{fl}} = (13.2f - 2.5) \text{ W}$ , where  $f$  is the frequency. This equation corresponds to a linear fit of the experimental test results obtained at different frequencies. Since the experiments presented here were all carried out at 1.5 Hz, then the heat transferred to the fluid is assumed to be  $\dot{Q}_{\text{fl}}(f=1.5 \text{ Hz}) \simeq 17.3 \text{ W}$ . The assumption that half the heat is transferred to the fluid adds to the uncertainty of the thermal losses, which are discussed below.

The magnetic work,  $\dot{W}_{\text{mag}}$ , which includes magnetic parasitic losses, such as eddy currents, is estimated from the experimental results as follows:

$$\frac{\dot{W}_{\text{mag}}}{\eta_{\text{M}}} = \dot{W}_{\text{no-fl}} - \dot{W}_{\text{nl}} \quad (6.17)$$

It should be noted that the value of  $\dot{W}_{\text{mag}}$  estimated with this experimental procedure is not the actual magnetic work on the regenerator when either a temperature gradient in the matrix or a net cooling capacity are produced. This is because  $\dot{W}_{\text{no-fl}}$  and  $\dot{W}_{\text{nl}}$  were measured at a constant temperature in the regenerator (zero regenerator temperature span), thus taking into account only the effect of frequency. However, the error associated with this approximation is expected to be small since  $\dot{W}_{\text{mag}}/\eta_{\text{M}}$  is much smaller than  $\dot{W}_{\text{M}}$  (see Fig. 105).

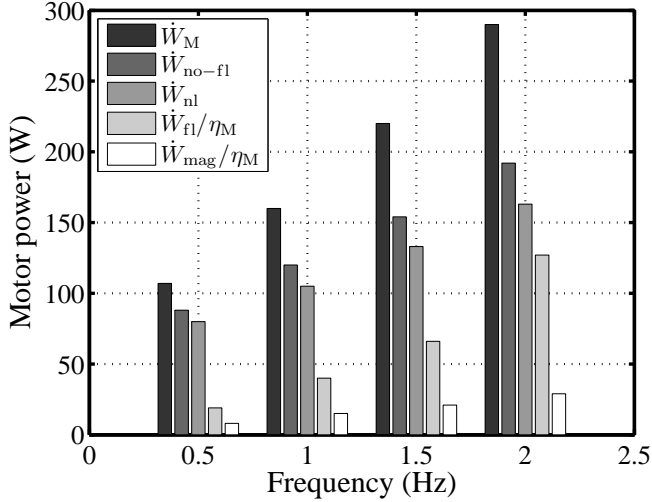


Figure 105 – Breakdown of the motor power for different operating frequencies. Measurements were performed at 295 K.

In Fig. 105,  $\dot{W}_{mag}/\eta_M$  is seen to be much smaller than the friction power loss in the flow distributor. For comparison purposes,  $\dot{W}_P$  at 1.5 Hz, calculated through Eq. (4.4), for  $\Delta T_{reg} = 10$  K and  $\dot{V}_f = 400$  L/h, is about 42 W.

The calculated thermal resistances for each component are summarized on Table 18. From a Computational Fluid Dynamics (CFD) analysis of the heat transfer in the flowhead, it was found that most of the heat is lost from the flow channel nearest the outer wall through the outer wall, to the ambient rather than conducted to the adjacent fluid stream. Since the flowhead is rotating with the regenerator and has a relatively large diameter, the heat transfer through its outer surface was modeled as forced convection over a flat plate. With this boundary condition the COMSOL simulation of the heat transfer in the fluid channels yielded an overall thermal resistance of 1.05 K/w in the flowhead.

The estimated parasitic losses associated with each component as a function of  $T_C$  is shown in Fig. 106 for  $T_R = 295$  K,  $T_H = 300$  K and  $f = 1.5$  Hz. The total heat loss,  $\dot{Q}_{total}$ , is calculated as the sum of all parasitic losses including  $\dot{Q}_{fl}$ , which is considered independent of  $T_C$ . As expected, thermal parasitic losses increase as  $T_C$  decreases and  $\Delta T_{reg}$  increases. When  $T_C$  is above room tempera-

Table 18 – Thermal resistances of the components at the cold end and the regenerator beds.

Component	Thermal Resistance (K/w)
Insulated brass tubes	9.21
Plastic tubes	1.84
Filter	1.66
Flowhead	1.05
Regenerator beds	0.54

ture, there are negative heat losses as the working fluid rejects heat to the ambient, which artificially increases the cooling capacity. The total parasitic losses at a regenerator temperature span of 25 K are estimated to be 74 W, a significant value which must be overcome by the AMR in order to maintain the temperature span.

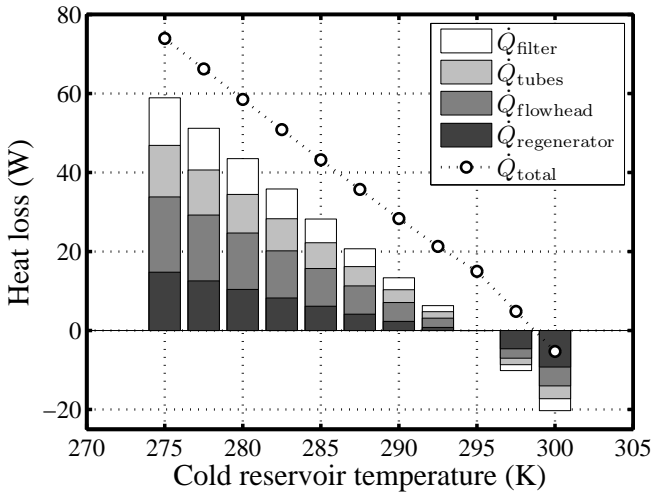


Figure 106 – Parasitic losses for the different components at different temperatures at the cold reservoir and an operating frequency of 1.5 Hz.  $\dot{Q}_{total}$  corresponds to the total parasitic losses including also  $\dot{Q}_{fl} = 17.3$  W.

When operating at high frequencies, the most important contribution to the parasitic losses is the flow distributor friction, which, in principle, is only a function of frequency. This contribution can be minimized with a new hydraulic design of the flow distribution system. Additionally, in order to achieve higher temperature spans

or cooling capacities, a good thermal insulation of the flowhead, tubes and filter should be implemented or, instead, these components should be redesigned to minimize the heat transfer area. The regenerator bed losses are more complicated to deal with because any increase in the wall thickness will reduce the amount of magnetized volume occupied by the regenerator. The regenerator wall also participate in the regeneration process as it is subjected to oscillating flow and temperature conditions. Improving the regenerator insulation involves a trade-off between the volume of magnetocaloric material and parasitic losses. However, this requires a more detailed analysis, which is outside the scope of this thesis.

Heat leaks at the hot end were also investigated. However, they are less important because the heat rejected at the hot end is not measured experimentally and is not a major performance parameter. Heat leaks from most of the hot end components can be viewed as additional heat exchanger area for heat rejection as they are at approximately the same temperature as the hot heat exchanger. The situation is also different at the hot end because the fluid is cooled by the ambient but heated by the flow distributor friction. The main concern from a modeling standpoint is that the experimental hot reservoir temperature may differ from the fluid temperature at the inlet of the regenerator. Because the hot reservoir temperature is measured before the fluid enters the flow distributor upstream the regenerator, there will be a difference between the measured hot reservoir temperature and that of the fluid entering the regenerator, which is the temperature needed in the numerical model. An analysis of heat losses at the hot end revealed that in the worst case scenario, i.e., when the hot reservoir temperature is 290 K, a loss of approximately 20 W from the fluid in the hot reservoir would take place. For a volumetric flow rate of 200 L/h, this loss results in a reduction of 0.09 K between the measurement point and the regenerator inlet, which is within the uncertainty of the thermocouple measurements. Therefore, hot end losses are not considered further.

### 6.5.2 Experimental results

The experimental study of the device consists of evaluating the regenerator temperature span,  $\Delta T_{\text{reg}}$ , as a function of the hot reservoir temperature,  $T_{\text{H}}$ , and the volumetric flow rate,  $\dot{V}_{\text{f}}$ , at different cooling (thermal) loads,  $\dot{Q}_{\text{C}}$ .

### 6.5.2.1 Hot reservoir temperature dependence

The influence of the hot reservoir temperature on the regenerator temperature span for cooling loads of 200 and 400 W was determined experimentally by varying the temperature in the control bath at the hot end. The experimental data are plotted in Fig. 107 and compared with the 1-D model results with and without the influence of the post-calculated parasitic losses. The experiments reported in Fig. 107 were carried out with a volumetric flow rate of 400 L/h ( $\phi$  is approximately 0.37, depending on the operating temperature), measured at the cold end. The regenerator temperature span corresponds to the temperature difference between the temperature of the fluid exiting the hot end and the temperature of the fluid exiting the cold end of the regenerator.

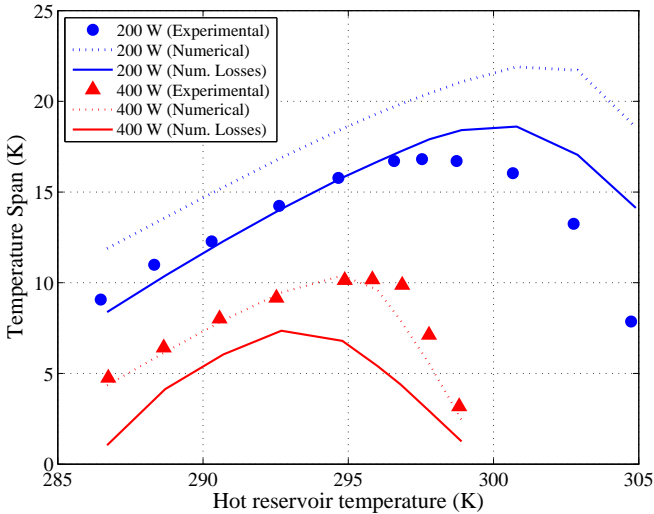


Figure 107 – Experimental data and numerical predictions of regenerator temperature span with and without the post-calculated parasitic losses for cooling loads of 200 and 400 W effect of hot reservoir temperature.

In Fig. 107, the shape and peak temperature of the  $\Delta T_{\text{reg}}$  curve as a function of  $T_{\text{H}}$  is related to the magnetocaloric properties of the refrigerant. As explained by Trevizoli *et al.* (2011), the maximum regenerator temperature span,  $\Delta T_{\text{reg,max}}$ , does not occur at the Curie temperature, but at a hot reservoir temperature above the Curie temperature. For cooling loads of 200 and 400 W,  $\Delta T_{\text{reg,max}}$

values of 16.8 K and 10.2 K were obtained for  $T_H$  of 297.7 K and 296 K, respectively. The dependence of the optimum hot reservoir temperature on cooling load shown in Fig. 107 can be explained by studying the operating temperatures of the regenerator. The optimum hot reservoir temperature for a given cold reservoir temperature is one that maximizes the magnetocaloric effect over the entire regenerator, which will generally occur when the Curie temperature of the material is near the midpoint between the hot and cold reservoir temperatures. As the cooling load increases, the cold reservoir temperature increases. As the cold reservoir temperature increases, the optimum hot reservoir temperature will decrease accordingly to keep the material's Curie temperature near the midpoint between the two reservoir temperatures.

As can be seen from Fig. 107, there is good agreement between model and experiment when  $T_H$  is below 300 K for a cooling capacity of 200 W. For higher values of  $T_H$ , the model underpredicts the experiment when thermal losses are included. However, when thermal losses are ignored, the model overpredicts the cooling capacity as would be expected. The reason for the discrepancy is not known, but it may be caused by variation in the friction heating in the flow distributors with varying temperature. Considering results when  $T_H$  is approximately 302 K, for example, the hot flow distributor will be at a higher temperature than other experiments, but the cold flow distributor will also be at a higher temperature than the 300 K case. If thermal expansion in the flow distributors and changing properties in the radial seals causes flow distributor friction to be reduced with increasing temperature, this could explain the reason that thermal losses seem to be overpredicted at higher  $T_H$  values.

Experimental results for a cooling capacity of 400 W differ somewhat significantly from the numerical results with post-calculated parasitic losses. Although no clear cause of the discrepancy has been identified, this may be due to a number of reasons. At a higher cooling capacity the device operates at a lower regenerator temperature span and a larger portion of the regenerator operates near the Curie temperature where the magnetocaloric effect is highest. Therefore the high cooling capacity experiments are more sensitive to material properties. Because the Gd used in the regenerator is commercial grade purchased from a commercial supplier it is possible that the average Curie temperature in the regenerator is different than small sample that was measured, causing the device to produce a higher cooling capacity than predicted at

a certain temperature range. Another area of uncertainty is the experimental characterization of the particle size distribution, which becomes more pronounced at higher cooling capacity conditions. An extended discussion on this issue will be presented in Section 6.5.3.

### 6.5.2.2 Volumetric flow rate dependence

In the second set of experiments, the hot reservoir temperature was kept approximately at 297.7 K and the volumetric flow rate was varied. The dependence of the latter on regenerator temperature span as well as the values predicted from the numerical model including the parasitic losses are plotted in Fig. 108. The regenerator temperature span increases with increasing volumetric flow rate. Due to working pressure limitations and internal leakage in the flow distribution system, it was not possible to operate the device at flow rates above 600 L/h.

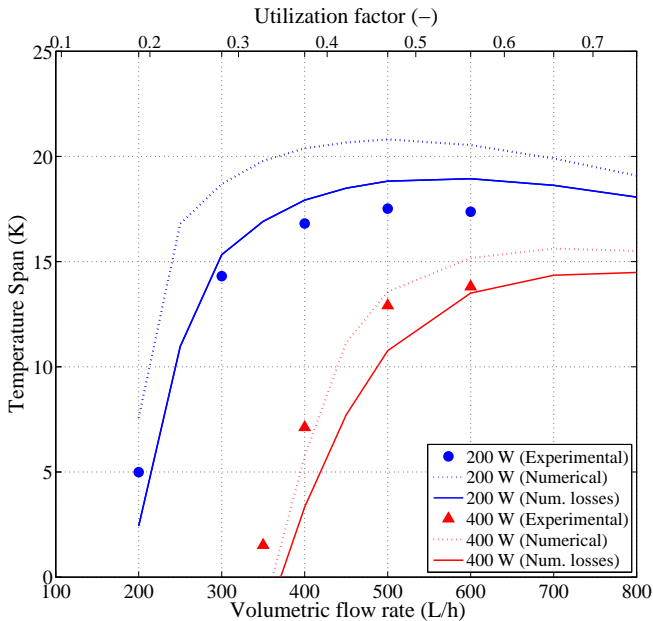


Figure 108 – Experimental data and numerical predictions of the regenerator temperature span with and without the post-calculated parasitic losses for cooling loads of 200 and 400 W effect of volumetric flow rate.

Based on results shown in Fig. 108, the regenerator temperature span is expected to continue to decrease at higher flow rates as viscous flow losses increase with the square of the flow rate for the 200 W case. A slight increase in regenerator temperature span for the 400 W case may be possible for higher flow rates, but the model predicts only a small increase regenerator temperature span at higher flow rates. As can be seen in the figure, there is good agreement between the experimental data and the model results. At lower volumetric flow rates, the numerical results underpredicts the performance while at higher volumetric flow rates the model overestimates the temperature span results. The highest experimental regenerator temperature spans at 200 W and 400 W were attained at 500 L/h and 600 L/h with values of 17.5 K and 13.8 K, respectively.

### 6.5.3 Inputs Sensitivity

Achieving excellent agreement between model and experiment is challenging due to the level of uncertainty associated with the input parameters. In the regenerator, each bed will experience a unique flow rate due to differences in flow resistances between the beds. The parasitic losses are based on simplified correlations; however, air flow and conditions in the room where the device is placed can change from day to day and even with the time of day, so the exact parasitic losses to the ambient may be highly variable and are difficult to predict accurately. The regenerator is modeled as a monodisperse matrix, but the actual regenerators contain a distribution of sphere sizes. It is also known that there is internal leakage in the flow distributor at the hot and cold side, which results in the actual flow rate in the regenerator being different than the flow rate that goes to the heater to accept a cooling capacity. There are many other uncertainties such as heat transfer in the packed bed, properties of the housing materials, etc. A thorough understanding of these effects is outside the scope of this thesis and, therefore, a more simplified approach is considered appropriate.

To estimate the effect of these uncertainties on the modeling results, a sensitivity study was performed and the results are summarized in Fig. 109. This figure shows two different cases; one case where the cooling capacity is 200 W and the volumetric flow rate is 400 L/h and the other where the cooling capacity is 400 W and the flow rate is 600 L/h. It can be seen that if the sphere diameters are changed within  $\pm 25\%$  the predicted regenerator temperature span will change  $\pm 12\%$  and  $\pm 20\%$  at 200 and 400 W cooling loads,

respectively. Conversely, if the total heat losses are increased by a factor of 1.25 the regenerator temperature span is decreased about 4%. The values in Fig. 109 will not be the same for each experimental condition, but they do give an estimate of how each uncertainty affects the results and what the modeling uncertainty is.

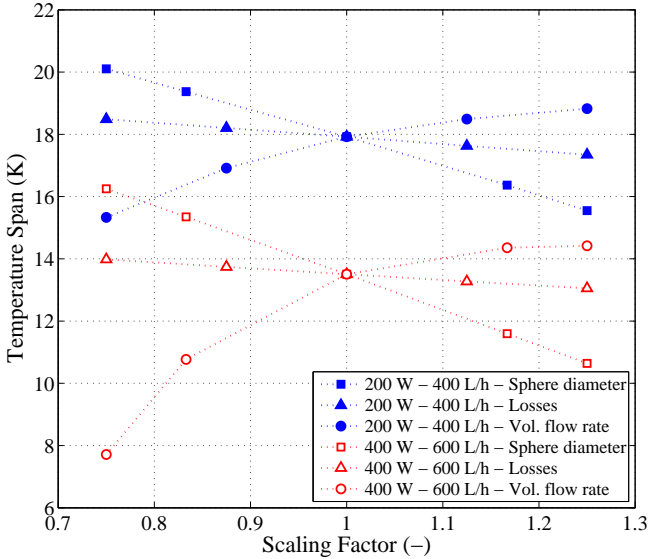


Figure 109 – Regenerator temperature span as a function of the scaling factor of the volumetric flow rate, total losses and sphere diameter for cases with volumetric flow rates of 400 L/h and 600 L/h and cooling capacity of 200 W and 400 W, respectively.

## 6.5.4 Performance evaluation results

### 6.5.4.1 COP analysis

The different COPs proposed in this work were calculated for all the experiments using Eqs. 6.3-6.13, where the cooling capacity  $\dot{Q}_C$  corresponds to the thermal load applied at the cold end by the electrical resistance heater. Figs. 110 and 111 show the results of COP,  $\text{COP}_{\text{no-fl}}$  and  $\text{COP}_{\text{AMR}}$  as a function of the hot reservoir temperature and the volumetric flow rate, respectively. The regenerator temperature span for each COP value corresponds to those plotted in Figs. 107 and 108.

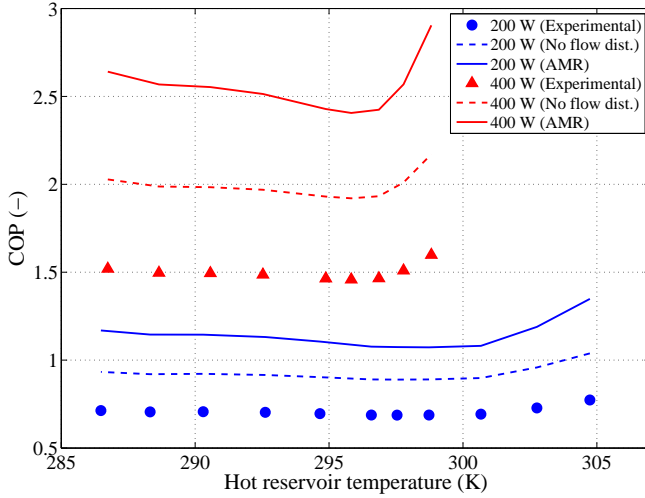


Figure 110 – Comparison of COP,  $COP_{no-fl}$  and  $COP_{AMR}$  as a function of the hot reservoir temperature for cooling loads of 200 W and 400 W.

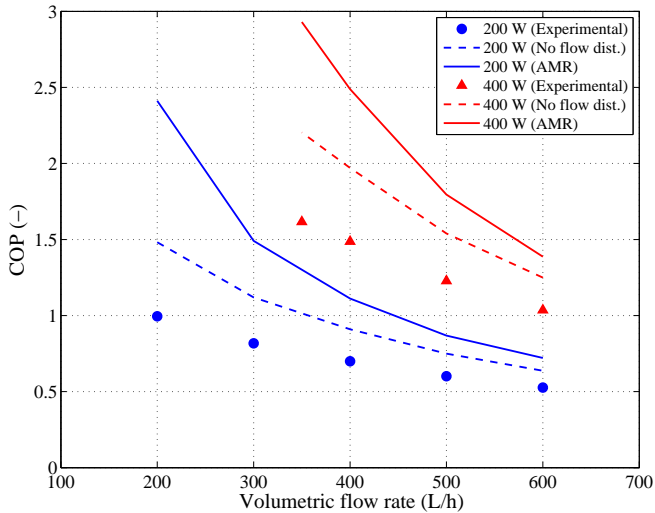


Figure 111 – Comparison of COP,  $COP_{no-fl}$  and  $COP_{AMR}$  as a function of the volumetric flow rate for cooling loads of 200 W and 400 W.

In Fig. 110, the (experimental) COP seems to be almost independent of the hot reservoir temperature, with average results for cooling capacities of 200 W and 400 W of 0.71 and 1.50 and maximum COP of 0.77 at  $T_H = 304.7$  K and 1.60 at  $T_H = 298.8$  K, respectively. However, the COP increases at higher hot reservoir temperatures probably due to a decrease in the power of the motor since the hot and cold ends are warmer (the regenerator temperature span is lower) and the gadolinium is less ferromagnetic. On the other hand, even though  $\Delta T_{\text{reg}}$  increases with  $\dot{V}_f$  (Fig. 108), the COP is inversely proportional to the volumetric flow rate, with a maximum of 1.00 at  $\dot{V}_f = 200$  L/h and  $\dot{Q}_C = 200$  W, and 1.62 at  $\dot{V}_f = 350$  L/h and  $\dot{Q}_C = 400$  W, as shown in Fig. 111.

From the results presented in Figs. 110 and 111 it can be inferred that an improvement of the performance of the system could be attained by reducing the power applied to the motor. The motor power is consumed by its internal losses, gear couplings, frequency inverter, belt drive, friction in the flow distributors and bearings and, to a lesser extent, by the magnetization and temperature change of the Gd with the fluid flow. Therefore, a hypothetical enhancement of the performance of this machine could be achieved with an improved design of the flow distributors. Assuming a new design with no friction in the flow distributors, the increase in COP can be as high as 24%, as shown in Figs. 110 and 111 for  $\text{COP}_{\text{no-fl}}$ .

The electrical motor is oversized in order to cover a broad range of experiments, with high torques at operating frequencies up to 10 Hz (Lozano *et al.*, 2014). In a real application, the motor would be selected for a specific narrow range of operating conditions of the AMR. Therefore, an estimate was made for the COP of an actual AMR using an appropriate motor to overcome the magnetic torque at a frequency of 1.5 Hz. Supposing the efficiency of an appropriate motor for these conditions is included in the calculated values from Eqs. 6.16 and 6.17, an average improvement of  $\text{COP}_{\text{AMR}}$  of 48% over  $\text{COP}_{\text{no-fl}}$ , with values of  $\text{COP}_{\text{AMR}}$  up to 3.5, can be accomplished if a high-efficiency motor is employed. In Figs. 110 and 111,  $\text{COP}_{\text{AMR}}$  is consistently higher than  $\text{COP}_{\text{no-fl}}$  because the motor losses are bigger than those in the flow distributors, as seen in Fig. 105.

A typical value of  $\text{COP}_{\text{cy}}$ , derived from the results presented in Section 6.5.1, for  $f = 1.5$  Hz,  $\dot{Q}_C = 400$  W,  $T_H = 295$  K,  $\Delta T_{\text{reg}} = 10$  K and  $\dot{V}_f = 400$  L/h, was calculated to be of about 8.6. It is worth mentioning that COP and  $\text{COP}_{\text{id}}$  for this case are 1.46 and 30.4, respectively, which represent a  $\eta_{2\text{nd}} = 4.8\%$  and a

$$\eta_{2\text{nd},\text{cy}} = 28.4\%.$$

### 6.5.4.2 Exergetic-equivalent cooling capacity

The exergetic-equivalent cooling capacity,  $Ex_Q$ , of the system as a function of the hot reservoir temperature and volumetric flow rate is shown in Figs. 112 and 113, respectively. The trend of  $Ex_Q$  as a function of the hot reservoir temperature resembles those reported in the literature (Russek *et al.*, 2010). For a volumetric flow rate of 400 L/h and cooling capacities of 200 and 400 W, the maximum  $Ex_Q$  obtained was 12.0 and 14.2 W, respectively. For a fluid flow rate of 600 L/h the  $Ex_Q$  was 19.4 W.

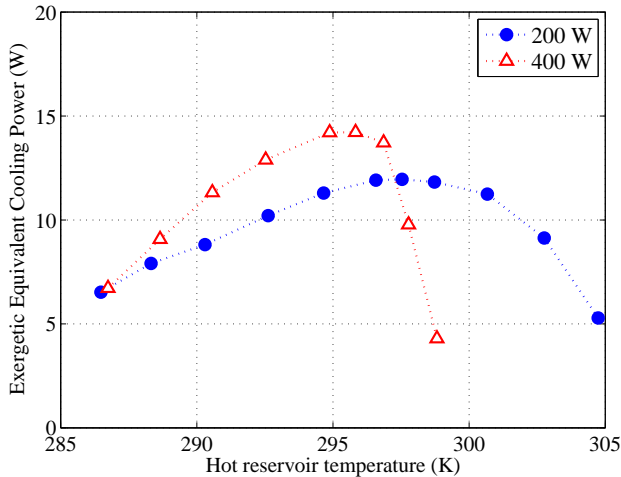


Figure 112 – Exergetic-equivalent cooling capacity as a function of the hot reservoir temperature for cooling capacities of 200 W and 400 W.

### 6.5.4.3 Second law efficiency

Overall and cycle second-law efficiencies as a function of the hot reservoir temperature and volumetric flow rate are presented in Figs. 114 and 115, respectively.

The results for the cycle second-law efficiency,  $\eta_{2\text{nd},\text{cy}}$ , somewhat mirrors the behavior of  $\Delta T_{\text{reg}}$  and  $Ex_Q$ , in the sense that it is high when  $\Delta T_{\text{reg}}$  is large. This is because the regenerator temperature span becomes small at high and low values of  $T_H$  and, in

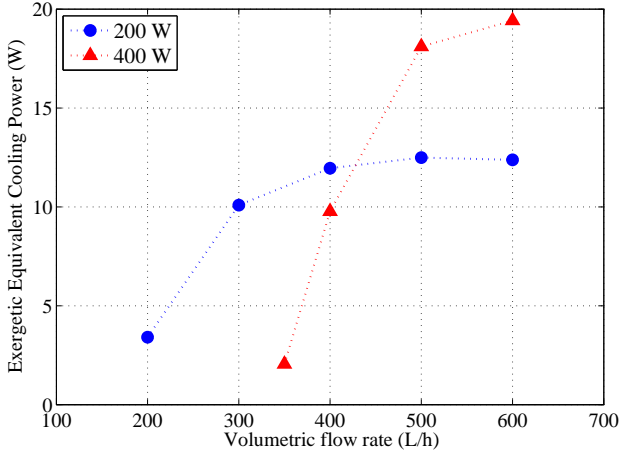


Figure 113 – Exergetic-equivalent cooling capacity as a function of the volumetric flow rate for cooling capacities of 200 W and 400 W.

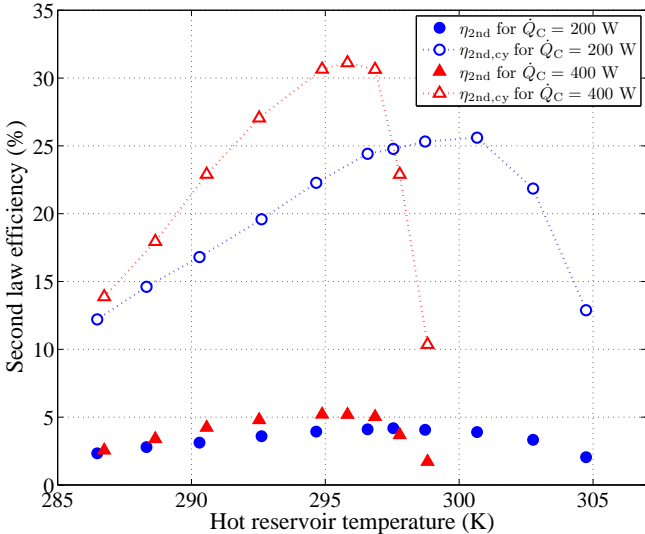


Figure 114 – Overall and cycle second-law efficiency as a function of the hot reservoir temperature for cooling loads of 200 and 400 W.

behaving as such, gives rise to high values of  $COP_{id}$  (see Eq. 2.13). At intermediate values of  $T_H$ ,  $\eta_{2nd,cy}$  becomes high due to the more

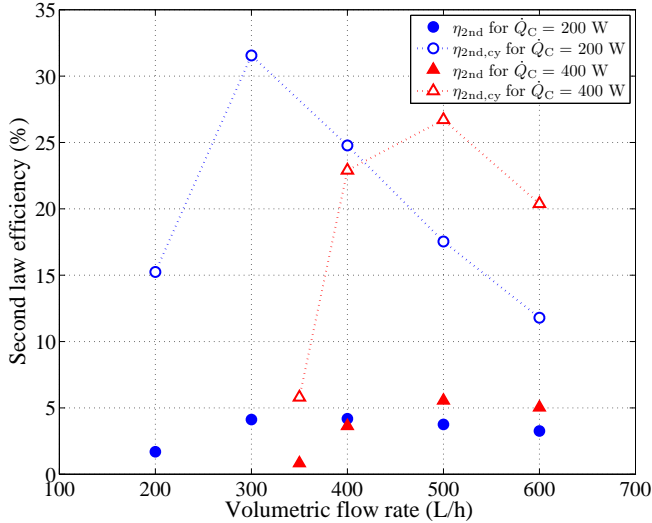


Figure 115 – Overall and cycle second-law efficiency as a function of the volumetric flow rate for cooling loads of 200 W and 400 W.

efficient conversion of magnetic work into cooling effect, which results in larger values of  $\Delta T_{reg}$ , and hence smaller values of  $COP_{id}$ .

The behavior of the overall second-law efficiency,  $\eta_{2nd}$ , is flatter due to the mechanical losses which are less dependent on  $T_H$  and  $\dot{V}_f$  than the thermodynamic losses accounted for in  $\eta_{2nd,cy}$ . The cycle second-law efficiency depends mainly on the regenerators end temperatures and at higher hot reservoir temperatures  $\eta_{2nd,cy}$  strongly decreases since the cold end temperatures are higher and the temperature spans are lower. Moreover, the results in Figs. 114 and 115 help to quantify the influence of these mechanical losses as well as the maximum achievable efficiency (in comparison with a Carnot refrigerator operating within the same environment temperature span).

The maximum values of  $\eta_{2nd}$  and  $Ex_Q$  obtained with the present system were of the order of 5% and 15-20 W, which are somewhat modest figures in comparison with established cooling technologies. For instance, in a household refrigerator of average cooling capacity of 80 W at  $T_H \sim 305$  K,  $\eta_{2nd}$  approaches 21% with an  $Ex_Q \sim 15$  W (average  $\Delta T_{sys}$  of 47 K) (Gonçalves *et al.*, 2011). The 30-W (nominal) cooling capacity Stirling, reciprocating compressor and linear compressor portable coolers investigated by

Hermes & Barbosa (2012) exhibited, at  $T_H \sim 305$  K, overall second-law efficiencies of around 14%, 14% and 8%, respectively, which corresponded to  $Ex_Q$  of 4.3, 4.7 and 5.9 W. A thermoelectric cooler of similar characteristics evaluated in the same study presented an overall second-law efficiency of only 1%.

Considering the fact that magnetic cooling at room temperature is still a developing technology, improvements in mechanical design and material selection can certainly contribute to reducing the gap between actual and idealized performance (Figs. 114 and 115), as well as the gap between the performance of competing technologies for certain niche applications.

A summary of the results generated in this study is presented on Table 19.

Table 19 – Selected experimental results obtained at the AMR running at an operational frequency of 1.5 Hz.

$T_H$ (K)	$\dot{V}_f$ (L/h)	$\phi$ (–)	$\Delta T_{reg}$ (K)	$\dot{Q}_C$ (W)	$\dot{W}_M$ (W)	$\dot{W}_P$ (W)	COP (–)	$Ex_Q$ (W)	$\eta_{2nd}$ (%)	$\eta_{2nd,cy}$ (%)
297.7	400	0.37	16.8	200	241	45	0.70	12.0	4.2	24.8
297.7	300	0.28	14.3	200	223	22	0.82	10.1	4.1	31.6
297.7	600	0.56	13.8	400	274	112	1.04	19.4	5.0	20.4
297.7	500	0.47	12.9	400	253	73	1.23	18.1	5.6	26.7
296.0	400	0.37	10.2	400	233	41	1.46	14.2	5.2	31.1
286.9	400	0.37	4.8	400	218	45	1.52	6.7	2.6	13.9
299.0	400	0.37	3.2	400	215	35	1.60	4.3	1.7	10.4
297.7	350	0.33	1.5	400	221	26	1.62	2.1	0.8	5.8

## 6.6 SUMMARY

In this chapter, experimental results obtained with a novel rotary magnetic cooler prototype for a range of hot reservoir temperatures, cooling capacities and volumetric flow rates were presented. As a part of the analysis of the AMR performance, a detailed study of parasitic losses external to the regenerator beds was carried out. It was shown that flow distributor friction, heat transfer from the regenerator housing, heat losses from the connecting piping and heat losses from the cold end fluid filter contributed to reducing the performance of the AMR. When the AMR operates with a regenerator temperature span of 25 K, the losses to the ambient are estimated at approximately 74 W, which will directly reduce the power available for cooling. The efficiency of the AMR was studied

for a range of operating conditions. For an operating frequency of 1.5 Hz, a volumetric flow rate of 400 L/h, and a hot reservoir temperature of 297.7 K, a cooling capacity of 200 W produced over a  $\Delta T_{\text{reg}}$  of 16.8 K with a COP of 0.69. For a 400-W cooling capacity, the regenerator temperature span was 7.1 K, with a COP of 1.51. The maximum experimentally measured COP was 1.62 when absorbing 400 W cooling capacity at a span of 1.5 K.

The power loss associated with various components was quantified, which made clear that efficiency can be significantly increased by reducing friction in the fluid flow distributors. Efficiency can be further increased by reducing parasitic losses, which will increase the effective cooling capacity of the device.

The experiments were compared to predictions from a 1D numerical AMR model for all experiments presented. When the calculated parasitic losses are included, good agreement between the model and experiment is achieved. This suggests that a simple 1D regenerator model can be used to predict a large scale AMR device with some accuracy.

This chapter also presented a systematic performance evaluation of the AMR device, which incorporated the data on mechanical losses in the various components and quantified the thermodynamic and mechanical efficiencies in a second-law framework. The maximum overall second-law efficiency was around 5%, which corresponded to approximately one-sixth of the maximum second-law efficiency calculated excluding the mechanical losses. This, together with the possibility of advanced magnetocaloric materials with multiple layers can certainly make magnetic refrigeration at room-temperature more competitive at certain niche applications.



## Chapter 7

# CONCLUSIONS

This thesis aimed at analyzing several aspects of magnetic refrigeration, with contriariobutions on four research fronts as follows: (i) characterization of promising magnetic refrigerants and their magnetocaloric effect (MCE), (ii) high-efficiency magnetic circuits design for magnetic cooling, (iii) development of novel magnetic refrigerator prototypes and (iv) thermodynamic performance evaluation of magnetic refrigerators for efficiency-oriented designs.

A temperature controlled facility was constructed to improve the direct measurements of the magnetocaloric effect by means of the adiabatic temperature change,  $\Delta T_{\text{ad}}$ . Measurements of the benchmark magnetocaloric material Gd were initially investigated and the results were in good agreement with the literature. The reversibility of the MCE and its dependence on the demagnetization factor were experimentally investigated. Samples of one of the most promising magnetic refrigerants, MnFe(P,As), were characterized through direct measurements of  $\Delta T_{\text{ad}}$ . A training effect characterized by a lower  $\Delta T_{\text{ad}}$  was found during the first thermal cycles. After eliminating the training effect, a peak  $\Delta T_{\text{ad}}$  of 3.9 K was attained at a  $T_C$  of 290 K for an applied magnetic field of 1.75 T. It was found out that the thermal hysteresis of the Mn-based first-order transition samples was about 0.6 K. The advantage to tune the Curie temperature together with the low cost of the raw materials and the synthesis make the MnFe(P,As) compounds promising room-temperature magnetic refrigerants.

A magnetic circuit with a 2-pole rotor-stator configuration was designed aiming at an efficient use of the permanent magnets. A novel method to optimize the magnetic circuit was proposed, which employed the magnet wedges concept of Abele *et al.* (1997) and replaced part of the permanent magnet and the air between the wedges by soft magnetic material. The resulting total volume of the permanent magnet, Nd-Fe-B, for a 150-mm long magnetic circuit was approximately 1.91 L. Numerical simulation of the magnetic circuit employing a final remanence of the permanent magnet of 1.47 T, for which the maximum energy density would be  $409.3 \text{ kJ/m}^3$ ,

resulted in a calculated average energy product of the permanent magnets in the magnetic circuit of  $382.1 \text{ kJ/m}^3$ . For an opening angle of 45 degrees, the average applied magnetic fields in the adjacent high and low field regions were 1.096 and 0.153 T, respectively, which resulted in a  $\Lambda_{\text{cool}}$  of  $0.192 \text{ T}^{2/3}$ . The magnetic circuit was manufactured and its magnetic effectiveness was characterized and validated experimentally by measuring the magnetic flux density in the gap and the experimental results were in very good agreement with the numerical simulations.

A novel rotary magnetic refrigerator was built using the 2-pole rotor-stator magnetic circuit and a stationary packed regenerator. The device was designed so that the fluid flow was always unidirectional in the hot and cold heat exchangers. A flow distribution system, composed mainly by two rotary valves, was specially designed and built to be positioned at the hot end to avoid undesirable heat generation due to seal friction at the cold end. The flow distribution system generated alternating fluid flows through the regenerator beds synchronized with the magnetic circuit rotation. The ring-shaped regenerator is composed by 8 pairs beds packed with 1.7 kg of Gd spheres with diameters between 425 and 600  $\mu\text{m}$ . The heat transfer fluid was a mixture of distilled water and commercial ethylene-glycol with corrosion inhibitors.

The UFSC rotary magnetic refrigerator was experimentally analyzed. Measurement of pressure drop in both the empty and packed regenerators was carried out for different fluid flow rates. Large flow resistances were observed, which were probably associated with entrance losses in the regenerator beds. These prevented high flow rates from being developed in the device. The system performance was evaluated independently in terms of the regenerator temperature span,  $\Delta T_{\text{reg}}$ , as a function of the operating frequency, volumetric flow rate, hot reservoir temperature and thermal load, respectively. The experimental analysis resulted in a maximum cooling capacity of 150 W (about  $88.2 \text{ W/kg}$  of Gd) at zero-span and a maximum no-load  $\Delta T_{\text{reg}}$  of 12 K. The device was able to absorb 80.4 W (approximately  $47.3 \text{ W/kg}$ ) while maintaining a  $\Delta T_{\text{reg}}$  of 7.1 K at an operating frequency of 0.8 Hz and a flow rate of 200  $\text{L/h}$  ( $\phi = 0.47$ ). The experimental operating torque and the motor power was investigated at different AMR frequencies. The maximum torque was 7.2 Nm for an operating frequency of 0.4 Hz, while the maximum motor power was of 159.2 W at 1.6 Hz. The thermodynamic performance of the device was evaluated in terms of the coefficient of

performance (COP) and the overall second-law efficiency ( $\eta_{2nd}$ ). A COP of 0.58 was calculated for an experimental condition of 0.8 Hz, 175 L/h, a thermal load of 81 W, resulting in a  $\Delta T_{reg}$  of 6.5 K. The maximum value of  $\eta_{2nd}$  obtained for the UFSC system was 1.16% for an experiment at 0.8 Hz, 200 L/h, a thermal load of 80.4 W and a  $\Delta T_{reg}$  of 7.1 K.

The experimental results obtained with the UFSC rotary magnetic refrigeration system are yet modest in comparison with other state-of-the-art magnetic refrigerators and with established cooling technologies. Improvements in the experimental performance and efficiency are expected at higher fluid flow rates and operating frequencies. It has been demonstrated that there is still room for improvements, specially regarding the regenerator configuration, for which a decrease in pressure drop, a better insulation with the magnet and the inclusion of a flow-mixture chamber is fundamental to enhance the AMR performance. Additionally, the asymmetry between the high and low field regions of the magnetic profile is detrimental to the AMR performance due to the existence of a no-flow period subjected to thermal conduction in the regenerator. Ways to improve the performance of the device are currently being sought and will be the subject of further studies.

The last part of this thesis comprised an experimental analysis and a thermodynamic performance evaluation of the DTU rotary magnetic cooler prototype. Experimental results for a range of hot reservoir temperatures, cooling capacities and volumetric flow rates were presented. A cooling capacity of 200 W (about 71.4 W/kg) was produced at a span of 16.8 K with a calculated COP of 0.69. A detailed study of the losses external to the regenerator led to the conclusion that the efficiency can be further enhanced through improvements in the flow distributor design and reductions of thermal parasitic losses in the regenerator housing, connecting piping and cold end fluid filter. The experimental results were compared with predictions of a 1D numerical AMR model for all experiments presented. When the calculated parasitic losses are included, good agreement between the model and experiment is achieved. This suggests that a simple 1D regenerator model can be used to predict a large scale AMR device with some accuracy.

A systematic thermodynamic performance evaluation of the DTU device was performed for a range of operating conditions. A methodology to breakdown the COP and the motor power was developed to quantify the efficiency improvements of the system and

the major losses. The maximum overall second-law efficiency was around 5%, which corresponded to approximately one-sixth of the maximum second-law efficiency calculated excluding the mechanical losses.

Whether magnetocaloric refrigeration at near room temperature will succeed or not commercially is still an open question. It certainly has great potential from a fundamental thermodynamic perspective, but it also has several challenges in terms of cost, availability of materials, manufacturing processes and thermal-hydraulic performance. Significant progress has been made regarding the characterization of material properties, mathematical modeling of transport phenomena and development of magnetic refrigerator prototypes. Future activities will involve further integration of these three research fronts in order to improve basic understanding of the physical processes and increase the efficiency of the cooling devices.

## Chapter 8

---

# RECOMMENDATIONS FOR FUTURE WORK

Based on the results obtained in this thesis, some recommendations for further investigations in magnetic refrigeration can be made, especially concerning the development of experimental apparatuses. The following activities are suggested as future research topics:

- To improve the design of the direct measurement facility by including a permanent magnet circuit with a variable applied magnetic field over a broader magnetic gap in a more compact temperature controlled chamber. This will enable faster and more accurate thermal cycles over broader temperature and magnetic field ranges. More complete and reliable databases of  $\Delta T_{\text{ad}}$  will result for different promising magnetic refrigerants.
- To extend the thermodynamic performance analysis methodology developed in this thesis (Chapter 6) to the UFSC magnetic refrigerator by identifying the thermal, mechanical and magnetic parasitic losses found in the actual device. Systematic 1-D numerical simulations of the actual AMR and experimental studies of the torque and power consumption for different operating conditions can be carried out to quantify and evaluate the losses external to the regenerator. This quantification will enable improvements that could enhance the efficiency of the actual system.
- To study the synchronization between the fluid flow profile and the magnetic profile (Fig. 64) and its influence on the UFSC system performance. This study can be carried out by means of a 1-D numerical model which could be experimentally validated via the versatile flow distribution system developed in this thesis that allows establishing different fluid flow profiles. The resulting optimal synchronization parameters can be used as a guideline either for a novel design of the flow distribution system or a novel design of the magnetic circuit.
- To study the the possibility of using promising magnetocaloric

refrigerants with multiple layers in the regenerator beds either of the actual UFSC or DTU devices. The magnetocaloric properties of the magnetic refrigerants with different  $T_C$ 's can be implemented in a 1-D numerical model allowing for systematic simulations of the AMRs to optimize the substitution of the actual single-layer Gd-spheres packed AMRs for multi-layer regenerators.

- To perform systematic numerical simulations of the AMR aiming at the design of a new regenerator for the UFSC magnetic refrigerator. For instance, an improvement of the system efficiency is expected for reducing demagnetization factors and pressure drops in the packed beds. Since NTU is large for the actual packed-spheres regenerator, the use of larger sphere diameters is expected to reduce the pressure drops without harming the heat transfer in the regenerator. Moreover, a mixing chamber at the entrances of the beds could increase the effectiveness of the AMR. However, a dead volume analysis should be carried out to avoid much blow mixing at the ends of the regenerator, which can harm the performance of the AMR.
- To improve the DTU system performance by means of a new flow distributor design and by reducing the thermal losses in the regenerator housing, piping and in the cold end fluid filter. Additionally, the use of more appropriate high-efficiency motor and pump is expected to enhance the efficiency of the device which can certainly make this magnetic refrigerator a more competitive device to the state-of-the-art refrigerators.

## BIBLIOGRAPHY

- ABELE, M. G.; JENSEN, J. H.; RUSINEK, H. Generation of uniform high fields with magnetized wedges. *IEEE Transaction on Magnetics*, v. 33, p. 3874 – 3876, 1997.
- AHARONI, A. Demagnetizing factors for rectangular ferromagnetic prisms. *Journal of Applied Physics*, v. 83, p. 3432–3434, 1998.
- ALLAB, F. *Etude et conception d'un dispositif de refrigeration magnetique base sur l'effect magnetocalorique geant*. Phd Thesis (PhD Thesis) — L'institut polytechnique de Grenoble, 2008.
- APREA, C.; MAIORINO, A. A flexible numerical model to study an active magnetic refrigerator for near room temperature applications. *Applied Energy - Kidlington*, v. 87, p. 2690, 2010. ISSN 03062619.
- ARNOLD, D. S.; TURA, A.; ROWE, A. Experimental analysis of a two-material active magnetic regenerator. *Int. J. Refrig.*, v. 34, p. 178–191, 2011. ISSN 01407007, 18792081.
- BAHL, C.; ENGELBRECHT, K.; BJØRK, R.; ERIKSEN, D.; SMITH, A.; NIELSEN, K.; PRYDS, N. Design concepts for a continuously rotating active magnetic regenerator. *International Journal of Refrigeration*, Elsevier Ltd., v. 34, n. 8, p. 1792–1796, 2011. ISSN 0140-7007.
- BAHL, C.; PETERSEN, T.; PRYDS, N.; A., S. A versatile magnetic refrigeration test device. *Review of Scientific Instruments*, v. 79, 2008.
- BAHL, C. R. H.; ENGELBRECHT, K.; ERIKSEN, D.; LOZANO, J. A.; BJØRK, R.; GEYTI, J.; NIELSEN, K. K.; SMITH, A.; PRYDS., N. Development and experimental results from a 1 kW prototype AMR. *International Journal of Refrigeration*, v. 37, p. 78–83, 2014.
- BAHL, C. R. H.; NIELSEN, K. K. The effect of demagnetization on the magnetocaloric properties of gadolinium. *Journal of Applied Physics*, v. 105, n. 013916, p. 1–5, 2009.

BARBOSA, J.; LOZANO, J.; TREVIZOLI, P. Magnetocaloric refrigeration research at the inct in cooling and thermophysics. In: *Proceedings of the 15th Brazilian Congress of Thermal Sciences and Engineering (ENCIT)*. Belén: [s.n.], 2014.

BARBOSA, J.; LOZANO, J.; TREVIZOLI, P. Magnetocaloric refrigeration research at the inct in cooling and thermophysics. In: *Proceedings of the ENCIT 2014*. [S.l.: s.n.], 2014.

BARCLAY, J. A. The theory of an active magnetic regenerative refrigerator. In: *Nasa Conference Publication*. [S.l.: s.n.], 1983.

J. A. Barclay & W. A. Steyert Jr. *Active Magnetic Regenerator*. 1982. U.S. Patent No. 4,332,135.

BASTOS, J. P. A. *Eletromagnetismo para Engenharia: Estática e Quase-estática*. [S.l.]: Editora da UFSC, 2004.

BENFORD, S. M.; BROWN, G. V. T-S diagram for gadolinium near the curie temperature. *Journal of Applied Physics*, v. 52, p. 2110–2112, 1981.

BJØRK, R. *Designing a magnet for magnetic refrigeration*. Phd Thesis (PhD Thesis) — Risø DTU, 2010.

BJØRK, R.; BAHL, C.; SMITH, A.; PRYDS, N. Review and comparison of magnet designs for magnetic refrigeration. *International Journal of Refrigeration*, v. 33, p. 437–448, 2010.

BJØRK, R.; BAHL, C.; SMITH, A.; PRYDS, N. Improving magnet designs with high and low field regions. *Institute of Electrical and Electronics Engineers*, Accepted for publication, 2011.

BJØRK, R.; BAHL, C. R. H.; SMITH, A.; PRYDS, N. Optimization and improvement of halbach cylinder design. *Journal of Applied Physics*, v. 104, 2008.

BJØRK, R.; BAHL, C. R. H.; SMITH, A.; CHRISTENSEN, D. V.; PRYDS, N. An optimized magnet for magnetic refrigeration. *Journal of Magnetism and Magnetic Materials*, v. 322, p. 3324–3328, 2010.

BJØRK, R.; BAHL, C. R. H.; SMITH, A.; CHRISTENSEN, D. V.; PRYDS, N. An optimized magnet for magnetic refrigeration. *J. Magn. Magn. Mater.*, v. 322, p. 3324–3328, 2010.

- BJØRK, R.; BAHL, C. R. H.; SMITH, A.; PRYDS, N. Improving magnet designs with high and low field regions. *IEEE Trans. Magn.*, v. 47, p. 1687–1692, 2011.
- BJØRK, R.; ENGELBRECHT, K. The influence of the magnetic field on the performance of an active magnetic regenerator (amr). *International Journal of Refrigeration*, v. 34, p. 192–203, 2011.
- BJØRK, R.; SMITH, A.; BAHL, C. R. H. Analysis of the magnetic field, force, and torque for two-dimensional halbach cylinder. *Journal of Magnetism and Magnetic Materials*, v. 322, p. 133–141, 2010.
- BLEANEY, B.; HULL, R. The effective susceptibility of a paramagnetic powder. *Proc. R. Soc.*, v. 178, p. 86–83, 1941.
- BLUMENFELD, P. E.; PRENGER, F. C.; STERNBERG, A.; ZIMM, C. High temperature superconducting magnetic refrigeration. *Advances in Cryogenic Engineering*, v. 47, p. 1019–1026, 2002.
- BOUCHEKARA, H. *Recherche sur les systemes de refrigeration magnetique. Modelisation numerique, conception et optimisation.* Phd Thesis (PhD Thesis) — L’institut polytechnique de Grenoble, 2008.
- BROWN, G. V. Magnetic heat pumping near room temperature. *Journal of Applied Physics*, v. 47, p. 3673–3680, 1976.
- BRÜCK, E. Developments in magnetocaloric refrigeration. *Journal of Physics D: Applied Physics*, v. 38, p. R381–R391, 2005.
- BRÜCK, E. Magnetocaloric refrigeration at ambient temperature. In: \_\_\_\_\_. [S.l.]: North-Holland, 2007. chap. 4, p. 235–291.
- BRÜCK, E.; TEGUS, O.; THANH, D. T. C.; TRUNG, N. T.; BUSCHOW, K. H. J. A review on Mn based materials for magnetic refrigeration: Structure and properties. *International Journal of Refrigeration*, v. 31, p. 763–770, 2008.
- BRÜCK, E.; TEGUS, O.; ZHANG, L.; LI, X. W.; DEBOER, F. R.; BUSCHOW, K. H. J. Magnetic refrigeration near room temperature with fe<sub>2</sub>p-based compounds. *Journal of Alloys and Compounds*, v. 383, p. 32–36, 2004.

- BUHELNIKOV, V. D.; TASKAEV, S. V.; BYCHKOV, I. V.; CHERNETS, I. A.; DENISOVSKIY, A. M. The prototype of effective device formagnetic refrigeration. In: POREDOS, A.; SARLAH, A. (Ed.). *Proceedings in 2nd International Conference on Magnetic Refrigeration at Room Temperature*. Portoroz, Slo: [s.n.], 2007.
- CALLISTER, W. *Materials Science and Engineering: An Introduction*. [S.l.]: John Wiley and sons, 2002.
- CAMPBELL, P. *Permanent Magnet Materials and their Application*. [S.l.]: Cambridge University Press, 1999.
- CAMTHANH, D. T.; BRÜCK, E.; TEGUS, O.; KLAASSE, J. C.; GORTENMULDER, T. J.; BUSCHOW, K. H. J. Magnetocaloric effect in mnfe(p,si,ge) compounds. *Journal of Applied Physics*, v. 99, p. 08Q107, 2006.
- CANEPA, F.; CIRAFICI, S.; NAPOLETANO, M.; CICCARELLI, C.; BELFORTINI, C. Direct measurement of the magnetocaloric effect of microstructured gd eutectic compounds using a new fast automatic device. *Solid State Communications*, v. 133, p. 241–244, 2005.
- CARON, L.; OU, Z. Q.; NGUYEN, T. T.; THANH, D. T. C.; TEGUS, O.; BRÜCK, E. On the determination of the magnetic entropy change in materials with first-order transitions. *Journal of Magnetism and Magnetic Materials*, v. 321, p. 3559, 2009.
- Jeremy Chell & Carl B. Zimm. *Permanent magnet assembly*. 2006. 7148777 B2.
- CHEN, F.; MURPHY, R. W.; MEI, V. C.; CHEN, G. Thermodynamic anlysis of four magnetic heat-pumps cycles. *Journal of Engineering for Gas Turbines and Power*, v. 114, p. 715–720, 1992.
- CHEN, Y. F.; WANG, F.; SHEN, B. G.; HU, F. X.; SUN, J. R.; WANG, G. J.; CHENG, Z. H. Magnetic properties and magnetic entropy change of LaFe<sub>11.5</sub>Si<sub>1.5</sub>Hy interstitial compounds. *J. Phys. Condens. Matter*, v. 15, p. L161, 2003.
- CHEN, Y. G.; TANG, Y. B.; WANG, B. M.; XUE, Q. X.; TU, M. J. A permanent magnet rotary magnetic refrigerator. In: POREDOS, A.; SARLAH, A. (Ed.). *Proceedings in 2nd*

*International Conference on Magnetic Refrigeration at Room Temperature*. Portoroz, Slo: [s.n.], 2007.

COELHO, A. A.; GAMA, S.; MAGNUS G CARVALHO, A. Prototype of a Gd-based rotating magnetic refrigerator for work around room temperature. In: *Proceedings in 3rd International Conference on Magnetic Refrigeration at Room Temperature*. [S.l.: s.n.], 2009.

COLEMAN, H.; STEELE, W. *Experimentation, Validation, and Uncertainty Analysis for Engineers*. 3rd ed.. ed. Hoboken: John Wiley & Sons, Inc., 2009. 317 p.

COMSOL. 2008. AB, Tegnérgatan 23, SE-111 40 Estocolmo, Suécia.

COMSOL Multiphysics®. *Version 4.2*. 2011. COMSOL, Inc. Burlington, MA, USA.

CULLITY, B. D. *Introduction to magnetic materials*. [S.l.]: Addison-Wesley Publishing Company Inc., 1972.

DAGULA, W.; TEGUS, O.; FUQUAN, B.; ZHANG, L.; SI, P.; ZHANG, W. S.; BRÜCK, E. H.; DEBOER, F. R. D.; BUSCHOW, K. H. J. Magnetic-entropy change in  $\text{mn}_1.1\text{fe}_0.9\text{p}_1\text{-xgex}$  compounds. *IEEE Transactions on Magnetics*, v. 41, p. 2778–2780, 2005.

DAN'KOV, S. Y.; TISHIN, A. M.; PECHARSKY, V. K.; GSCHNEIDNER JR., K. A. Experimental device for studying the magnetocaloric effect in pulse magnetic fields. *Review of Scientific Instruments*, v. 68, p. 2432–2437, 1997.

DAN'KOV, S. Y.; TISHIN, A. M.; PECHARSKY, V. K.; GSCHNEIDNER JR., K. A. Magnetic phase transitions and the magnetothermal properties of gadolinium. *Physical Review B*, v. 57, p. 3478–3490, 1998.

DEBYE, P. Einige bemerkungen zur magnetisierung bei tiefer temperatur. *Ann. Phys. (Leipzig)*, v. 386, p. 1154–1160, 1926.

DIKEOS, J. *Development and validation of an active magnetic regenerator refrigeration cycle simulation*. Master's Thesis (Master's Thesis) — University of Victoria, 2006.

T. Edison. *Pyromagnetic Motor*. 1888. US380100.

ENGELBRECHT, K. *A numerical model of an active magnetic regenerator refrigerator with experimental validation*. Phd Thesis (PhD Thesis) — University of Wisconsin-Madison, 2008.

ENGELBRECHT, K.; BAHL, C.; NIELSEN, K. Experimental results for a magnetic refrigerator using three different types of magnetocaloric material regenerators. *International Journal of Refrigeration*, v. 34, p. 1132–1140, 2011.

ENGELBRECHT, K.; BAHL, C. R. H. Evaluating the effect of magnetocaloric properties on magnetic refrigeration performance. *J. Appl. Phys.*, v. 108, p. 123918, 2010. ISSN 00218979, 10897550.

ENGELBRECHT, K.; ERIKSEN, D.; BAHL, C.; BJØRK, R.; GEYTI, J.; LOZANO, J.; NIELSEN, K.; SAXILD, F.; SMITH, A.; PRYDS, N. Experimental results for a novel rotary active magnetic regenerator. *International Journal of Refrigeration*, Elsevier Ltd., v. 35, n. 6, p. 1498–1505, 2012. ISSN 0140-7007.

ENGELBRECHT, K.; JENSEN, J. B.; BAHL, C. R. H.; PRYDS, N. Experiments on a modular magnetic refrigeration device. In: *Proceedings in 3rd International Conference on Magnetic Refrigeration at Room Temperature*. Des Moines, USA: [s.n.], 2009.

ENGELBRECHT, K.; NELLIS, G.; KLEIN, S. Predicting the performance of an active magnetic regenerator refrigerator used for space cooling and refrigeration. *HVAC&R Res.*, v. 12, p. 1077–1095, 2006.

ENGELBRECHT, K.; ROWE, A.; BJØRK, R.; NIELSEN, K. K.; BAHL, C. R. H.; ERIKSEN, D.; PRYDS, N. Magnetic cooling: From fundamentals to high efficiency refrigeration. In: \_\_\_\_\_. [S.l.]: Wiley, 2015. chap. Active Magnetic Regenerator System Design.

ERGUN, S. Fluid flow through packed columns. *Chem. Process Eng. London*, v. 48, p. 89–94, 1952.

ERK, H. F. *Heat regenerators with phase-change materials*. Phd Thesis (PhD Thesis) — Washington University, 1990.

FERREIRA, A. P.; COSTA, A. F. Projeto e seleção de materiais magnéticos permanentes. *Engineering and Technology Journal*, v. 2, 2011.

FRANCO, V.; BLÁZQUEZ, J.; INGALE, B.; CONDE, A. The magnetocaloric effect and magnetic refrigeration near room temperature: Materials and models. *Annual Review of Materials Research*, v. 42, p. 305–342, 2012.

FUJIEDA, S.; FUJITA, A.; FUKAMICHI, K. Large magnetocaloric effect in  $\text{La}(\text{Fe}_{x}\text{Si}_{1-x})_{13}$  itinerant-electron metamagnetic compounds. *Applied Physics Letters*, v. 81, n. 7, p. 1276–1278, 2002.

FUJITA, A.; AKAMATSU, Y.; FUKAMICHI, K. Itinerant electron metamagnetic transition in  $\text{La}(\text{Fe}_{x}\text{Si}_{1-x})_{13}$  intermetallic compounds. *Journal of Applied Physics*, AIP, v. 85, n. 8, p. 4756–4758, 1999.

FUJITA, A.; FUJIEDA, S.; HASEGAWA, Y.; FUKAMICHI, K. Itinerant-electron metamagnetic transition and large magnetocaloric effects in  $\text{La}(\text{Fe}_{x}\text{Si}_{1-x})_{13}$  compounds and their hydrides. *Physical Review B*, APS, v. 67, n. 10, p. 104416, 2003.

FURLANI, E. P. *Permanent Magnet and Electromechanical Devices*. [S.l.]: Elsevier, 2001.

GAO, Q.; YU, B. F.; WANG, C. F.; ZHANG, B.; YANG, D. X.; ZHANG, Y. Experimental investigation on refrigeration performance of a reciprocating active magnetic regenerator of room temperature magnetic refrigeration. *International Journal of Refrigeration*, v. 29, p. 1274–1285, 2006.

GIAUQUE, W. A thermodynamic treatment of certain magnetic effects. a proposed method of producing temperatures considerably below  $1^{\circ}$  absolute. *J. Am. Chem. Soc.*, v. 49, p. 1864–1870, 1927.

GIGUÈRE, A.; FÖLDEÀKI, M.; GOPAL, B. R.; CHAHINE, R.; BOSE, T. K.; FRYDMAN, A.; BARCLAY, J. A. Direct measurement of the giant adiabatic temperature change in  $\text{Gd}_{5}\text{Ge}_{2}\text{Si}_{2}$ . *Physical Review Letters*, v. 83, p. 2262–2265, 1999.

GONÇALVES, J. M.; MELO, C.; HERMES, C. J. L.; BARBOSA, J. R. Experimental mapping of the thermodynamic losses in vapor compression refrigeration systems. *Journal of the Brazilian Society of Mechanical Sciences and Engineering*, scielo, v. 33, p. 159 – 165, 2011. ISSN 1678-5878.

GOPAL, B. R.; CHAHINE, R.; BOSE, T. K. A sample translatory type insert for automated magnetocaloric effect measurements. *Review Scientific Instruments*, v. 68, n. 4, p. 1818–1822, 1997.

GREEN, G.; SCHROEDER, E. A finite element model of an experimental magnetocaloric refrigerator. In: *Proceedings of International Cryocooler Conference*. Monterey, CA, USA: [s.n.], 1988. p. 69–80.

GSCHEIDNER JR., K. A.; PECHARSKY, V. K. Magnetocaloric materials. *Annual Review of Materials Science*, v. 30, p. 687–429, 2000.

GSCHEIDNER JR., K. A.; PECHARSKY, V. K. Rare earths and magnetic refrigeration. *Journal of Rare Earths*, v. 24, p. 641–647, 2006.

GSCHEIDNER JR., K. A.; PECHARSKY, V. K. Thirty years of near room temperature magnetic cooling: Where we are today and future prospects. *International Journal of Refrigeration*, v. 31, p. 945–961, 2008.

GSCHEIDNER JR., K. A.; PECHARSKY, V. K.; TSOKOL, A. O. Recent developments in magnetocaloric materials. *Reports on Progress in Physics*, v. 68, p. 1479–1539, 2005.

GUTFLEISCH, O.; YAN, A.; MÜLLER, K. H. Large magnetocaloric effect in melt spun lafe13xsix. *Journal of Applied Physics*, v. 97, 2005.

HERMES, C. J. L.; BARBOSA, J. R. Thermodynamic comparison of peltier, stirling, and vapor compression portable coolers. *Appl. Energy*, v. 91, p. 51–58, 2012.

HUANG, J. H.; QIU, J. F.; LIU, J. R.; JIN, P. Y.; XU, L. Z.; ZHANG, J. X. A direct measurement set-up for the magnetocaloric effect. In: *Proceedings in First International Conference on Magnetic Refrigeration at Room Temperature*. Montreux, Switzerland: [s.n.], 2005.

ISO, I. O. for S. *Guide to the Expression of Uncertainty in Measurement*. Geneva: [s.n.], 1995.

JACOBS, S. Modeling and optimal design of a multiplayer active magnetic refrigeration system. In: *Third International Conference on Magnetic Refrigeration at Room Temperature*. [S.l.: s.n.], 2009.

JASINSKI, M.; LIU, J.; JACOBS, S.; ZIMM, C. La(Fe,Co,Si)<sub>13</sub> bulk alloys and ribbons with high temperature magnetocaloric effect. *Journal of Applied Physics*, AIP, v. 107, n. 9, p. 09A953–09A953, 2010.

JEPPESEN, S.; LINDEROTH, S.; PRYDS, N.; KUHN, L. T.; JENSEN, J. B. Indirect measurement of the magnetocaloric effect using a novel differential scanning calorimeter with magnetic field. *Rev. Sci. Instrum.*, American Institute of Physics, v. 79, 2008. ISSN 00346748.

KANOĞLU, M.; ÇENGEL, Y. A.; DINÇER, İ. *Efficiency Evaluation of Energy Systems*. [S.l.]: Springer, 2012. 170 p.

KATTER, M.; ZELLMANN, V.; REPPPEL, G. W.; UESTUENER, K. Magnetocaloric properties of La(Fe,Co,Si)<sub>13</sub> bulk material prepared by powder metallurgy. *IEEE TRANSACTIONS ON MAGNETICS*, v. 44, p. 3044–3047, 2008.

KAWANAMI, T.; CHIBA, K.; SAKURAI, K.; IKEGAWA, M. Optimization of a magnetic refrigerator at room temperature for air cooling systems. *International Journal of Refrigeration*, v. 29, p. 1294–1301, 2006.

KHOVAYLO, V. V.; SKOKOV, K. P.; GUTFLEISCH, O.; MIKI, H.; KAINUMA, R.; KANOMATA, T. Reversibility and irreversibility of magnetocaloric effect in a metamagnetic shape memory alloy under cyclic action of a magnetic field. *Applied Physics Letters*, v. 97, n. 052503, 2010.

KIM, J. H.; SIMON, T. W. Journal of heat transfer policy on reporting uncertainties in experimental measurements and results. *Journal of Heat Transfer*, v. 115, p. 5–6, 1993.

KITANOVSKI, A.; TUŠEK, J.; TOMC, U.; PLAZNIK, U.; OŽBOLT, M.; POREDOS, A. *Magnetocaloric Energy Conversion: From theory to applications*. [S.l.]: Springer, 2015.

KRAUTZ, M.; MOORE, J.; SKOKOV, K.; LIU, J.; TEIXEIRA, C.; SCHAFFER, R.; SCHULTZ, L.; GUTFLEISCH, O. Reversible solid-state hydrogen-pump driven by magnetostructural transformation in the prototype system La(Fe,Si)<sub>13</sub>H<sub>y</sub>. *Journal of Applied Physics*, AIP, v. 112, n. 8, p. 083918–083918, 2012.

- KUPPAN, T. *Heat exchanger design handbook*. [S.l.]: Marcel Dekker, 2000.
- LANGEBACH, R.; KLAUS, M.; HABERSTROH, C.; HESSE, U. Magnetocaloric cooling near room temperature – a status quo with respect to household refrigeration. In: *15th International Refrigeration and Air Conditioning Conference at Purdue*. [S.l.: s.n.], 2014.
- LIU, G. J.; SUN, J. R.; WANG, J. Z.; ZHAO, T. Y.; SHEN, B. G. A comparison study of the entropy changes in materials with and without short-range magnetic order. *Journal of Physics: Condensed Matter*, v. 19, n. 466215, p. 1–8, 2007.
- LIU, J. Optimizing and fabricating magnetocaloric materials. *Chinese Physics B*, v. 23, p. 047503, 2014.
- LIU, J.; GOTTSCHALL, T.; SKOKOV, K.; MOORE, J.; GUTFLEISCH, O. Giant magnetocaloric effect driven by structural transitions. *Nature Materials*, v. 11, p. 620, 2012.
- LOZANO, J. A. *Síntese e caracterização de materiais com efeito magnetocalórico à base de manganês para aplicações em refrigeração magnética*. Master's Thesis (Master's Thesis) — Universidade Federal de Santa Catarina, 2009.
- LOZANO, J. A.; ENGELBRECHT, K.; BAHL, C. R. H.; NIELSEN, K. K.; ERIKSEN, D.; OLSEN, U. L.; BARBOSA, J. R.; SMITH, A.; PRATA, A. T.; PRYDS, N. Performance analysis of a rotary active magnetic refrigerator. *Applied Energy*, v. 111, p. 669–680, 2013. ISSN 0306-2619.
- LOZANO, J. A.; ENGELBRECHT, K.; BAHL, C. R. H.; NIELSEN, K. K.; BARBOSA, J. R.; PRATA, A. T. Experimental and numerical results of a high frequency rotating active magnetic refrigerator. *International Journal of Refrigeration*, Elsevier Ltd., v. 37, p. 92–98, 2014. ISSN 0140-7007.
- LU, D. W.; XU, X. N.; WU, H. B.; JIN, X. A permanent magnet magnetocaloric refrigerator study on using Gd / Gd-Ge-Si / Gd-Ge-Si-Ga alloys. In: *Proceedings in 1st International Conference on Magnetic Refrigeration at Room Temperature*. Montreux, SWI: [s.n.], 2005.

MADIREDDI, S.; ZHANG, M.; PECHARSKY, V. K.; JR., K. A. G. Magnetocaloric effect of  $\text{gd}_5\text{si}_2\text{ge}_2$  and its characteristics under different operating conditions. In: *Proceedings in 3rd International Conference on Magnetic Refrigeration at Room Temperature*. Ames, IA, USA: [s.n.], 2009.

MELINDER, A. Thermophysical properties of liquid secondary refrigerants. *International Institute of Refrigeration*, 1997.

MILLS, A. F. *Heat and Mass Transfer*. Concord (MA): Richard D. Irwin, 1995. 1240 p. (Irwin heat transfer series).

MOFFAT, R. Describing the uncertainties in experimental results. *Experimental thermal and fluid science*, v. 1, p. 3–17, 1988.

MONFARED, B.; FURBERG, R.; PALM, B. Magnetic vs. vapor-compression household refrigerators: A preliminary comparative life cycle assessment. *International Journal of Refrigeration*, v. 42, p. 69–76, 2014.

MOORE, J.; SKOKOV, K. P.; LIU, J.; GUTFLEISCH, O. Procedure for numerical integration of the magnetocaloric effect. *Journal of Applied Physics*, v. 112, p. 063920, 2012.

MORRISON, K.; MOORE, J. D.; SANDEMAN, K. G.; CAPLIN, A. D.; COHEN, L. F. Capturing first- and second-order behavior in magnetocaloric  $\text{CoMnSi}_{0.92}\text{Ge}_{0.08}$ . *Physical review B*, v. 79, p. 134408, 2009.

MULTIPHYSICS, A. C. *Tegnergatan 23, SE-111 40 Stockholm, Sweden*. 2008.

NELLIS, G.; KLEIN, S. *Heat Transfer*. [S.l.]: Cambridge University Press, 2009.

NIELSEN, K. K. *Numerical modeling and analysis of the active magnetic regenerator*. Phd Thesis (PhD Thesis) — Technical University of Denmark, 2010.

NIELSEN, K. K.; BAHL, C. R. H.; SMITH, A. Constraints on the adiabatic temperature change in magnetocaloric materials. *Physical Review B*, American Physical Society, v. 81, n. 5, p. 054423, Feb 2010.

NIELSEN, K. K.; BAHL, C. R. H.; SMITH, A.; ENGELBRECHT, K.; OLSEN, U. L.; PRYDS, N. The influence of non-magnetocaloric properties on the AMR performance. In: *Proceeding in 5th International Conference on Magnetic Refrigeration at Room Temperature (THERMAG V)*. Grenoble, France: [s.n.], 2012.

NIELSEN, K. K.; BJØRK, R.; ENGELBRECHT, K.; BAHL, C. R. H.; A., S.; PRYDS, N. Magnetic cooling: From fundamentals to high efficiency refrigeration. In: \_\_\_\_\_. [S.l.]: Wiley, 2015. chap. Active Magnetic Regenerator Modelling.

NIELSEN, K. K.; TUŠEK, J.; ENGELBRECHT, K.; SCHOPFER, S.; KITANOVSKI, A.; BAHL, C. R. H.; SMITH, A.; PRYDS, N.; POREDOS, A. Review on numerical modeling of active magnetic regenerators for room temperature applications. *International Journal of Refrigeration*, v. 34, p. 603–616, 2011.

OESTERREICHER, H.; PARKER, F. T. Magnetic cooling near curie temperatures above 300 k. *Journal of Applied Physics*, v. 55, p. 4334–4338, 1984.

OKAMURA, T.; RACHI, R.; HIRANO, N.; NAGAYA, S. Improvement of 100W class room temperature magnetic refrigerator. In: POREDOS, A.; SARLAH, A. (Ed.). *Proceedings in 2nd International Conference on Magnetic Refrigeration at Room Temperature*. Portoroz, Slo: [s.n.], 2007.

OKAMURA, T.; YAMADA, K.; HIRANO, N.; NAGAYA, S. Performance of a room-temperature rotary magnetic refrigerator. *International Journal of Refrigeration*, v. 29, p. 1327–1331, 2006.

OLIVEIRA, P. M. de. *On Air-Water Two-Phase Flows in Return Bends*. Master's Thesis (Master's Thesis) — Federal University of Santa Catarina, 2013.

PALSTRA, T.; WERIJ, H.; NIEUWENHUYS, G.; MYDOSH, J.; BOER, F. de; BUSCHOW, K. Metamagnetic transitions in cubic  $\text{La}(\text{Fe}_x\text{Al}_{1-x})_{13}$  intermetallic. *Journal of Physics F: Metal Physics*, IOP Publishing, v. 14, p. 1961, 1984.

PECHARSKY, V. K.; GSCHNEIDNER, J. K. A.; PECHARSKY, A. O.; MTISHIN, A. Thermodynamics of the magnetocaloric effect. *Physical Review B*, v. 64, p. 144406(1–13), 2001.

- PECHARSKY, V. K.; GSCHNEIDNER JR., K. A. Magnetocaloric effect and magnetic refrigeration. *Journal of Magnetism and Magnetic Materials*, v. 200, p. 44–56, 1999.
- PECHARSKY, V. K.; GSCHNEIDNER JR., K. A. Advanced magnetocaloric materials: What does the future hold? *International Journal of Refrigeration*, v. 29, p. 1239–1249, 2006.
- PECHARSKY, V. K.; GSCHNEIDNER, K. A. Giant magnetocaloric effect in  $\text{Gd}_5\text{Ge}_2\text{Si}_2$ . *Physical Review Letters*, v. 78, p. 4494–4497, 1997.
- PETERSEN, T. F.; ENGELBRECHT, K.; BAHL, C. R. H.; ELMGAARD, B.; PRYDS, N.; SMITH, A. Comparison between a 1D and a 2D numerical model of an active magnetic regenerative refrigerator. *Journal of Physics D: Applied Physics*, v. 41, p. 105002(1–8), 2008.
- PETERSEN, T. F.; PRYDS, N.; SMITH, A.; HATTEL, J.; SCHMIDT, H.; KNUDSEN, H. J. H. Two-dimensional mathematical model of a reciprocating room-temperature Active Magnetic Regenerator. *International Journal of Refrigeration*, v. 31, p. 432–443, 2008.
- REAY, D. *Heat Recovery Systems: A Directory of Equipment and Techniques*. [S.l.]: E & FN Spon, 1979.
- RICHARD, M. A.; ROWE, A.; CHAHINE, R. Magnetic refrigeration: Single and multimaterial active magnetic regenerator experiments. *Journal of Applied Physics*, v. 95, p. 2146–2150, 2004.
- ROMERO, J.; FERREIRO, R.; CARBIA, J.; ROMERO, M. Experimental analysis of a reciprocating magnetic refrigeration prototype. *International Journal of Refrigeration*, v. 36, p. 1388–1398, 2013.
- ROSCA, M.; ZAWILSKI, B.; PLAINDOUX, P.; LYARD, L.; MARCUS, J.; FRUCHART, D.; MIRAGLIA, S. Direct measurements of magnetocaloric parameters. In: *Proceedings in 4th International Conference on Magnetic Refrigeration at Room Temperature*. Baotou, China: [s.n.], 2010.
- ROWE, A. Performance metrics for active magnetic refrigerators. In: *Proceedings in 3rd International Conference on Magnetic Refrigeration at Room Temperature*. Des Moines, USA: [s.n.], 2009.

- ROWE, A. Configuration and performance analysis of magnetic refrigerators. *Int. J. Refrig.*, v. 34, p. 168 – 177, 2011. ISSN 0140-7007.
- ROWE, A.; BARCLAY, J. A. Design of an active magnetic regenerator test apparatus. *Advances in Cryogenic Engineering*, v. 47, p. 995–1002, 2002.
- ROWE, A.; DIKEOS, A.; TURA, A. Experimental studies of a near room temperature magnetic refrigeration. In: *Proceedings 1st International Conference on Magnetic Refrigeration at Room Temperature*. Montreux, SWI: [s.n.], 2005.
- ROWE, A.; TURA, A.; DIKEOS, J.; CHAHINE, R. Near room temperature magnetic refrigeration. In: *Proceedings of the International Green Energy Conference*. [S.l.: s.n.], 2005.
- RUSSEK, S.; AURINGER, J.; BOEDER, A.; CHELL, J.; JACOBS, S.; ZIMM, C. The performance of a rotary magnet magnetic refrigerator with layered beds. *Proceedings of the 4<sup>th</sup> International Conference on Magnetic Refrigeration at Room Temperature, Baotou, Inner Mongolia, China*, p. 339–349, 2010.
- SANDEMAN, K. G. Magnetocaloric materials: The search for new systems. *Scripta*, v. 67, p. 566–571, 2012.
- SARLAH, A.; KITANOVSKI, A.; POREDOS, A.; EGOLF, P. W.; SARI, O.; GENDRE, F.; BESSON, C. Static and rotating active magnetic regenerators with porous heat exchangers for magnetic cooling. *International Journal of Refrigeration*, v. 29, n. 8, p. 1332–1339, 2006.
- SCHMIDT, F. W.; WILLMOTT, A. J. *Thermal Energy Storage and Regeneration*. [S.l.]: Hemisphere Publishing Co., 1981.
- SHAH, R. K.; BELL, K. J. Heat exchangers. In: KREITH, F. (Ed.). *The CRC Handbook of thermal engineering*. [S.l.]: CRC Press, 2000.
- SHAH, R. K.; SEKULIĆ, D. P. *Fundamentals of Heat Exchanger Design*. Hoboken, New Jersey: John Wiley & Sons, Inc, 2003. 941 p.
- SHEN, B. G.; SUN, J. R.; HU, F. X.; ZHANG, H. W.; CHENG, Z. H. Recent progress in exploring magnetocaloric materials. *Advanced Materials*, v. 21, p. 4545–4564, 2009.

- SIDDIKOV, B. M.; WADE, B. A.; SCHULTZ, D. H. Numerical simulation of the active magnetic regenerator. *Computers and Mathematics with Applications*, v. 49, p. 1525–1538, 2005.
- SMITH, A. Who discovered the magnetocaloric effect? *The European Physical Journal H*, v. 38, p. 507–517, 2013.
- SMITH, A.; BAHL, C.; BJØRK, R.; ENGELBRECHT, K.; NIELSEN, K.; PRYDS, N. Materials challenges for high performance magnetocaloric refrigeration devices. *Advanced Energy Materials*, v. 2, p. 1288–1318, 2012.
- SMITH, A.; NIELSEN, K. K.; CHRISTENSEN, D. V.; BAHL, C. R. H.; BJØRK, R.; HATTEL, J. The demagnetizing field of a nonuniform rectangular prism. *Journal of Applied Physics*, v. 107, 2010.
- SPALDIN, N. *Magnetic Materials: Fundamentals and device applications*. Cambridge, UK: Cambridge University Press, 2003.
- SPICHKIN, Y. I.; DERKACH, A. V.; TISHIN, A. M.; KUZMÍN, M. D.; CHERNYSHOV, A. S.; JR, K. A. G.; PECHARSKY, V. K. Thermodynamic features of magnetization and magnetocaloric effect near the magnetic ordering temperature of gd. *Journal of Magnetism and Magnetic Materials*, v. 316, n. 2, p. e555–e557, 2007.
- STEFAN, J. Ueber die gesetze der electrodynamischen induction. *Wien. Ber.*, v. 64, p. 193–224, 1871.
- TEGUS, O. *Novel materials for magnetic refrigeration*. Phd Thesis (PhD Thesis) — Universiteit van Amsterdam, 2003.
- TEGUS, O.; BRÜCK, E.; BUSCHOW, K. H. J.; BOER, F. R. de. Transition-metal-based magnetic refrigerants for room-temperature applications. *Nature*, v. 415, p. 150–152, 2002.
- TEGUS, O.; BRÜCK, E.; LI, X. W.; ZHANG, L.; DAGULA, W.; DEBOER, F. R. D.; BUSCHOW, K. H. J. Tuning of the magneto-caloric effects in mnfe(p,as) by substitution of elements. , v. 272-276, part 3, p. 2389-2390, 2004. *Journal of Magnetism and Magnetic Materials*, v. 272-276, p. 2389–2390, 2004.
- TEIXEIRA, C.; CARON, L.; ANASTASOPOL, A.; EIJT, S.; LOZANO, J.; BRÜCK, E.; WENDHAUSEN, P. A new feature

of the reduction diffusion process applied for the synthesis of magnetocaloric  $\text{LaFe}_{13} - x\text{Si}_13$  compounds. *Journal of Alloys and Compounds*, v. 541, p. 84–87, 2012.

N. Tesla. *Thermo-Magnetic Motor*. 1889. US396121.

TREVIZOLI, P. V.; Barbosa, J. R.; TURA, A.; ARNOLD, D.; ROWE, A. Modeling of thermo-magnetic phenomena in active magnetocaloric regenerators. *Journal of Thermal Science and Engineering Applications*, v. 6, p. 031016, 2014.

TREVIZOLI, P. V.; Barbosa, Jr., J. R.; FERREIRA, R. T. S. Experimental evaluation of a Gd-based linear reciprocating active magnetic regenerator test apparatus. *International Journal of Refrigeration*, v. 34, p. 1518–1526, 2011.

TREVIZOLI, P. V.; Barbosa, Jr., J. R.; OLIVEIRA, P. A.; PRATA, A. T.; FERREIRA, R. T. S. Direct measurements of the magnetocaloric effect of gadolinium samples at near room temperature. In: *Proceedings of the 20th International Congress of Mechanical Engineering, COBEM 2009*. Gramado, RS, Brazil: [s.n.], 2009.

TREVIZOLI, P. V.; OLIVEIRA, P. A.; CANESIN, F. C.; Barbosa, J. R.; FERREIRA, R. T. S. Assessment of demagnetization phenomena in the performance of an active magnetic regenerator. *International Journal of Refrigeration*, v. 35, n. 4, p. 1043–1054, 2012.

TURA, A. *Active Magnetic Regenerator Experimental Optimization*. Master's Thesis (Master's Thesis) — University of Victoria, 2005.

TURA, A.; ROSZMANN, J.; DIKEOS, J.; ROWE, A. Cryogenic active magnetic regenerator test apparatus. *Advances in Cryogenic Engineering: Transactions of the Cryogenic Engineering Conference*, v. 823, p. 985–992, 2006.

TURA, A.; ROWE, A. Design and testing of a permanent magnet magnetic refrigerator. In: POREDOS, A.; SARLAH, A. (Ed.). *Proceedings in 2nd International Conference on Magnetic Refrigeration at Room Temperature*. Portoroz, Slo: [s.n.], 2007.

TURA, A.; ROWE, A. Progress in the characterization and optimization of a permanent magnet magnetic refrigerator. In: *Proceedings in 3rd International Conference on Magnetic Refrigeration at Room Temperature*. Des Moines, USA: [s.n.], 2009.

- TURA, A.; ROWE, A. Permanent magnet magnetic refrigerator design and experimental characterization. *International Journal of Refrigeration*, v. 34, p. 628–639, 2011.
- TUŠEK, J.; ZUPAN, S.; SARLAH, A.; PREBIL, I.; POREDOS, A. Development of a rotary magnetic refrigerator. In: *Proceedings in 3rd International Conference on Magnetic Refrigeration at Room Temperature*. Des Moines, USA: [s.n.], 2009.
- TUŠEK, J.; ZUPAN, S.; SARLAH, A.; PREBIL, I.; POREDOS, A. Development of rotary magnetic refrigerator. *International Journal of Refrigeration*, v. 33, p. 294–300, 2010.
- URBAIN, G.; WEISS, P.; TROMBE, F. Un nouveau métal ferromagnétique, le gadolinium. *Comptes Rendus*, v. 200, p. 2132–2134, 1935.
- VELAZQUEZ, D.; PALACIOS, E.; ESTEPA, C.; BURRIEL, R. A versatile magnetic refrigeration demonstrator. In: *6th IIF-IIR International Conference on Magnetic Refrigeration*. [S.l.: s.n.], 2014.
- von Moos, L.; NIELSEN, K. K.; ENGELBRECHT, K.; BAHL, C. R. H. Experimental investigation of the effect of thermal hysteresis in first order material MnFe(P,As) applied in an AMR device. *International Journal of Refrigeration*, v. 37, p. 303–306, 2014.
- WAKAO, N.; KAGUEI, S. *Heat and Mass Transfer in Packed Beds*. [S.l.]: Gordon and Breach Science Publishers, 1982. 364 p.
- WEISS, P.; PICCARD, A. Sur un nouveau phénomène magnétocalorique. *Comptes Rendus*, v. 166, p. 352–354, 1918.
- YAN, A.; MÜLLER, K.; GUTFLEISCH, O. Magnetocaloric effect in  $\text{LaFe}_{11.8-x}\text{Co}_x\text{Si}_{1.2}$  melt-spun ribbons. *Journal of Alloys and Compounds*, Elsevier, v. 450, n. 1, p. 18–21, 2008.
- YARON, R.; SHOKRALLA, S.; YUAN, J.; BRADLEY, P. E.; RADEBAUGH, R. Etched foil regenerator. *Advances in Cryogenic Engineering*, v. 41, p. 1339–1346, 1996.
- YU, B.; LIU, M.; EGOLF, P. W.; KITANOVSKI, A. A review of magnetic refrigerator and heat pump prototypes built before the year 2010. *International Journal of Refrigeration*, v. 33, p. 1029–1066, 2010.

YU, B.; ZHANG, Y.; GAO, Q.; YANG, D. Research on performance of regenerative room temperature magnetic refrigeration cycle. *International Journal of Refrigeration*, v. 29, p. 1348–1357, 2006.

ZHANG, Y. X.; LIU, Z. G.; ZHANG, H. H.; XU, X. N. Direct measurement of thermal behaviour of magnetocaloric effects in perovskite-type  $\text{La}_{0.75}\text{Sr}_x\text{Ca}_{0.25-x}\text{MnO}_3$ . *Materials Letters*, v. 45, p. 91–94, 2000.

ZHENG, Z. G.; YU, H. Y.; ZHONG, X. C.; ZENG, D. C.; LIU, Z. W. Design and performance study of the active magnetic refrigerator for room-temperature application. *International Journal of Refrigeration*, v. 32, p. 78–86, 2009.

ZIMM, C.; AURINGER, J.; BOEDER, A.; CHELL, J.; RUSSEK, S.; STERNBERG, A. Design and initial performance of a magnetic refrigerator with a rotating permanent magnet. In: POREDOS, A.; SARLAH, A. (Ed.). *Proceedings in 2nd International Conference on Magnetic Refrigeration at Room Temperature*. Portoroz, Slo: [s.n.], 2007.

ZIMM, C.; BOEDER, A.; CHELL, J.; STERNBERG, A.; FUJITA, A.; FUJIEDA, S.; FUKAMICHI, K. Design and performance of a permanent-magnet rotary refrigerator. *International Journal of Refrigeration*, v. 29, p. 1302–1306, 2006.

ZIMM, C.; JASTRAB, A.; STERNBERG, A.; PECHARSKY, V.; GSCHNEIDNER JR., K. A.; OSBORNE, M.; ANDERSON, I. Description and performance of a near room temperature magnetic refrigerator. *Advances in Cryogenic Engineering*, v. 43, p. 1759–1766, 1998.

## LIST OF PUBLICATIONS

### PAPERS IN PEER-REVIEWED JOURNALS

1. Engelbrecht, K., Eriksen, D., Bahl, C.R.H., Bjørk, R., Geyti, J., Lozano, J.A., Nielsen, K.K., Saxild, F., Smith, A., Pryds, N. Experimental results for a novel rotary active magnetic regenerator. *International Journal of Refrigeration*, v. 35, p. 1498-1505, 2012. (Awarded by the Editorial Board of the International Journal of Refrigeration (IJR) and Elsevier Ltd as 'Best Paper of the Year' published in the International Journal of Refrigeration in 2012/2013)
2. Teixeira, C.S., Lozano, J.A., Caron, L., Anastasopolc, A., Eijt, S.W.H., Bruck, E., Wendhausen, P.A.P. A new feature of the reduction diffusion process applied for the synthesis of magnetocaloric  $\text{LaFe}_{13-x}\text{Si}_x$  compounds. *Journal of Alloys and Compounds*, v. 541, p. 84-87, 2012.
3. Lozano, J.A., Engelbrecht, K., Bahl, C.R.H., Nielsen, K.K., Eriksen, D., Olsen, U.L., Smith, A., Barbosa Jr., J.R., Prata, A.T., Pryds, N. Performance analysis of a rotary active magnetic refrigerator. *Applied Energy*, v. 111, p. 669-680, 2013.
4. Bez, H.N., Teixeira, C.S., Eggert, B., Lozano, J.A., Capovilla, M.S., Barbosa Jr., J.R., Wendhausen, P.A.P. Synthesis of Room-Temperature Magnetic Refrigerants Based on La-Fe-Si by a Novel Process. *IEEE Transactions on Magnetics*, v. 49, p. 4626-4629, 2013.
5. Lozano, J.A., Engelbrecht, K., Bahl, C.R.H., Nielsen, K.K., Barbosa Jr., J.R., Prata, A., Pryds, N. Experimental and numerical results of a high frequency rotating active magnetic refrigerator. *International Journal of Refrigeration*, v. 37, p. 92-98, 2014.
6. Bahl, C.R.H., Engelbrecht, K., Eriksen, D., Lozano, J.A., Bjørk, R., Geyti, J., Nielsen, K.K., Smith, A., Pryds, N. Development and experimental results from a 1 kW prototype AMR. *International Journal of Refrigeration*, v. 37, p. 78-83, 2014.

7. Bez, H.N., Eggert, B.G.F., Lozano, J.A., Bahl, C.R.H., Barbosa Jr., J.R., Teixeira, C.S., Wendhausen, P.A.P., Magnetocaloric effect and H gradient in bulk  $\text{La}(\text{Fe},\text{Si})_{13}\text{H}_y$  magnetic refrigerants obtained by HDSH, *Journal of Magnetism and Magnetic Materials*, v. 386, p. 125-128, 2015.
8. Trevizoli, P.V., Lozano, J.A., Peixer, G.F., Barbosa Jr., J.R. Design of nested Halbach cylinder arrays for magnetic refrigeration applications. *Journal of Magnetism and Magnetic Materials*, v. 395, p. 109-122, 2015.

#### PAPERS IN PREPARATION FOR PEER-REVIEWED JOURNALS

1. Lozano, J.A., Capovilla, M.S., Trevizoli, P.V., Engelbrecht, K., Bahl, C.R.H., Barbosa Jr., J.R. Development of a novel rotary magnetic refrigerator. In preparation for *International Journal of Refrigeration*, 2015.
2. Capovilla, M.S., Lozano, J.A., Trevizoli, P.V., Barbosa Jr., J.R. Performance evaluation of a magnetic refrigeration system. In preparation for *Applied Energy*, 2015.
3. Lozano, J.A., Bjørk, R., Bahl, C.R.H., Barbosa Jr., J.R. Design of a rotor-stator magnetic circuit for magnetic refrigeration. In preparation for *Journal of Magnetism and Magnetic Materials*, 2015.

#### PAPERS IN CONFERENCE PROCEEDINGS

1. Lozano, J.A., Teixeira, C.S., Zhang, L., Brück, E., Prata, A.T., Wendhausen, P.A.P. Variation of the transition-metals ratio on  $\text{Mn}_{1-x}\text{Fe}_{1+x}\text{P}_{0.6}\text{Si}_{0.3}\text{Ge}_{0.1}$  compounds. In: *Proceedings of 4th International Conference on Magnetic Refrigeration at Room Temperature (THERMAG IV)*, Baotou, China, 2010.
2. Teixeira, C.S., Kostow, M.P., Lozano, J.A., Wendhausen, P.A.P. Room-temperature magnetocaloric effect in  $\text{LaFe}_{13-x}\text{Si}_x$  compounds synthesized by calciothermic reduction-diffusion. In: *Proceedings of 4th International Conference on Magnetic Refrigeration at Room Temperature (THERMAG IV)*, Baotou, China, 2010.
3. Lozano, J.A., Engelbrecht, K., Bahl, C.R.H., Nielsen, K.K., Barbosa Jr., J.R., Prata, A.T., Pryds, N. Experimental and

- numerical results of a high frequency rotating active magnetic refrigerator. In: *Proceedings of 5th International Conference on Magnetic Refrigeration at Room Temperature (THERMAG V)*, p. 373-380, Grenoble, France, 2012.
4. Canesin, F.C., Trevizoli, P.V., Lozano, J.A., Barbosa Jr., J.R. Modeling of a parallel plate active magnetic generator using an open source CFD program. In: *Proceedings of 5th International Conference on Magnetic Refrigeration at Room Temperature (THERMAG V)*, p. 509-516, Grenoble, France, 2012.
  5. Bahl, C.R.H., Engelbrecht, K., Eriksen, D., Lozano, J.A., Bjork, R., Geyti, J., Nielsen, K.K., Smith, A., Pryds, N. Development and experimental results from 1 kW prototype AMR. In: *Proceedings of 5th International Conference on Magnetic Refrigeration at Room Temperature (THERMAG V)*, p. 53-60, Grenoble, France, 2012.
  6. Lozano, J.A., Capovilla, M.S., Zhang, L., Barbosa Jr., J.R., Direct measurement of the magnetocaloric effect in promising magnetic refrigerants. In: *Proceedings of the COBEM 2013, 22nd International Congress of Mechanical Engineering (COBEM)*, Riberão Preto, Brazil, 2013.
  7. Capovilla, M.S., Lozano, J.A., Trevizoli, P.V., Barbosa Jr., J.R. A versatile experimental setup for direct measurements of the magnetocaloric temperature change. In: *Proceedings of 6th International Conference on Magnetic Refrigeration at Room Temperature (THERMAG VI)*, Victoria, Canada, 2014.
  8. Barbosa Jr., J.R., Lozano, J.A., Trevizoli, P.V. Magnetocaloric refrigeration research at the INCT in cooling and thermophysics. In: *Proceedings of the ENCIT 2014, 15th Brazilian Congress of Thermal Sciences and Engineering (ENCIT)*, Belém, Brazil, 2014.
  9. Lozano, J.A., Capovilla, M.S., Trevizoli, P.V., Barbosa Jr., J.R. Development of a novel rotary magnetic refrigerator. In: *Proceedings of the 24th IIR International Congress of Refrigeration (ICR)*, Yokohama, Japan, 2015.



## APPENDIX A

# DEMAGNETIZATION FACTOR OF A RECTANGULAR PRISMATIC BODY

The analytical expression proposed by Aharoni (1998) for calculating the demagnetization factor,  $N_D$ , of a rectangular prismatic body, such that shown in Fig. 116, for an applied magnetic field parallel to the  $z$ -axis, is given by:

$$\begin{aligned}
 \pi N_D = & \frac{b^2 - c^2}{2bc} \ln \left( \frac{\sqrt{a^2 + b^2 + c^2} - a}{\sqrt{a^2 + b^2 + c^2} + a} \right) & (A.1) \\
 & + \frac{a^2 - c^2}{2ac} \ln \left( \frac{\sqrt{a^2 + b^2 + c^2} - b}{\sqrt{a^2 + b^2 + c^2} + b} \right) \\
 & + \frac{b}{2c} \ln \left( \frac{\sqrt{a^2 + b^2} + a}{\sqrt{a^2 + b^2} - a} \right) + \frac{a}{2c} \ln \left( \frac{\sqrt{a^2 + b^2} + b}{\sqrt{a^2 + b^2} - b} \right) \\
 & + \frac{c}{2a} \ln \left( \frac{\sqrt{b^2 + c^2} - b}{\sqrt{b^2 + c^2} + b} \right) + \frac{c}{2b} \ln \left( \frac{\sqrt{a^2 + c^2} - a}{\sqrt{a^2 + c^2} + a} \right) \\
 & + 2 \arctan \left( \frac{ab}{c\sqrt{a^2 + b^2 + c^2}} \right) + \frac{a^3 + b^3 - 2c^3}{3abc} \\
 & + \frac{a^2 + b^2 - 2c^2}{3abc} \sqrt{a^2 + b^2 + c^2} \\
 & + \frac{c}{ab} \left( \sqrt{a^2 + c^2} + \sqrt{b^2 + c^2} \right) \\
 & - \frac{(a^2 + b^2)^{3/2} + (a^2 + c^2)^{3/2} + (b^2 + c^2)^{3/2}}{3abc}
 \end{aligned}$$

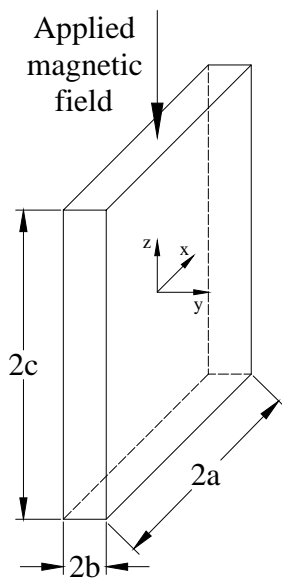


Figure 116 – Coordinate system employed for the calculation of the demagnetization factor of a rectangular prism body. The applied magnetic field,  $\mathbf{H}_{\text{appl}}$ , is parallel to the  $z$ -axis (Aharoni, 1998).

## APPENDIX B

# CHARACTERIZATION OF THE Gd SPHERES EMPLOYED AT THE UFSC MAGNETIC REFRIGERATOR

The gadolinium (Gd) spheres employed at the UFSC and DTU magnetic refrigerators were purchased from Baotou Research Institute of Rare Earth (BRIRE) in China. This appendix describes the complete characterization performed to the Gd spheres purchased at UFSC. The purchased order for the UFSC Gd spheres supposed a Curie temperature of 20°C, a purity of more than 99.8%wt and sizes between 0.3 and 0.5 mm. The Gd spheres were characterized by means of electronic microscopy, mass spectrometry, calorimetry and magnetically.

### B.1 ELEMENTAL AND MICROSCOPY ANALYSES

Initially, an elemental and microscopy analyses of the Gd spheres were carried out in the energy dispersive X-ray spectrometer (EDS) of an Scanning electron microscope (SEM), respectively, at LCME-UFSC. Figs. 117(a) and (b) show the SEM micrographs for the Gd spheres. An spherical morphology was verified with diameters between 0.3 to 0.7 mm.

The chemical composition of the spheres were initially characterized in the EDS installed at the SEM on a transversal sample, as shown in Fig. 118. The elemental analysis determined that above 98%wt of the sample contains a Gd, while some calcium (Ca) and oxygen (O) rich-phases were detected, as shown in Fig. 119. The oxygen was found specially at the surface of the spheres, while the calcium (darker spots) precipitates in the interior of the Gd phase. Usually, the EDS measurement error could be up to 2%, so a more precise chemical analysis is required.

After verifying with the manufacturer, the Gd spheres were produced starting from the  $Gd_2O_3$  mineral which is reduced with hydrofluoric acid to produce gadolinium fluoride ( $GdF_3$ ). From the latter, a calciothermic reduction is performed to obtained the Gd.

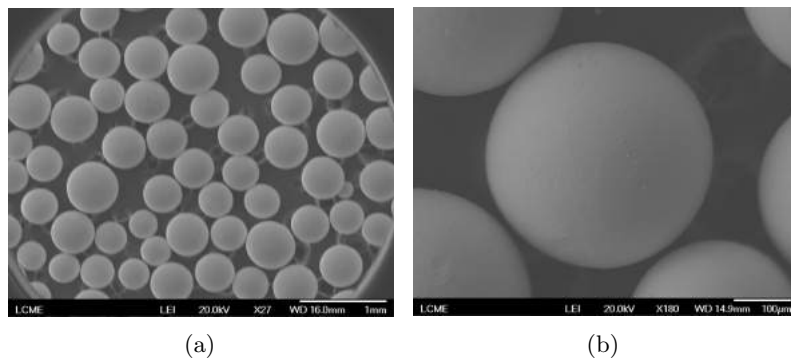


Figure 117 – SEM micrographs of the Gd spheres employed at the UFSC magnetic refrigerator at zooms (a) 27x and (b) 180x.

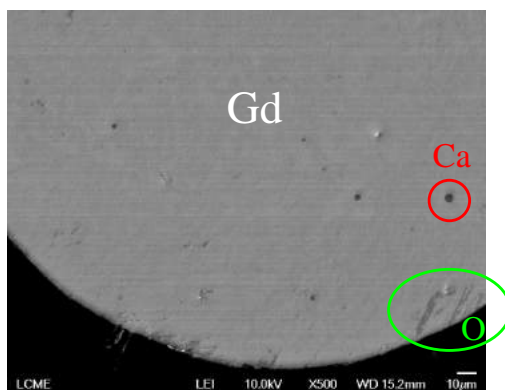


Figure 118 – Transversal SEM micrograph at 500x indicating the presence of impurities in the interior of the Gd sphere as calcium (Ca) and oxygen (O).

Thus, some oxidation can be left from the original mineral while some calcium can be precipitated from the latter chemical reduction. The spheres were produced from centrifugal atomization method under argon atmosphere, but still some oxidation could occur in this process.

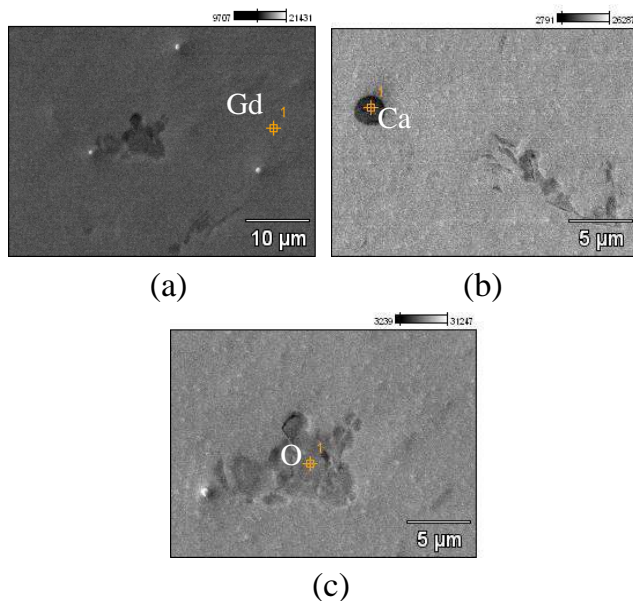


Figure 119 – EDS analysis have detected the presence of the element (a) Gd and the impurities (b) Ca and (c) O.

## B.2 MASS SPECTROMETRY ANALYSIS

A semiquantitative multielemental analysis for the determination of impurities present in the Gd spheres was performed in an inductively coupled plasma mass spectrometer (ICP-MS) at the Chemistry Department of the UFSC. An initial scan of present elements was carried out and the analyte concentration determination in % is summarized in Table 20. From these results, it can be inferred that the purity of the Gd is approximately 99.74%. However, lighter elements, such as oxygen and fluorine, can not be detected by this technique. Moreover, heavier elements, such as rare-earth, were not analyzed since the accuracy of the test would decrease, and more extensive researches would be required and that is out of the scope of this thesis. Thus, the purity of the sample was expected to be lower.

A more detailed, i.e. more accurate, scan ICP analysis was performed for the most abundant elements found in the initial test and only Ca and Fe were detected in significant concentrations. The

Table 20 – Element concentration in % in the Gd spheres.

Element	Concentration (%)
Al	0,0048
Ca	0,1757
Cu	0,0038
Fe	0,0443
Mg	0,0094
Y	0,0157
W	0,0039

results for the second ICP analysis are presented in Table 21. Three Gd samples were tested in this experiment and the measurement error was calculated in terms of the standard deviation of the concentration (concentration  $\pm\sigma$ ). Previously to this determination, a calibration curve is performed with six known standard solutions (blanks) of the selected elements to be determined, thus, the accuracy of this measurement is much higher than for the initial (scan) test. The limit of detection (LOD) for each element and it was calculated as three times the standard deviation of the blank measurements. Therefore, the detected concentration in this specific test was expected to be different, at least from the Ca and Fe content, than from the first experiment. The results have shown that the impurities contents in the Gd spheres are lower.

Table 21 – Valores das concentrações obtidas para a amostra de Gd por ICP-MS: Analyte concentration in % in the Gd spheres.

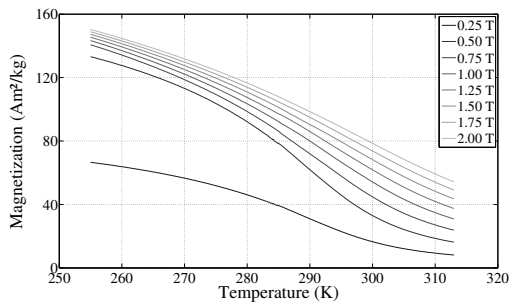
Element	Concentration ( $\mu\text{g/g}$ )	%	LOD ( $\mu\text{g/g}$ )
Ca	$12.4 \pm 1.9$	0.00124	0.56
Fe	$61.4 \pm 2.9$	0.00614	0.44

Further work, such as LECO combustion analysis, would be required to determine other impurities as oxygen, nitrogen, carbon or hydrogen. Moreover, a deeper spectrometry analysis should be perform to determine the presence of other rare-earth elements in the Gd samples. Up to this point, it is difficult to specify the exact purity of the Gd samples, but at least it should be closer to that indicated by the manufacturer (higher than 99.8%).

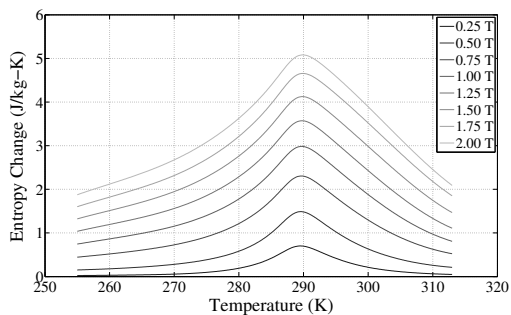
### B.3 MAGNETOMETRY CHARACTERIZATION

Th Gd samples were characterized in a magnetometer and in a calorimeter to calculate the magnetocaloric properties following the procedure presented in Section 4.5.1. The characterization of the Gd spheres employed at the UFSC magnetic refrigerator was performed at BASF in The Netherlands. The magnetization as a function of temperature was measured at different applied magnetic fields in a SQUID magnetometer and the results are shown in Fig. 120(a). The isothermal entropy change,  $\Delta S$ , and the adiabatic temperature change,  $\Delta T_{\text{ad}}$ , of the Gd spheres were calculated from combining the magnetization data obtained from these spheres and the zero-field specific heat capacity data obtained from the Gd spheres employed at the DTU magnetic refrigerator (Fig. 67(a)). The results for  $\Delta S$  and  $\Delta T_{\text{ad}}$  are shown in Figs. 120(b) and (c), respectively. The reason to employ the zero-field specific heat data from DTU is that the calorimetry measurements performed at BASF for the UFSC spheres presented an anomalous behavior in the paramagnetic state of the Gd, probably due to the very low signal of Gd at higher temperatures. Further work is suggested to improve the calorimetry characterization of the UFSC Gd spheres.

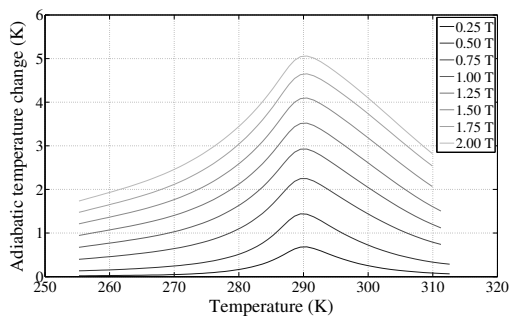
The results of the UFSC Gd spheres have shown for an applied magnetic field  $\Delta S$  peaks at  $3.0 \text{ J/kg.K}$  for 289.7 K, while  $\Delta T_{\text{ad}}$  peaks at 2.9 K for 290.5 K. These values are slightly lower than those obtained for the DTU Gd spheres (Fig. 67) with peaks at higher temperatures. The differences can be attributed to impurities and to the measurement dissimilitude.



(a)



(b)



(c)

Figure 120 – Properties of the commercial Gd spheres employed at UFSC device: (a) Magnetization, (b) integrated entropy change and (c) adiabatic temperature change derived from the  $\Delta S$  data and the zero-field specific heat capacity of the DTU Gd spheres (Fig. 67(a)).

## APPENDIX C

---

# UNCERTAINTY ANALYSIS

This appendix presents the uncertainty analysis of the UFSC magnetic refrigerator for the experimental results presented in Chapter 5.

### C.1 DEFINITIONS

The *standard uncertainty*,  $u$ , is defined as an estimate of the standard deviation of the parent population from which a particular elemental error originates (ISO, 1995). A parameter  $X$  is influenced by two error sources: *systematic* and *random*. The elemental systematic error sources do not vary during a measurement period and are the same in each measurement (Coleman & Steele, 2009). Therefore, the *systematic standard uncertainty*,  $b$ , depends mainly on the instrument errors. On the other hand, the elemental random error sources vary during the measurement period and represent the scatter of the measurements. Normally, the *random standard uncertainty*,  $s$ , is approximated by a Gaussian, or normal, distribution. Thus, the *combined standard uncertainty*,  $u_c$ , for a parameter  $X$  is described as the combination of the elemental standard uncertainties as:

$$u_X^2 = b_X^2 + s_X^2 \quad (\text{C.1})$$

The estimate of the standard deviation of the parent population for the measurements of  $X$  is calculated as (Coleman & Steele, 2009):

$$s_X = \sqrt{\frac{1}{(N-1)} \sum_{i=1}^N (X_i - \bar{X})^2} \quad (\text{C.2})$$

where  $\bar{X}$  is the mean value of the experimental values of  $X$  calcu-

lated from  $N$  measurements as:

$$\bar{X} = \frac{1}{N} \sum_{i=1}^N X_i \quad (\text{C.3})$$

In the case of a calculated parameter from multiple variables, such as  $R = f(X_1, X_2, \dots, X_J)$ , the Taylor Series Method (TSM) propagation equation can be employed to obtain the combined standard uncertainty of  $R$  as (Moffat, 1988):

$$u_R^2 = \sum_{i=1}^J \left( \frac{\partial R}{\partial X_i} \right)^2 u_{X_i}^2 \quad (\text{C.4})$$

Since the parameters are affected by two or more independent error sources, by applying the central limit theorem (CLT) the resulting distribution of  $X$  will be approximately normal (Coleman & Steele, 2009). The results are presented as expanded uncertainties,  $U$ , calculated for a 95% confidence interval for which the coverage factor  $k_{95} = 1.96$  (Kim & Simon, 1993):

$$U_{95} = k_{95} u_R = 1.96 u_R \quad (\text{C.5})$$

When the parameter  $X$  varies with time,  $X = f(t)$ , and the variations of the measurements during the sampling period are not dominated by the elemental random errors, but due to the physical phenomena itself, such as the torque and the motor power due in this work, the standard uncertainty for a typical observation of  $X$  at a specific time instant  $t_j$  can be treated as the systematic standard uncertainty of the instrument as follows (Coleman & Steele, 2009; Oliveira, 2013):

$$u_{X_j} = b_{X_j} \quad (\text{C.6})$$

Additionally, the characteristic value of  $X$  in the sampling period is the time-averaged value  $\bar{X}$  obtained as the arithmetic mean given by:

$$\bar{X} = \frac{1}{n} \sum_{j=1}^n X_j \quad (\text{C.7})$$

where  $n$  is number of observations of  $X$  during the sampling period. And the combined uncertainty of  $\bar{X}$  is obtained by the TSM

propagation method, Eq. (C.4), by employing the single observation standard uncertainties, Eq. (C.6), resulting in:

$$u_{\bar{X}} = \frac{1}{n} \sum_{j=1}^n \left( u_{X_j}^2 \right) \quad (\text{C.8})$$

## C.2 UNCERTAINTY OF THE MEASURED PARAMETERS

The uncertainty analysis assumes a cyclic steady-state, in which there are some variables that are time independent. The combined standard uncertainty of the time independent parameters in a sampling period is calculated using Eq. (C.1), while for the time-dependent parameters (i.e. torque and motor power) the combined standard uncertainty is calculated employing Eq. (C.8)<sup>1</sup>. The experimental unsteadiness in the time independent measurements is accounted for the random standard uncertainty given by Eq. (C.2). Steady-state is attained in an experiment when the standard deviation for the measurements of the regenerator temperature span is lower than 0.03 K for more than 120 s ( $s_{\Delta T_{\text{reg}}} < 0.03 \text{ K}$ )<sup>2</sup>. The original sampling frequency of the experimental measurements was 1 kHz, but since the transient physical phenomena in the experiment are not high-frequency, the samples are averaged and recorded every 0.5 s (sampling rate 2 Hz), for a better representation of the measured parameters and to eliminate any high frequency noise. The sampling period is 120 s, which results in a number of measurements  $N \simeq 240$  per experiment. The standard uncertainties associated with the data acquisition system are neglected in this analysis due to the high accuracy of the voltage readings and data conversion in comparison with the standard uncertainties of the transducers.

The systematic standard uncertainties,  $b$ , that have not been corrected by calibration are calculated from the uncertainty information provided by the transducer manufacturer. However, since most of the manufacturers did not present the confidence interval for the expanded uncertainty of the transducers used in this thesis, a rectangular (uniform) probability distribution was assumed for the transducers that were not calibrated (ISO, 1995). In such a distribution the actual value may occur anywhere within the distribution

<sup>1</sup> The *overline* notation in the time-averaged values  $\bar{X}$  has been omitted for convenience.

<sup>2</sup> This value is much lower than the expanded uncertainty for an RTD at room-temperature which was approximately  $U_{T_f,95} \sim 0.22 \text{ K}$ .

with equal probability. Thus, the systematic standard uncertainty estimate would be given by (Coleman & Steele, 2009):

$$b_X = \frac{a_X}{\sqrt{3}} \quad (\text{C.9})$$

where  $a_X$  corresponds to the upper and lower limits for the value of the measured parameter  $X$ .

The remainder of this section presents the calculation of the systematic standard uncertainty for each measured parameter,  $b_X$ , for which the value of  $a_X$  corresponds to the accuracy given by the transducer manufacturer, as summarized in Table 14.

### C.2.1 Temperature

The systematic standard uncertainty of the fluid temperature measurements was calculated using the expanded uncertainty of the resistance temperature detector (RTD)<sup>3</sup> provided by the manufacturer:

$$b_{T_f} = \frac{a_{T_f}}{\sqrt{3}} = \frac{[0.15 + 0.002 (T - 273.15 \text{ K})]}{\sqrt{3}} \quad (\text{C.10})$$

Moreover, the systematic standard uncertainty for the ambient temperature measurements were evaluated from the calibration data and the uncertainty of the reference. The T-type thermocouple was calibrated between 15 to 35°C with a reference thermometer with expanded uncertainty ( $U_{\text{ref}}$ ) of 0.09°C between 0 to 50°C for a 95.45 % level of confidence ( $k = 2.00$ ). The systematic standard uncertainty is calculated as:

$$b_{T_{\text{amb}}} = \sqrt{u_{T_{\text{amb,ref}}}^2 + u_{T_{\text{amb,fit}}}^2} = \sqrt{0.045^2 + 0.154^2} = 0.161 \text{ K} \quad (\text{C.11})$$

where  $u_{T_{\text{amb,fit}}}$  corresponds to the standard uncertainty associated with the curve fitting of data.

<sup>3</sup> The RTDs were calibrated for zero centering.

### C.2.2 Pressure

The systematic standard uncertainty for the pressure measurements was calculated from the expanded uncertainty of the pressure transducers provided by the manufacturer as:

$$b_p = \frac{a_p}{\sqrt{3}} = \frac{16}{\sqrt{3}} = 9.238 \text{ mbar} \quad (\text{C.12})$$

### C.2.3 Hot end volumetric flow rate

The systematic standard uncertainty for the hot end volumetric flow rate measurements was calculated from the expanded uncertainty of the electromagnetic flowmeter provided by the manufacturer and assuming a rectangular distribution as follows:

$$b_{\dot{V}_H} = \frac{a_{\dot{V}_H}}{\sqrt{3}} = \frac{0.005}{\sqrt{3}} \dot{V}_H \quad (\text{C.13})$$

### C.2.4 Cold end volumetric flow rate

The elemental standard uncertainties associated with the measurements of the cold end volumetric flow rate are based on the *in situ* calibration of the turbine flowmeter connected in series with the electromagnetic flowmeter (consider as a reference) for a the heat transfer fluid mixture. The standard uncertainty was calculated based on the maximum deviation between the flow rates of the turbine and the electromagnetic flowmeter (3.3%), and assuming an uniform distribution. The systematic standard uncertainty for the cold end volumetric flow rate was calculated as:

$$b_{\dot{V}_C} = \sqrt{b_{\dot{V}_H}^2 + \left(\frac{0.033}{\sqrt{3}} \dot{V}_C\right)^2} \quad (\text{C.14})$$

### C.2.5 AMR operating frequency

The systematic standard uncertainty for the AMR operating frequency was calculated from the resolution of the motor frequency inverter (0.2 RPM over the entire range) provided by the manufac-

turer and the gear couplings reduction ratio between the motor and the AMR (1:13.84):

$$b_f = \frac{a_f}{\sqrt{3}} = \frac{0.2}{\sqrt{3}} = 0.00834 \text{ RPM} = 0.139 \text{ mHz} \quad (\text{C.15})$$

### C.2.6 Thermal load

The systematic standard uncertainty of the thermal load measurements was calculated from the expanded uncertainty of the single-phase power transducer provided by the manufacturer:

$$b_{\dot{Q}_C} = \frac{a_{\dot{Q}_C}}{\sqrt{3}} = \frac{2.5}{\sqrt{3}} = 1.443 \text{ W} \quad (\text{C.16})$$

### C.2.7 Torque

The systematic standard uncertainty of the torque measurements was calculated from the expanded uncertainty of the torque transducer provided by the manufacturer:

$$b_\tau = \frac{a_\tau}{\sqrt{3}} = \frac{0.003}{\sqrt{3}} \tau \quad (\text{C.17})$$

### C.2.8 Motor power

The systematic standard uncertainty of the motor power measurements was calculated from the expanded uncertainty of the three-phase power transducer provided by the manufacturer:

$$b_{\dot{W}_M} = \frac{a_{\dot{W}_M}}{\sqrt{3}} = \frac{8.227}{\sqrt{3}} = 4.75 \text{ W} \quad (\text{C.18})$$

## C.3 UNCERTAINTY OF THE CALCULATED PARAMETERS

The combined standard uncertainty of the calculated parameters was obtained by the TSM propagation method, Eq. (C.4). The corresponding values of the measured parameters are the mean values,  $\bar{X}$ , calculated using Eq. (C.3) in the sampling period. The *overbar* notation has been omitted for convenience.

### C.3.1 Utilization

The utilization factor is given by:

$$\phi = \frac{m_f c_f}{m_s c_s} = \mathbb{C} \frac{\dot{V}_f}{f} \quad (\text{C.19})$$

where  $\mathbb{C}$  include the constant parameters:

$$\mathbb{C} = \frac{\rho_f c_f}{m_s c_s} = 0.00187374 \frac{\text{Hz}}{\text{L/h}} \quad (\text{C.20})$$

The combined uncertainty of the calculated utilization can be expressed as:

$$u_\phi^2 = \left( \frac{\partial \phi}{\partial \dot{V}_f} \right)^2 u_{\dot{V}_f}^2 + \left( \frac{\partial \phi}{\partial f} \right)^2 u_f^2 \quad (\text{C.21})$$

Substituting Eqs. (C.19) and (C.20) in Eq. (C.21) results in:

$$u_\phi = \frac{\mathbb{C}}{f} \left[ u_{\dot{V}_f}^2 + \left( \frac{\dot{V}_f}{f} \right)^2 u_f^2 \right]^{1/2} \quad (\text{C.22})$$

### C.3.2 Temperature span

In Section 5.2, four temperature differences were defined, which can take the general form:

$$\Delta T_{yz} = T_y - T_z \quad (\text{C.23})$$

The combined uncertainty of the temperature differences is given by the following expression,

$$u_{\Delta T_{yz}} = (u_y^2 + u_z^2)^{1/2} \quad (\text{C.24})$$

### C.3.3 Pressure drop

In Section 5.1, four pressure drops were defined, which can take the general form:

$$\Delta p_{yz} = p_y - p_z \quad (\text{C.25})$$

The combined uncertainty for any of the four calculated pressure drops can be expressed as:

$$u_{\Delta p_{yz}} = \left( u_{p_y}^2 + u_{p_z}^2 \right)^{1/2} \quad (\text{C.26})$$

### C.3.4 Pumping power

The pumping power is calculated as:

$$\dot{W}_P = \frac{\dot{W}_{\text{visc}}}{\eta_{\text{OP}}} = \frac{\dot{V}_f \Delta p_{\text{sys}}}{\eta_{\text{OP}}} \quad (\text{C.27})$$

The combined uncertainty of the calculated pumping power can be expressed as:

$$u_{\dot{W}_P}^2 = \left( \frac{\partial \dot{W}_P}{\partial \dot{V}_f} \right)^2 u_{\dot{V}_f}^2 + \left( \frac{\partial \dot{W}_P}{\partial \Delta p_{\text{sys}}} \right)^2 u_{\Delta p_{\text{sys}}}^2 \quad (\text{C.28})$$

Substituting Eq. (C.27) in Eq. (C.28) results in:

$$u_{\dot{W}_P} = \frac{1}{\eta_{\text{OP}}} \left[ (\Delta p_{\text{sys}})^2 u_{\dot{V}_f}^2 + (\dot{V}_f)^2 u_{\Delta p_{\text{sys}}}^2 \right]^{1/2} \quad (\text{C.29})$$

### C.3.5 Transmission power

The transmission power is calculated as:

$$\dot{W}_{\text{tr}} = \omega \bar{\tau} = 2\pi f \bar{\tau} \quad (\text{C.30})$$

The combined uncertainty of the calculated transmission power can be expressed as:

$$u_{\dot{W}_{\text{tr}}}^2 = \left( \frac{\partial \dot{W}_{\text{tr}}}{\partial f} \right)^2 u_f^2 + \left( \frac{\partial \dot{W}_{\text{tr}}}{\partial \bar{\tau}} \right)^2 u_{\bar{\tau}}^2 \quad (\text{C.31})$$

Substituting Eq. (C.30) in Eq. (C.31) results in:

$$u_{\dot{W}_{\text{tr}}} = 2\pi \left[ (\bar{\tau})^2 u_f^2 + (f)^2 u_{\bar{\tau}}^2 \right]^{1/2} \quad (\text{C.32})$$

### C.3.6 Coefficient of performance (COP)

The coefficient of performance (COP) of the actual system is calculated as:

$$\text{COP} = \frac{\dot{Q}_C}{\dot{W}_P + \dot{W}_M} \quad (\text{C.33})$$

The combined uncertainty for the calculated COP can be expressed as:

$$u_{\text{COP}}^2 = \left( \frac{\partial \text{COP}}{\partial \dot{Q}_C} \right)^2 u_{\dot{Q}_C}^2 + \left( \frac{\partial \text{COP}}{\partial \dot{W}_P} \right)^2 u_{\dot{W}_P}^2 + \left( \frac{\partial \text{COP}}{\partial \dot{W}_M} \right)^2 u_{\dot{W}_M}^2 \quad (\text{C.34})$$

Substituting Eq. (C.33) in Eq. (C.34) results in:

$$u_{\text{COP}(\dot{W}_M)} = \left( \frac{1}{\dot{W}_P + \dot{W}_M} \right) \left[ u_{\dot{Q}_C}^2 + \left( \frac{\dot{Q}_C}{\dot{W}_P + \dot{W}_M} \right)^2 (u_{\dot{W}_P}^2 + u_{\dot{W}_M}^2) \right]^{1/2} \quad (\text{C.35})$$

Moreover, the COP as a function of the transmission power (Eq. (C.30)) is given by:

$$\text{COP}(\dot{W}_{\text{tr}}) = \frac{\dot{Q}_C}{\dot{W}_P + \dot{W}_{\text{tr}}} \quad (\text{C.36})$$

The combined uncertainty for  $\text{COP}(\dot{W}_{\text{tr}})$  is calculated by substituting Eq. (C.36) in Eq. (C.34) which results in:

$$u_{\text{COP}(\dot{W}_{\text{tr}})} = \left( \frac{1}{\dot{W}_P + \dot{W}_{\text{tr}}} \right) \left[ u_{\dot{Q}_C}^2 + \left( \frac{\dot{Q}_C}{\dot{W}_P + \dot{W}_{\text{tr}}} \right)^2 (u_{\dot{W}_P}^2 + u_{\dot{W}_{\text{tr}}}^2) \right]^{1/2} \quad (\text{C.37})$$

### C.3.7 Ideal COP

The COP of the ideal (Carnot) device is given by:

$$\text{COP}_{\text{id}} = \frac{T_C}{T_H - T_C} = \frac{T_C}{\Delta T_{\text{sys}}} \quad (\text{C.38})$$

The combined uncertainty for the calculated ideal COP can be expressed as:

$$u_{\text{COP}_{\text{id}}}^2 = \left( \frac{\partial \text{COP}_{\text{id}}}{\partial T_{\text{C}}} \right)^2 u_{T_{\text{C}}}^2 + \left( \frac{\partial \text{COP}_{\text{id}}}{\partial \Delta T_{\text{sys}}} \right)^2 u_{\Delta T_{\text{sys}}}^2 \quad (\text{C.39})$$

Substituting Eq. (C.38) in Eq. (C.39) results in:

$$u_{\text{COP}_{\text{id}}} = \left( \frac{1}{\Delta T_{\text{sys}}} \right) \left[ u_{T_{\text{C}}}^2 + \left( \frac{T_{\text{C}}}{\Delta T_{\text{sys}}} \right)^2 u_{\Delta T_{\text{sys}}}^2 \right]^{1/2} \quad (\text{C.40})$$

### C.3.8 Second law efficiency

In terms of the COPs, the second law efficiency ( $\eta_{2\text{nd}}$ ) is given by:

$$\eta_{2\text{nd}} = \frac{\text{COP}}{\text{COP}_{\text{id}}} \quad (\text{C.41})$$

The combined uncertainty for the calculated second law efficiency can be expressed as:

$$u_{\eta_{2\text{nd}}}^2 = \left( \frac{\partial \eta_{2\text{nd}}}{\partial \text{COP}} \right)^2 u_{\text{COP}}^2 + \left( \frac{\partial \eta_{2\text{nd}}}{\partial \text{COP}_{\text{id}}} \right)^2 u_{\text{COP}_{\text{id}}}^2 \quad (\text{C.42})$$

Substituting Eq. (C.41) in Eq. (C.42) results in:

$$u_{\eta_{2\text{nd}}(\dot{W}_{\text{M}})} = \left( \frac{1}{\text{COP}_{\text{id}}} \right) \left[ u_{\text{COP}}^2 + \left( \frac{\text{COP}}{\text{COP}_{\text{id}}} \right)^2 u_{\text{COP}_{\text{id}}}^2 \right]^{1/2} \quad (\text{C.43})$$

Moreover, the calculated second law efficiency as a function of  $\text{COP}(\dot{W}_{\text{tr}})$  (Eq. (C.36)) is defined as:

$$\eta_{2\text{nd}}(\dot{W}_{\text{tr}}) = \frac{\text{COP}(\dot{W}_{\text{tr}})}{\text{COP}_{\text{id}}} \quad (\text{C.44})$$

The combined uncertainty for  $\eta_{2\text{nd}}(\dot{W}_{\text{tr}})$  is calculated by substituting Eq. (C.44) in Eq. (C.42) which results in:

$$u_{\eta_{2\text{nd}}(\dot{W}_{\text{tr}})} = \left( \frac{1}{\text{COP}_{\text{id}}} \right) \left[ u_{\text{COP}(\dot{W}_{\text{tr}})}^2 + \left( \frac{\text{COP}(\dot{W}_{\text{tr}})}{\text{COP}_{\text{id}}} \right)^2 u_{\text{COP}_{\text{id}}}^2 \right]^{1/2} \quad (\text{C.45})$$



**ANNEX A**

---

**DATASHEET FOR SINTERED Nd-Fe-B**



**NEODYMIUM SINTERED**

Grade	Corrosion stable *1		Remanence		Normal coercivity		Intrinsic coercivity H <sub>J</sub>				Max. energy product		Max. operating temp.**
	specify as: grade +"/S"	specify as: grade +"/ST"	Br mT		H <sub>cb</sub> kA/m		kA/m (min)				BH(max) kJ/m3		
			min	typ	min	typ	20 °C	120°C for °/ST*	150°C for °/ST*	180°C for °/ST*	min	typ	
N 35			1170	1220	870	920	955				263	279	80
N 38			1220	1260	870	920	955				279	303	80
N 40			1260	1300	870	920	955				303	318	80
N 42			1300	1330	870	920	955				318	334	80
N 45			1330	1370	900	930	955				334	358	80
N 48			1370	1410	900	930	955				358	382	80
N 50			1410	1440	830	850	875				382	398	70
N 52			1440	1470	830	850	875				398	414	70
N 33 M			1140	1170	830	880	1114				239	263	100
N 35 M			1170	1220	870	920	1114				263	279	100
N 38 M			1220	1260	900	950	1114				279	303	100
N 40 M			1260	1300	930	980	1114				303	318	100
N 42 M			1300	1330	950	1000	1114				318	334	100
N 45 M			1330	1370	980	1030	1114				334	358	100
N 48 M			1370	1410	1010	1060	1114				358	382	90
N 50 M			1410	1440	1030	1080	1114				382	398	90
N 30 H			1080	1140	810	860	1353				223	239	120
N 33 H			1140	1170	830	880	1353				239	263	120
N 35 H	35 H/S		1170	1220	870	920	1353				263	279	120
N 38 H	38 H/S	38 H/ST	1220	1260	900	950	1353	500			279	303	120
N 40 H	40 H/S	40 H/ST	1260	1300	930	980	1353	500			303	318	120
N 42 H	42 H/S	42 H/ST	1300	1330	950	1000	1353	500	500		318	334	120
N 44 H	44 H/S	44 H/ST	1330	1360	970	1020	1353	500	500		334	350	120
N 46 H	46 H/S	46 H/ST	1360	1380	980	1040	1353	500	500		350	366	120
N 48 H	48 H/S		1380	1410	1010	1060	1353				366	382	120
N 30 SH			1080	1140	810	860	1592				223	239	150
N 33 SH			1140	1170	830	880	1592				239	263	150
N 35 SH	35 SH/S	35 SH/ST	1170	1220	870	920	1592	500			263	279	150
N 38 SH	38 SH/S	38 SH/ST	1220	1260	900	950	1592	500			279	303	150
N 40 SH	40 SH/S	40 SH/ST	1260	1300	930	980	1592	500	500		303	318	150
N 42 SH	42 SH/S	42 SH/ST	1300	1330	950	1000	1592	500	500		318	334	150
N 44 SH	44 SH/S	44 SH/ST	1330	1360	970	1020	1592	500	500		334	350	150
N 46 SH	46 SH/S		1360	1380	980	1040	1592				350	366	150
N 28 UH			1040	1080	770	810	1989				199	223	180
N 30 UH	30 UH/S	30 UH/ST	1080	1140	810	860	1989	720			223	239	180
N 33 UH	33 UH/S	33 UH/ST	1140	1170	830	880	1989	720			239	263	180
N 35 UH	35 UH/S	35 UH/ST	1170	1220	870	920	1989	720			263	279	180
N 38 UH	38 UH/S	38 UH/ST	1220	1260	900	950	1989	720	720		279	303	180
N 40 UH	40 UH/S		1260	1300	930	980	1989				303	318	180
N 42 UH	42 UH/S		1300	1330	950	1000	1989				318	334	180
N 28 EH			1040	1080	770	810	2387				199	223	200
N 30 EH	30 EH/S	30 EH/ST	1080	1140	810	860	2387	950			223	239	200
N 33 EH	33 EH/S	33 EH/ST	1140	1170	830	880	2387	950			239	263	200
N 35 EH	35 EH/S	35 EH/ST	1170	1220	870	920	2387	950	950		263	279	200
N 38 EH	38 EH/S		1220	1260	900	950	2387				279	303	200
N 25 AH	25 AH/S	25 AH/ST	970	1020	730	770	2787	1200	900		180	200	220
N 28 AH	28 AH/S	28 AH/ST	1040	1080	770	810	2787	1200	900		203	218	220
N 30 AH	30 AH/S	30 AH/ST	1080	1140	810	860	2787	1200	900		220	250	220
N 25 BH	25 BH/S	25 BH/ST	950	1000	710	750	3000		1300	950	170	190	230

**Physical properties at room temperature (20°C)**

Temp.Coeff. of Br:	-0.11%/°C (20-100C)	Temp. Coeff. of iHc:	-0.60%/°C (20-100°C)
Density:	7.4-7.6g/cm <sup>3</sup>	Electrical resistivity:	144 µΩ cm
Vickers Hardness:	570 Hv	Flexural Strength:	25kg/mm
Tensile strength:	8.0kg/mm <sup>2</sup>	Coeff. of Thermal Expansion:	4 x 10 <sup>-6</sup> /°C
Specific Heat:	0.12Kcal/(kg.°C)	Thermal Conductivity:	7.7kcal/(m.h.°C)
Young's Modulus:	1.6 x 10 <sup>11</sup> N/m <sup>2</sup>	Rigidity:	0.64N/m <sup>2</sup>
Poisson's Ratio:	0.24	Compressibility:	9.8 x 10 <sup>-12</sup> m <sup>2</sup> /N
Curie Temperature:	310-340°C		

**\*1 Corrosion stable grades:**

Standard PCT test: P=2,0 atm, RH=100%, 120°C, after 7 x 24 hours, weight loss < 5mg/cm<sup>2</sup>  
 Alternative HAST test: P=2,6 atm, RH= 95%, 130°C, after 4 x 24 hours, weight loss < 3mg/cm<sup>2</sup>

**\*\*The maximum operating temperature**

The maximum operating temperature is determined by the final lay-out of the magnetic circuit. The estimated values refer to magnets which are operating at the working point of B<sub>J</sub>μ<sub>H</sub>=-1